CHARACTERIZATION OF CHROMATIN REMODELING ENZYMES IN *PLASMODIUM FALCIPARUM IN VITRO* AND *IN VIVO* AND VALIDATION AS PUTATIVE DRUG TARGETS

DISSERTATION

DISSERTATION ZUR ERLANGUNG DES DOKTORGRADES
DER NATURWISSENSCHAFTEN (DR. RER. NAT.) DER FAKULTÄT FÜR BIOLOGIE
UND VORKLINISCHE MEDIZIN DER UNIVERSITÄT REGENSBURG

vorgelegt von

Maria Theresia Watzlowik

aus

Rosenheim, Deutschland

im Jahr

2023

Das Promotionsgesuch wurde eingereicht am:
09.06.2023

Die Arbeit wurde angeleitet von:
Prof. Dr. Gernot Längst

Unterschrift

(Maria Theresia Watzlowik)

TABLE OF CONTENTS

LIST OF FIGURES

LIST OF TABLES

LIST OF ABBREVIATIONS

aa	amino acid
ac	acetylation
ADP/ATP	Adenosine diphosphate / Adenosine triphosphate
Å	Angström
AT	Adenine/Thymine
bp	Base pair
BSA	bovine serum albumin
Bt	*Bos taurus*
C	Cytosine
canon.	canonical
ChIP	chromatin immunoprecipitation
cKO	conditional knockout
CP	cytoplasm
CRE	chromatin remodeling enzyme
DAPI	4′,6-diamidino-2-phenylindole
DEG	differentially expressed gene
(h)DHFR	(human) dihydrofolate reductase
DIC	differential interference contrast
DiCre	dimerisable Cre recombinase
DMSO	dimethylsulfoxide
DNA	deoxyribonucleic acid
dNTP	2’-desoxyribonucleotide-triphosphate
(nano)DSF	(nano) differential scanning fluorimetry
DSG	disuccinimidyl glutarate
EDTA	ethylenediaminetetraacetic acid
EGTA	ethylene glycol-bis(β-aminoethyl ether)-N,N,N′,N′-tetraacetic acid
EMSA	Electrophoretic Mobility Shift Assay
etc.	*et cetera*
FBS	fetal bovine serum
FDR	false discovery rate
FPKM	fragments per kilobase of transcript per million
GC	Guanine/Cytosine
GCR	gametocyte conversion rate
GFP	green-fluorescent protein
Gg	*Gallus gallus*
GO	Gene ontology
GOI	gene of interest
HA-tag	hemagglutinin-tag
His-tag	histidine-tag
HFF	human foreskin fibroblast
hpi	hours post invasion
Hs	*Homo sapiens*
HSS	HAND-SANT-SLIDE
H1 / H2A / H2B / H3 /H4	histone 1 / 2A / 2B / 3 / 4
IFA	immunofluorescence assay
(Co)IP	(co-)immunoprecipitation
ISWI	imitation-SWI
Kb	kilobases
kDa	kilodalton

(no/i)KO	(not-induced/induced) knockout
LC-MS/MS	liquid chromatography–mass spectrometry
LECA	last eukaryotic common ancestor
loxP	locus of X-over P1
me	methylation
mFA	minimal fatty acid
MNase	Micrococcal Nuclease
mRNA	messenger RNA
MS	mass spectrometry
MST	MicroScale Thermophoresis
MW	molecular weight
NFR	nucleosome-free region
NHS	N-Hydroxy Succinimide
Ni-NTA	nickel-nitrilotriacetic acid
NP	nucleoplasma
NPCs	nucleosome positioning changes
NPS	nucleosome positioning sequence
nt	nucleotides
NTR	N-terminal region
oct	octamer
PAGE	polyacrylamide gel electrophoresis
PBS	phosphate-buffered saline
PCR	polymerase chain reaction
Pf	*Plasmodium falciparum*
PFA	paraformaldehyde
PIC	protease inhibitor cocktail
ppHSA	post-post-helicase-SANT-associated
PTM	post-translational modification
(i)RBC	(infected) red blood cell
R	ring stage
RNA	ribonucleic acid
rpm	rounds per minute
RT	room temperature
S	schizont stage
SANT	Swi3, Ada2, N-Cor, TFIIIB-domain
Sc	*Saccharomyces cerevisiae*
SD	standard deviation
SDS	sodium dodecyl sulfate
seq	high-throughput sequencing
Sf	*Spodoptera frugiperda*
SLIDE	SANT-like ISWI domain
SWI2/SNF2	switch / sucrose non-fermentable
T	trophozoite stage
TF	transcription factor
Tris	tris (hydroxymethyl) aminomethane
TSS	transcription start site
TTS	transcription termination site
UTR	untranslated region
WT	wildtype

Protein symbols are not included in the list of abbreviations.

1 SUMMARY

The complex life cycle of the malaria parasite *Plasmodium falciparum (Pf)* with its multifaceted morphological stages is accompanied by a high transcriptional variation. The orchestrated gene expression program is only explained in part by stage-specific transcription factors like the ApiAP2 family, as these factors are strongly under-represented in *Pf*. Global and local changes in chromatin structure during life cycle progression suggest the contribution of epigenetic mechanisms as a critical mechanism for fine-tuning gene regulation during malaria parasite development. The organization of genomic DNA in chromatin, which is relatively conserved across eukaryotes, exhibits remarkable differences in *Pf*, likely to accommodate the highly A/T-rich genome with > 90 % AT content in non-coding regions.

Chromatin remodeling enzymes (CREs) – responsible for re-positioning and eviction of nucleosomes at specific loci – are strongly reduced in number and highly divergent comparing *Pf* to other eukaryotes. We characterized the function of *Pf*Snf2L (PF3D7_1104200), an ISWI-related CRE, by combining *in vitro* approaches, conditional knockout studies *in vivo* and specific drug targeting. We found *Pf*Snf2L to be essential for parasite development in blood stages and to globally control just-in-time transcription regulation. Analyzing the enzymatic activity and its autoregulatory mechanism *in vitro* revealed qualitative and quantitative differences to known ISWI enzymes. *In vivo* mapping of the chromatin landscape showed that *Pf*Snf2L shapes the promoter architecture of stage-specific genes through its nucleosome remodeling activity, thereby regulating the timing of gene activation and repression. The unique properties of the Plasmodium Snf2L allowed us to set up a customized drug screen specifically targeting the activity of the remodeling enzyme. The screen identified a potent inhibitor that specifically kills the parasite, phenocopies gene expression defects of *Pf*Snf2L-KO, and inhibits the formation of sexual stages.

The findings of this study provide new insights in the complex epigenetic gene regulation of the parasite and highlight the crucial role of *Pf*Snf2L - and CREs in general - in shaping and maintaining the unique nucleosomal landscape in *Plasmodium falciparum.* Furthermore, with their functional divergence, plasmodial CREs represent a potential target for new antimalarial drugs that will be required in view of emerging resistant parasite strains.

2 INTRODUCTION

This section contains verbatim and analogous quotations from a review I published during the preparation of this work. Content from Watzlowik et al. 2021 (see Appendix) has been shortened in some parts or supplemented with new findings. Direct and indirect citations are not marked as such; only primary references are cited. This is limited to the introduction section.

2.1 *Plasmodium falciparum* – a parasite with many faces

Plasmodium falciparum, a unicellular eukaryotic parasite, causes the most severe and deadly form of the human disease malaria. In 2021, 247 million people were infected with malaria and about 619 000 died as a consequence, mostly children under the age of five (World Health Organization, 2022). Malaria remains a major threat to humans, and the situation may worsen as parasites increasingly develop resistance to the frontline choice of treatment, the Artimisinin-based combinational therapy, just as resistance to other effective drugs has emerged (Haldar et al., 2018). An urgent need for new antimalarial drugs is evident, but this requires a better understanding of the physiological, biochemical and pathological mechanisms of the parasite.

The parasite *P. falciparum* is characterized by a complex life cycle, which includes two different hosts, sexual and asexual reproduction as well as the invasion of various cell types (Lucius et al., 2017; Sato, 2021) (Figure 2-1). The infection of humans - the intermediate host - begins with the bite of an Anopheles mosquito, whereby *Pf* sporozoites are transmitted into the human bloodstream. The infective sporozoites are transported to the liver, where they invade hepatocytes and undergo one cycle of asexual reproduction (Prudêncio et al., 2006). After accomplishing the so-called exoerythrocytic schizogony, the parasites release up to 36 merozoites, haploid daughter cells, into the bloodstream. The invasion of erythrocytes initiates the intra-erythrocytic developmental cycle, in which the parasites develop from ring stage to trophozoite stage before undergoing multiple rounds of replication to schizonts (Arnot et al., 2011; Cowman and Crabb, 2006). With rupture of the red blood cells (RBCs), merozoites are released and able to infect new erythrocytes completing the asexual reproduction cycle of approximately 48 h. This cyclical process causes the typical malaria symptoms of fever, with relapses occurring at two-day intervals or more irregularly in *P. falciparum* infection (Trampuz et al., 2003). During this phase, one of 60 virulence factors encoded by *var* genes is mutually exclusively expressed and exported to the RBC surface for adhesive interaction with the host. Regular switching of *var* gene generates antigenic variation to evade host cell immune response (Scherf et al., 2008). Within the intraerythrocytic cycle, a small proportion of parasites (<10 %) differentiate into male micro- and female macro-gametocytes (Josling and Llinás, 2015). For transmission, these sexual erythrocytic parasites are taken up by a mosquito, where further maturation occurs in the midgut. After fusion of micro- and macrogametes to form a diploid zygote, it develops into an oocyst, from which numerous sporozoites emerge in the epithelial cells. Migration into the salivary glands and further maturation allows infection of new host organisms (Aly et al., 2009).

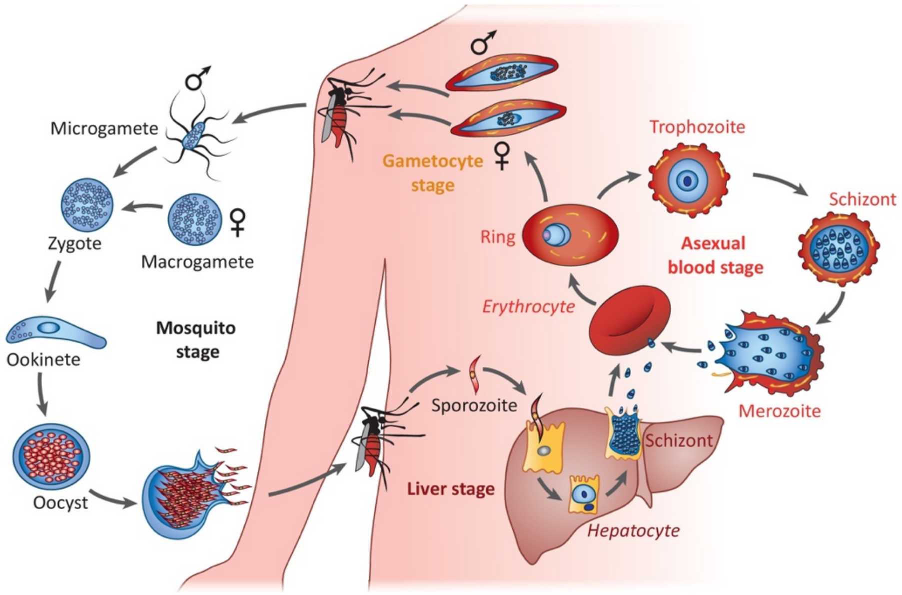

Figure 2-1: Schematic illustration of the Plasmodium falciparum life cycle *(Maier et al., 2019).*

This versatile multi-stage life cycle is tightly regulated, with defined sets of proteins being concertedly expressed in specific phases of the life cycle. The underlying regulatory mechanisms of this highly orchestrated gene expression program in *Plasmodium falciparum* are poorly understood. As a common principle in eukaryotes, gene regulation occurs at many levels, starting with the control of DNA accessibility within chromatin, followed by transcriptional control, post-transcriptional regulation, translational control, protein stability and activity and additional mechanisms (Reece and Campbell, 2011).

2.2 Plasmodium chromatin – a special case

2.2.1 A genome architecture AT the extreme

The *Plasmodium falciparum* (*Pf*) genome, sequenced in 2002 (Gardner et al., 2002), consists of 23.3 million base pairs, organized in 14 chromosomes, plus 6 kb of mitochondrial and 34 kb of apicoplast DNA located in the respective extranuclear organelles (Böhme et al., 2019). The parasite features one of the most AT-rich genomes among eukaryotes with an overall AT-content of 80.7 % and up to 95 % within intergenic regions and introns (Su et al., 2019). This comes along with numerous regions of low complexity, simple sequence repeats and a skewed codon usage bias. Transcriptome-wide studies have shown that ~85 % of all 5400 genes are transcribed at detectable levels in asexual blood stages (Bunnik et al., 2013; Le Roch et al., 2003; Otto et al., 2010). Most of them (> 75 %) reach high mRNA abundance at only one time-point in their 48-hour life cycle creating a cyclic pattern that requires a complex regulatory network (Alvarez et al., 2021; Bozdech et al., 2003).

In general, the *Pf* genome exhibits typical eukaryotic features, with genes consisting of exons and introns separated by intergenic regions. However, gene architecture clearly differs in some respect from other unicellular eukaryotes (Table 2-1). Yeast, for example, has a comparable number of genes encoded in a genome half the size. Most features, such as mean gene length, mean exon length, intergenic regions and 5' untranslated regions (5'UTR) are unusually long in *Pf* and a remarkable large proportion of genes larger than 4000 bp are found (Francis and Wörheide, 2017; Gardner et al., 2002). Exon and 5'UTR length are exceptional even in comparison with higher eukaryotes such as human cells. This correlates with large low-complexity regions encoding putatively unstructured protein domains.

As in other eukaryotes, *Pf* genes exhibit the characteristic bipartite structure of *cis*-regulatory regions with enhancer elements and basal promoters required for the recruitment of RNA polymerase II to the transcription start site (TSS) (reviewed in (Horrocks et al., 2009; Toenhake and Bártfai, 2019)). Most primary TSSs are relatively distant from the first exon and generate long 5'UTRs, but the majority of genes were shown to have multiple clusters of TSSs generating alternative mRNA 5' ends (Adjalley et al., 2016; Pesole, 2002; Shaw et al., 2022; Watanabe et al., 2002). Thus, genome-wide mapping of TSSs revealed highly diverse sets of start sites, that are far more variable than those of human or yeast genes (Carninci et al., 2006; Lu and Lin, 2019). While the complexity in human gene expression is highly dependent on splicing-related regulation, the variability of *Pf* gene expression is more controlled by transcriptional control (Ast, 2004; Yeoh et al., 2019).

Table 2-1: Comparison of gene architecture *in Homo sapiens (Hs) / Saccharomyces cerevisiae (Sc) / Plasmodium falciparum (Pf). Remarkable differences in Pf pointing towards transcriptional gene regulation are highlighted bold.*

	%AT	Mean length (bp) of …					#	% of genes with...		
	genome	gene	5'UTR	exon	intron	inter-genic	TFs	multiple TSSs	introns	altern. splicing
Sc	62 %	1400	150	200-300	~100	500	170	56 %	5 %	<1%
Pf	**81 %**	2300	**346**	949	180	1700	**73**	**92 %**	54 %	<5%
Hs	59 %	12000	150	200-300	<200		>1500	58 %	99 %	~50%

Packaging of the promoter DNA into nucleosomes and changes in nucleosome positioning and histone composition have been shown to affect gene activity (Bártfai et al., 2010; Horrocks and Lanzer, 1999; Kensche et al., 2016). Using *in silico* approaches, very few putative *cis*-regulatory motifs could be predicted, but these few are overrepresented in the upstream region of genes and do not share sequence similarity with those of other eukaryotic organisms (Iengar and Joshi, 2009; Wu et al., 2008; Young et al., 2008). Recent studies showed that the majority of the plasmodial genome is organized in regulatory units containing multiple genes and multiple regulatory elements with coordinated activity, rather than a one-on-one allocation of *cis*-regulatory elements to their neighboring genes (Wang et al., 2020).

2.2.2 The trans-acting factors – *is that all there is*?

The principle of gene expression regulation is based on the binding of specific transcription factors (TFs) to *cis*-regulatory motifs. Surprisingly, only 73 TFs were identified in *Pf* for more than 5000 genes, far below the numbers in yeast and human cells (Bischoff and Vaquero, 2010; Hahn and Young, 2011; Zhang et al., 2012). In addition, most of the major families of eukaryotic TFs such as homeodomains, basic leucine zippers, GATA fingers, nuclear hormone receptors and FKH domains could not be identified by homology search (Lambert et al., 2018). Apart from some low-conserved general transcription factors, helix-turn-helix proteins and C2H2-type zinc fingers, *Pf* possess only a few sequence-specific factors (Bischoff and Vaquero, 2010). 27 ApiAP2 proteins belong to an Apicomplexan-specific TF family that is proposed to be the main regulator of transcription in the parasite life cycle (Balaji et al., 2005; Coulson et al., 2004; Toenhake and Bártfai, 2019). Most ApiAP2 proteins have been shown to exhibit sequence-specific DNA binding, with some of them driving transcriptional regulation of stage-specific genes, such as invasion genes (AP2-I), gametocyte genes (AP2-G), or liver-stage genes (AP2-L) (Campbell et al., 2010; Iwanaga et al., 2012; Jeninga et al., 2019; Kafsack et al., 2014; Modrzynska et al., 2017; Santos et al., 2017). Still the question remains, how such a small number of factors is sufficient to coordinate the complex gene expression profile of more than 5000 genes, even if they act in a combinatorial fashion or with additional interacting proteins (Levo and Segal, 2014; Modrzynska et al., 2017; Russell et al., 2014; Santos et al., 2017; Vannoort and Huynen, 2006).

The interplay between *cis*-acting elements and *trans*-acting factors is strongly influenced by the packaging of the genomic DNA into chromatin. Nucleosome positioning and dynamics control the accessibility of the regulatory DNA elements for the *trans*-acting factors, as histones would mask the binding sites and inhibit DNA sequence recognition. Therefore, nucleosome positioning plays an essential role and well-defined chromatin architectures can be observed at regulatory regions. *Pf* chromatin structure analysis is still in its infancy, but first genome-wide profiling studies using MNase-Seq or ATAC-Seq addressed this question and indicate an organized system (Kensche et al., 2016; Toenhake et al., 2018). However, the detailed relationship between promoter architecture and transcription factor binding remains to be elucidated. Chromatin dynamics and nucleosome positioning may be a consequence of transcription factor binding or represent a preceding event regulated by chromatin remodeling enzymes that determine DNA accessibility.

2.2.3 Plasmodium nucleosomes – *the same and yet different*

Nucleosomes are the basic packaging unit of chromatin, consisting of a histone octamer associated with 147 base pairs of DNA wrapped around the proteins in 1.65 turns (Figure 2-2A). The octamer typically consists of the four canonical histones H2A, H2B, H3 and H4, which are - due to their central function in DNA packaging - highly conserved in sequence throughout eukaryotic evolution (Baxevanis and Landsman, 1998). However, the *Pf* histones show exceptionally high divergence with sequence identities of only 68 %, 58 %, 93 % and 91 % between human and *Pf* H2A, H2B, H3 and H4 respectively (Figure 2-2B). The fifth histone H1, usually linking nucleosomes and promoting higher order structure, is not present in *Pf* (Gardner et al., 2002).

In accordance with the diverging sequence of histones, plasmodial nucleosomes exhibit distinct biochemical properties when compared to human nucleosomes. Wrapping of DNA around a histone octamer requires bending of the relatively rigid molecule, which is determined by the sequence composition, as GC and AT base pairs do not have the same size and geometry. Repetition of certain motifs can induce a directed DNA curvature, that mimics the folding around the histone octamer, requiring less bending energy for nucleosome formation and thus, representing preferential binding sites for nucleosomes (Widom, 2001). It is a general eukaryotic principle that the genome sequence encodes a basic chromatin architecture in which the sequence of base pairs favors nucleosome positioning and occupancy at specific sites (Linzweiler and Horz, 1985; Mengeritsky and Trifonov, 1983; Segal et al., 2006). However, the AT-rich plasmodial genome sequence, especially in the regulatory regions, creates a very different basis for chromatin structure, and *Pf* histones also show deviating affinities when forming nucleosomes. *Pf* nucleosomes have an overall reduced nucleosome stability with a weaker binding of H2A and H2B. An attenuated histone-DNA interaction increases the mobility of nucleosomes on DNA and they have intriguingly lost the capability of sequence-dependent nucleosome positioning (Silberhorn et al., 2016). *In silico* modeling and cryo-EM structures of *Pf* nucleosome suggest an overall similar nucleosome core structure with some divergent amino acids in the histone-DNA interacting

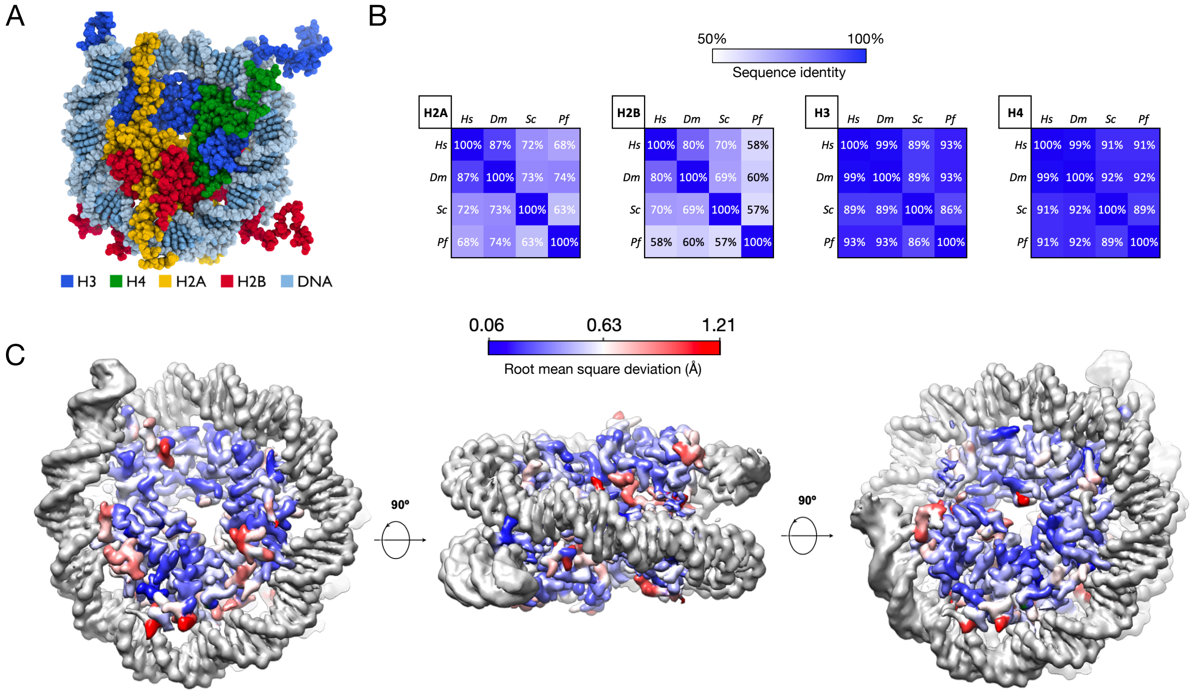

H2A	Hs	Dm	Sc	Pf
Hs	100%	87%	72%	68%
Dm	87%	100%	73%	74%
Sc	72%	73%	100%	63%
Pf	68%	74%	63%	100%

H2B	Hs	Dm	Sc	Pf
Hs	100%	80%	70%	58%
Dm	80%	100%	69%	60%
Sc	70%	69%	100%	57%
Pf	58%	60%	57%	100%

H3	Hs	Dm	Sc	Pf
Hs	100%	99%	89%	93%
Dm	99%	100%	89%	93%
Sc	89%	89%	100%	86%
Pf	93%	93%	86%	100%

H4	Hs	Dm	Sc	Pf
Hs	100%	99%	91%	91%
Dm	99%	100%	92%	92%
Sc	91%	92%	100%	89%
Pf	91%	92%	89%	100%

Figure 2-2: Divergent structure of* Pf *nucleosomes. A. *Human nucleosome core particle structure with histones and DNA depicted in space filling representations and colored as indicated (McGinty and Tan, 2015).* ***B.*** *Sequence identity of Hs/Dm/Sc/Pf canonical histones.* ***C.*** *Structural divergence between P. falciparum and Xenopus laevis canonical nucleosome (G. Längst, manuscript in preparation).*

regions and remarkable variation in the flexible histone tail regions (Silberhorn et al. 2016, manuscript in preparation) (Figure 2-2C). The contribution of histone tails to nucleosome positioning is widely acknowledged. However, the altered nucleosome properties in *Pf* don't represent an adaption to the AT-rich plasmodial genome. *In vivo* analysis revealed a significant number of positioned nucleosomes, mainly located at regulatory regions, raising the question of the mechanisms being responsible for nucleosome positioning *in vivo,* although the *Pf* histone octamer does not recognize the underlying sequence code.

In addition to canonical histones, eukaryotes express histone variants throughout the cell cycle, that differ in amino acid sequence (Martire and Banaszynski, 2020). Sequence variation occurs predominantly in the (N-)terminal histone tails and leads to novel and different sites of post-translational modifications, potentially affecting their function and interaction with chromatin modifying enzymes (Miao et al., 2006). Among eukaryotic species, different sets of variant histones are prevalent, with some ubiquitous variants having specialized functions in DNA repair (H2A.X), transcription activation (H2A.Z), kinetochore formation (CenH3) and transcription in general (H3.3) (Kamakaka, 2005). In *P. falciparum*, a homologue of the universally present H2A.Z has been identified, but no H2A.X. Surprisingly, Apicomplexa additionally express an unusual H2B variant histone, termed H2B.Z, the function of which is still unclear. Genome-wide profiling revealed similar binding sites of *Pf*H2A.Z and *Pf*H2B.Z and co-immunoprecipitation experiments confirmed the existence of nucleosomes containing both, H2A.Z and H2B.Z in the same octamer (Hoeijmakers et al., 2013; Petter et al., 2013). This observation is shared with studies in other Apicomplexa, including *Toxoplasma gondii*, indicating a role in the regulation of gene expression (reviewed in (Vanagas et al., 2019)). Histones H3.3 and CenH3, the two universal variants replacing histone H3, are present in *P. falciparum*, although they have not been characterized in detail. The relatively divergent histone H3.3 (eight amino acid substitutions compared to canonical H3) is proposed to preferentially bind GC-rich repetitive regions, independent of transcriptional activity , potentially contributing to the regulation of *var* gene expression and immune evasion (Fraschka et al., 2016). The second H3 variant, CenH3, is enriched at AT-rich sequences of the centromere and is implicated in chromosome segregation (Fraschka et al., 2016; Hoeijmakers et al., 2012).

All histones are furthermore targets for post-translational modifications (PTMs), mainly involving acetylation, methylation, and phosphorylation of the histone amino termini, which alter histone properties and their interactions with DNA and chromatin proteins, thereby affecting the functionality of the underlying DNA. The combinatorial nature and functional impact of these epigenetic modifications is defined as the “histones code” amplifying the information content and plasticity of chromatin with respect to the regulation of all DNA-dependent processes (Ay et al., 2015; Jenuwein, 2001). Again, *P. falciparum* exhibits striking differences to other eukaryotes with an unusually large proportion of constitutively acetylated histones and the high number of 500 identified PTMs, including several novel modifications specific to *Plasmodium* or Apicomplexa (Ay et al., 2015; Salcedo-Amaya et al., 2009; Saraf et al., 2016). A recent study showed, that some universal eukaryotic PTMs, initially proposed to be absent in *P. falciparum*, are tightly regulated and their presence is restricted to specific life cycle stages (Coetzee et al., 2017; Jeninga et al., 2023). The presence of some dynamic PTMs that peak at particular stages, such as H3K4 and H3K27 modifications, highlights their contribution to gene expression regulation throughout stage development (Ay et al., 2015; Coetzee et al., 2017; Read et al., 2019).

2.2.4 Nucleosomes positioning – *should I stay, or should I go*?

Definitions acc to. (Segal and Widom, 2009):

Nucleosome occupancy: probability of a base pair to be covered by a nucleosome.

Nucleosome positioning: probability of a base pair to serve as nucleosome start, dyad or end.

The reduced stability and loss of sequence-dependent positioning of plasmodial nucleosomes *in vitro* is reflected by the genome-wide analysis of chromatin structure *in vivo*.

In *Pf*, large genomic regions lack positioned nucleosomes or even appear to lack histone octamers on DNA at all. Several studies have addressed the in *P. falciparum*, using Sonication-ChIP, MNase-ChIP, MNase-Seq and other methods such as ATAC-Seq and FAIRE to detect nucleosome-free regions (NFRs) (Bunnik et al., 2014; Kensche et al., 2016; Ponts et al., 2011, 2010; Ruiz et al., 2018; Toenhake et al., 2018; Westenberger et al., 2009). In summary, these studies show higher nucleosome density in heterochromatin, but contradicting experimental results have been obtained regarding the nucleosome occupancy in genic or intergenic regions. Considering only studies with partial MNase digestion conditions that avoid over-digestion of less stable nucleosomes suggests a rather genome-wide organized nucleosomal landscape, that might require more careful digestion due to low nucleosome stability (Chereji et al., 2016; Kensche et al., 2016; Schwartz et al., 2019).

Intriguingly, the transcription unit of a typical gene in *P. falciparum* is framed by positioned nucleosomes upstream and downstream of the coding region resulting in the covering of regulatory regions and functional elements in the genome by positioned nucleosomes. A positioned +1 nucleosome can be mapped directly at the TSS next to an upstream NFR of variable size and a detectable -1 nucleosome further upstream. This is a common pattern in eukaryotes, albeit the clarity and effectiveness of nucleosome positioning at these sites appear to be relaxed. The width of the NFR varies between individual *Pf* promoters with larger NFRs tending to be associated with higher transcription levels. Positioned nucleosomes can also be detected at start and stop codons, as well as at exon-intron-boundaries. These observations suggest that nucleosome positions somehow highlight transcriptionally relevant landmarks, but positioning is less stringent and more fuzzy, when compared to other eukaryotes.

Comparative analysis of nucleosome positioning dynamics at different life cycle stages shows that most nucleosomes in the transcription unit are static and non-dynamic, indicating no gross changes in chromatin structure with variable gene expression. However, upstream promoter regions show significant changes in nucleosome occupancy levels during the life cycle, correlating with changes in gene transcription. With increasing transcriptional activity, NDRs appear, that may be related to the formation of the RNA polymerase II initiation complexes. Accordingly, gene repression correlates with a dynamic increase of nucleosome levels inhibiting transcription initiation (Bunnik et al., 2014; Kensche et al., 2016; Ponts et al., 2011). The data suggest local changes in nucleosome occupancy around specific DNA motifs within these 5' intergenic regions being indicative of transcription factor binding, whereas global chromatin structure remains unaltered throughout the life cycle (Kensche et al., 2016).

Studies mapping the genomic localization of nucleosomes containing the histone variants

H2A.Z and H2B.Z identified them in the intergenic regions of euchromatin domains, particularly enriched at gene promoters (Bártfai et al., 2010; Hoeijmakers et al., 2013; Petter et al., 2013; Vanagas et al., 2019). The levels of variant nucleosome do not change over the life cycle, suggesting that they permanently mark promoters and regulatory regions with *var* genes as an exception (Petter et al., 2013). Moreover, the histone variant *Pf*H3.3 is preferentially located at euchromatic coding and subtelomeric repetitive sequences unrelated to transcription, whereas in other eukaryotes H3.3 is incorporated at sites of active transcription (Mito et al., 2005). Interestingly, *Pf*H3.3 incorporation was also found at promoters of poised and active (but not inactive) *var* genes pointing to its putative contribution to epigenetic memory in *var* gene expression (Fraschka et al., 2016).

Not only the distribution of histone variants, but the occupancy and positioning of *Pf* nucleosomes in general do not quite follow known eukaryotic principles. As the erythrocyte life cycle progresses, major global changes in nucleosome occupancy have been reported, which is also unique to *Plasmodium falciparum* (Ay et al., 2014; Bunnik et al., 2014; Ponts et al., 2010). The highly divergent underlying determinants – DNA and histone properties – appear to shape a very different chromatin landscape in *Pf,* and potential novel mechanisms may have evolved to enable the tightly regulated gene expression program in the parasite.

Nuclear organization is proposed to be another epigenetic layer contributing to gene expression regulation using mechanisms such as rearrangement of chromosomes, locus repositioning and heterochromatic silencing (Abel and Le Roch, 2019). Various studies have attempted to unveil the three-dimensional nuclear organization of *Plasmodium falciparum* using chromosome conformation capture techniques (reviewed in (Abel and Le Roch, 2019; Hollin et al., 2020)). Characteristic for *P. falciparum* is the absence of chromosome territories which supports the presence of a relatively accessible chromatin structure. Although clustering could be demonstrated for certain genomic domains, such as heterochromatin foci, telomeres and ribosomal DNA, no pronounced chromosome condensation comparable to other eukaryotes was observed (Rowley and Corces, 2016).

2.3 Epigenetic regulation of Plasmodium transcriptional activity

As described in previous sections, gene transcription is impacted by a combination of epigenetic features shaping the chromatin landscape: The main determinants are the variations of nucleosome occupancy and nucleosome positioning at specific DNA elements, histone variants, in addition to the dynamic histone PTMs as well as higher order chromatin structures. Finally, the driving force is the accessibility of promoters and enhancers within chromatin – implemented by correct nucleosome positioning – for transcription factor binding and initiation complex formation (Zhu et al., 2018). Genome-wide MNase-Seq (Kensche et al., 2016) and ATAC-Seq data (Toenhake et al., 2018) confirm this principle in *P. falciparum*: The majority of dynamic nucleosomes, as well as the most accessible regions, were found to be located in promoter regions and correlate with the transcriptional activity of the downstream gene.

For some genes with high transcriptional variation, the epigenetic mechanisms have been studied in more detail, such as invasion genes or *var* genes (reviewed in (Abel and Le Roch, 2019)). Sexual commitment is also known to be regulated by the epigenetic cascade, starting with Ap2-G expression being repressed by HP1, which is evicted upon association of gametocyte development 1 (GDV1) with heterochromatin, and GDV1 itself controlled by the *gdv1* antisense RNA (Brancucci et al., 2014; Filarsky et al., 2018; Kafsack et al., 2014; Sinha et al., 2014). The aspect of concomitant nucleosome occupancy and positioning has been hardly taken into consideration describing these epigenetic mechanisms, but it determines any interactions with the underlying DNA locus and certainly contributes. The importance of nucleosome occupancy was highlighted in a machine learning model, where the relevance of individual epigenetic features in relation to the entirety of transcription regulation was assessed (Read et al., 2019): A collection of genomic and epigenomic datasets including information on transcription factor binding motifs, patterns of covalent histone modifications, nucleosome occupancy, GC content and global 3D genome architecture were analyzed for their prevalence in high/low-expression genes. This kind of comparative analysis emphasizes the relevance of histone modifications, nucleosome occupancy and 3D chromatin architecture and suggest transcription factor binding to be less important for transcription regulation.

2.4 Chromatin remodeling enzymes

All DNA-dependent processes require dynamic changes of chromatin organization to exert their DNA specific activities. For this, eukaryotic cells have evolved numerous enzymes that change the organization of DNA packaging (Narlikar et al., 2002). CREs alter chromatin structure by moving nucleosomes, while chromatin modifiers leave their chemical marks on chromatin to alter the physicochemical properties of the chromatin fiber, or to target protein/RNA complexes to specific genomic loci. The high variability of global and local chromatin packaging states and the numerous chromatin modifications associated with different functional processes, demonstrate the superordinate role of chromatin proteins in eukaryotic cells.

2.4.1 Diversity of chromatin remodeling enzymes

CREs and the large multiprotein complexes they form exert a direct ATP-dependent effect on nucleosomes. The enzymes alter histone-DNA interactions, resulting in eviction, exchange and assembly of individual histones or histone octamers, changing the structure and stability of nucleosomes, or the movement of histone octamers on DNA to re-position nucleosomes (Figure 2-3A, reviewed in (Bartholomew, 2014a; Becker and Workman, 2013)). To disrupt the highly stable interaction between histones and DNA, these enzymes couple their activity to ATP hydrolysis. All CREs share a highly conserved ATPase module, which is split into a Snf2_N and a Helicase C domain, separated by a P-loop. The enzymes generally contain several additional protein domains, that determine specificity in substrate recognition and interaction with other proteins or RNA to form a variety of protein complexes (Erdel et al., 2011).

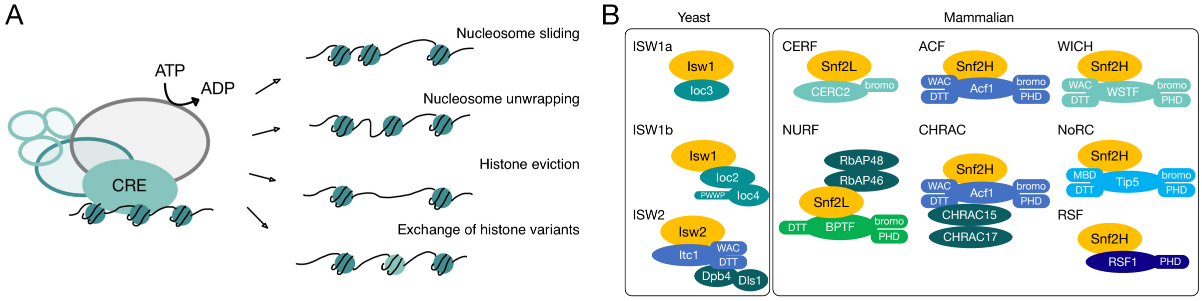

Figure 2-3: Diversity in function and composition of chromatin remodeling complexes. A. *Schematic representation of CRE functions, adapted from (Zhong, Kanagaratham, and Radzioch 2013).* ***B.*** *Identified ISWI-containing complexes in yeast and mammalian cells.*

The essential molecular function of this family of enzyme is to move of nucleosomes in order to provide or restrict access to certain DNA regions. However, the exact regulatory mechanisms of this process – in terms of which nucleosomes are recognized to be moved and what the target position is – are not completely uncovered. There is some evidence that “high affinity” and “low affinity” nucleosomes represent a putative mechanism or at least an aspect of defining reaction educts and products (Rippe et al., 2007). Thereby, multiple factors such as the recognition of DNA sequences and structures, nucleosome composition and histone PTMs play a crucial role. The specificity of remodeling machines also depends on the central motor protein as well as the composition of all the associated complex subunits, dramatically altering the responsiveness to various substrates and recruitment mechanisms (Bartholomew, 2014a; Becker and Workman, 2013). In human and mouse cells, it has been estimated that over 1000 different chromatin remodeling complexes with distinct functions may exist. Their cell type-specific combination and dosage is likely to determine the cell type-specific chromatin architecture, the gene expression network and the responsiveness to specific signaling pathways in the cell (Bartholomew, 2014a; Becker and Workman, 2013; Clapier et al., 2017; Narlikar et al., 2013; Rippe et al., 2007). As an example, Imitation-SWI (ISWI) proteins can form three complexes with different subunits in yeast, while even more conserved complexes such as NoRC, NURF and ACF have been identified in mammalian cells (Figure 2-3B). *Hs*Snf2H has been purified in 18 different multiprotein complexes emphasizing the complexity of the “remodeling code” (Oppikofer et al., 2017).

The functionally distinct subfamilies of SWI2/SNF2 ATPases are grouped by the homology of the helicase region (indicated by coloring in Figure 2-4) (Flaus, 2006). Starting with the Snf2-like group, the ISWI subfamily is mainly responsible for nucleosome re-positioning, playing a role in nucleosome stabilization and higher order structure (Corona et al., 2007; Strohner et al., 2005). In contrast, Snf2 enzymes have a more disruptive effect on nucleosomes and Lsh proteins are associated with transcription silencing in cooperation with methyltransferases (Dechassa et al., 2010; Myant and Stancheva, 2008; Ren et al., 2015). Chd proteins, comprising the Chd1, Mi-2 and Chd7 subfamily, possess specific nucleosome remodeling activities and are characterized by their additional chromodomain being involved in processes such as nucleosome spacing during chromatin assembly (Ocampo et al., 2016; Pointner et al., 2012), or acting as regulators of gene expression in functionally distinct complexes (Bowen et al., 2004; Hoffmeister et al., 2017). The principal functions of the Swr1-

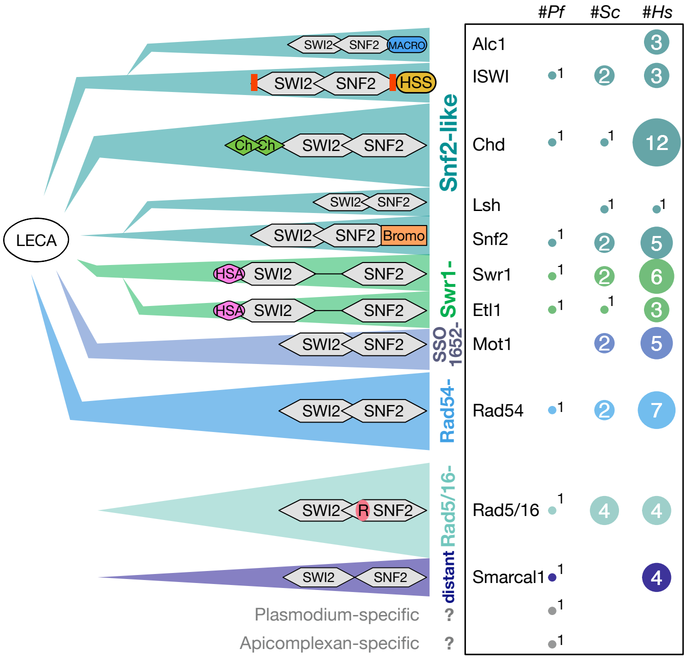

Figure 2-4: Evolutionary and phylogenetic development of SWI2/SNF2 ATPases *with triangles grouping together multiple subfamilies and their conserved domain architecture illustrated. Grouping of subfamilies and their names according to Flaus et al. 2006 are indicated by coloring and circles represent numbers of prevalent proteins for P. falciparum, S. cerevisiae and H. sapiens (Iyer et al., 2008; Watzlowik et al., 2021). Domain names: Ch=Chromo, R=RING, HSA=helicase/SANT-associated.*

like group – identifiable by the split helicase domain and the HSA domain – include histone eviction and variant exchange (Morrison and Shen, 2009). Rad54-like proteins appear to alter DNA topology and alter nucleosomal accessibility (Heyer et al., 2006), while Rad5/16 is involved in DNA repair pathways via its characteristic RING finger domain (Unk et al., 2010). The SSO1652-like family does not directly alter nucleosome structure, but is proposed to interact with transcription factors and is recruited to DNA lesions (Svejstrup, 2003). Finally, a function for the distant group has not yet been determined.

2.4.2 ISWI-type remodeling enzymes

The ISWI subfamily with its essential function in every eukaryotic cell and its characteristic domain architecture is relatively well studied. ISWI enzymes contain the typical ATPase domain consisting of two parts, the DEXDc domain and the HELICc domain, which are responsible for nucleotide binding and hydrolysis (Figure 2-5). The ATPase domain has been shown to associate independently with DNA and nucleosomes and is sufficient for DNA translocation (Mueller-Planitz et al., 2013). In addition, three other domains in the C-terminal region are characteristic for ISWI-type proteins forming the HSS module: The HAND domain, whose four helices form an open hand-like structure, the SANT domain, named after four proteins (SWI3, ADA2, N-CoR and TFIIIB) that contain this domain, and the SLIDE (SANT-like) domain. The combined HSS module is required for the recognition of nucleosomes and extra-nucleosomal DNA, thus increasing the affinity and specificity of the ISWI remodeler (Clapier et al., 2001; Längst and Manelyte, 2015). By releasing the flanking DNA in a nucleotide-dependent manner, the HSS module undergoes major conformational changes, allowing to measure the linker length in order to even out the spacing of nucleosomes (Leonard and Narlikar, 2015; Lieleg et al., 2015). The detailed role of the three individual domains in CREs, however, is not fully understood (Dang and Bartholomew, 2007; Grüne et al., 2003; Harrer et al., 2018).

Two small domains flanking the ATPase domain, the N-terminal region (NTR) and the NegC domain, fulfill autoregulatory functions. The NTR consists of the motifs ppHSA, AThook, AutoN and AcidicN, and has been shown to inhibit ATPase activity until histone H4 tail binding near the NTR-ATPase interface releases this inhibition (Clapier and Cairns, 2012; Ludwigsen et al., 2017; Yan et al., 2016). The C-terminally located NegC domain inhibits the coupling of ATP hydrolysis to DNA translocation by binding and shielding the catalytic cleft of the ATPase domain. In this conformation, ATP hydrolysis is still possible, but it cannot be transferred to nucleosome movement. In the presence of extra-nucleosomal (linker) DNA, the HSS module binds to the DNA, thereby releasing NegC through conformational changes. The ISWI-characteristic requirement of extra-nucleosomal DNA and H4-tail to allow nucleosome

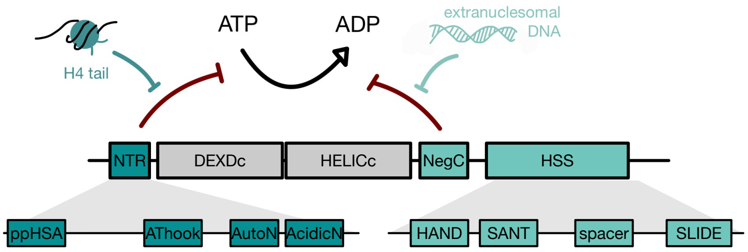

Figure 2-5: Characteristic ISWI domain architecture and autoregulatory mechanism *– schematic representation. Abbreviations: NTR – N-terminal domain, HSS – HAND-SANT-SLIDE, ppHSA - post-post-helicase-SANT-associated, HAND – SANT – Swi3, Ada2, N-Cor, TFIIIB-domain, SLIDE – SANT-like domain.*

remodeling can be explained by these two regulatory domains, but the detailed interaction sites of the underlying mechanism are subject of ongoing studies.

The enzymatic activity of CREs is tightly regulated, as illustrated by the example of ISWI-type proteins. The selective overview in the previous chapter showed the functional diversity between the subfamilies, which depends on accessory domains but also on the interaction with additional complex subunits. The interplay of all these complexes in the cell organizes the nucleosomal landscape and thus the accessibility of regulatory DNA elements in a complex manner. Regulation of nucleosome positioning, keeping nucleosomes over regulatory sites – OFF state – or moving them next to the binding sites of regulatory factors – ON state configuration – is likely to determine local gene activity states. This mechanism can be paraphrased as “barcoding” the nucleosome landscape and highlights the essential role of CREs in regulation and cellular differentiation (Diermeier et al., 2014).

2.4.3 Chromatin remodeling enzymes in *Plasmodium falciparum*

The superordinate function of CREs in eukaryotic cells suggests an equally relevant role in apicomplexan parasites such as *Plasmodium falciparum.* To date, chromatin proteins, and in particular the family of CREs, is not well studied in Plasmodium. In a comparative genomics study, the evolution of transcription factors, chromatin modifying and remodeling enzymes in parasitic protists has been reconstructed (Iyer et al., 2008): Intriguingly, chromatin proteins evolved over millions of years in independent eukaryotic lineages by proliferation of paralogous families and acquisition of novel domain architectures, leading to an enormous variety and to highly diverse sets of enzymes. Some chromatin modifying enzymes have been identified in *Plasmodium falciparum* (reviewed in (Croken et al., 2012)). CREs had their origins in the bacteriophage replication system and subsequently a set of six enzymes with conserved domain architectures was proposed to be present in the last eukaryotic common ancestor (LECA) (Figure 2-4, left panel) (Iyer et al., 2008). During evolution, prior to the origin of kinetoplasts and then chromalveolates, new families of CREs evolved with precursors of the Rad5/16 group, the distant group, ALC1, Lsh and Etl1. Early on, the apicomplexan lineage evolved ten SWI2/SNF2 ATPases, eight of which could be allocated in the evolutionary model of Iyer and colleagues, based on homology searches and domain architecture (Horrocks et al., 2009), Figure 2-4, right panel). In comparison to higher eukaryotes, *Plasmodium falciparum* possesses a limited set of CREs, with no redundancy in subfamilies and suggesting that these enzymes perform essential functions in the cell. The fundamental difference in number between human cells and *P. falciparum* is accompanied by highly divergent domain architectures. Some domains such as PhD, Chromo, SANT domains, could be identified by sequence comparison at very low stringency, but without any indication of their specific functions in *Pf*. The individual plasmodial CREs remain poorly characterized so far. In a pioneering study, Ji and Arnot identified and classified the first SWI2/SNF2 enzyme (Snf2L) with approximately 60 % sequence homology to the ATPase domain of the yeast ISWI remodeler. Since then, only a few studies have focused on apicomplexan CREs . A genome-wide mutagenesis screen proposed *Pf*Snf2L to be essential and another two of the plasmodial remodelers as putatively essential in asexual blood stages (Zhang et al., 2018a). The authors suggest that the rest is not crucial for parasite fitness, not precluding the possibility of significant roles in chromatin organization. Plasmodial CREs, like most CREs except for Chd1, may be part of large multiprotein complexes, but no subunits are known or proposed so far. This astonishing lack of known interactors in combination with the reduced number and high divergence in sequence indicates that the chromatin remodeling system in *Plasmodium* differs from known mechanisms in higher eukaryotes. How CREs pave the way for transcription factor and polymerase binding and how they are regulated is completely unexplored in *P. falciparum.* In conjunction with the nucleosome landscape and transcription factor binding, it is proposed that *Pf* remodeling complexes form a complex regulatory network with major differences in comparison to other eukaryotes (Watzlowik et al., 2021). The decryption of this system is indispensable for understanding the mechanism of transcription regulation in the parasite and will provide new insights and novel approaches for fighting malaria.

3 OBJECTIVES

The crucial role of chromatin regulation and epigenetics for the transcriptional heterogeneity in *Plasmodium falciparum* has become evident. However, the contribution of *Pf* chromatin remodeling enzymes is largely unknown, yet fundamental to understanding the complexity of the chromatin landscape. Here, we investigate the functional role of Plasmodium CREs focusing on the only ISWI-related enzyme, *Pf*Snf2L (PF3D7_1104200). The characterization of *Pf*Snf2L within this study comprises a detailed analysis from different perspectives, including *in silico / in vitro* approaches, knockout studies in parasites and systematic screening for an inhibitor.

The first part focuses on the classification of *Pf*Snf2L in comparison with characterized CREs and attempts to identify common features and differences. Comparative studies *in vitro* of recombinantly expressed *Pf*Snf2L and its human orthologue *Hs*Snf2L reveal information on substrate preferences, enzymatic activity, and the autoregulatory mechanism of ISWI enzymes. In the main part, the functional characterization of *Pf*Snf2L in the cellular context is addressed using a transgenic *Plasmodium falciparum* strain with endogenous tagging and a conditional knockout system. Cellular and genomic localization as well as interacting proteins in asexual blood stage are investigated. Detailed phenotyping with stage-dependent KO induction and transcriptome analysis aim to unravel the impact of *Pf*Snf2L deletion on gene expression throughout the parasite life cycle. The underlying epigenetic mechanism is addressed by analyzing the nucleosome landscape in KO parasites. In a third part, the suitability of *Pf*Snf2L as potential drug target is investigated. Establishing and performing an *in vitro* screen targeting *Pf*Snf2L enzymatic activity aims to identify potential inhibitors and to determine the druggability of *Pf*Snf2L. Promising candidates will be validated and further characterized for their toxicity and impact on parasite development.

The study aims to elucidate the function of a previously uncharacterized protein in Plasmodium falciparum and may provide new insights into the complex regulation of its life cycle. A comprehensive characterization will serve as a basis for further investigation into detailed epigenetic mechanisms and as a target for antimalarial drugs.

4 *Pf*Snf2L CHARACTERIZATION *IN VITRO*

4.1 RESULTS

4.1.1 *In silico* analysis and classification of *Pf*Snf2L as ISWI-type remodeler

Plasmodium falciparum enzymes are in general very divergent compared to well-characterized proteins in *Homo sapiens* or in model organisms such as *Saccharomyces cerevisiae*, as the apicomplexan phylum separated very early in evolution. This is also true for the ten identified enzymes in *Pf*, that were suggested to be CREs. For this reason, it is not possible to derive a clear enzymatic function for these uncharacterized proteins based on similarity. Nevertheless, *in silico* comparison with well-studied homologues can be used to gain basic information. Previously, the SWI2/SNF2-characteristic ATPase domain was used to group the divers CREs in subfamilies. In order to classify the ten plasmodial CREs, a reconstitution of the phylogenetic tree with representative proteins of *H. sapiens, D. melanogaster* and *S. cerevisiae* was performed. Following Flaus et al., I trimmed the protein sequences to their helicase region based on multiple sequence alignments (Appendix 2), and subsequently used them for the phylogenetic analysis including also all *Pf*CREs (7.9.1). Eight of the ten *Pf* enzymes could be assigned to the established subfamilies, with a maximum of one protein in each subgroup, and the Mot1 family as well as the Lsh group being unrepresented (Figure 4-1A). Two enzymes could not be classified: PF3D7_0624600 - previously mistakenly designated as ISWI - belongs to an Apicomplexan-specific group and the occurrence of PF3D7_0106000 is limited to *Plasmodium species. Pf*Snf2L, the protein of interest with the gene ID PF3D7_1104200, was one of the shortest in sequence length and most similar to ISWI. Therefore, it was of special interest to the AG Längst that aimed to recombinantly express and study the function of these enzymes. Further phylogenetic analysis with full-length sequences of the ISWI members from various species throughout the tree of life confirms the assignment of *Pf*Snf2L and emphasizes the early separation in evolution of Apicomplexans also within this protein family (Figure 4-1B). Multiple sequence alignments within this family and its quantitative comparison unravel regions of conservation and regions of divergence across the protein architecture (Appendix 1, Figure 4-1C,D). Among Metazoan, ISWI enzymes show a relatively high degree of conservation throughout all domains. Comparing apicomplexan with metazoan enzymes, only parts of the typical ISWI domain architecture are conserved with >50 % pairwise identity for the ATPase region. The autoregulatory NegC domain is only partially conserved, while the N-terminal region (NTR), which also has an autoregulatory function, is not identifiable in *Pf*Snf2L. The conservation of the HSS module – usually determining affinity and specificity of ISWI remodeler by

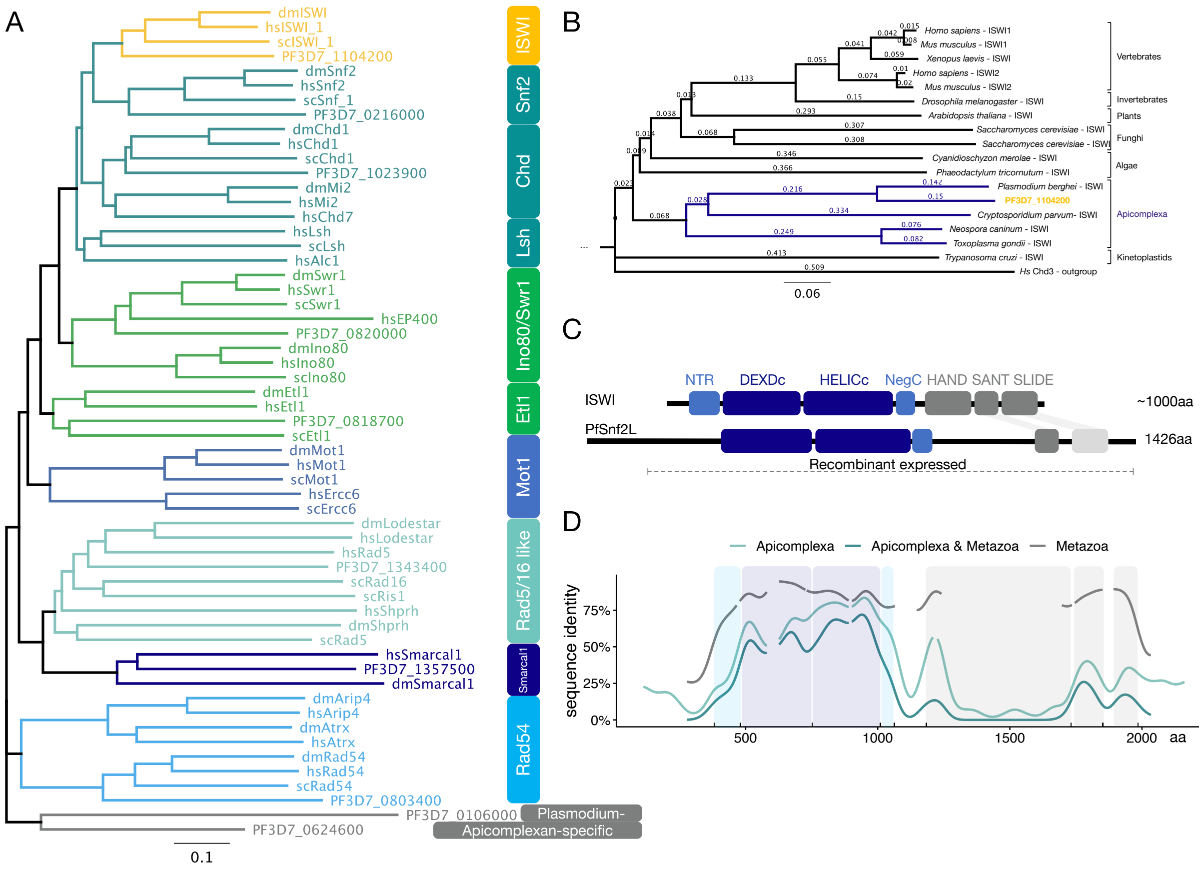

Figure 4-1: ***PfSnf2L is an ISWI-type chromatin remodeling enzyme with high divergence. A.*** *Phylogenetic analysis of the helicase region with subfamily representatives of Hs, Dm and Sc and predicted Pf SWI2/SNF2-ATPases (listed in Appendix 2), coloring represents SWI2/SNF2 subgroups according to (Flaus, 2006).* ***B.*** *Rooted phylogenetic tree of the full length ISWI homologues from different organisms representing eukaryotic (sub-) kingdoms with Apicomplexa highlighted (blue) and HsChd3 as outgroup. Numbers indicating substitutions per site.* ***C.*** *ISWI domain architecture with ATPase region (dark blue), autoregulatory domains (light blue) and HAND-SANT-SLIDE (grey) and partly conservation in PfSnf2L.* ***D.*** *Pairwise identity among metazoanISWI, apicomplexanISWI and between them based on multiple sequence alignment (Appendix 1), gaps represent insertions, coloring represent predicted domains.*

recognition of nucleosomes and extra-nucleosomal DNA – is questionable. The SANT domain is relatively conserved, but the existence of the SLIDE domain can be only speculated as the sequence identity is close to random. The HAND domain is not present in *Pf*Snf2L or apicomplexan orthologues, and large insertions are found there. Within Apicomplexans, the sequence identity is moderately enhanced in the (lacking) HAND domain region, suggesting a conserved – but different – domain among this phylum instead.

In total, the *in silico* results suggest *Pf*Snf2L to be an ISWI-type CRE with putative ATPase activity, but with differences when it comes to the autoregulatory mechanism and substrate preferences and/or interacting proteins. In addition to the high divergence in the known domains, the 167 kDa protein acquired the asparagine-rich patches typical for plasmodial proteins resulting in a long N-terminus (1-245 aa). The function of these unstructured regions in *Pf* is still unclear and no similarity within the family of CREs can be found.

4.1.2 Preferential binding of *Pf*Snf2L to linker-containing and to canonical nucleosomes

To enable a characterization of *Pf*Snf2L substrates and its enzymatic activity in *in vitro* assays, the protein was recombinantly expressed and purified in large amounts (7.9.5). The full-length protein, lacking only the unstructured asparagine-rich N-terminus (aa1-245) with a 10xHis tag fused to the C-terminus, was expressed in *Spodoptera frugiperda* insect cells (Sf21) using the baculovirus system. At the beginning of this work, the constructs for *Pf*Snf2L and *Hs*Snf2L expression were already cloned, baculoviruses V_1 were generated, and test expressions were performed in the AG Längst. For all CRE mutants used, I mutated these plasmids and used them for baculovirus generation. The recombinant protein *Pf*Snf2L was purified via affinity purification on Ni-NTA agarose whereby high purity and yields of ~1 mg/250 ml culture were achieved (Figure 4-2A). Likewise, the human ISWI enzyme *Hs*Snf2L and several mutants were expressed and purified for comparative experiments.

The binding properties of *Pf*Snf2L to different substrates were addressed in electromobility shift assays (EMSAs) in comparison to *Hs*Snf2L. Both enzymes bind to *in vitro* reconstituted chromatin, consisting of recombinantly expressed histone octamers assembled on pT11 plasmid DNA (Figure 4-2B). Binding to nucleosome arrays occurred with similar affinities for both proteins, regardless of whether the histones originate from the own or foreign species (canonical *Hs* / *Pf* histones). Furthermore, *Pf*Snf2L also binds to free DNA in a length-dependent manner, preferentially binding to longer DNA (Figure 4-2B,C). Still, *Pf*Snf2L can bind short DNA fragments as short as 20 bp, whereas other ISWI CREs have been proposed to have a minimum DNA length of ~23 bp to bind (Whitehouse et al., 2003). Competitive EMSAs containing a mixture of two or more species of mononucleosomes showed that *Pf*Snf2L binds in a linker-sensitive manner. There is a clear preference for shifting linker-containing nucleosomes over linker-free nucleosomes (Figure 4-2D). The comparison of different linker lengths also indicates a higher affinity for mononucleosomes having extra-nucleosomal DNA of a certain length (Figure 4-2E,F). There is a slight tendency for longer DNA linker lengths to shift at lower *Pf*Snf2L concentration. An increasing affinity for longer DNA linkers is typical for ISWI (Kagalwala et al., 2004). The fact, that not only free DNA but also linker-free nucleosomes are shifted demonstrates that *Pf*Snf2L binds to nucleosomal structures as well as to DNA. This finding is also consistent with studies of other ISWI CREs, that have been shown to bind nucleosomes close to the dyad, but also extra-nucleosomal DNA close to the nucleosome entry-site (Dang and Bartholomew, 2007; Längst and Becker, 2001).

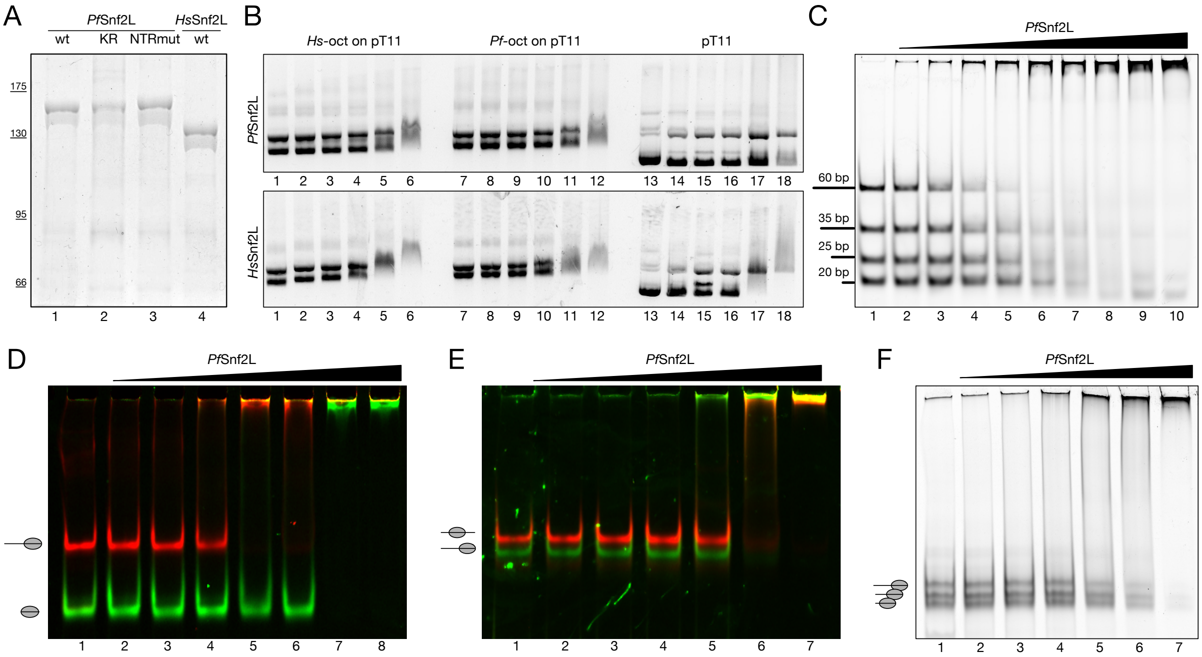

Figure 4-2: Recombinant* PfSnf2L *binds nucleosomal structures in a linker-sensing manner. A. *SDS-PAGE (6 %, Coomassie-stained) of remodeling enzymes, recombinantly expressed in SF21 cells and purified via affinity chromatography. Protein sizes of marker are indicated in kDa.* ***B.*** *Chromatin binding was analyzed by EMSA with titration of PfSnf2L (0.08-1.3 µM)/HsSnf2L (0.09-1.5 µM) to 2 µg circular DNA occupied with Hs-octamers (lane 1-6), Pf-octamers (lane 7-12) or unoccupied (lane 13-18) and analyzed on a 0.8 % agarose gel, stained with ethidium bromide.* ***C.*** *DNA binding was analyzed in a competitive EMSA with increasing amount of PfSnf2L (0.05-12.5 µM) titrated to an equimolar mixture of Cy5-labeled DNA with varying length (20 nM). DNA length is indicated.* ***D.*** *Linker-dependent nucleosome binding was analyzed in a competitive binding assay with PfSnf2L-titration (0.02-0.6 µM) to an equimolar mixture (15 nM) of Gg/6-NPS-47-Cy5 (red) and Gg/0-NPS-0-Cy3 (green) nucleosomes and subsequent analysis via native PAGE. Merged channels are shown with nucleosome positions indicated.* ***E.*** *as in D. with Gg/29-NPS-29-Cy5 (red) and Gg/6-NPS-47-Cy3 (green) nucleosomes* ***F.*** *PfSnf2L-titration (0.05-1.7 µM) to an equimolar mixture (20 nM) of Bt/29-NPS-0-Cy5, Bt/40-NPS-0-Cy5, Bt/60-NPS-0-Cy5 with nucleosome positions indicated. Lane 1 serves as negative control not containing the respective CRE in B.-F.*

In addition to nucleosomes composed of canonical histones, *Pf* also encodes variant histones, which are incorporated into nucleosomes as H2A.Z/H2B.Z dimers and mark specific regions in the genome (Hoeijmakers et al., 2013; Petter et al., 2013). Next, I addressed whether *Pf*Snf2L has a binding preference for variant or canonical nucleosomes. Binding to mononucleosomes containing the Apicomplexan-characteristic H2A.Z/B.Z dimer was examined in a competitive EMSA with canonical histones (Figure 4-3A). Quantification of gel band intensity changes with increasing *Pf*Snf2L / *Hs*Snf2L concentration shows, that *Pf*Snf2L binds preferentially to canonical nucleosomes. In contrast, the human enzyme doesn't show any affinity differences. Canonical *Pf* nucleosomes – the potentially preferred substrate of *Pf*Snf2L – are remarkable in their instability and in their reduced sequence-dependent positioning (Silberhorn et al., 2016). This is reflected in the multiple bands of *Pf* histones assembled on a 200 bp DNA (Widom 601), the sequence of which favors the formation of asymmetric nucleosomes. Comparing this with the assembly of *Gg* octamers on the same DNA (Figure 4-2D), we can conclude that the middle band represents a well-positioned octameric nucleosome (Figure 4-3B lane 1). The other bands could represent hexameric nucleosomes with one H2A/B dimer missing or undefined histone-DNA-aggregates. Incubation of the histone-DNA mixture with *Pf*Snf2L and subsequent release with competitor DNA results in a different picture with only one predominant band (lane 2). Temporary binding of *Pf*Snf2L appears to shift the distribution towards well-positioned octameric nucleosomes. The additional presence of ATP in the reaction results in a band shift representing actively moved nucleosomes (lane 3). This assay indicates that *Pf*Snf2L functions as an assembly factor for canonical histones, which by their intrinsic properties are unable to form stable nucleosomes. The observed activity is independent of ATP hydrolysis, presumably mediated by its histone binding properties. The proposed chaperone function of *Pf*Snf2L and the underlying mechanism need to be investigated in the future.

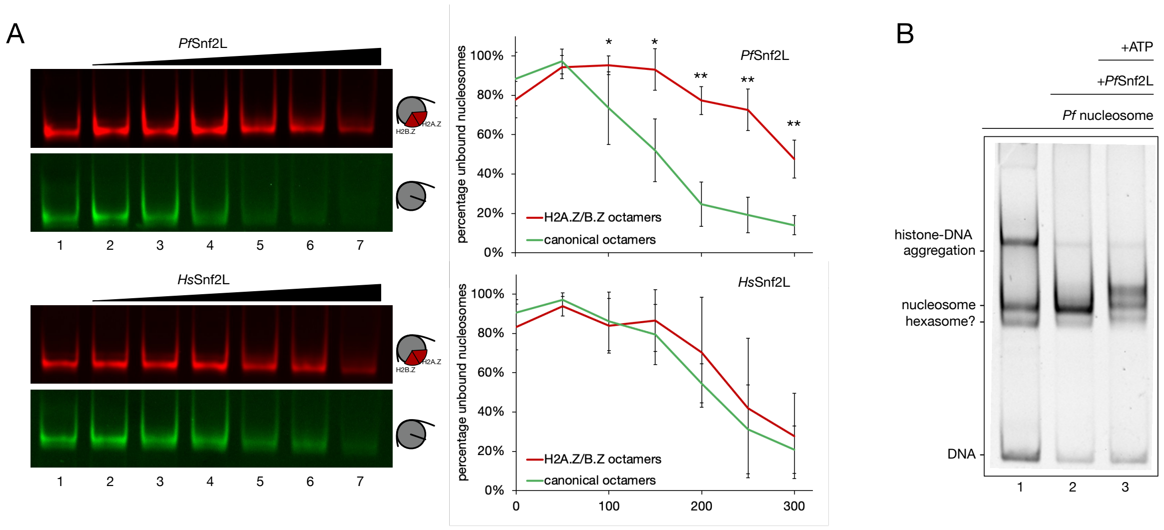

Figure 4-3: Nucleosome variant recognition and assembly activity of* PfSnf2L*. A. *Variant recognition was analyzed in competitive binding assays with PfSnf2L/HsSnf2L-titration (0.05-0.3 µM) to an equimolar mixture (15 nM) of canonical Pf nucleosomes or Pf H2A.Z/B.Z containing nucleosomes on differently labeled 0-NPS-0 DNA. Representative EMSA with canonical (green) and variant (red) nucleosomes in separate channels is shown (left panel). Quantification of EMSAs shows the proportion of unbound nucleosomes in the respective color with CRE titration (right panel). Mean and standard deviation of five replicates for PfSnf2L and four replicates for HsSnf2L is shown. Canonical/variant nucleosomes were labeled with Cy3/Cy5 and vice versa. Significance is indicated (two-tailed Student's t-test, unpaired, ns p>0.05, * p<0.05, ** p<0.01, ***p<0.005).* ***B.*** *ATP-independent assembly activity was analyzed by EMSA with 0.7 µM PfSnf2L on 120 nM canonical Pf/6-NPS-47 nucleosome in absence/presence of ATP. Presumed histone-DNA species are indicated. Lane 1 serves as negative control not containing the respective CRE in A/B.*

4.1.3 ATP-dependent nucleosome remodeling activity of *Pf*Snf2L

ISWI enzymes are known to hydrolyze ATP and convert the energy into movement of the histone octamer along DNA. Whether *Pf*Snf2L is capable of nucleosome repositioning was studied using a nucleosome remodeling assay in which nucleosomes with a defined position are incubated with a CRE in absence or presence of ATP. As shown in Figure 4-4A, *Pf*Snf2L can move edge-positioned nucleosomes towards the middle of the DNA template when ATP is available, similar to the activity of *Hs*Snf2L. The ATPase-deficient mutant of *Pf*Snf2L, where a residue within the ATP-binding Walker A motif – lysine353 – has been mutated to arginine, is unable to efficiently move nucleosomes. The important motifs within the ATPase domain, as well as this central enzymatic function of CREs, is evidently preserved in *Pf*Snf2L. The ATP hydrolysis activity and its regulation by availability of substrates was investigated in an end-point ATPase assay with radiolabeled ATP (Figure 4-4B). *Pf*Snf2L shows a basal hydrolysis rate in the absence of any substrate, which increases by a factor of ~2.5 in the presence of nucleosomes. This is also observed for *Hs*Snf2L and is known for ISWI enzymes in general, but there is a clear quantitative difference. *Pf*Snf2L, in comparison to *Hs*Snf2L, shows a clearly enhanced level of ATPase activity, both under basal and stimulating conditions. The *Pf*Snf2L-KR mutant doesn't exhibit any stimulatory response to substrates, but has a remaining, albeit reduced, rate of ATP hydrolysis. Kinetic measurements of ATP hydrolysis

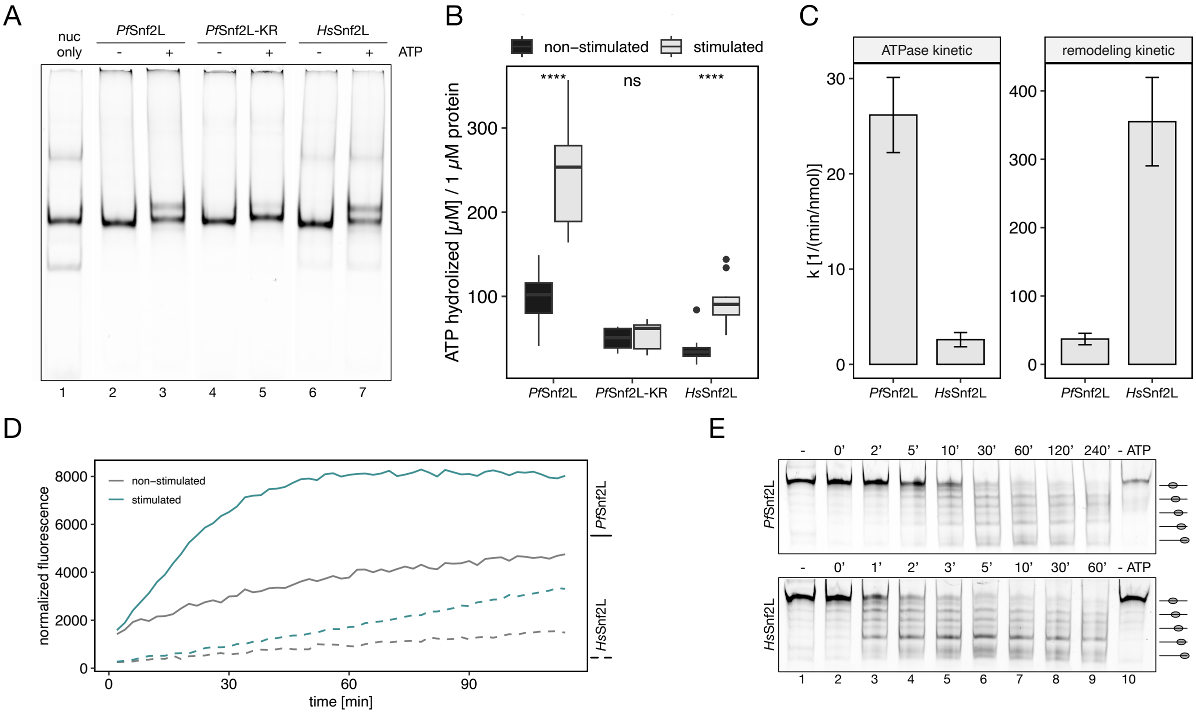

Figure 4-4: Coupling of ATP-hydrolysis to nucleosome remodeling activity. A. *ATP-dependent remodeling was analyzed by incubation of 0.3 μM CRE (PfSnf2L/PfSnf2L-KR/HsSnf2L) with 30 nM Gg/6-NPS47-Cy5 nucleosomes in absence/presence of ATP.* ***B.*** *Substrate-dependent ATPase activity of CREs (0.13-0.7 μM) was analyzed in end-point ATPase assay in absence/presence of mononucleosomes (60-350 nM, various compositions): Boxplot showing non-stimulated / stimulated ATP hydrolysis rate per enzyme for $n=18$/$n=10$ independent experiments. Significance is indicated (two-tailed Student's t-test, unpaired, ns $p>0.05$, * $p<0.05$, ** $p<0.01$, ***$p<0.005$).* ***C.*** *Quantification of ATPase kinetic and remodeling kinetic for PfSnf2L and HsSnf2L: Linear segment of normalized fluorescence (in D.) was analyzed with simple linear regression. Band intensity (in E.) was quantified, and fraction of centered-positioned nucleosomes was calculated. Decrease over time was fitted with one-phase exponential decay. Time- and concentration-normalized reaction constant with 95 % confident interval is shown.* ***D.*** *ATPase kinetic of PfSnf2L/HsSnf2L (0.4 μM) was analyzed via ADP biosensor assay in absence (grey)/presence (petrol) of substrates (50 ng DNA + 2.5 μM H4 tail per reaction). Fluorescence was normalized and mean of two replicates is shown.* ***E.*** *Chromatin remodeling activity of PfSnf2L/HsSnf2L (0.3 μM) was analyzed in a time-limited remodeling assay on centered-positioned nucleosomes (30 nM Bt/77-NPS-77-Cy5). Representative gel is shown with relative positions of nucleosomes indicated. Lane 10 represents the no ATP control, lane 1 serves as negative control not containing the respective CRE in A/E.*

confirmed the observation of the end-point ATPase assay. Using a fluorescent ADP biosensor protein, the ADP produced was quantified over time in the absence or presence of substrates (Figure 4-4D). Taking into account the initial hydrolysis rate, *Pf*Snf2L showed a ten-fold higher ATPase activity than *Hs*Snf2L (Figure 4-4C). The time-course remodeling assays using centrally positioned nucleosomes with a 77-bp linker at each site revealed the kinetics of the remodeling reaction (Figure 4-4E). Despite higher ATPase hydrolysis, *Pf*Snf2L moves nucleosomes less efficiently than *Hs*Snf2L. Quantification of band intensities suggests a ten-fold lower remodeling rate constant for *Pf*Snf2L (Figure 4-4C). The contradicting enzyme activity rates point towards a less efficient coupling of ATP hydrolysis to nucleosome remodeling for *Pf*Snf2L compared to *Hs*Snf2L, at least when both recombinant enzymes are analyzed in the *in vitro* context on purified calf histones without putative interacting proteins.

4.1.4 ISWI-untypical autoregulatory mechanism of *Pf*Snf2L

The characterization of CRE ATPase activity in the previous section already suggests it to be autoregulated, as differences in enzyme activity were monitored in the presence/absence of substrate. ISWI enzymes such as *Hs*Snf2L are known to interact with the histone H4 tail, which is required for full stimulation of its ATPase activity and nucleosome remodeling. In order to investigate the role of the H4 tail in *Pf*Snf2L activity, nucleosomes were reconstituted with H4 lacking its N-terminal tail (aa1-24). Analysis of the remodeling activity on these nucleosomes in comparison with intact nucleosomes clearly shows a dependence on the H4 tail, as *Pf*Snf2L is unable to move H4 tail-depleted nucleosomes (Figure 4-5A). Its substrate-specificity for H4 tail-containing nucleosomes is in accordance with *Hs*Snf2L and known ISWI characteristics. Typically, the H4 tail-dependency in remodeling is due to restricted ATPase activity in the absence of this peptide. Therefore, the ATP hydrolysis rate of *Pf*Snf2L and *Hs*Snf2L was examined in the presence and absence of a variety of substrates (Figure 4-5B). For both enzymes, the basal non-stimulated ATPase activity could not be enhanced by the presence of RNA or the H4 tail peptide (aa8-25) alone. Full stimulation by a factor of ~3-4 was achieved by the presence of intact nucleosomal arrays, but also by DNA plus the H4 tail peptide. This confirms the finding, that ISWI CREs recognize these two structures when binding to a nucleosome. Current knowledge suggests that the ATPase is autoinhibited by the two regulatory domains – NTR and NegC – until it is antagonized by the histone H4 tail and extra-nucleosomal DNA (Clapier and Cairns, 2012; Ludwigsen et al., 2017). However, when DNA is provided as the sole substrate, there are striking differences between *Hs*Snf2L as a typical ISWI enzyme and *Pf*Snf2L. *Hs*Snf2L is only partially stimulated, while *Pf*Snf2L shows full ATP hydrolysis in the presence of DNA only. Accordingly, *Pf*Snf2L ATPase activity is dependent on the presence of extra-nucleosomal DNA. This is proposed to be mediated by the NegC domain, which inhibits the helicase in a non-stimulated state, and releases it when bound to DNA. Since the NegC domain was identified in *Pf*Snf2L with a sequence identity of ~50 %, it can be assumed, that it functions similarly to the typical ISWI autoinhibition. However, due to the full stimulation by DNA alone, the ATPase activity appears to be independent of the H4 tail. Conversely, the remodeling experiment showed a strict dependence of the remodeling reaction on the nucleosomal H4 tail. In conclusion, *Pf*Snf2L exhibits clear differences from typical ISWI enzymes in terms of disinhibition, showing an atypical mechanism of autoregulation in this protein.

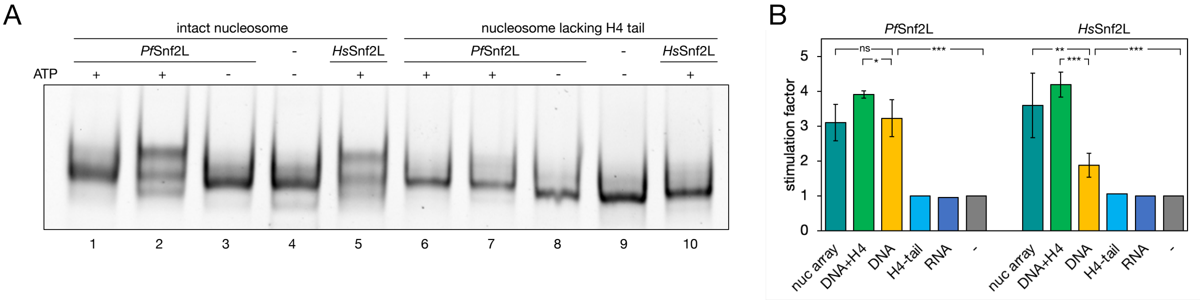

Figure 4-5: H4 tail-dependent remodeling but H4 tail-independent ATPase activity of* PfSnf2L*. A. *H4 tail-dependency of remodeling activity was analyzed by comparative remodeling of PfSnf2L/HsSnf2L on 120 nM intact nucleosomes (Hs/6-NPS-47) or H4 tail truncated nucleosomes (HsH4ΔN/6-NPS-47): Lanes 1/6 contain 0.13 µM PfSnf2L, lanes 2/7 0.7 µM PfSnf2L, lanes 3/8 (0.7 µM) PfSnf2L in absence of ATP, lanes 4/8 nucleosome only, lanes 5/10 0.13 µM HsSnf2L.* ***B.*** *ATPase stimulation of PfSnf2L / HsSnf2L (0.3-0.6 µM) was analyzed in end-point ATPase assay in absence/presence of various substrates: nucleosomal array (Bt-oct on 100 ng plasmid DNA – petrol), plasmid DNA + H4 tail (100 ng + 5 µM – green), plasmid or linear DNA (100-200 ng – yellow), H4tail (5 µM – light blue), En3 RNA (30 ng – dark blue) or no substrate (grey). Mean of stimulation factor (stimulated/non-stimulated) of 3 or more replicates and standard deviation are shown, significance is indicated (two-tailed Student's t-test, unpaired, ns $p>0.05$, * $p<0.05$, ** $p<0.01$, ***$p<0.005$).*

To address the mechanism of autoregulation and to identify the role of the less conserved domains in *Pf*Snf2L, a series of mutants were generated. The NTR domain, which has beenn proposed to be responsible for the H4 tail-dependence (Clapier and Cairns, 2012; Ludwigsen et al., 2017; Yan et al., 2016), was shown to be highly divergent in *Pf*Snf2L, potentially not conserved at all, using *in silico* analysis (Figure 4-1D, Appendix 1). In detail, the ISWI-NTR domain contains four characteristic motifs (Figure 4-6A). Ludwigsen et al. claimed that ten residues within these motifs are central to the inhibitory effect. The *Hs*Snf2L sequence matches the conserved sequence logo, and all ten relevant amino acids are present in *Hs*Snf2L (highlighted in green). *Pf*Snf2L on the other hand exhibits only a few matching residues within these motifs and the AT hook is not identified in the protein. Of the ten amino acids proposed to be important, five are conserved in *Pf*Snf2L.

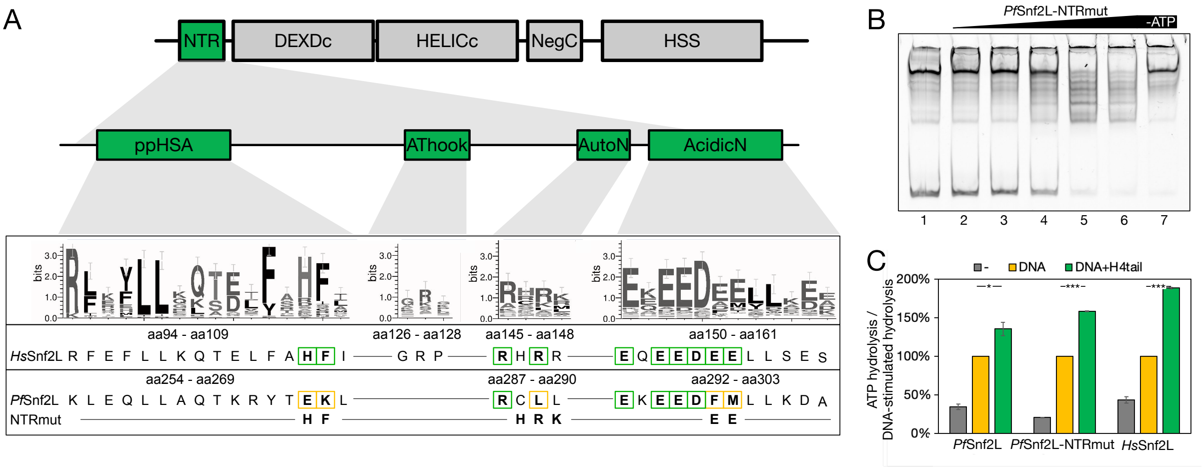

*Figure 4-6: **Sequence divergence in NTR domain. A**. ISWI domain architecture with sequence logos of motifs responsible for aut-inhibition and their conservation in HsSnf2L/PfSnf2L. Amino acids contributing to the autoinhibition according to (Ludwigsen et al., 2017) are marked, green if conserved, yellow if divergent. Residues mutated in PfSnf2L-NTRmut are shown. Abbreviations: NTR (N-terminal region), HSS (HAND-SANT-SLIDE, ppHSA (post-post-helicase-SANT-associated). **B.** Remodeling activity of PfSnf2L-NTRmut (0.06-1 µM) on nucleosomes (50 nM Bt/77-nps-77-Cy5). Lane 7 represents the no ATP control, lane 1 serves as negative control not containing the CRE. **C.** ATP hydrolysis of PfSnf2L/PfSnf2L-NTRmut/HsSnf2L (0.5 µM) in an end-point ATPase assay in absence (grey)/presence of DNA (100 ng – yellow) or additional H4 tail (5 µM – green) normalized to DNA-stimulation. Mean of two replicates and standard deviation are shown, significance is indicated (two-tailed Student's t-test, unpaired, ns p>0.05, * p<0.05, ** p<0.01, ***p<0.005).*

In an attempt to regain the lacking autoinhibition, a *Pf*Snf2L-NTR mutant was generated by back-mutating the critical residues to the human enzyme. The five divergent residues were mutated, as well as two others in the AutoN motif (E267H, K268F, C288H, L289R, L290K, F297E, M298E). This mutant enzyme was expressed and purified from insect cells and was confirmed to be an active CRE via remodeling assay (Figure 4-6B). The autoinhibition in the *Pf*Snf2L-NTR mutant was investigated by measuring ATP hydrolysis in an end-point ATPase assay (Figure 4-6C) and normalizing to ATP hydrolysis in the presence of DNA (100 %). *Pf*Snf2L and *Hs*Snf2L both show ~40 % activity under non-stimulated conditions. *Pf*Snf2L-NTR mutant was significantly lower in absence of both substrates. The presence of DNA and additional H4 tail showed a moderate stimulation of *Pf*Snf2L (x 1.4), a high stimulation (x1.9) of *Hs*Snf2L and the effect on *Pf*Snf2L-NTR mutant is somewhere in between. From this analysis it can be concluded that the introduced mutations reduced the ATPase activity when compared to *Pf*Snf2L-wildtype. Nevertheless, the proposed ten regulatory residues are not sufficient to fully restore the H4 tail-dependence. The published study claiming that these ten residues are responsible for the autoregulation is incorrect. Additional residues or domains are required for the full H4 tail-dependent autoregulatory mechanism in typical ISWI enzymes, which are not conserved in *Pf*Snf2L.

In silico analysis of *Pf*Snf2L not only revealed low conservation of the NTR domain, but also parts of the HSS module show an extremely high divergence (Figure 4-7A). These three domains – HAND-SANT-SLIDE – are required for the recognition of nucleosomes and extra-nucleosomal DNA and increase the affinity and specificity of ISWI remodelers (Clapier et al., 2001; Längst and Manelyte, 2015). The SANT domain, with its key motifs and structural relevant residues, seems to be preserved in *Pf*Snf2L, sharing > 40 % sequence identity with metazoan enzymes. The existence of a SLIDE-like domain can be assumed based on a low sequence identity of ~16 %. The HAND domain and the spacer, in contrast, cannot be identified in *Pf*Snf2L, as the multiple sequence alignment shows insertions within the highly divergent region. To study the function of the HSS module in *Pf*Snf2L compared to *Hs*Snf2L, both enzymes were truncated C-terminally and N-terminally, leaving only the core enzymes (*Pf*Snf2L aa246 – 843, *Hs*Snf2L aa79 – 715). A previous study that truncated *dm*ISWI accordingly found the core protein to be an autonomous remodeling machine (Mueller-Planitz et al., 2013). The truncated proteins were expressed and purified (Figure 4-7B) and analyzed for their capability of nucleosome remodeling activity, ATPase activity, and stimulation by substrates. *Hs*Snf2L core exhibits a low (~10-fold reduction to *Hs*Snf2L in Figure 4-4E) but still existing remodeling activity (Figure 4-7C). *Pf*Snf2L core, on the other hand, was not able to move nucleosomes to new positions, even after 16 hours of incubation. However, the ATPase activity of *Pf*Snf2L was not significantly affected by truncation, whereas the *Hs*Snf2L core hydrolyzed ~4-5 times less ATP than the full-length protein (Figure 4-7D). These results confirm that the HSS module of *Hs*Snf2L contributes to both enzymatic activities, ATP hydrolysis and nucleosome remodeling. However, it doesn't seem to be essential since both activities are attenuated but not completely inhibited upon truncation. The C-terminal region of *Pf*Snf2L seems to have a different function. Unchanged ATPase activity but lack of nucleosome remodeling activity upon *Pf*Snf2L truncation suggests a function in coupling the energy of ATP hydrolysis to an actual nucleosome movement.

Enzyme autoinhibition upon protein truncation was analyzed by measuring the ATP hydrolysis after adding different stimulatory substrates (Figure 4-7E). Normalized to their maximum activity, both core enzymes show a slight increase in ATP hydrolysis under non-stimulated conditions in comparison to the respective full-length protein. This means that the truncation reduces the autoinhibition of the CREs. In typical ISWI enzymes, the HSS module is proposed to be involved in antagonizing the inhibition by the NegC domain, when extra-nucleosomal DNA is present. The fact that the core enzyme shows reduced autoinhibition supports this hypothesis also for *Pf*Snf2L. For the human enzyme, no clear conclusion can be drawn from these studies, because *Hs*Snf2L core exhibits a very low ATPase rate resulting in high experimental error. The stimulation of *Pf*Snf2L by DNA only remains unchanged, since

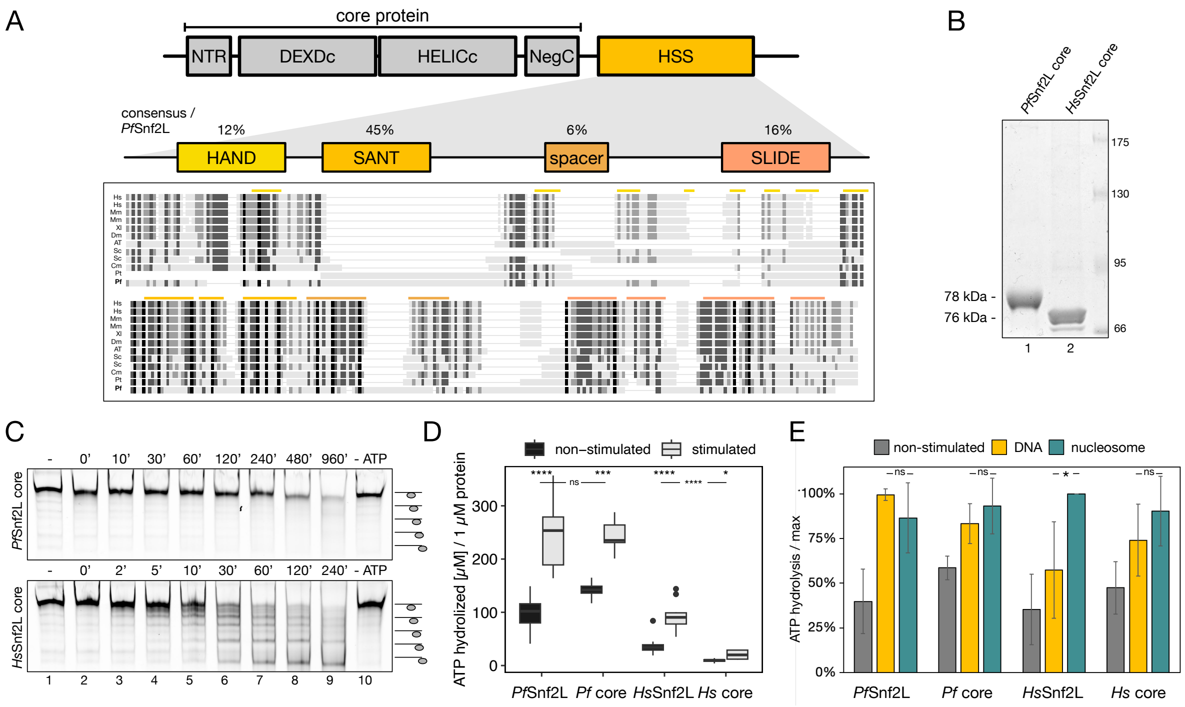

Figure 4-7: Sequence divergence in the HSS module. A. *ISWI domain architecture with HAND/SANT/SLIDE domains and their conservation in ISWI CREs from different species shown as multiple sequence alignment of the C-terminal region. Similarity is indicated by coloring (black-high; white-low). Structurally conserved helices according to (Grüne et al., 2003) are marked in the respective color. Sequence identity between PfSnf2L (bottom line) and consensus sequence of metazoan ISWI within the individual domains is depicted. Abbreviations: NTR (N-terminal region), HSS (HAND-SANT-SLIDE), SANT (SWI3, ADA2, N-CoR, TFIIIB), SLIDE (SANT-like).* ***B.*** *SDS-PAGE (6 %, Coomassie-stained) of remodeling core enzymes, recombinantly expressed in SF21 cells and purified via affinity chromatography. Sizes of marker and proteins are indicated in kDa* ***C.*** *Chromatin remodeling activity of PfSnf2L core/HsSnf2L core (0.3 µM) was analyzed in a time-limited remodeling assay on centered-positioned nucleosomes (30 nM Bt/77-NPS-77-Cy5). Representative gel is shown with relative positions of nucleosomes indicated. Lane 10 represents the no ATP control, lane 1 serves as negative control not containing the respective CRE.* ***D.*** *Substrate-dependent ATPase activity of PfSnf2L/HsSnf2L full length/core (0.13-0.7 µM) was analyzed in end-point ATPase assay in absence/presence of mononucleosomes (60-350 nM, various compositions): Boxplot showing non-stimulated / stimulated ATP hydrolysis rate / enzyme for five or more independent experiments.* ***E.*** *Fraction of maximal ATP hydrolysis of CREs (0.3/0.6 µM) in an end-point ATPase assay in absence (grey)/presence of 0.2x DNA (yellow) or 0.2x mononucleosomes (petrol). Mean of four replicates and standard deviation are shown, significance is indicated (two-tailed Student's t-test, unpaired, ns p>0.05, * p<0.05, ** p<0.01, ***p<0.005, ****p>0.001).*

both the core enzyme and the full-length enzyme are fully stimulated by DNA. In conclusion, I suggest that the C-terminal region of *Pf*Snf2L functions differently with respect to autoinhibition than the HSS module in ISWI enzymes. Nevertheless, they share a recognizable similarity in two of the three domains, and both are presumably involved in the binding of extra-nucleosomal DNA and with that associated in the autoregulatory mechanism.

4.2 DISCUSSION

Inefficient coupling of ATP hydrolysis to remodeling activity

In silico and *in vitro* analyses of *Pf*Snf2L in comparison with *Hs*Snf2L show some shared ISWI-typical characteristics, but also some remarkable differences. The relatively conserved helicase region in *Pf*Snf2L consisting of two lobes suggests an enzymatic ATPase activity similar to ISWI enzymes, which could be confirmed experimentally. Nevertheless, *Pf*Snf2L exhibits an exceptionally high hydrolysis rate, pointing towards quantitative differences in enzyme activity. Although the enzyme hydrolyzes high levels of ATP, its chromatin remodeling activity is greatly reduced compared to *Hs*Snf2L. These quantitative differences can be explained by several factors: The enzymatic activity of CREs is known to be influenced by auxiliary subunits. The formation of specific complexes has been shown to increase the efficiency of remodeling enzymes. However, orthologues of known interactors, such as *Sc*Ioc2/3/4, *Sc*Itc1 or mammalian ACF1, CECR2, Tip5, RSF11 or others (Bartholomew, 2014b), could not be identified in *Plasmodium falciparum* using homology search tools. The absence of any subunits is surprising and future investigations will reveal putative complexes. With no putative interacting proteins, no assumptions can be made about stimulatory or repressive effects on *Pf*Snf2L in the context of complexes. It may well be that *Pf*Snf2L functions as a single protein, like Drosophila Chd1 (McKnight et al., 2011; Petty and Pillus, 2013), with only transient interactions, which would be atypical for ISWI enzymes. Another conceivable option is the formation of Apicomplexan-/Plasmodium-specific chromatin complexes with non-homologous unknown proteins associated with *Pf*Snf2L. Considering only the activity of the motor protein itself, it must be mentioned, that all *in vitro* studies were performed with recombinant proteins expressed in insect cells, where potential protein processing, folding or modification may not occur in the same way as in the natural system. Based on the observed enzymatic activity and reproducibility of the expressed proteins, this is unlikely. The recombinantly expressed *Pf*Snf2L$_{aa246\text{-}1426}$ lacks 245 amino acids at the N-terminus of the protein. This additional region, although suspected to be unstructured and nonfunctional (Muralidharan and Goldberg, 2013), could influence the absolute enzymatic activity of the protein. Despite the divergence in sequence and domain architecture and the observed quantitative differences, *Pf*Snf2L could be classified as an active CRE with ISWI-typical features.

Pending disentanglement of NTR-mediated ISWI-regulation

Besides some ISWI-characteristic features, the enzyme doesn't follow the rule of the ISWI-type autoregulatory mechanism. The autoinhibitory domains NTR and NegC are apparently not as conserved as the ATPase domain in the ISWI subfamily throughout evolution. The mechanisms of these two regulatory domains need to be considered separately. The NegC domain is proposed to inhibit the ATPase domain by interacting with it. Several attempts to resolve the structure of the NegC domain, were unsuccessful, but crosslinking data revealed likely connections to both lobes of the helicase domain as well as to the C-terminal HSS module (Harrer et al., 2018). The NegC-mediated inhibition is released upon binding of the HSS module to extra-nucleosomal DNA, explaining ATPase activity in the presence of DNA (Clapier and Cairns, 2012). When I examined the ATPase stimulation of *Pf*Snf2L, I found that this dependency also applies to this CRE. NegC, in combination with the HSS, may be the critical module of ISWI enzymes that measure DNA linker length (Leonard and Narlikar, 2015). Competitive binding and remodeling assays showed that *Pf*Snf2L is linker dependent as well. These findings are consistent with the conservation of ~50 % sequence identity within this domain and suggest that *Pf*Snf2L-NegC functions similarly to ISWI-type enzymes.

In contrast, the N-terminal regulatory domain (NTR) does not seem to have a universal function in ISWI enzymes, as *Pf*Snf2L shows hardly any of the described characteristics. The domain contains four conserved motifs, ppHSA, AThook, AutoN and AcidicN, of which only ppHSA and AcidicN can be identified in *Pf*Snf2L (Ludwigsen et al., 2017). A recent study proposed that AutoN and AcidicN are responsible for the main function of NTR, which is the autoinhibition of the ATPase until the H4 tail binds close to the NTR-ATPase interface (Ludwigsen et al., 2017). Whether the inhibition is based on molecular mimicry of the H4 tail and released upon competitive binding or whether the binding of AutoN and H4 tail is adjacent and simultaneous, is discussed (Clapier and Cairns, 2012; Ludwigsen et al., 2017; Yan et al., 2019). Regardless, the ten NTR residues proposed to be essential for inhibition, could be shown to be not sufficient in *Pf*Snf2L. Back-mutation of these crucial residues in *Pf*Snf2L-NTRmut to the *Hs*Snf2L residues didn't fully restore the dependence on the presence of the H4 tail. From this it can be concluded that further amino acids or motifs are required for the full function of the NTR domain. These additional features may not be involved in direct interaction but may be indispensable for structural arrangement or ensure functionality in some other way. The ATPase autoinhibition in *Pf*Snf2L appears to be less strict than in other ISWI enzymes studied, as it only requires the presence of DNA for full activity. Contradictory at first glance is the inability of *Pf*Snf2L to remodel H4 tail depleted nucleosomes. Apparently, the enzyme is not able to convert the ATP hydrolysis in presence of nucleosomes lacking the H4 tail into movement. This suggests a function of the H4 tail in docking and coupling the ATP-driven power stroke to actual nucleosome movement. The acidic patch within lobe2 of the ATPase domain, which was found to be the binding site for the H4 tail, is conserved in *Pf*Snf2L in the region of ~aa600 - 700 (Chittori et al., 2019). Consequently, the binding of the H4 tail may still be possible or even necessary for proper positioning of *Pf*Snf2L onto the nucleosome. Structural investigation and binding studies would be required to confirm the interaction between *Pf*Snf2L and the H4 tail.

Speculations about *Pf*Snf2L C-terminal region

The role of the HSS module in the ISWI family is still not completely explored. The SLIDE domain has been shown to bind extra-nucleosomal DNA, while HAND has been suggested to be located near the nucleosome entry site (Dang and Bartholomew, 2007). Other structural studies indicate that SANT-SLIDE directly interacts with the ATPase, while the HAND domain appears to be solvent-exposed and relatively distant (Harrer et al., 2018). The high dynamics of this part of the protein may be the reason for difficulties in structural approaches. However, several studies suggest a function in the autoregulatory mechanism, as crosslinking experiments show connections to all other protein domains (Harrer et al., 2018) and a truncation of the domain results in altered responses to stimulating substrates (Dang and Bartholomew, 2007; Grüne et al., 2003; Mueller-Planitz et al., 2013). Although *Pf*Snf2L has a very different C-terminal region, I was able to identify an involvement in ATPase autoregulation. One remaining mystery is the highly different or absent HAND domain of *Pf*Snf2L. The domain is either interrupted by large insertions or is not related to the HAND domain at all. Sequence comparison with other apicomplexan or evolutionarily distant ISWI enzymes didn't reveal any clear conservation within this region. However, structure prediction tools predict protein folding within this domain with moderate confidence, suggesting some functional relevance (Jumper et al., 2021). The structure and function of this potentially specific domain need to be further investigated. It may be unnecessary for the process of nucleosome remodeling or may still be functionally active despite its sequence divergence. This could be addressed by functional studies of deletion mutants or swap mutants with *Hs*Snf2L. This might also provide an explanation for the observation that the C-terminal region is required for nucleosome remodeling of *Pf*Snf2L, while the truncated *Hs*Snf2L core is able to move nucleosomes. Furthermore, the divergent region of ~400 residues where other ISWIs have the HAND domain, could potentially be responsible for the unique ability of *Pf*Snf2L to discriminate between canonical and H2A.Z/B.Z histones. Shift assays with variant nucleosomes and the truncated *Pf*Snf2L core will determine whether variant recognition is attributed to the ATPase or the C-terminal part of the protein.

Recently, a conserved motif upstream of the HAND domain was identified in ISWI enzymes and named acidic-patch-binding motif (ABP) (Dao et al., 2020). The core motif KRERK has been proposed to bind to the acidic patch of the nucleosome surface, mainly within H2A, and thus play a critical role in coupling ATPase activity to DNA translocation. It's been described to communicate with HAND-SANT to facilitate DNA movement from the entry site into the nucleosome. Like the HAND domain, the ABP domain is not identifiable in *Pf*Snf2L. This provides a potential reason, why the Plasmodium enzyme appears to be a highly active ATPase with very low remodeling efficacy. Since *Hs*Snf2L and *Pf*Snf2L show a similar affinity for nucleosomes, it is not the binding to the substrate that is limiting. Despite binding to nucleosomes, the energy of ATP hydrolysis is not efficiently coupled to translocation. This observation may be explained by an unknown underlying mechanism that excludes dissipation of energy.

Moreover, the large unstructured asparagine-rich N-terminus of *Pf*Snf2L still remains a mystery. Since several cloning attempts failed, this part of the protein could not be expressed recombinantly and was excluded from the characterization. It must be mentioned, that in *Plasmodium falciparum* > 30 % of all proteins contain amino acid repeats that are primarily composed of asparagine residues (Muralidharan and Goldberg, 2013). These low-complexity regions are a feature specific to *Pf* proteins and are very rare in other Plasmodium species or in eukaryotes in general. They are found in each protein family regardless of their function. The role of these poly-asparagine/glutamine repeats is rather unclear, but they are inherently prone to aggregation (Rajapandi, 2020). There is speculation that *Pf* proteins may form prions and mediate protein aggregation for a biologically beneficial reason. During this process of rapid refolding, novel domains may be formed. Another explanatory approach finds an advantage at the underlying AT-rich DNA level, which could serve as a recombination hotspot (Singh et al., 2004). Still, there is no universal functional or adaptive explanation for these regions (Zilversmit et al., 2010).

Within this study, first steps to characterize *Pf*Snf2L revealed qualitative and quantitative differences in comparison to known ISWI enzymes. To fully uncover the regulatory mechanism of *Pf*Snf2L, further studies need to be performed, including additional mutants, or using structural solution. Even though the N-terminal region of *Pf*Snf2L was omitted, the characterization of a very distinct ISWI type protein is a very good system to study ISWI-type regulatory principles that are yet not fully understood. More importantly, the functional divergence of PfSnf2L provides the basis to specifically target the enzyme with antimalarial drugs. The objective of validating *Pf*Snf2L as a drug target and screening for specific inhibitors will be addressed in the third part of this study.

5 *Pf*Snf2L CHARACTERIZATION *IN VIVO*

5.1 RESULTS

5.1.1 Transgenic parasites enable *Pf*Snf2L-detection and conditional knockout.

A comprehensive enzyme characterization requires addressing the enzyme function in the cellular context. To functionally analyze chromatin remodeling enzymes in *Plasmodium falciparum* blood stages, transgenic parasite lines were established, carrying endogenously tagged enzymes and enabling a conditional knockout (cKO) (Birnbaum et al., 2017; Collins et al., 2013). The knockout strategy is based on DiCre-mediated gene excision upon induction, and it was applied to *Pf*Snf2L and a second CRE, *Pf*Snf2P. To generate transgenic parasites, I made use of a 3D7 strain that already expresses a Cre recombinase in the form of two separate, enzymatically inactive polypeptides (DiCre). The polypeptides are fused to the rapamycin-binding proteins, either FKBP or FRB. Addition of rapamycin mediates their heterodimerization and restores the recombinase activity. Rapamycin-activated DiCre then excises the loxP-flanked sequences from a genomic locus. This strategy represents an efficient and conditionally inducible knockout system (Figure 5-1A). Aiming for a *Pf*Snf2L-/ *Pf*Snf2P-knockout, parasites were transfected with pT2A-GOI-cKO constructs that contain the following features: ~1 kb native nucleotides from the N-terminal part of the gene of interest (GOI), allowing homologous recombination with the genome. This is followed by an artificial intron with a loxP site, which represents the first cleavage site of DiCre. The rest of the GOI was recodonized to <80 % sequence identity and a 3xHA tag sequence was added to the C-terminus. Downstream of the GOI, a skip peptide and a neomycin resistance gene were fused within the same open reading frame, to enable selection-linked integration. Following a second loxP site, a green fluorescent protein (GFP) gene was integrated, and the plasmid furthermore contains an independent human dihydrofolate reductase (hDHFR) gene as a drug resistance marker.

After transfection, parasites were selected for expression of hDHFR as consequence of episomal plasmid uptake using the drug WR99210. Subsequent cultivation on G-418 selected for parasites that integrated the cassette into their genome by homologous recombination and thus express neomycin. Drug-resistant parasite clones were isolated by limiting dilution. For *Pf*Snf2L-cKO and *Pf*Snf2P-cKO parasites, the genomic DNA was isolated from five clones each. Using suitable primer pairs, the wildtype locus can be distinguished from the integrant locus by genotyping PCR (Figure 5-1B). In the uncloned bulk populations, both wildtype and integrant primers led to DNA amplification (lane 6), while all obtained clones were pure integrants (lanes 1-5). After confirming a similar growth behavior

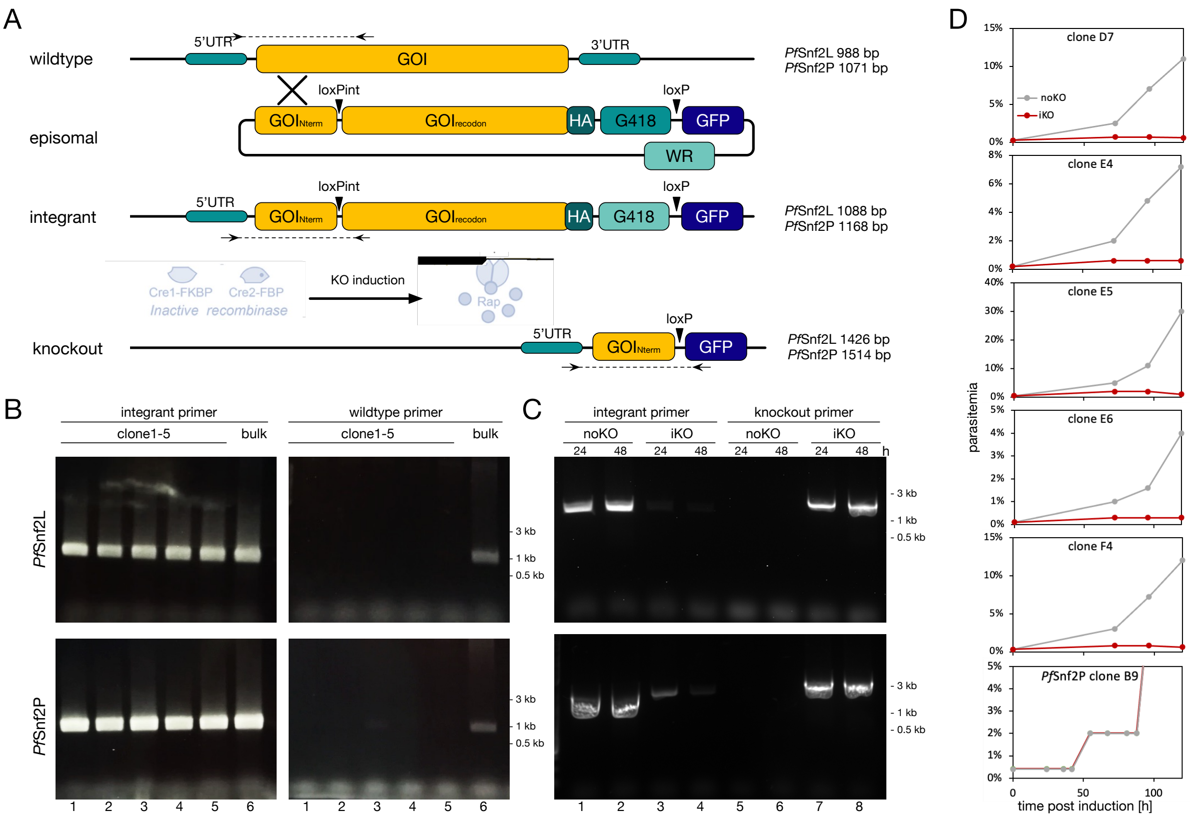

Figure 5-1: Generation of PfSnf2L-/PfSnf2P-HA-cKO parasites. A. *Schematic representation of the generation of transgenic GOI-HA-cKO parasites. Transfection of DiCre-expressing parasite line with the plasmid leads to endogenous integration of the GOI-cassette containing recodonized and C-terminally HA-tagged protein encoding sequence flanked by loxP sites. Upon rapamycin addition, the catalytically active part of the gene locus is excised. Primers for genotyping PCR are drawn and expected fragment sizes for PfSnf2L/PfSnf2P parasites are indicated. Abbreviations: GOI (gene of interest), Rap (rapamycin), UTR (untranslated region), Nterm (N-terminal), recodon (recodonized), loxPint (artificial intron with loxP site), G418/WR (resistance genes), GFP (green-fluorescent protein).* ***B.*** *Validation of locus integration by genotyping PCR with primers indicated in A. Lane 1-5 represent genomic DNA of individual clones of PfSnf2L-/PfSnf2P-HA-cKO parasites, respectively, lane 6 shows bulk genomic DNA before clone separation. DNA sizes of marker are indicated.* ***C.*** *Validation of locus excision of clone PfSnf2L-F4 (upper) and PfSnf2P-B9 (lower panel), respectively, by genotyping PCR 24/48 hours post KO induction with primers indicated in A. Lane 1,2,5,6 represent genomic DNA of not induced knockout (noKO), lane 3,4,7,8 of induced knockout (iKO) parasites. DNA sizes of marker are indicated.* ***D.*** *Parasite growth curve of five PfSnf2L-HA-cKO clones post KO induction in unsynchronous culture and of PfSnf2P-HA-cKO cloneB9 post KO induction in a synchronous culture (lower panel).*

of all *Pf*Snf2L-cKO clones upon rapamycin addition (Figure 5-1D), clone F4 was selected for further analysis. *Pf*Snf2P-cKO parasites didn't show any growth effect upon rapamycin addition. To demonstrate successful gene excision upon KO induction, genotyping PCR was performed 24/48 hours after induction using wildtype and knockout-specific primers (Figure 5-1C). The *Pf*Snf2L locus was shown to be completely excised after one day, while the *Pf*Snf2P locus was mostly but not fully depleted after one day.

After confirming the successful genetic modification on DNA level, the abundance of the tagged protein was examined. Western blot analysis probing the HA-tag in mixed blood stages of the respective parasites revealed the presence of *Pf*Snf2L-HA, while *Pf*Snf2P could not be detected neither in ring stage, trophozoite stage or unsynchronous population (Figure

5-2A). Protein levels were analyzed after fractionation of the parasite into cytoplasmic (CP) and nuclear extracts. The nuclear fraction was further treated with increasing salt concentrations to solubilize chromatin-associated proteins. The 167 kDa protein *Pf*Snf2L was shown to be a nuclear protein, mainly soluble in the nucleoplasm (NP, lane 2). Although 800 M salt should release all chromatin-bound proteins, parts of *Pf*Snf2L remain insoluble (lane 6). *Pf*Snf2P, a 240 kDa protein, was nont detected in any of the fractions or in whole cell extracts (Figure 5-2B). This points towards very low or absent protein levels in blood stages, which is in accordance with expression data obtained from bulk parasites (López-Barragán et al., 2011) and recent single cell data (Howick et al., 2019).

Parasites were synchronized and *Pf*Snf2L levels were monitored by western blot analysis to provide a more detailed view on *Pf*Snf2L expression. When equal numbers of parasites were loaded, increasing levels of *Pf*Snf2L can be seen towards the end of the cycle in late trophozoite stage (Figure 5-2C). Immunofluorescence assays (IFA) using anti-HA to stain *Pf*Snf2L and DAPI to stain DNA show a clear nuclear localization of the protein (Figure 5-2D). The signal is not evenly distributed through the nucleus but shows faint local accumulation. Signal intensity is very low in early rings and increases as parasites progress through the cycle, pointing towards activation of *Pf*Snf2L expression 10-20 hours post invasion (hpi). When quantifying the anti-HA signal and normalizing it to the amount of DNA (DAPI signal), the signal ratio decreases with schizogony (Figure 5-2E). This indicates that *Pf*Snf2L

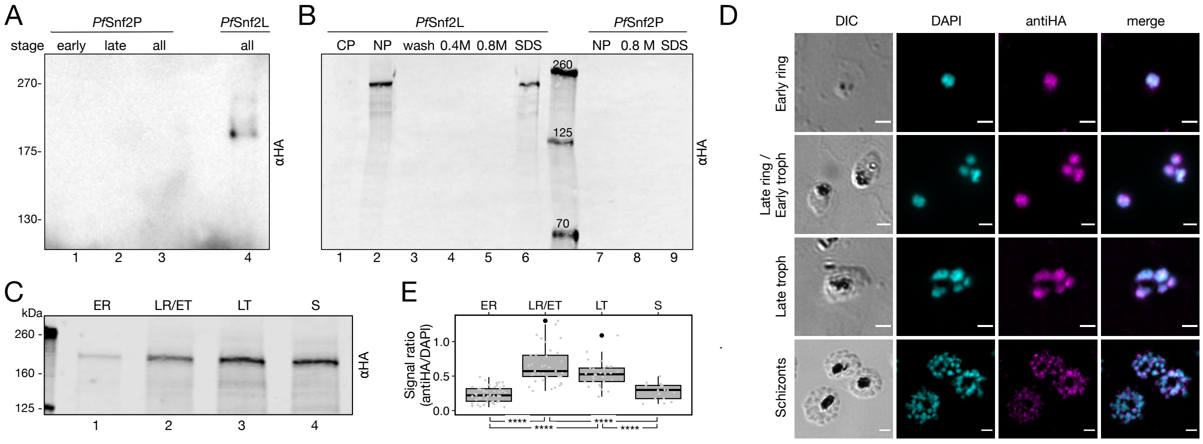

Figure 5-2: Detection of **Pf*****Snf2L in blood stage parasites. A.*** *Western blot analysis of PfSnf2L-/PfSnf2P levels with αHA antibody in whole cell extract of early/late/mixed stages using chemiluminescence readout.* ***B.*** *Western blot analysis of PfSnf2L-/PfSnf2P levels with αHA antibody in cytoplasm (CP), nucleoplasm (NP), wash fraction, chromatin extraction with 0.4/0.8 M NaCl or SDS using fluorescence readout.* ***C.*** *Western blot analysis of PfSnf2L levels using αHA antibody on whole cell extract of synchronized PfSnf2L-HA expressing parasites harvested after 11/22/33/44 hours post invasion. Equal number of infected erythrocytes were loaded on 4-20 % SDS-PAGE. Protein sizes of markers are indicated in kDa in A-C.* ***D.*** *Detection and colocalization of PfSnf2L-HA in asexual blood stages using immunofluorescence analysis (IFA), representative images shown, scale bar: 2 µm.* ***E.*** *Quantification of IFA signal as in D. For 178 parasites in four different stages, αHA and DAPI signal intensities were measured, corrected for background and αHA/DAPI signal ratio for single parasites is shown as boxplot. Significance, where present, is indicated (two-tailed Student's t-test, unpaired, ns p>0.05, ****p<0.001). Abbreviations: ER/LR (early/late ring), ET/LT, (early/late trophozoite), T (trophozoite), S (schizont), DIC (differential interference contrast), DAPI (4′,6-diamidino-2-phenylindole).*

production occurs mainly prior to replication and that in the final phase of the asexual cycle, existing protein molecules are diluted with the nuclear divisions.

The transgenic parasite strain not only allows the detection of *Pf*Snf2L-HA by western blot or immunofluorescence, but also allows inducible gene excision at specific stages of the cycle. To test the efficacy of *Pf*Snf2L-KO, synchronous parasites were treated with rapamycin immediately after invasion (0-4 hpi). Sequencing of isolated mRNA showed a clear downregulation of *Pf*Snf2L-mRNA knockout induced parasites (iKO) compared to non-induced parasites (noKO) (Figure 5-3A). The first effects are visible 10 h after induction, with maximum downregulation at 25 h. The reduction of mRNA also affects *Pf*Snf2L protein levels. Western blot analysis and IFA show that *Pf*Snf2L is strongly reduced after 46 hours, with only small amounts of protein remaining (Figure 5-3B, C), and completely disappeared one cycle later. Looking at individual parasites in IFA, the knockout was demonstrated to be highly efficient with the majority of cells being affected (>95 %) (Figure 5-3C). Based on these observations, the knockout was defined to be complete at approximately 45 hours post induction, although RNA turnover and protein turnover may vary depending on the parasite stage.

With the generation of the transgenic *Pf*Snf2L-HA-cKO strain, we have a tool to study the protein function *in vivo* in the erythrocytic cycle. The data demonstrate an inducible and efficient system for *Pf*Snf2L-depletion. Complete depletion of *Pf*Snf2L takes about one cycle, giving an idea of the timing of phenotyping. The generation of a *Pf*Snf2P-HA-cKO strain was

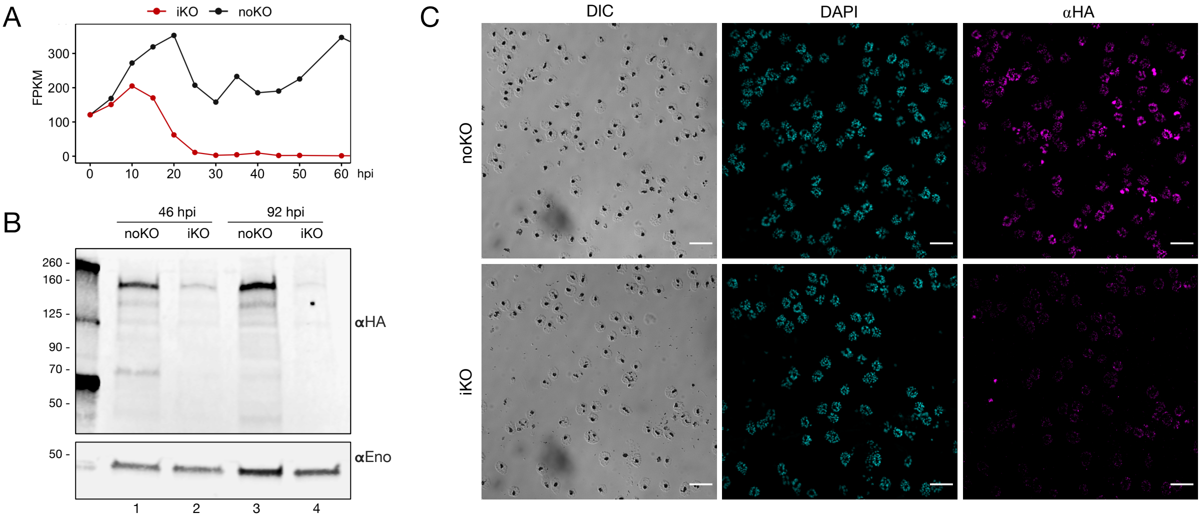

Figure 5-3: Validation of* Pf*Snf2L-KO efficacy. A. *Snf2L*$_{recodon}$*-mRNA levels (Fragments Per Kilobase of transcript per Million) upon KO induction in synchronized parasites obtained by RNA isolation and sequencing in 5 h intervals. One representative replicate of three is shown.* ***B.*** *Western blot analysis of PfSnf2L levels with αHA antibody in whole cell extracts with and without rapamycin one/two cycles after induction, antiEnolase was used as loading control. Protein sizes of marker are indicated in kDa.* ***C.*** *Immunofluorescence analysis of schizont stage parasites one cycle after KO induction with αHA antibody and DAPI, scale bar: 20 µm. Abbreviation: hpi (hours post invasion), DIC (differential interference contrast), DAPI (4′,6-diamidino-2-phenylindole).*

also successful. However, due to the lack of expression, it was not possible to detect *Pf*Snf2P via the C-terminal HA-tag, and accordingly, no growth or developmental defect was observed in the *Pf*Snf2P-KO. Therefore, a further characterization was approached only for *Pf*Snf2L.

5.1.2 Protein interaction network of *Pf*Snf2L

The fused C-terminal HA-tag opens the possibility to pull down *Pf*Snf2L and to identify interacting molecules. Since CREs are known to act in large complexes associated with different subunits, a pulldown followed by mass spectrometry (MS) analysis was performed. Based on the *in vitro* characterization and the parasite fractionation (Figure 5-2), *Pf*Snf2L is known to be chromatin-associated. Therefore, the protein was released from chromatin by DNA hydrolysis, testing DNaseI and Benzonase treatment. Nuclei were incubated with DNaseI and the chromatin was digested into 100-700 bp DNA fragments (Figure 5-4A, left). To use the digested nuclear fraction as input for the immunoprecipitation (IP), a large proportion of *Pf*Snf2L was ensured to be soluble by fractionation and subsequent western blot analysis (as in Figure 5-2B). The pulldown was mediated by αHA-coupled magnetic beads, which precipitated *Pf*Snf2L as well as other chromatin proteins, among them histones (Figure 5-4A, right). In addition, the nuclei were treated with benzonase under conditions that completely hydrolyze all types of nucleic acids. The input fraction was shown to contain only nucleotides or very short DNA fragments (Figure 5-4 B, left) with the aim of disrupting all DNA-mediated interactions. Silver stained SDS-PAGE and western blot analysis showed the pulldown of *Pf*Snf2L to be successful (Figure 5-4B, right). In both experiments, untagged 3D7 parasites were treated accordingly and served as a negative control.

The co-immunoprecipitated proteins were analyzed by mass spectrometry after liquid-chromatography (LC-MS/MS), performed by the Protein Analysis Unit (ZfP, LMU). Statistical analysis of three replicates revealed 114 enriched proteins that were considered significant in the DNaseI digested condition, excluding ribosomal proteins (Figure 5-4C). Among them are several nuclear proteins suggested to be involved in chromatin organization, but also numerous uncharacterized proteins. However, the number of hits within this experiment suggests a non-specific pulldown of many proteins with *Pf*Snf2L, probably mediated by DNA interaction. The benzonase treatment is considered to be more suitable to monitor specific and direct protein interactions of *Pf*Snf2L. Apart from ribosomal proteins, 40 significant interactors of *Pf*Snf2L were identified (Figure 5-4D, Table 5-1). This group of enzymes shares a partial overlap of 10 proteins with the hits from the DNaseI-treated pulldown (Figure 5-4E). The list of 40 hits includes several very abundant and well-known chromatin proteins such as histones or heterochromatin protein 1, which are likely interactors of *Pf*Snf2L. Besides,

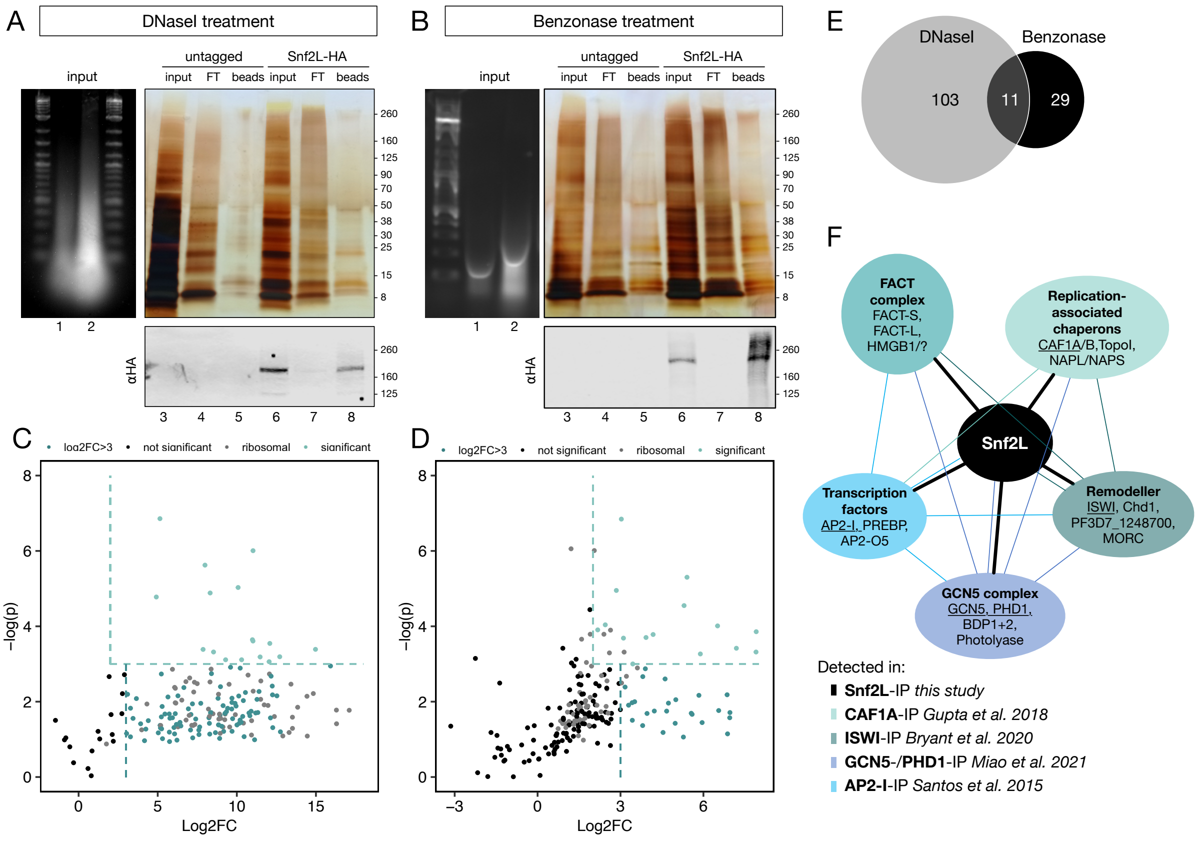

Figure 5-4: Interaction network of* PfSnf2L. *A. *DNaseI-treated anti-HA immunoprecipitation samples obtained from unsynchronized untagged 3D7 and PfSnf2L-HA parasites of one representative experiment were analyzed. Left panel shows PfSnf2L-HA-input (lane 1 – 20 %, lane 2 – 80 %) analyzed on a 2 % agarose gel. Right panel shows input (8 %), flowthrough (FT) (3 %) and beads (25 %) analyzed on 4-20 % SDS-PAGE and silver-stained (upper panel) and probed with αHA antibody on western blot (lower panel).* ***B.*** *Benzonase-treated anti-HA immunoprecipitation samples obtained from unsynchronized untagged 3D7 and PfSnf2L-HA parasites of one representative experiment were analyzed. Left panel shows PfSnf2L-HA-input (lane 1 – 10 %, lane 2 – 40 %) analyzed on a 2 % agarose gel. Right panel shows input (3 %), flowthrough (FT) (3 %) and beads (25 %) analyzed on 4-20 % SDS-PAGE and silver-stained (upper panel) and probed with αHA antibody on western blot (lower panel).* ***C.*** *Scatterplot of DNaseI-treated PfSnf2L-IP LC-MS/MS results showing -log(p-value) of a two-sided Student's t-test over log2FC(IP/ctrl) for three biological replicates: significantly enriched (turquoise), highly enriched (petrol), ribosomal proteins (grey), rest (black).* ***D.*** *Scatterplot of Benzonase-treated PfSnf2L-IP LC-MS/MS results for three biological replicates as described in C.* ***E.*** *Venn diagram of proteins significantly or highly enriched in DNaseI-treated (grey) and benzonase-treated (black) PfSnf2L-HA-IP LC-MS/MS.* ***F.*** *PfSnf2L interaction network with selected proteins identified in benzonase-treated PfSnf2L-HA-IP LC-MS/MS (black) and additional interactions detected in complementary IP experiments (underlined) with corresponding colors. Full protein names and gene IDs can be found in Table 5-1.*

several proteins and complexes specifically associated with chromatin assembly were detected (Figure 5-4F): Replication-associated chaperones such as chromatin assembly factors (CAFs) and nucleosome assembly proteins (NAPS/NAPL) and Topoisomerase I (TopoI) were enriched. The detection of all three proposed subunits of the FAcilitates Chromatin Transcription complex (FACT-L/FACT-S/HMGB1) indicates an interaction with FACT and suggests a contributing role in nucleosome assembly during transcription elongation. Furthermore, an interaction between different types of remodelers was observed, as shown for other eukaryotic CREs (Ocampo et al., 2016; Oppikofer et al., 2017). *Pf*Snf2L interacts with ISWI, Chd1 and MORC. Interestingly, some transcription factors and numerous GCN5 (General control non-depressible 5) complex subunits were also co-immunoprecipitated with *Pf*Snf2L. These proteins are known to act on promoter regions and are involved in transcription regulation (Cui et al., 2007; Fan et al., 2004; Miao et al., 2021), which could a hint to the molecular role in *Pf*Snf2L, potentially regulating gene expression.

Table 5-1: List of proteins identified in benzonase-treated **Pf*****Snf2L-HA-IP LC-MS/MS*** *with log2FC and p-value. Product description and name are derived from PlasmoDB,* **+** *indicates the identification in complementary IP experiments (Bryant et al., 2020; Gupta et al., 2018; Miao et al., 2021; Santos et al., 2017),* ***A****-marked proteins are Plasmodium or Apicomplexan-specific,* ⚭ *-marked proteins were also detected in DNaseI-treated IP.*

Gene ID	Product Description	Name	Log 2FC	p-value	AP2-I	ISWI	CAF1	GCN	PHD1		
PF3D7_0510500	topoisomerase I	TopoI	7.9	0.0211							⚭
PF3D7_1234900	CHCH domain-containing protein		7.9	0.0363		+				**A**	
PF3D7_1033300	conserved protein. unknown function		7.2	0.0328						**A**	⚭
PF3D7_1449500	AP2 domain transcription factor AP2-O5	ApiAP2	7.0	0.1806						**A**	
PF3D7_0801000	Plasmodium exported protein (PHISTc)		7.0	0.2074		+				**A**	
PF3D7_0501800	chromatin assembly factor 1 subunit A	CAF1A	6.9	0.1127			+		+		
PF3D7_1441400	FACT complex subunit SSRP1	FACT-S	6.6	0.1713	+	+			+		
PF3D7_1143200	DnaJ protein. putative		6.5	0.0181							
PF3D7_0517400	FACT complex subunit SPT16	FACT-L	6.0	0.2357	+	+			+		
PF3D7_1033700	bromodomain protein 1	BDP1	5.8	0.1144	+			+	+	**A**	⚭
PF3D7_1212900	bromodomain protein 2	BDP2	5.6	0.1894						**A**	
PF3D7_0823300	histone acetyltransferase GCN5	GCN5	5.6	0.1841	+			+	+		
PF3D7_1107300	polyA-binding protein-interacting protein 1	PAIP1	5.4	0.0050							⚭
PF3D7_1329300	chromatin assembly factor 1 subunit B	CAF1B	5.3	0.3459			+			**A**	
PF3D7_1220900	heterochromatin protein 1	HP1	5.0	0.1285		+	+	+	+	**A**	⚭
PF3D7_1008700	tubulin beta chain		5.0	0.2404		+					
PF3D7_1203700	nucleosome assembly protein	NAPL	4.7	0.1407		+			+		
PF3D7_0919000	nucleosome assembly protein	NAPS	4.7	0.1739		+		+	+	**A**	
PF3D7_1104200	chromatin remodeling protein	SNF2L	4.6	0.0741	+	+			+		⚭
PF3D7_1345100	thioredoxin 2	TRX2	4.5	0.3066						**A**	
PF3D7_1468100	MORC family protein	MORC	4.2	0.1736		+		+		**A**	
PF3D7_1408500	unknown function		4.2	0.0228						**A**	⚭
PF3D7_0500800	mature erythrocyte surface antigen	MESA	4.0	0.1851				+	+	**A**	
PF3D7_0320900	histone H2A.Z	H2A.Z	3.9	0.0247		+					⚭
PF3D7_0624600	ISWI chromatin-remodeling ATPase	ISWI	3.9	0.0565	+	+			+	**A**	
PF3D7_1021900	PHAX domain-containing protein		3.8	0.0696							⚭
PF3D7_1138800	WD repeat-containing protein		3.8	0.2552							
PF3D7_1011800	PRE-binding protein	PREBP	3.5	0.1355		+				**A**	
PF3D7_1147300	unknown function		3.4	0.0497						**A**	⚭
PF3D7_1008100	PHD finger protein PHD1	PHD1	3.4	0.2219	+			+	+	**A**	
PF3D7_1330800	RNA-binding protein, putative		3.4	0.1390		+		+	+	**A**	
PF3D7_1023900	chromodomain-helicase-DNA-binding protein 1 homolog	CHD1	3.3	0.1486	+				+		
PF3D7_0201900	erythrocyte membrane protein 3	EMP3	3.2	0.0918						**A**	
PF3D7_1317400	zinc finger protein		3.0	0.0011		+				**A**	⚭
PF3D7_0513600	deoxyribodipyrimidine photo-lyase		2.8	0.0071				+	+		
PF3D7_1036900	unknown function		2.2	0.0201				+		**A**	

Among these co-immunoprecipitated proteins, no orthologues of any known ISWI-associated subunits from other eukaryotes, such as Itc1, Ioc2/3/4, ACF1, Dpb4, etc., could be detected. However, *in silico* attempts didn't reveal any orthologues of these interactors to be present in *Plasmodium falciparum,* suggesting that *Pf*Snf2L functions as a single protein or that it forms atypical complexes*.* Indeed, 21 Apicomplexan or Plasmodium-specific proteins were found in the IP experiment, among them several uncharacterized proteins, (marked with **A** in Table 5-1). These uncharacterized proteins don't allow any functional conclusions. In general, this finding points to the possibility of novel chromatin complexes around *Pf*Snf2L, that are specific for Plasmodium or Apicomplexans and not known from other eukaryotes studied.

*Pf*Snf2L has been shown to be chromatin-associated (5.1.1) and the *in vitro* characterization revealed binding to DNA (Figure 4-2). This raises the question of whether *Pf*Snf2L has specific binding sites on the genome. Therefore, chromatin-immunoprecipitation (ChIP) was performed using the HA-tag of *Pf*Snf2L and crosslinked chromatin. The precipitated DNA was used for library preparation and high-throughput sequencing. Since CREs usually exhibit only transient binding to DNA, these enzymes are difficult to crosslink. Two different crosslinking methods – formaldehyde only and formaldehyde plus disuccinimidyl glutarate (DSG) – were tested. The DNA co-immunoprecipitated with *Pf*Snf2L-HA was analyzed by

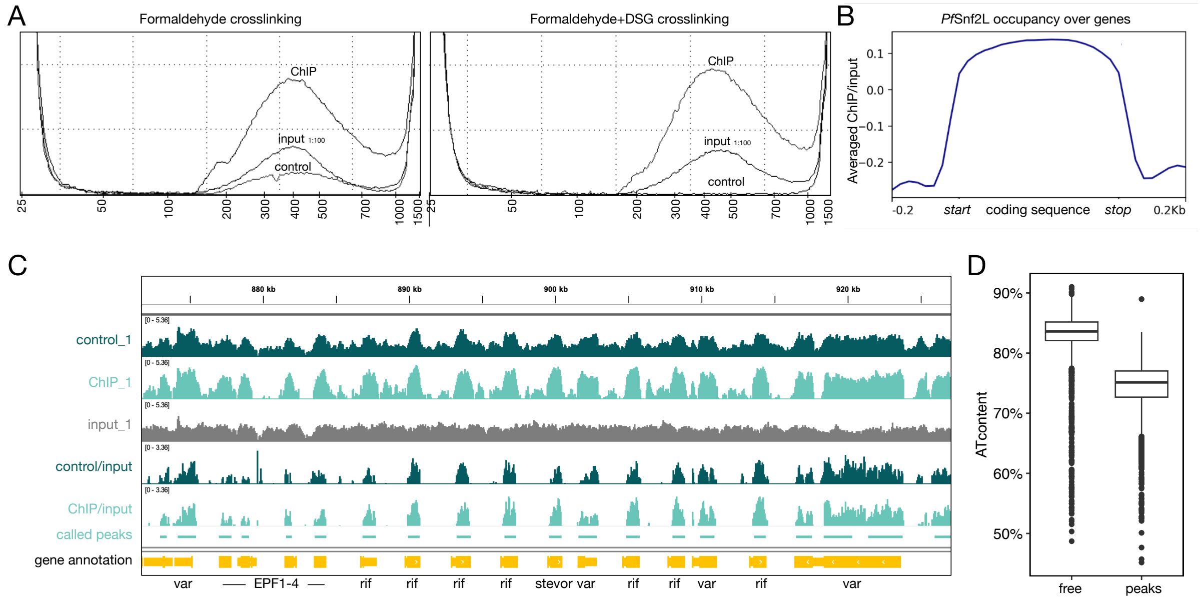

Figure 5-5: GC-enrichment in ChIP-experiment. A. *Tapestation profile with quantitative DNA fragment size distribution of Chromatin-immunoprecipitation samples of PfSnf2L-HA-IP using either formaldehyde or formaldehyde+DSG crosslinking: input (diluted 1:100), ChIP (anti-HA pulldown), control (no-antibody pulldown). One of three replicates shown. DNA lengths are indicated in bp.* ***B.*** *Occupancy profile of ChIP/input (six replicates averaged) over all genes aligned to start and stop codon of coding sequences.* ***C.*** *Exemplary coverage plot of one representative replicate of PfSnf2L-HA-ChIP using formaldehyde+DSG for fixation: input, ChIP, control. Input-normalized tracks are shown in log-scale. Called peaks and gene annotation are indicated, regions shown is chr2:872000–926000.* ***D.*** *GC-enrichment in PfSnf2L-HA-ChIP peaks. For every peak and free region in between, the AT-content was calculated and is shown as boxplot.*

automated electrophoresis and quantification showed a clear enrichment of DNA in the *Pf*Snf2L-IP compared to the no-antibody control for both crosslinking conditions (Figure 5-5A). Input and ChIP-DNA (and control samples where possible) were sequenced and mapped to the *Pf* genome. In all ChIP samples, regardless of crosslinking method, mainly coding regions were enriched (Figure 5-5B,C). As this pattern was also visible in the no-antibody control, I assume a non-specific enrichment of these regions. Due to the peculiar nature of the *Pf* genome with its very high AT-content of up to 90 % in non-coding regions, it may occur that a bias towards GC-enrichment arises in ChIP-Seq (Baumgarten and Bryant, 2022). The correlation of GC-content with supposed *Pf*Snf2L occupancy is very strong in these data (Figure 5-5D), so I don't consider these findings to be true *Pf*Snf2L binding sites.

5.1.3 Multiple KO phenotypes of essential *Pf*Snf2L

***Pf*Snf2L-KO results in a developmental defect.**

The integrated conditional KO system in the transgenic *Pf*Snf2L-HA-cKO strain and the previous knockout validation enabled us to study the function of *Pf*Snf2L in the erythrocytic life cycle. As first KO induction experiments of unsynchronous parasites showed, the parasitemia (defined as infected red blood cells / red blood cells) is reduced upon KO (Figure 5-1D). These experiments demonstrate the essential role of *Pf*Snf2L in *Plasmodium falciparum* blood stages. To characterize the timing of this lethal effect, *Pf*Snf2L-HA-cKO were tightly synchronized and KO was induced immediately after invasion (0 hpi) or at late ring stage (24 hpi) or treated with DMSO as control. The number of parasites and their morphological appearance were monitored for >2 cycles. As shown by the growth curves and Giemsa-stained blood smears of two biological replicates, both induction timepoints lead to parasite death approximately one cycle after induction (Figure 5-6A,B). Furthermore, parasite development in the second cycle is severely impaired. However, there is no specific event in the cycle progression that is blocked and that would kill the parasites. Rather, the effect depends on the timing of KO induction, harming the parasites at different functional levels. The early iKO parasites (iKO0) don't develop beyond the ring stage, while the late iKO parasites (iKO24) seem to reach a trophozoite-like stage before arresting and dying. The quantification of nuclei at the end of the second cycle (46 hpi) reflects the replication defect caused by knockout induction (Figure 5-6C). In the noKO population, most of the parasites completed multiple rounds of nuclear division and possess up to 32 nuclei per infected cell. The proportion of parasites with more than 8 nuclei is greatly reduced in late iKO, while early iKO parasites were shown to hardly accomplish any nuclear division. An exemplary IFA with *Pf*Snf2L-HA staining, nuclear staining and antiAma1 – an invasion organelle marker named

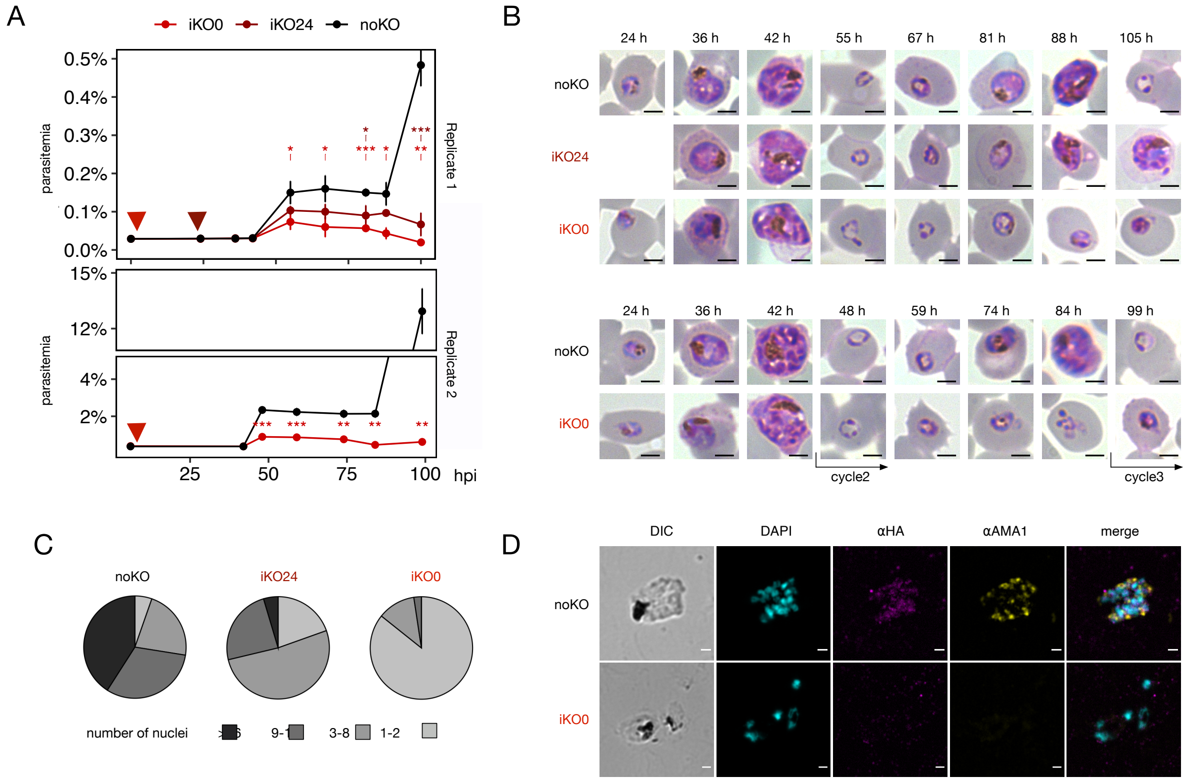

Figure 5-6:* PfSnf2L *is essential for parasite development. A. *Growth curve assay of synchronized Snf2L-HA-cKO parasites not-induced (black), induced at 24 hpi (dark red), induced at 0 hpi (light red) in two biological replicates. Mean ± SD of technical replicates is shown, significance is indicated (two-tailed Student's t-test, unpaired, ns p>0.05, * p<0.05, ** p<0.01, ***p<0.005).* ***B.*** *Representative Giemsa-stained blood smears of parasites as in A, scale bar: 2 µm.* ***C.*** *Quantification of nuclei per cell in noKO/iKO24/iKO0 schizonts as in A (upper panel) harvested 46 hpi of cycle2 (n=100 each).* ***D.*** *Immunofluorescence analysis of noKO/iKO0 schizonts harvested 46 hpi of cycle2 stained with DAPI, anti-HA and anti-AMA1 as apicoplast marker, scale bar: 1 µm.*

Apical membrane antigen 1 – demonstrates that no schizogony, nuclear division or invasion organelle formation occur in the second cycle with *Pf*Snf2L being absent (Figure 5-6D).

***Pf*Snf2L-KO results in impaired egress.**

With early knockout induction, already transition to the second cycle seems to be impaired. The growth curves of both replicates show a significantly reduced parasitemia for very early rings, right after invasion of new red blood cells. To investigate this phenomenon in detail, the parasite reproduction rate was determined. Mature schizonts were purified and incubated with fresh red blood cells (RBCs) for two hours and quantified subsequently (Figure 5-7A). With early KO induction, the number of newly invaded RBCs was reduced by a factor of ~3, while the late iKO showed a reproduction rate comparable to non-induced parasites. To ensure that this effect was not due to impaired nuclear division within the first cycle of iKO0, the number of nuclei of individual noKO/iKO0 schizonts was quantified (Figure 5-7B). Since no difference in the number of nuclei is observable, I assumed the process of host cell exit or entry to be affected. Indeed, live cell imaging of parasite egress revealed an aberrant

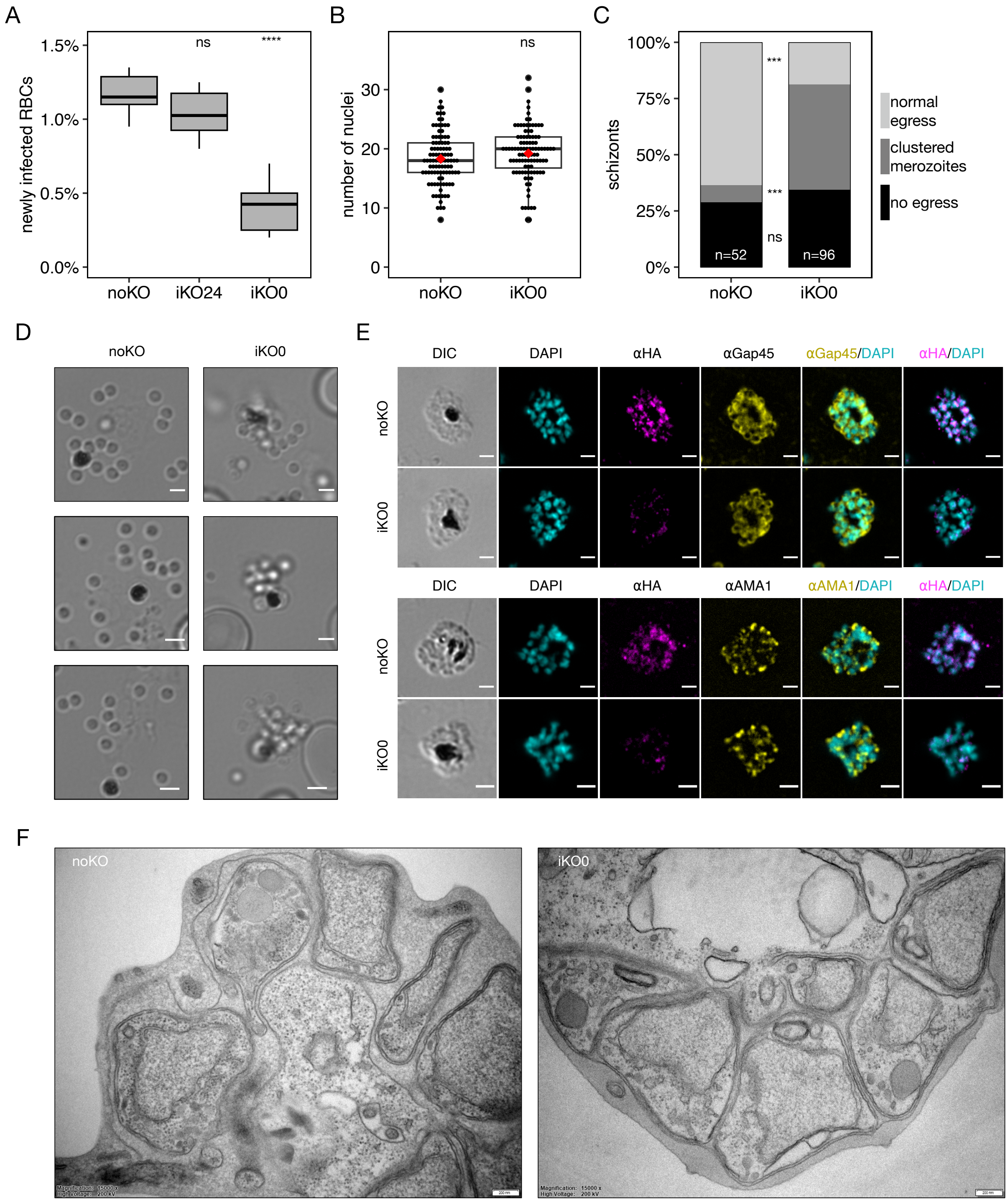

Figure 5-7: Egress defect upon* PfSnf2L-KO *despite unaffected schizogony. A. *Reproduction rate of noKO/iKO24/iKO0 schizonts (46 hpi) after 2 h with fresh RBCs ($n_{parasites}$>100 each) for two replicates.* ***B.*** *Quantification of nuclei in noKO /iKO0 parasites 46 h after induction, each dot representing one schizont.* ***C.*** *Classification and quantification of egress phenotype in live imaging of noKO/iKO schizonts 46 h after induction* ***D.*** *Three representative images of noKO/iKO0 parasites after egress in live imaging, scale bar: 1 µm.* ***E.*** *Immunofluorescence analysis of noKO/iKO schizonts 46 h after induction stained with DAPI, anti-HA and anti-Gap45 as cytogenesis marker, anti-AMA1 as apicoplast marker, respectively, scale bar: 2 µm* ***F.*** *Representative transmission electron microscopy image of PfSnf2L-HA-cKO parasites not-induced/induced 46 hpi plus additional maturation in presence of compound2, scale bar: 0.2 µm. Significance is indicated (two-tailed Student's t-test, unpaired, ns $p>0.05$, ***$p<0.005$, ****$p<0.001$).*

behavior of iKO0 schizonts in comparison with noKO schizonts during RBC exit (Figure 5-7D). Highly mature noKO schizonts show an abrupt rupture of the host cell, releasing all merozoites as individual daughter cells distant from the food vacuole (black). The iKO0 merozoites, in contrast, appear to cluster together after host cell rupture and only a few daughter cells separate gradually. Classification and quantification of these observations in live imaging shows the effect to be significant (Figure 5-7C). The reason for the host cell exit defect in iKO0 could be due to defective cytokinesis during schizogony. To investigate this process, mature schizonts were analyzed in IFAs by staining for glideosome associated protein 45 (Gap45), a protein anchored to the inner membrane complex that is formed late during cytokinesis (Figure 5-7E, upper panel). Anti-HA staining confirmed the absence of *Pf*Snf2L in iKO0 schizonts, but no difference regarding Gap45 could be observed, indicating normal cytokinesis. IFA of iKO0/noKO staining for Ama1 also showed no obvious defects in microneme formation (Figure 5-7E, lower panel). Using transmission electron microscopy, iKO0 schizonts were shown to have accomplished merozoite segregation similar to noKO schizonts (Figure 5-7F). Summarizing these results, imaging phenotyping of schizonts didn't reveal a clear cause for the exit defect in *Pf*Snf2L-iKO parasites.

***Pf*Snf2L-KO results in reduced *exportome* gene expression.**

To find the link between the lack of *Pf*Snf2L and the resulting host cell exit defect, transcriptomic analysis was employed. Sequencing of mRNA obtained from iKO0/noKO parasites every five hours didn't reveal any differentially expressed genes (DEGs) until 40 hpi (Figure 5-8A). The appearance of the first changes in gene expression after 40 hours corresponds to the duration of *Pf*Snf2L-depletion. At schizont stage (45 hpi), 217 genes exhibit significantly reduced expression levels upon *Pf*Snf2L-KO. Gene ontology (GO) term enrichment analysis with respect to cellular compartment showed that primarily proteins belonging to the Maurer's cleft, proteins in the host cell cytoplasm and on the host cell surface, are downregulated (Figure 5-8B). Maurer's clefts are parasite-derived membranous structures in the host cell cytoplasm, that are involved in trafficking and are unique to *Plasmodium falciparum* (Mundwiler-Pachlatko and Beck, 2013). In view of these enriched GO terms, mainly transcripts of exported proteins seem to be affected by *Pf*Snf2L-KO. At least 83 of the 217 downregulated genes are known or proposed to be part of the *exportome* – the totality of exported proteins*,* with some of them predicted to be essential for the parasite (Figure 5-8C). Looking more closely at the intersection of downregulated and exported proteins, several protein families are affected with more than one member. In addition to *var* genes – the clonally variant genes encoding for surface antigens – several trafficking proteins (PTPs, MAHRPs, DNAJs) are less expressed. Furthermore, a large number of downregulated proteins are proposed to be involved in red blood cell remodeling through cytoskeleton interaction, such as SBP1, RESAs, some pHISTa-c (Jonsdottir et al., 2021; Mills et al., 2007). These candidates could potentially be associated with the defect in host cell exit, as the

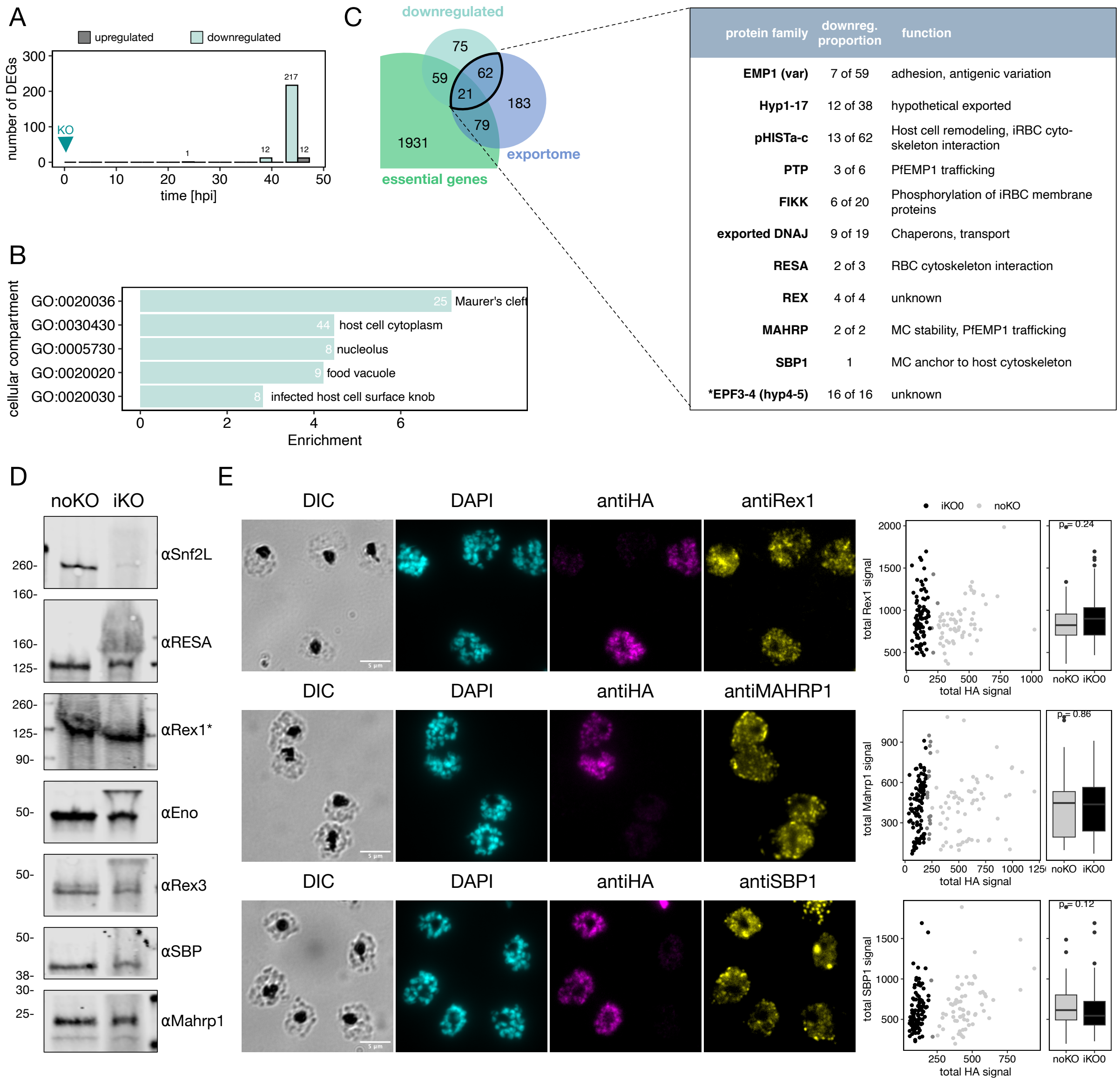

protein family	downreg. proportion	function
EMP1 (var)	7 of 59	adhesion, antigenic variation
Hyp1-17	12 of 38	hypothetical exported
pHISTa-c	13 of 62	Host cell remodeling, iRBC cyto-skeleton interaction
PTP	3 of 6	PfEMP1 trafficking
FIKK	6 of 20	Phosphorylation of iRBC membrane proteins
exported DNAJ	9 of 19	Chaperons, transport
RESA	2 of 3	RBC cytoskeleton interaction
REX	4 of 4	unknown
MAHRP	2 of 2	MC stability, PfEMP1 trafficking
SBP1	1	MC anchor to host cytoskeleton
*EPF3-4 (hyp4-5)	16 of 16	unknown

Figure 5-8: Reduced expression of exported protein upon* PfSnf2L-KO. *A. *Number of differentially expressed genes (DEGs) – down-/upregulated – in RNA-Seq of synchronous iKO0 / noKO parasites over life cycle, harvested in 5 h intervals after induction at t0 in three biological replicates.* ***B.*** *Gene ontology (GO) term enrichment regarding cellular compartment of genes downregulated at schizont stage, 45 hpi (as in A). Numbers of DEGs within the GO Terms are indicated (white).* ***C.*** *Venn diagram showing the intersection of DEGs at 45 hpi (as in A) with genes predicted to be essential ((Zhang et al., 2018b), MIS<0.3) and with genes encoding exported proteins, combining predicted (Boddey and Cowman, 2013) and proven (Jonsdottir et al., 2021) exportome (listed in Appendix 3), among all genes being expressed at schizont stage. Right panel shows a list of exported protein families, their function and the number of group members being downregulated in PfSnf2L-KO parasites 45 hpi.* ***D.*** *Western blot analysis of exported proteins with significantly reduced mRNA level in whole cell extracts in noKO/iKO parasites 46 hours after induction. Detecting PfSnf2L via anti-HA serves as KO confirmation, anti-Enolase was used as loading control.* ***E.*** *Immunofluorescence analysis of a mixture of noKO/iKO schizonts 46 h after induction with DAPI, anti-HA and antibodies targeting exported proteins downregulated on mRNA level (left panel), scale bar: 5 µm. Total fluorescence intensity of PfSnf2L (αHA) and exported proteins was quantified per parasite (mid panel) and low/high HA levels enabled the identification of noKO/iKO parasites. Total Rex1-/MAHRP1-/SBP1-signal in noKO/iKO parasites is shown as boxplot, p-values are indicated (two-tailed Student's t-test, unpaired).*

properties of red blood cells play an important role in this process (de Koning-Ward et al., 2016; Millholland et al., 2011; Sherling and van Ooij, 2016).

To analyze whether the reduced mRNA levels are also reflected in reduced protein levels, western blot analysis of late schizonts (iKO0/noKO) was performed with available antibodies targeting RESA, Rex1/3, SBP1, MAHRP1 (Figure 5-8D). *Pf*Snf2L was again demonstrated to be largely absent, but all targeted exported candidates show comparable levels in iKO/noKO when compared to the loading control anti-Enolase. Since western blot analysis did not show a conclusive reduction for any of the proteins analyzed, IFA experiments were performed to see effects in individual parasites (Figure 5-8E). To compensate for differences in staining, noKO and iKO0 parasites were mixed and stained for αHA and the respective exported antigen (αRex1, αSBP1, αMAHRP1). Signal intensities per parasite were automatically quantified and individual parasites were assigned to noKO or iKO0 based on their anti-HA signal. Neither Rex1 nor SBP1 or MAHRP1 showed a significant reduction of protein levels in iKO0 versus noKO. From this it can be concluded that although the expression of these exported proteins is regulated by *Pf*Snf2L, downregulation cannot explain the detected egress phenotype. Looking at the expression and export timing of the analyzed proteins, their transcription is only being activated in late schizont stage. The expression peaks in early ring stage, where these proteins are then exported in order to modify the newly invaded erythrocyte. Their dysregulation may affect the following cycle but doesn't account for the egress defect.

_Pf_Snf2L-KO alters red blood cell properties.

Interestingly, the list of downregulated genes in iKO0 schizonts contains 16 members of the exported protein family (EPFs). The abundance and the role of these proteins couldn't be investigated in more detail due to lacking antibodies. From literature I have reason to assume, that their downregulation might explain the observed exit defect as discussed in 5.2. In this context, I investigated the contribution of the red blood cell to the egress defect upon *Pf*Snf2L-KO. Therefore, I monitored the egress process in live imaging supplemented with phalloidin, which stains the RBC cytoskeleton. The impermeable dye enters the host cell only with membrane rupture, marking the start of the egress event. The image sequence of an exemplary noKO parasite during egress shows that the RBC membrane curls up quickly immediately after rupturing (Figure 5-9A, upper panel). The remaining residuals – termed RBC ghost – accumulate relatively distant to the released merozoites. In contrast, the iKO0 egress process is characterized by an RBC that gets perforated (visualized by phalloidin-influx) but doesn't curl up (Figure 5-9A, lower panel). The RBC cytoskeleton remains in its original spherical shape, preventing the daughter cells from dispersing. Even after some time, the

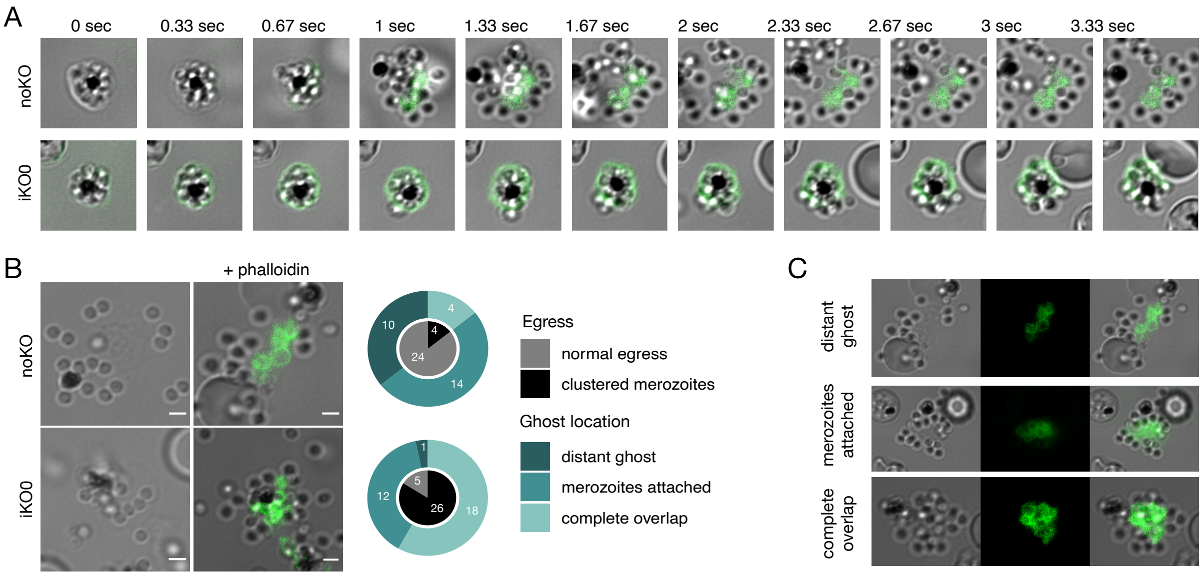

Figure 5-9: Attached red blood cell (RBC) ghost during egress in PfSnf2L-KO. A. *Time series of noKO/iKO0 parasite egress 46 h after induction in phalloidin-supplemented live imaging, one representative parasite shown.* ***B.*** *Representative images and quantification of egress phenotype and RBC ghost phenotype (with classification as in C.) of individual egressed noKO/iKO schizonts 46 h after induction during phalloidin-supplemented live imaging, scale bar: 1 µm.* ***C.*** *Exemplary images of RBC ghost classification as distant/merozoites attached/ complete overlap determined 40 sec after egress start.*

RBC ghost doesn't dissociate from the merozoites but remains attached to the merozoites. Classification and quantification of the RBC ghost location 40 sec after egress start as *distant*, *merozoites attached* or *completely overlapping* correlates with the egress phenotype (Figure 5-9B,C). Attached ghosts and accompanying clustering of merozoites are mainly observable in iKO0 parasites. This experiment provides a possible explanation for why the KO parasite daughter cells are not efficiently released. Red blood cell properties such as rigidity and permeability are known to be important for parasite exit and are also known to be actively modified by the parasite (Glenister et al., 2002; Maier et al., 2009, 2008). Among other exported and Maurer's cleft-associated proteins, the exported protein family (EPFs) has been proposed to contribute to the host cell renovation (Mbengue et al., 2013). Knockout of *Pf*Snf2L apparently results in decreased EPF transcript abundance. Most likely, this also leads to a reduction of EPF protein in the parasite, but also in the host cell. This in turn could be the reason for the altered properties of the erythrocyte, that hinder the iKO merozoites from detaching from the parental cell.

5.1.4 *Pf*Snf2L controls just-in-time transcription of stage-specific genes.

The developmental defects observed in *Pf*Snf2L-KO are likely a consequence of dysregulated gene expression. To investigate the different effects of early (iKO0) and late (iKO24) KO, a detailed transcriptomic analysis was performed by inducing the knockout as before and sequencing extracted mRNA +45 / +50 / +60 hours after induction (Figure 5-10A). This allows to follow the KO-caused differential expression over time in direct comparison to noKO control. Additional sampling and sequencing of noKO parasites every 5 hours was used to create a reference transcriptome representing the whole asexual cycle of the used parasite strain, to which the KO-affected samples can be compared. Visualization of the entire transcriptome of the reference cycle using a principal component analysis shows a circular trajectory of the samples (Figure 5-10B, circles). Looking at the later timepoints (+45/+50/+60) within the analysis, the noKO data points largely fit into the trajectory according to their cycle progression, while the iKO samples deviate. *Pf*Snf2L-KO induction leads to a delay in the appearance of the stage-specific transcriptome, which is visible in delayed data points. Already +45 hours after KO induction, there is a gap between noKO and iKO transcriptome, which increases with further cycle progression (+50 / +60). This delay effect is true for both induction timepoints (early/late KO), they only differ in the parasite stage. Early KO parasites show a delay in late schizont to early ring stage, while late KO parasites are delayed in late ring stage, which in both cases is the time it takes to diminish *Pf*Snf2L levels. Another common method to determine cell cycle progression in *Plasmodium falciparum* is to compare transcriptomes to an existing highly synchronous transcriptome data set to estimate the most likely age using a maximum likelihood approach. Applying this analysis and comparing the obtained RNA-Seq data to (Painter et al., 2018), I found a very similar picture of iKO parasites progressing slower through the life cycle than the noKO parasites, regardless of induction timing (Figure 5-10C). The delay in the transcriptome reflects the observed developmental defects in Giemsa-stain.

Analysis of individual differentially expressed genes may explain this in more detail. In the schizont stage sample (early KO +45), ~200 genes are differentially expressed. However, the number of DEGs is much larger in all other samples, with 1000-2000 genes dysregulated upon *Pf*Snf2L-KO (Figure 5-10E). As the *Pf*Snf2L genome contains only ~5500 genes, this corresponds to a large proportion. Summing up all DEGs upon *Pf*Snf2L-KO irrespective of timepoint, 75 % of all genes were found to show altered expression at least at one timepoint. A GO term enrichment analysis showed that all kinds of pathways are affected. Breaking it down into five major pathways shows that gene sets required for the same process are upregulated at one timepoint and downregulated at another. The expression of these groups of genes is usually highly regulated and timed with cycle progression, depending on when they are needed. Exported protein expression peaks in early ring stage, while translation-associated genes are expressed later. Genes required for metabolism and replication are activated in late ring stage, invasion and motility genes at trophozoite stage. Clustering of genes according to their temporal expression profile reveals a wave-like path with gene activation and silencing (Figure 5-10D). The iKO profile of the synchronous cells shows that the gene clusters undergoing actual regulation at the timepoint of sampling are dysregulated. Genes that are activated in noKO at this stage are not activated in iKO, and genes to be repressed in noKO remain active in iKO. This suggests that *Pf*Snf2L is not a gene-specific regulator, but rather globally regulates the just-in-time transcription of stage-specific genes. Thus, *Pf*Snf2L defines the timing of progression and coordination of the blood stages.

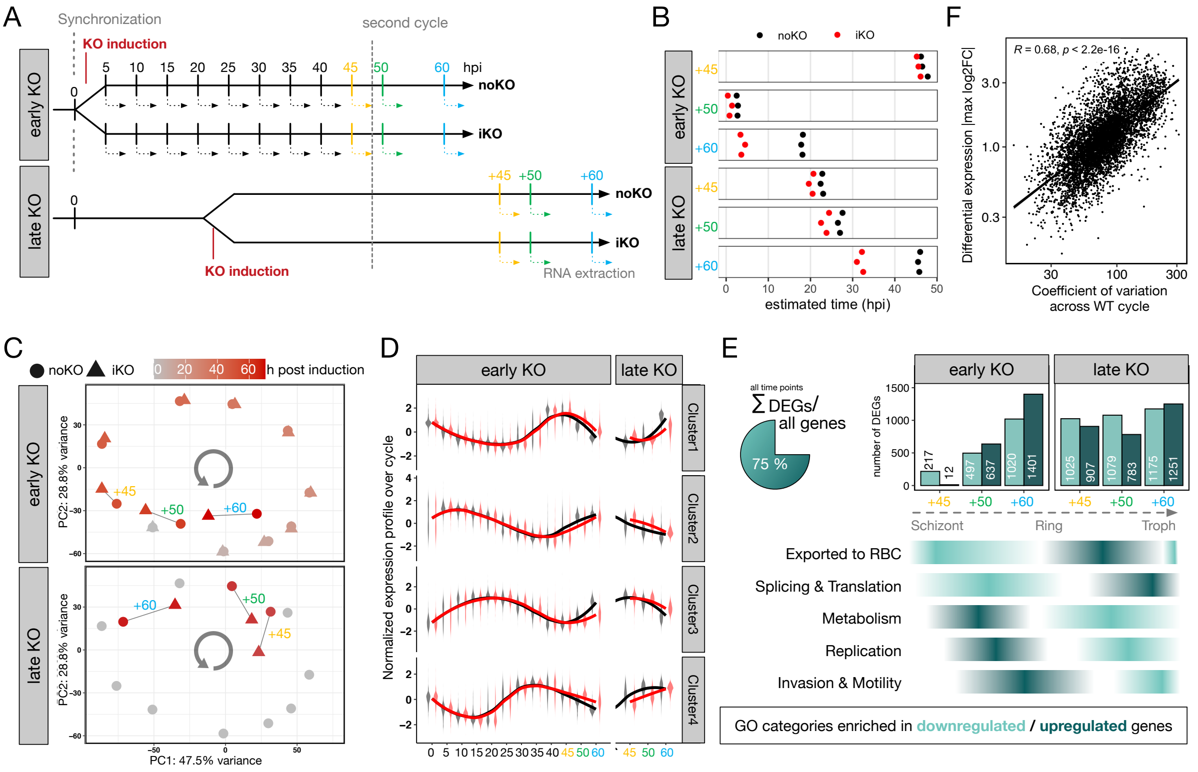

Figure 5-10: Delayed gene expression in* PfSnf2L*-KO parasites. A. *Experimental setup of timing and sampling for transcriptome analysis, noKO samples 0-45 hpi (black) serve as reference transcriptome. For PfSnf2L-KO analysis, RNA was isolated 45/50/60 hours post early KO induction or late KO induction, respectively.* ***B.*** *Principal component analysis of whole RNA-Seq data of highly synchronous noKO (circle) / iKO (triangle) parasites at different timepoints (45 h / 50 h / 60 h) post early (upper) or late KO induction (lower panel). Pool of three biological replicates shown.* ***C.*** *Cycle progression estimation of RNA-Seq samples as in A with three biological replicates each in relation to a hourly reference transcriptome (Painter et al., 2018).* ***D.*** *Normalized relative expression profile of genes that are differentially expressed over all timepoints in noKO (black) and iKO (red), clustered according to expression profiles over time.* ***E.*** *Summation (left) and timed numbers (right) of differentially expressed genes (DEGs) in iKO/noKO parasites as in A. Superordinate GO categories enriched in downregulated (turquoise) or upregulated (petrol) genes based on GO Term enrichment analysis are shown.* ***F.*** *Pearson correlation between the maximal differential expression of each gene and its expression variation across cycle in the reference transcriptome.*

Some genes undergo more transcriptional changes across the cycle than others, represented as coefficient of variation. Plotting this parameter against the maximum differential expression change upon *Pf*Snf2L-KO for each gene shows a significant correlation (Figure 5-10F). This suggests that genes with more transcriptomic variation are more dependent on *Pf*Snf2L, probably because they require more stringent regulation for correct gene expression throughout the cycle. The magnitude of the transcriptomic effect and the number of affected genes emphasize the importance of *Pf*Snf2L in the orchestrated gene expression program.

The described delay in gene expression mainly refers to genes having a function in the asexual erythrocytic stages. Beyond, the parasite genome encodes numerous genes required for other life cycle stages. It includes genes specific for the sexual erythrocytic stages, but also for mosquito stages or for transmission to the human liver. During the asexual cycle, these genes should largely be silenced. A subset of genes known to be specific for stages other than asexual blood stages – 288 gametocyte-specific genes, 66 ookinete-specific genes and 89 sporozoite-specific genes – were selected and analyzed for dysregulation in *Pf*Snf2L-KO (listed in Appendix 4). In ring stages, the expression of these genes is enhanced upon iKO, or rather, they are mistakenly expressed (Figure 5-11A). As the cycle progresses, this effect diminishes. This observation suggests a function of *Pf*Snf2L in keeping unneeded genes silenced, predominantly at the ring stage. The gametocyte-specific gene set changes later in the cycle, at late ring or trophozoite stage, towards reduced mRNA abundance in iKO. The process of gametocyte formation takes place in human erythrocytes, and commitment to gametocytogenesis occurs for a small proportion of asexual stages. The regulatory mechanism of sexual commitment is not entirely solved, but is mostly attributed to epigenetic regulation, with *Pf*Snf2L potentially contributing to this process. *Pf*Snf2L has previously been proposed as an upstream regulator of gametocyte formation, along with several other epigenetic regulator candidates (Poran et al., 2017; van Biljon et al., 2019).

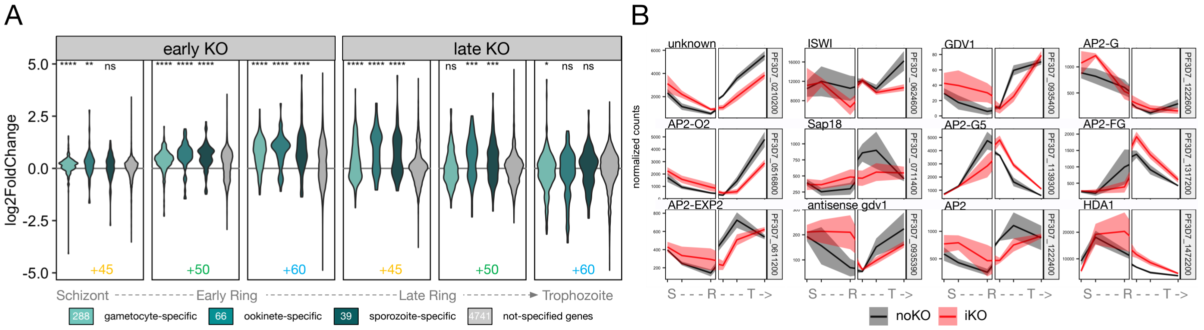

Figure 5-11: Dysregulation of stage-specific genes upon* PfSnf2L-KO. *A. *Expression change – log2(iKO/noKO) – at individual timepoints for stage-specific gene groups (listed in Appendix 4). The numbers of genes within the groups are shown (white), significance is indicated (two-tailed Student's t-test, unpaired, ns p>0.05, * p<0.05, ** p<0.01, ***p<0.005, ****p>0.001).* ***B.*** *Gene expression profiles over individual timepoints of exemplary epigenetic regulators involved in gametocyte commitment. Abbreviations: Schizont (S), Trophozoite (T), Ring (R). Gene symbols according to PlasmoDB.*

The expression profiles of twelve selected candidate genes upon *Pf*Snf2L-KO were plotted to address causal or temporal relationships (Figure 5-11B). The list comprises genes encoding epigenetic regulators and transcription factors, but also regulatory RNAs or unknown transcripts. Most of these them follow the pattern of being increased in early rings and being decreased in later stages. AP2-G5 and AP2-FG, two gametocytogenesis-associated transcription factors, show an inverse curve. Histone deacetylase 1 (HDA1) seems to be slightly upregulated at all timepoints, whereas the chromatin remodeling enzyme ISWI shows a tendency to be downregulated throughout the life cycle. However, the significance remains to be proven. Since the role of these genes has not been elucidated in detail, no regulatory cascade can be inferred. Nevertheless, the altered expression profiles of individual known regulators as well as the dysregulation of all gametocyte-specific genes suggest, that *Pf*Snf2L plays a role in the epigenetic regulation of gametocyte commitment.

5.1.5 *Pf*Snf2L shapes promoter architecture correlating with gene regulation.

As shown in the previous section, the absence of *Pf*Snf2L in asexual blood stages leads to a major perturbation in gene expression. Next, we tested the underlying mechanism of how an enzyme functioning in nucleosome assembly and remodeling controls gene expression. Therefore, I used the conditional knockout system to analyze the parasite chromatin landscape in presence and absence of *Pf*Snf2L. Analogous to the transcriptome analysis, *Pf*Snf2L-KO was induced early (0 hpi) and late (24 hpi) and chromatin was extracted 45 hours after KO induction, when *Pf*Snf2L has disappeared and first changes in gene expression were detected (Figure 5-12A,B, left panel). Parasite nuclei were treated with Micrococcal Nuclease (MNase) to digest DNA which is not occupied by nucleosomes. Chromatin digestion was performed at a constant MNase concentration for increasing times (2.5 / 5 / 10 min). Differential MNase digestion provides information on the general accessibility of chromatin (Schwartz et al., 2019).

***Pf*Snf2L-KO causes global chromatin perturbation in late ring stage.**

The length distribution of the resulting DNA fragments after MNase digestion shows that the accessibility of schizont chromatin is comparable between noKO and iKO (Figure 5-12A, right panel). In late ring stage, however, iKO chromatin is much more accessible than noKO chromatin as visualized by the increased release of shorter DNA fragments under the same conditions (Figure 5-12B, right panel). This suggests that *Pf*Snf2L is responsible for chromatin compaction at ring stage and that a depletion of the CRE results in a less compacted and thus more accessible chromatin structure. MNase digestion followed by DNA sequencing allows the detection of individual nucleosome positions across the genome. Chromatin samples of noKO and iKO digested to the same degree were sequenced and compared, for schizonts (early KO) as well as late rings (late KO). Exemplary coverage plots of MNase-Seq fragments show that in noKO/iKO schizonts hardly any changes in nucleosome positioning are observable (Figure 5-12C). In contrast, late ring chromatin shows substantial differences in nucleosome maps when comparing iKO to noKO (Figure 5-12D). Individual nucleosome calling and differential nucleosome analysis revealed those that changed significantly in iKO/noKO. Among these nucleosome positioning changes (NPCs), a distinction is made between changes in occupancy, fuzziness or position shift. These changes are defined as follows: Shifts represent the repositioning of the histone octamer forming a new dyad axis position. Fuzziness describes the broadness of the nucleosomal peak, being not fuzzy with

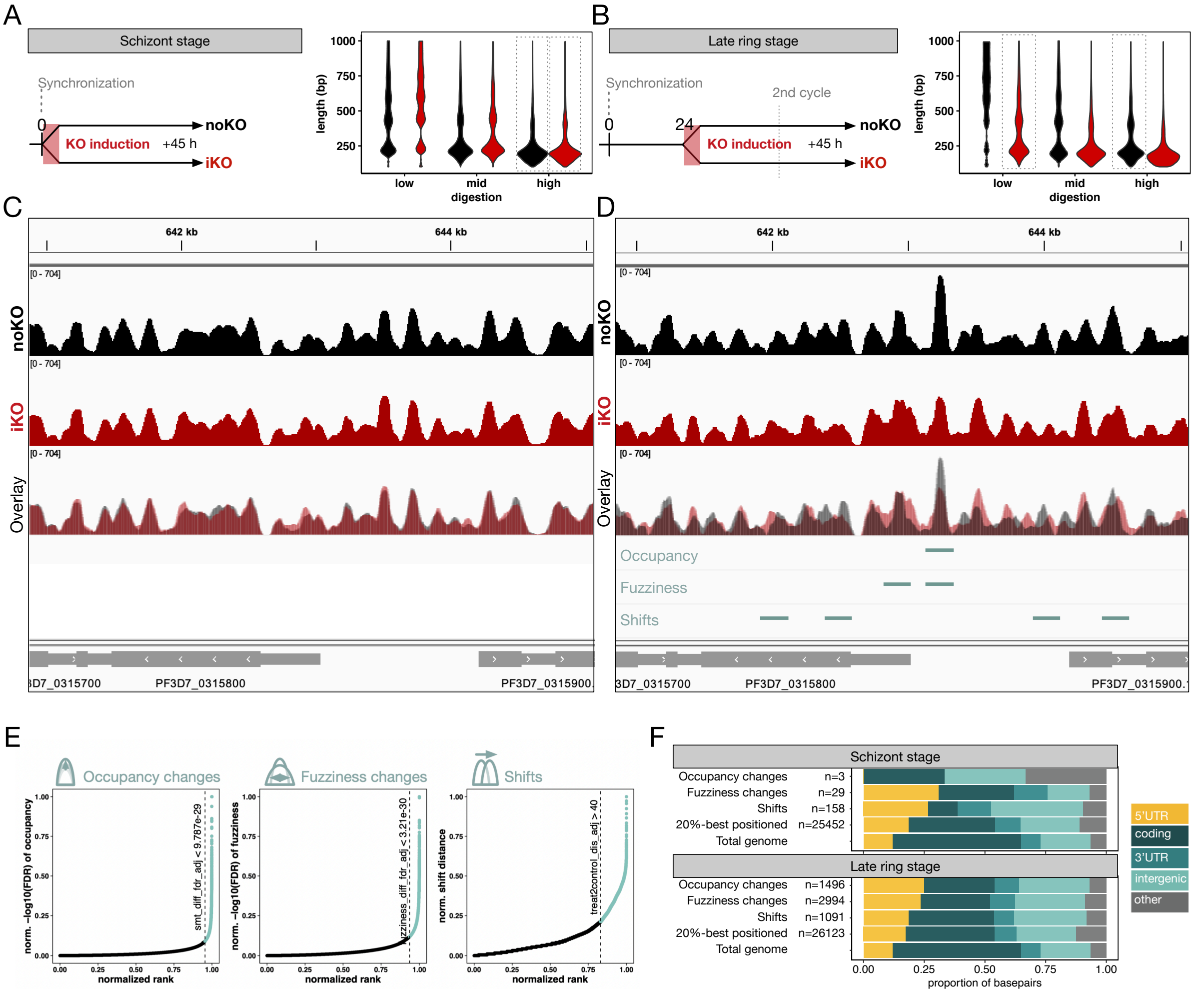

Figure 5-12:* PfSnf2L-KO leads to global alteration in ring stage chromatin. A.** *(S: schizont stage)* ***/ B. *(LR: late ring stage). Scheme of KO induction and chromatin extraction timing in S/LR (left panel). Molarity-normalized DNA size distribution of Tapestation electrophoresis for MNase digested chromatin in S/LR of noKO (black) /iKO (red) samples (right panel). One representative replicate is shown, dotted boxes indicate samples used for analysis.* ***C./D.*** *Exemplary coverage plots of MNase-Seq fragments of samples as in A (mean of three replicates)/B (mean of two replicates) including NPCs. Regions shown is chr3:641000–645000, genes are indicated in grey.* ***E.*** *Ranked normalized parameter (FDR of occupancy/fuzziness change or shift distance from differential nucleosome analysis) of iKO/noKO LR chromatin, NPC cut-off is defined as slope=1 and noted. Cut-off for 20% best-positioned nucleosomes is fuzziness_score (S) <47; fuzziness_score (LR) <49.* ***F.*** *Category, localization, numbers of NPCs in iKO/noKO in S/LR (cut-off from E. applied), assigned to gene section annotations relative to base pairs.*

a single translational position and a narrow peak, whereas fuzzy nucleosomes are characterized by a broad peak and many distinct translational positions close by. Occupancy changes imply a change in the number of cells with the nucleosome at a given location described by the change in the nucleosomal peak height. To identify NPCs, a cut-off was defined after ranking the normalized adjusted FDR values of these three categories in late ring stage (Figure 5-12E). The cut-off values were extracted and applied to detect NPCs in schizont stage. Among the NPCs, only those within the 20 % best-positioned nucleosomes in both stages were considered. In schizont stage, <1 % of well-positioned nucleosomes show positioning changes, while in late ring stage, approximately 20 % are affected (Figure 5-12F, included in the coverage track in Figure 5-12D). Consequently, *Pf*Snf2L has a more pronounced function in nucleosome positioning in late ring stage than in schizont stage. This fits with the importance of *Pf*Snf2L in chromatin compaction and gene expression regulation at this timepoint in the cycle as described above. In schizont stage, chromatin is being replicated and compacted to allow the release of numerous daughter cells. During this phase of the cycle, transcription is reduced to a minimum. This may explain the relatively small changes in chromatin landscape and suggest, that *Pf*Snf2L is required for chromatin organization associated with gene expression rather than replication.

Nucleosome positioning changes enriched in gene promoters.

The identified NPCs in iKO/noKO were annotated with respect to the gene region in which they were found. Changes of all three categories occurred preferentially in the 5'UTR and intergenic regions, and the enrichment is particularly strong for fuzziness and occupancy changes (Figure 5-12F). These regions are prominent regulatory regions, comprising promoters and *cis*-regulatory elements. They are characterized by a highly defined chromatin architecture and well-positioned nucleosomes.

To analyze nucleosome positioning around transcriptional landmarks, normalized coverage was aligned around these regions and averaged (Figure 5-13A). Nucleosome profiles around transcription start/stop and coding start/stop didn't show any notable differences between iKO and noKO at schizont stage. In contrast, late ring stage chromatin behaves differently. In general, there are more changes in the chromatin structure of iKO compared to noKO. The regions around start codon and stop codon as well as transcription termination site (TTS) are relatively similar in the nucleosome profiles of iKO and noKO. However, the zoom-ins show some changes in the dyad position of the nucleosomes, detectable as slightly shifted peaks (Figure 5-13B). In regions with very high AT-content (Figure 5-13A, lower panel), relative occupancy differences between samples are visible. Despite comparing similar digestion conditions, these highly MNase-sensitive regions are not digested uniformly. The 2000 bp

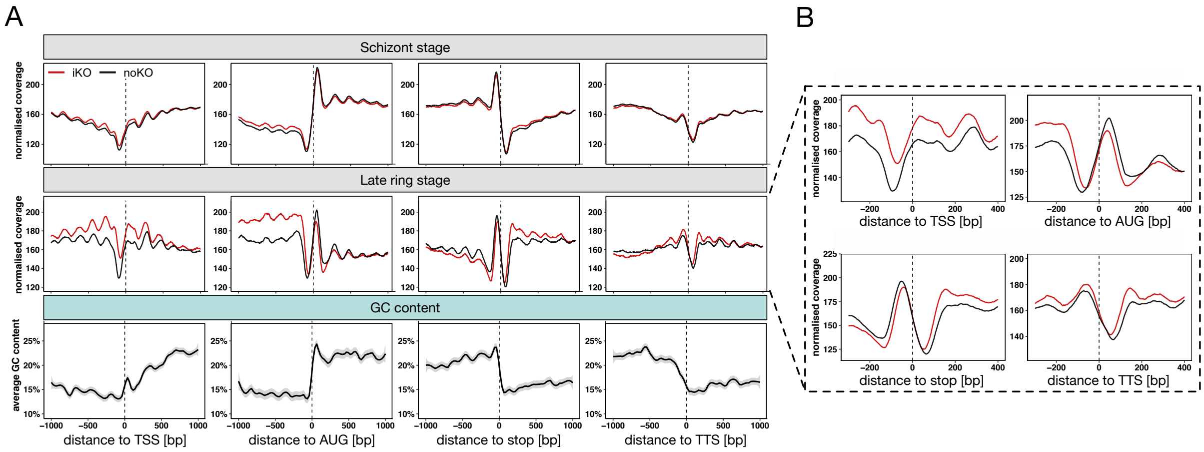

Figure 5-13: ***PfSnf2L-KO affects nucleosome positioning on landmark gene sites. A.*** *Average MNase-Seq occupancy profiles of noKO/iKO at schizont stage (S)/late ring stage (LR) around transcriptional landmark sites – start/stop of transcription and translation – and corresponding GC-content profiles.* ***B.*** *Zoomed occupancy profile at LR around landmark sites (-300 – 4000 bp) as in A.*

region around the transcription start site (TSS), which consists of 5'UTR and intergenic region for most genes, shows the greatest variation. Besides occupancy differences, clear positioning differences between noKO and iKO can be observed. This is consistent with the enrichment of dynamic nucleosomes in 5'UTRs and intergenic regions.

The TSS profile plot – even of noKO chromatin – doesn't correspond to the typical eukaryotic TSS profile, which is characterized by a pronounced +1 nucleosome, regularly spaced nucleosomes downstream and an upstream nucleosome-free region (NFR) (Figure 5-14A). The Plasmodium TSS profiles in my and previous studies (Kensche et al., 2016) do not show these features, which is due to the unclear TSS annotations. Different studies using different methods revealed TSS annotations that do not match for all genes (Adjalley et al., 2016; Chappell et al., 2020; Kensche et al., 2016; Shaw et al., 2021). This is compounded by the fact that *Plasmodium falciparum* has been shown to exhibit stage-dependent variation in TSS usage (Adjalley et al., 2016), resulting in a documented variability in TSS annotation. To resolve this ambiguity, we used an alternative chromatin-based method to determine the transcription start site in our data. The NucDyn pipeline identifies nucleosome-free regions and defines the first well-positioned nucleosome downstream as the +1 nucleosome of promoters (Buitrago et al., 2019). Aligning the MNase-Seq data to the identified +1 nucleosome of all genes restores the typical eukaryotic nucleosome profile (Figure 5-14B). This shows the bias of the previous profile alignment to annotated TSS and suggests that the identification of the +1 nucleosome is a more suitable method to annotate general promoter architecture. Again, huge changes in the chromatin structure of promoter regions can be observed for late ring stage iKO.

Promoter architecture changes correlate with gene expression.

Because the chromatin architecture of promoter regions strongly influences the transcriptional activity – and much more – of a gene, the nucleosome profile was subdivided into four quantiles based on gene expression at late ring stage (Figure 5-14C). This visualization of noKO shows well-positioned nucleosomes for low expressed genes (1st quantile) and a less defined pattern of nucleosome positioning for highly expressed genes (4th quantile). Furthermore, the width of the NFR upstream of the +1 nucleosome increases with expression quantile. Comparing the noKO profiles with the iKO profiles, larger changes can be observed for higher expressed genes, especially as a loss of nucleosome positioning due to the absence of *Pf*Snf2L. Quantifying the NFR widths and their distribution within the four quantiles, a correlation of wider and presumably more accessible NFRs with higher gene expression is striking (Figure 5-14C, right panel). This correlation appears to be disrupted upon *Pf*Snf2L-KO, as the distribution of NFRs is not shifted to an increased length in iKO as it is in noKO. *Pf*Snf2L-depletion results in a closure of NFR, suggesting that *Pf*Snf2L plays an intricate role in opening and maintaining an active promoter structure.

When we analyzed the dysregulated genes upon *Pf*Snf2L-KO in relation to promoter structure changes, a correlation with nucleosome fuzziness could be detected (Figure 5-14D). An increased mRNA abundance in *Pf*Snf2L-KO coincides with a loss of nucleosome positioning at promoter regions, which is accompanied by increased nucleosome fuzziness. For downregulated genes upon *Pf*Snf2L-KO, the opposite effect – an increased nucleosome

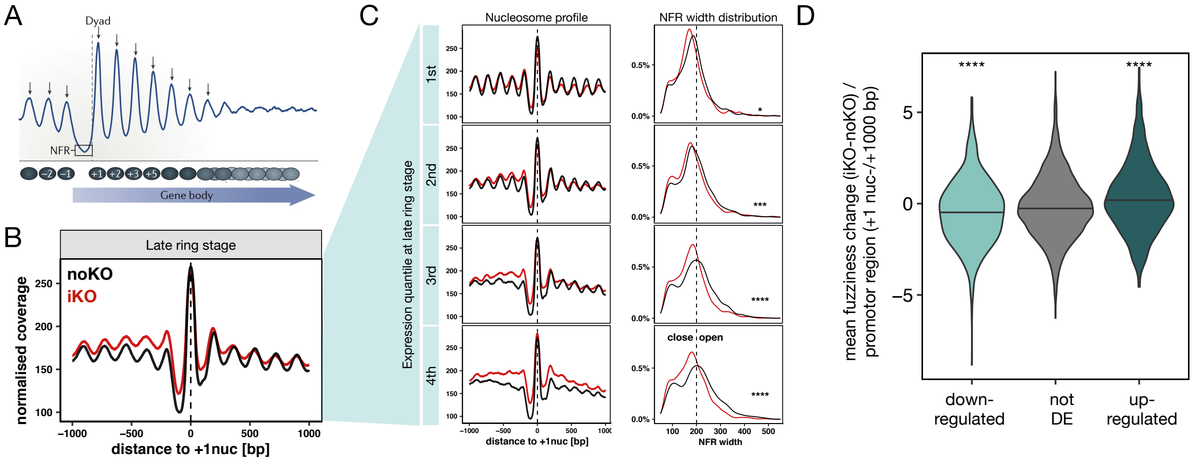

Figure 5-14: **PfSnf2L *shapes promoter architecture impacting gene expression. A.*** *Typical eukaryotic nucleosome organization in gene regions (Lai and Pugh, 2017)* ***B.*** *Average MNase-Seq occupancy profiles of iKO/noKO in S/LR around +1 nucleosome over all genes.* ***C.*** *Nucleosome profile around +1 nucleosomes as in B differentiated by gene expression quantiles in LR (upper panel). Accordingly, NFR width distribution differentiated by gene expression quantiles of iKO/noKO in LR (lower panel).* ***D.*** *Mean fuzziness change of all nucleosomes within region +/- 1000 bp around +1 nucleosome (iKO-noKO) over differential expression for each gene. Significance is indicated (two-tailed Student's t-test, unpaired, ns p>0.05, * p<0.05, ** p<0.01, ***p<0.005, ****p>0.001), Abbreviations: +1nuc (+1 nucleosome), TSS (transcription start site), TTS (transcription termination site), not DE (not differentially expressed), NFR (nucleosome-free region).*

fuzziness – is observed. This correlation indicates that a disruption of the promoter organization by knocking out *Pf*Snf2L is the reason for the observed dysregulation of transcription.

5.2 DISCUSSION

Evaluation of the used genetic modification strategy

Using endogenous tagging enabled to study the function of *Pf*Snf2L in blood stage parasites. This was not possible for *Pf*Snf2P, although the generation of transgenic parasites was successful. This is due to the fact that *Pf*Snf2P is not expressed in asexual blood stage parasites. New single cell transcriptomic data show the expression of *Pf*Snf2P mainly in gametocytes and ookinetes (Howick et al., 2019). This is consistent with the inability to detect *Pf*Snf2P-HA by IFA or western blot analysis probing for the HA-tag. During the process of establishing genetically modifying parasites, treatment with the usual G-418 concentration – 400 ng/µl – resulted in parasite death. However, lowering the G-418 concentration to 200 ng/µl, resulted in a very slow growth of the culture. This indicates, that *Pf*Snf2P is expressed at a very low levels in blood stages, resulting in a weak G-418 resistance, as the resistance gene is encoded by the same open reading frame as *Pf*Snf2P. On the other hand, the results demonstrate the effectiveness of selection-linked integration, whereby genomic integration can be forced by drug treatment. However, the weakness of the system is that this strategy is only applicable to blood stage proteins. *Pf*Snf2P has been suggested to play a role in other parasite stages. In a very recent study, the orthologous protein in *Plasmodium berghei* was found to be central for male gametocyte differentiation (Kaneko et al., 2023). With mice as the mammalian host, *Plasmodium berghei* is a popular model for *in host* studies, while stages other than the blood stages of *Plasmodium falciparum* are difficult to study due to the complex culture conditions. Cultivation of mosquito stage remains a major challenge, as an *in vivo* approach in mosquitoes but also as an *in vitro* model (Siciliano et al., 2020). The production of sporozoites – in mosquitoes or *in vitro* – is also a major bottleneck in *Plasmodium falciparum* research (Eappen et al., 2022). Transmission to human liver cells is being studied using primary hepatocytes or mice with humanized livers, but continuous culture techniques have yet to be developed (Button-Simons et al., 2021; Schuster, 2002). Gametocyte development strategies have recently improved, but the ability to form gametocytes is highly dependent on the strain of *Plasmodium falciparum* (Kafsack et al., 2014; Llorà-Batlle et al., 2020; Rovira-Graells et al., 2012; Usui et al., 2019). The 3D7 strain used in this study produces gametocytes only at low rates. Accordingly, the generated transgenic parasite strains are highly suitable to investigate asexual blood stages but have limitations with respect to other stages of the parasite life cycle. The protein characterization in this study cannot address putative functions of *Pf*Snf2P or *Pf*Snf2L in other than intraerythrocytic stages.

The DiCre-mediated gene excision appears to be a very effective knockout method. Another strategy, the glmS ribozyme system, was tested in comparison (data not shown). As has been shown for other enzymes, this approach did not achieve comparable levels of protein knockdown, which is crucial for studying the function of CREs (de Koning-Ward et al., 2015; Prommana et al., 2013). The inducibility of the DiCre-system allows complete depletion of essential proteins. A disadvantage of the used knockout strategy is the time lag before gene excision leads to depletion at the protein level, ~40 hours in the case of *Pf*Snf2L. A faster approach, such as the knock sideways method, which rapidly mis-localizes proteins, would take this into account (Spielmann et al., 2017). In summary, the method used is the state-of-the-art to address the fundamental question of *Pf*Snf2L function in blood stage parasites.

Contextualization and validation of detected interactome

In this study, *Pf*Snf2L interacting proteins were identified by pulldown and subsequent LC-MS/MS analysis. Immunoprecipitation of chromatin-associated proteins is often accompanied by solubility problems or by the pulldown of large and unspecific chromatin tangles. By testing two different nuclease treatments prior to preparation, I tried to minimize the risk of precipitating all DNA-associated molecules. The comparison of the two treatments - more and less stringent - shows an overlap of some, but not all, proteins (11 out of 40/114 respectively). This could be explained by the predominant pulldown of DNA-binding proteins in the DNaseI-digested condition, where DNA fragments are still present, and thus direct protein-protein-interaction detection is underrepresented in these conditions. Pulling down a chromatin-associated protein using the same strategy as control could provide information about unspecific hits, such as very abundant or very adhesive proteins. Unfortunately, parasites with a suitable tagged comparative control protein were not available, so I had to use untagged parasites as a control. The 40 proteins detected in the benzonase-treated conditions were considered as potential and specific protein-protein-interactors. The interaction with numerous proteins and complexes associated with chromatin assembly strongly suggests a function of *Pf*Snf2L in nucleosome assembly. ISWI enzymes in other eukaryotic organisms have been shown to be involved in the assembly of nucleosomes (Baldi et al., 2018; Fyodorov and Kadonaga, 2002; Lusser et al., 2005; Smolle et al., 2012). The focus of these studies, especially in the context of the *dm*ACF complex, is on the spacing activity of ISWI enzymes, which ensures a regular and defined linker length between the nucleosomes. In *Plasmodium falciparum*, however, the actual assembly of proper octameric nucleosomes on DNA may be an even more important and challenging task than in other eukaryotes. The extremely AT-rich genomic DNA, which is unfavorable for nucleosome formation, combined with the highly divergent *Pf* histones results in relatively unstable canonical nucleosomes with poor positioning properties (Gardner et al., 2002; Silberhorn et al., 2016). Structural studies indicate that plasmodial nucleosomes tend to exist not only as octameric nucleosomes but also in form of hexasomes with only one H2A/H2B copy per nucleosome (manuscript in preparation, LängstLab). A biological implication of this has not yet been identified. Nevertheless, the peculiar nature of *Pf* nucleosomes may require specialized assembly factors that correctly assemble and position nucleosomes at specific genomic loci.

The detection of several Apicomplexan or Plasmodium-specific proteins that have no orthologues in well-studied organisms makes it difficult to speculate about functional roles. Among them is a *Pf*-specific CRE that has been named ISWI, although it bears little resemblance to ISWI-type enzymes. This enzyme was previously shown to interact with *Pf*Snf2L, suggesting that CREs work cooperatively as known from literature (Bryant et al., 2020; Ocampo et al., 2016). The list also includes some proteins that are known or proposed to be transcription factors (e.g. PREBP, AP2-proteins). They suggest *Pf*Snf2L to be associated with promoter regions and to be involved in transcription regulation. The identified interaction with the bromodomain-containing proteins BDP1/2, which were found to activate invasion genes via histone acetylation binding, strengthens this hypothesis (Josling et al., 2015). BDP1 was also found to be one subunit of the GCN5 complex, some members of which were also detected in the *Pf*Snf2L-IP as well (Miao et al., 2021). The reciprocal detection and the common interactors in the *Pf*Snf2L-IP and the GCN5/PHD1-IP suggest this interaction to be true. The GCN5 complex has been shown to control transcription globally by mediating histone modification (Miao et al., 2021). These findings are in accordance with the function of *Pf*Snf2L in transcriptional regulation demonstrated in this study.

However, some other proteins detected are completely uncharacterized and point to novel complexes in Plasmodium, that are not conserved or present in higher eukaryotes. Since known ISWI interactors seem to be absent in Plasmodium, this is a likely possibility. To prove the proposed interactions as true, a cross-validation would be required by pulling down the prey protein and testing for *Pf*Snf2L co-immunoprecipitation. Unfortunately, antibodies are not available for most *Pf* proteins, especially the uncharacterized ones, and internal tagging or recombinant expression is quite laborious. Hence, with the presented co-immunoprecipitation we confirm some proposed interactions within the chromatin regulation network and moreover provide a list of putative interactors as a basis for future investigations.

Conjectures about the causes of the egress defect

One of the main objectives of the present study is the characterization of *Pf*Snf2L function using a knockout approach. With the chosen strategy I could prove that *Pf*Snf2L is essential for *Plasmodium falciparum* blood stages. In addition to developmental and replication defects, conditional *Pf*Snf2L-KO at 0 hpi resulted in impaired host cell exit. Despite great efforts, the link to this observation couldn't be clarified conclusively. The KO-caused downregulation of gene transcripts prior to cycle transition couldn't be confirmed on protein level. The expression timing of the regarding genes suggest that they have a function in the following cycle and are relevant for immediate parasite egress. A possible cause of incomplete merozoite release could be the downregulation of EPF3/4 genes, as observed by mRNA sequencing for all 16 members of this group. The EPF multigene family is organized in eight highly similar clusters of four genes (EPF1, Pfmc-2tm, EPF3, EPF4) in the subtelomeric region, and the products are exported to the Maurer's cleft. The exact biological role of these proteins has not been elucidated, but a collective downregulation of this protein family resulted in a similar phenotype of inefficient merozoite release (Mbengue et al., 2013). Due to the lack of available antibodies against EPF proteins, the reduced mRNA abundance in *Pf*Snf2L-KO parasites could not be tested on protein level. However, the strong decrease of EPF3/4-transcripts upon KO points towards gene expression regulation by *Pf*Snf2L. The very similar phenotype of merozoites being attached to each other and to the food vacuole, and not being efficiently released upon EPF knockdown and *Pf*Snf2L-KO indicates that EPF-downregulation may be the link to explain this observation.

The addition of phalloidin during live imaging of the egress provided insight into the role of the RBC cytoskeleton in parasite exit. The parasite is known to actively alter red blood cell properties by exporting parasite proteins to the host cell (de Koning-Ward et al., 2016; Glenister et al., 2002; Mills et al., 2007) . The process of egress and host cell exit has been reported to rely on the elastic instability of the erythrocyte membrane, which undergoes sequential curling and eversion to enable efficient angular dispersion within milliseconds (Abkarian et al., 2011). By staining erythrocyte actin during live imaging of *Pf*Snf2L-KO parasites, aberrant behavior of the host could be demonstrated. Future studies may specify the relevance of EPF proteins to red blood cell properties and prove that these or others factors link *Pf*Snf2L-KO to the host cell exit defect.

Life cycle variability complicates transcriptome and chromatin phenotyping.

The fundamental function of *Pf*Snf2L is to shape the chromatin landscape and to globally control stage-dependent gene expression. This was clearly demonstrated by the detailed transcriptomic analysis and the chromatin phenotyping using MNase-Seq. The major difficulty of *Plasmodium falciparum* transcriptome analysis is the additional variable of time. Progressing through the cycle, the entire parasite transcriptome undergoes enormous changes within every few hours. To achieve uniformity of parasite stages, a very tight synchronization is required. In this study, we approached a one-hour synchronicity window by isolating mature schizonts with two consecutive Percoll gradient steps. This technique ensures a high synchronicity of the parasite population but is accompanied by a loss of mRNA/chromatin yield. This must be compensated for by higher numbers of parasites, in particular for early stages as they contain low amounts of mRNA and chromatin compared to late stages. Not only is sampling of mRNA dependent on cycle timing, but KO-induction is also likely to be influenced by parasite stage. This leads to a potentiation of possible combinations of these two variables and can be applied to any chromatin mapping method as well. With the chosen setup, I tried to adjust this problem and investigated two different induction timepoints with transcriptomic sampling of three selected timepoints each, to cover the cycle as well as possible. Nevertheless, the analysis is based on bulk sequencing, which is always accompanied by a certain heterogeneity of stages. Recent methodological advances have addressed this by establishing single-cell transcriptome analysis (Howick et al., 2019; Ngara et al., 2018; Poran et al., 2017; Real et al., 2021; Reid et al., 2018). Chromatin accessibility analysis is now also being performed on single-cell level in eukaryotic cells, but these techniques are not yet established for *Plasmodium falciparum* (Harada et al., 2021). MNase-Sequencing faces some additional difficulties owing to the characteristic features of Plasmodium chromatin such as the high AT-content and a high proportion of relatively unstable or fragile nucleosomes (Bunnik et al., 2014; Kensche et al., 2016; Silberhorn et al., 2016). The only available dataset mapping nucleosome positions throughout cycle progression propose a lack of stereotypical nucleosomal array and less finely defined positioning around TSSs (Kensche et al., 2016). These observations may be biased by the meliorative TSS annotation and may not hold up with improvement of annotation. We addressed this issue by using an alternative annotation which is based on the identification of the +1 nucleosome via the NucDyn pipeline. Aligning to this annotation, we see regular nucleosome phasing and pronounced +1/-1 nucleosomes. A reanalysis of the aforementioned nucleosome mapping data (Kensche et al., 2016) with improved annotation may relativize some assumptions about Plasmodium chromatin and reveal that it is more organized than originally assumed.

Regarding the function of *Pf*Snf2L, the performed MNase digestion and sequencing upon KO provides information about the timing of action. *Pf*Snf2L seems to have a major role in shaping the chromatin landscape in late ring stage, and to be less important in the final phase of the intraerythrocytic life cycle. Including a kinetic analysis by varying the digestion time allows to extract information about the general chromatin accessibility. In particular, due to the intrinsic preference of MNase for AT-rich DNA (Nikitina et al., 2013), it is important to apply high and low digestion conditions to Plasmodium chromatin. This can compensate for over-digestion of the whole genome or specific AT-rich sites (Schwartz et al., 2019). Nucleosome positioning changes upon KO could be localized to promoter regions of genes, with a greater impact on highly transcribed and strongly regulated genes. A correlation between altered promoter architecture and differential expression is observable. However, this correlation requires further characterization to unravel the exact underlying mechanism and to find the order of recruitment of involved factors. One hypothesis is, that *Pf*Snf2L removes the nucleosome from *cis*-regulatory elements to enable transcription factor binding. It is also conceivable that transcription factors recruit CREs, and their nucleosome remodeling activity paves the way for polymerase binding (Dimova et al., 1999; Fry and Peterson, 2001; Vignali et al., 2000). Furthermore, the involvement of histone variants remains to be elucidated. *Pf* H2A.Z/H2B.Z dimers have been found to preferentially bind promoter regions (Bártfai et al., 2010; Hoeijmakers et al., 2013; Petter et al., 2013). The ChIP data – although potentially biased – suggest that *Pf*Snf2L is mainly located in coding regions, where canonical nucleosomes dominate. This observation is consistent with the preferential binding of *Pf*Snf2L to canonical nucleosomes over variant nucleosomes *in vitro*. However, investigating the relationship between CRE binding sites and CRE target sites is complex (Längst and Manelyte, 2015): According to the release model, the enzymes target “high affinity” substrates, which they remodel and convert to “low affinity” substrates and then release. The proposed mechanism involves mainly transient binding events and results in different patterns of binding sites in ChIP-Seq compared to the sites of action. Further efforts are being made to improve the *Pf*Snf2L-ChIP and to use synchronous parasite stages. Recently developed methods using antibody-targeted DNA cleavage (CUT&RUN) or DNA tagmentation (CUT&Tag) without crosslinking to identify chromatin binding sites would provide further information (Kaya-Okur et al., 2019; Skene and Henikoff, 2017). The MNase-Seq data monitoring *Pf*Snf2L activity clearly show that the promoter regions are strongly affected by loss of the enzyme. Since *Pf*Snf2L was found to interact with a histone acetyltransferase, changes in histone modifications upon *Pf*Snf2L-KO may complement the findings. Chromatin phenotyping can be extended in many directions and would certainly provide more insight into the complex epigenetic regulatory network that controls gene expression. From the nucleosome mapping combined with differential gene expression analysis upon *Pf*Snf2L-KO at two different stages it can be concluded, that *Pf*Snf2L shapes the nucleosome architecture of promoters, predominantly at late ring stage. The enzyme is crucial when changes in promoter architecture and gene expression are imminent to proceed in the life cycle, gene activation as well as gene repression. By influencing the NFR length and nucleosome positioning in its vicinity, *Pf*Snf2L globally co-controls the just-in-time transcription of stage-specific genes.

Role of *Pf*Snf2L in gametocyte commitment

Within this study, transcriptome and chromatin phenotyping was performed only on asexual blood stage parasites. As mentioned above, the 3D7 strain used is only conditionally capable of producing gametocytes, as isolates lose the ability of gametocyte formation after long periods in blood culture (Brockelman, 1982). After creating the 3D7-Snf2L-HA-cKO parasite strain, several studies were published that ascribe a role in gametocyte differentiation to *Pf*Snf2L. Transcriptomic analysis of gametocytes and sexually committed parasites proposed that *Pf*Snf2L is part of the epigenetic cascade of commitment (Poran et al., 2017; van Biljon et al., 2019). Another study identified *Pf*Snf2L together with MORC, FACT-L and ISWI to interact with the transcriptional repressor AP2-G2, which is important for gametocyte maturation (Singh et al., 2021). Gametocyte-specific genes are expressed at basal levels in asexual stages until one or more triggers induce gametocyte conversion (Poran et al., 2017). Individual steps in the regulatory cascade are known: GDV1, a key activator of gametocytogenesis, is controlled by the gdv1 antisense-RNA as a negative regulator (Filarsky et al., 2018). Downstream of GDV1, multiple transcription factors have been implicated in gametocytogenesis. The GDV1-activated factor AP2-G has been identified as the master regulator of sexual initiation (Kafsack et al., 2014; Sinha et al., 2014), while other enzymes have been shown to be important for gametocyte maturation, such as AP2-G2, AP2-G3, AP2G5 (Singh et al., 2021; Yuda et al., 2021). According to the time-resolved transcriptome studies, *Pf*Snf2L is one of the early upstream regulators of sexual commitment. Although we didn't use a good gametocyte-producing line, I analyzed the obtained *Pf*Snf2L-KO transcriptomic data with respect to expression of gametocyte-specific genes (Meerstein-Kessel et al., 2021). The observation that these gametocyte markers are dysregulated supports the hypothesis of *Pf*Snf2L contributing to this. However, when looking at ookinete- or sporozoite-associated genes, increased mRNA abundance upon *Pf*Snf2L-KO is also found. The silencing of genes specific to other stages might be generally disturbed. However, the mRNA profiles of epigenetic regulators argue for a gametocyte-specific gene dysregulation.

To address the question of whether *Pf*Snf2L is essential for sexual commitment, actual gametocyte formation in KO parasites needs to be examined. Despite the reduced ability of

the transgenic KO parasites to produce gametocytes, this is currently under investigation. One obstacle thereby is the timing of KO induction and gametocyte induction. The KO has been shown to be efficient within 2 days, whereas gametocyte quantification is typically performed 8 days after gametocyte induction. The temporal order of KO induction and gametocyte induction needs to be carefully tested to see effects on commitment and possibly maturation without killing the parasites beforehand.
Within the third objective of this work, a *Pf*Snf2L inhibitor was identified (see chapter 6). This chemical compound allowed the disruption of *Pf*Snf2L while avoiding complete gene excision. Using pulse treatment with this drug in the process of gametocyte induction, gametocyte formation could be studied in a gametocyte-producing parasite strain, bypassing the timing issue. As shown in Figure 6-8, the gametocyte conversion rate was significantly reduced by the putative inhibition of *Pf*Snf2L. This result strengthens the hypothesis that *Pf*Snf2L is essential for sexual commitment.

In conclusion, the *in vivo* characterization in blood stages revealed *Pf*Snf2L to be an essential enzyme, that decisively shapes promoter architecture in a stage-dependent manner and thus, globally controls the just-in-time transcription of stage-specific genes. Its crucial function in stage development was demonstrated by the multifaceted phenotype of conditional gene deletion of PfSnf2L. A highly altered chromatin landscape resulted in global changes in gene expression, observable as transcriptomic and developmental delay. The mis-regulation of stage-specific genes highlights its role in the progression through the asexual gene expression program, but also in gametocyte commitment.

6 *Pf*Snf2L INHIBITOR SCREEN

6.1 RESULTS

The *in vivo* characterization of *Pf*Snf2L clearly demonstrated the importance of the protein for parasite development and proved that *Pf*Snf2L is essential for the erythrocytic life cycle. Complementing these findings, the *in vitro* characterization of *Pf*Snf2L revealed several unique characteristics and mechanistic differences in comparison to *Hs*Snf2L. Consequently, *Pf*Snf2L may represent a promising drug target for antimalarial drugs. In the following section, I validated *Pf*Snf2L as a druggable target using a multi-step *in vitro* screen and characterized a resulting lead compound for its effect on the parasite.

6.1.1 Establishing an ADP biosensor screen

To set up an *in vitro* screening system customized for *Pf*Snf2L and with the potential for high-throughput application, observation from the *in vitro* characterization were harnessed. *Pf*Snf2L was found to be an active ATPase with high hydrolysis activity, requiring only DNA as stimulant. These attributes also apply to the truncated core enzyme. With that, it is possible to set up a screening assay, monitoring the enzymatic activity of *Pf*Snf2L. ATP hydrolysis activity was quantified by measuring the amount of generated ADP. Previously, the bacterial ADP-binding protein ParM was established as a fluorescent ADP biosensor. Introducing mutations in the active site of ParM reduced the affinity for ATP and the internal ATPase activity of this protein, and the attachment of two tetramethylrhodamines (TMR) in close proximity to each other allows fluorescence changes as readout (Kunzelmann and Webb, 2010, 2009). In the unbound state, fluorophore interactions quench the overall fluorescence of the protein. This is altered by the binding of ADP, which causes ParM to unndergo major conformational changes leading to a 15-fold increase in fluorescence. The functionality of this biosensor enables a real-time kinetic assay for ATPases such as *Pf*Snf2L (Figure 6-1A).

Furthermore, a high-throughput assay must meet certain criteria regarding its applicability. It is crucial to be able to produce both the biosensor and the protein to be targeted in large amounts with consistent quality. ParM expression and purification from *Escherichia coli* and subsequent TMR-labeling was established and performed by Elisabeth Silberhorn and a large batch of labeled ParM with tested quality was provided for this screen. As target protein, the previously characterized core protein (aa246 – 843) of *Pf*Snf2L was used (Figure 4-7). *Pf*Snf2Lcore contains the active part of the enzyme and is able to hydrolyze ATP at a rate comparable to the full-length protein. In addition, it has the advantage that it can be expressed and purified in large amounts (0.8 mg/100 ml). The ATP hydrolysis of *Pf*Snf2L and *Pf*Snf2Lcore measured with the ADP biosensor assay shows comparable kinetics (Figure 6-1B). To address species specificity, it was initially considered to also screen *Hs*Snf2L. However, as shown by the kinetics of the human enzyme, the hydrolysis rate for both – the full-length and the truncated version - is very low and thus not suitable to be measured with this assay. Another pleasant fact is the full activation of *Pf*Snf2L by DNA alone. The preparation of large amounts of plasmid DNA is much easier than preparing large quantities of nucleosomal substrates.

For setting up the high-throughput screening procedure, all substrates and conditions need to be titrated and optimized, so that a maximum of fluorescence enhancement is achieved and concurrently the consumption of substrates is kept low (Figure 6-1C). The reaction volume was adjusted to 20 µl and pipetted into a glass bottom plate for readout in a fluorescence plate reader. Titration of the biosensor ParM shows an optimal concentration of 200 nM. Very high ATP concentrations seem to have a suppressive effect on the fluorescence enhancement, leaving 125 µM as the optimal ATP concentration. The amount of substrate, plasmid DNA, doesn't seem to have a huge effect on the assay quality, so that

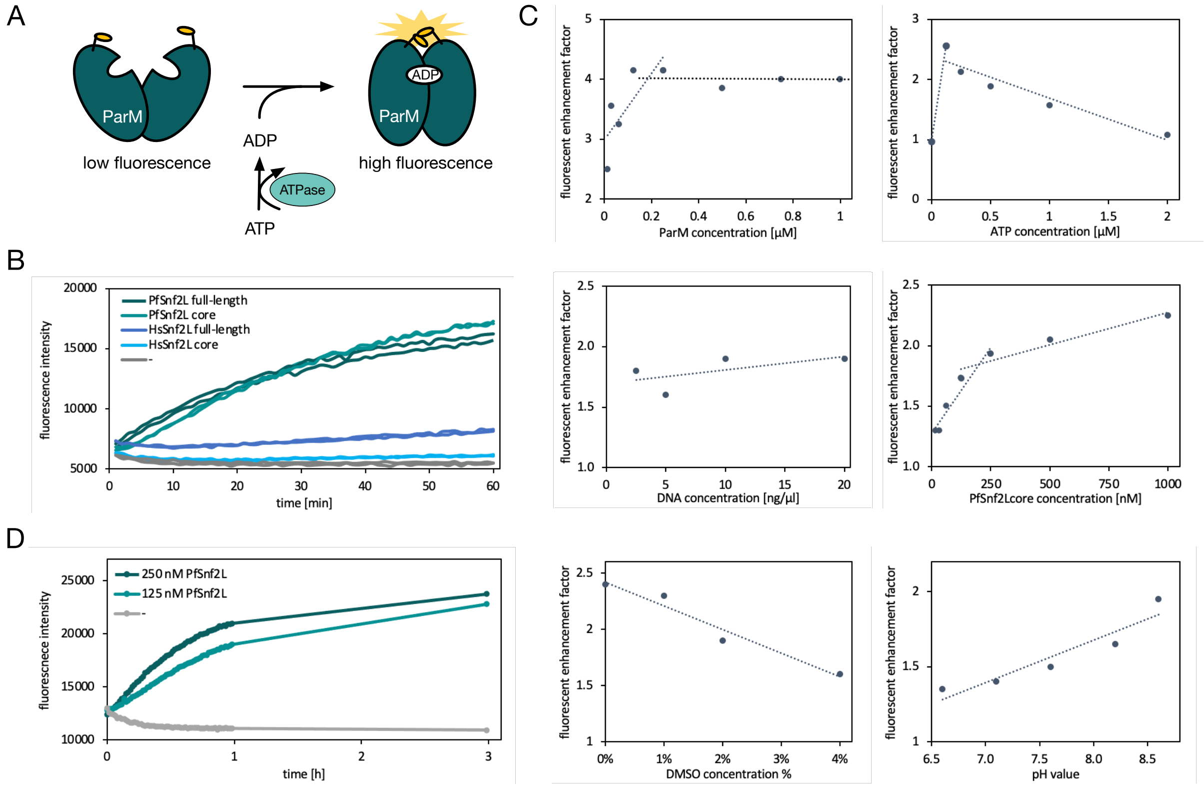

*Figure 6-1: **Setup of ADP biosensor assay. A.** Schematic representation of ADP biosensor assay principle. **B.** ATP hydrolysis kinetics of CREs in ADP biosensor assay. ParM fluorescence in 2-minute-intervals in presence of 0.2 µM PfSnf2L/HsSnf2L full-length/core, 10 ng/µl DNA and 125 nM ATP. **C.** Titration of reaction components. Fluorescence enhancement factor ($fluo_{end}/fluo_{start}$) was calculated for the titration of ParM, ATP, DNA, PfSnf2Lcore, DMSO and buffers with varying pH value. Trend lines are indicated dotted. **D.** Time-extended kinetics of PfSnf2Lcore (125 / 250 nM) to 3 h.*

10 ng/µl was used in the assay conditions. The enhancement numerically increases with increasing CRE concentration, but in order to save material a *Pf*Snf2Lcore concentration of 200 µM was chosen. Since the compounds of the small molecule library were dissolved in DMSO, the DMSO tolerance of the assay was tested and 1 % was found to be tolerable, corresponding to a compound concentration of 100 µM. Further optimization included adjusting the pH value of the biosensor buffer to pH 8.6. The duration of the measurement was set at two hours, with measuring the fluorescence in regular time intervals (Figure 6-1D). With this detailed analysis of each reaction component, an optimal reaction mix was determined that is applicable for large scale screening.

6.1.2 Pipeline and implementation of *Pf*Snf2L-inhibitor screen

The ADP biosensor assay described above is one of the two main pillars of the *in vitro* screening pipeline (Figure 6-2). Besides searching for molecules that inhibit the enzyme activity, all compounds are also screened for binding to *Pf*Snf2Lcore using Microscale Thermophoresis (MST). Both methods, the ADP biosensor assay and MST, offer the possibility to be performed as high-throughput screens. The assays require reasonable amounts of target protein and substrates and can be implemented in a semi-automatic manner. After identifying potential hits from large libraries, these chemical compounds are validated in two additional *in vitro* assays. Using the nanoDSF technology, the chemicals are analyzed for their impact on *Pf*Snf2Lcore stability. A destabilizing effect on proteins is another indicator of direct interaction and inhibition. The next validation step is applied to the recombinant full-length protein *Pf*Snf2L and involves testing for an inhibitory effect on nucleosome remodeling. The remaining hits are then tested in the *in vivo* context for their toxicity to *Plasmodium falciparum* parasites. Furthermore, the question of specificity is addressed by exemplary toxicity assays on cells of other species such as HeLa cells or *Toxoplasma gondii* parasites. Since the putative inhibitors were selected via a screen against *Pf*Snf2L *in vitro*, off-target effects *in vivo* cannot be excluded. To verify *Pf*Snf2L as the target of the hits, the effect of the drugs is compared to the previously analyzed *Pf*Snf2L-KO phenotype (5.1.3, 5.1.4).

This pipeline has been designed independently of the library to be screened. It is a general pipeline that starts with an *in vitro* screen suitable for high throughput, followed by *in vitro* validation and subsequent *in vivo* validation. Within this study an exemplary library – *Prestwick small molecule library* – with 1506 compounds was screened in an initial attempt. A second library – *Selleck Bioactive Compound Library* – of 2645 compounds was analyzed with a slightly modified pipeline. In principle, this or similar strategies can be applied to larger libraries as well.

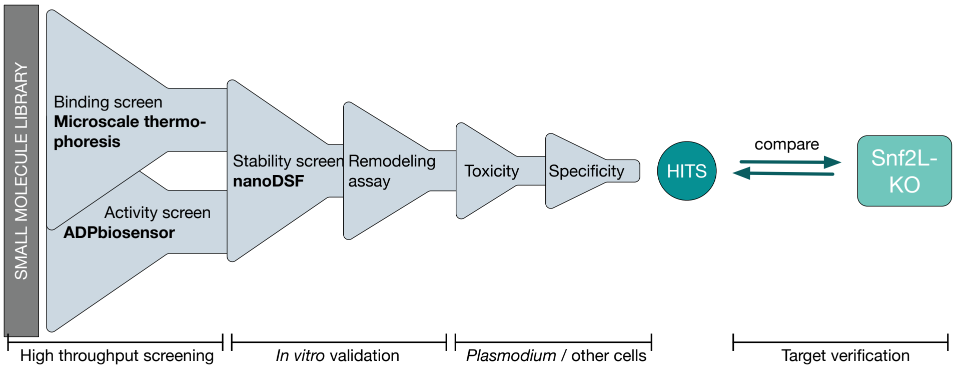

Figure 6-2:* Pf*Snf2L inhibitor screening pipeline *combining biophysical methods for high-throughput screening, hit validation in vitro and in vivo and subsequent target verification.*

For the initial screen, the entire library with 1506 chemical compounds was screened in the established ADP biosensor assay and additionally in the binding screen, performed by the company 2bind. The compounds were reorganized in 384-well plates, leaving 32 wells for positive controls (no compound) and 32 wells for negative controls (no ATPase). Using automated acoustic droplet ejection, 200 nl of each compound was transferred in triplicates to glass bottom plates suitable for fluorescence readout (by Fraunhofer-ITEM). For Microscale Thermophoresis measurement, the compounds were spotted accordingly (transfer of 100 nl for the same final compound concentration) into standard 384-well plates. For implementing the ADP biosensor screen, the infrastructure was optimized as follows and performed in the Fraunhofer-ITEM laboratory (Figure 6-3A): Two master mixes were prepared and automatically dispensed into 384-well plates using a Multidrop Combi system, whereby an early ATP hydrolysis was prevented. Readout was performed using an EnVision fluorescence reader, which is capable of measuring multiple plates successively. With that, five plates with 320 compounds and 2x32 controls on each plate were read in parallel at six-minute intervals for two hours. Second and third replicates were measured accordingly on different days using the same setup.

The kinetic curves of a subset of 100 compounds and all control samples demonstrate the robustness of the assay (Figure 6-3B). The fluorescence values for each compound were corrected for the rection without enzyme of the corresponding replicate (negative control) and the obtained kinetic curve was analyzed for two parameters. The slope of the first 60 min was calculated, as well as the difference between end and start point (Figure 6-3C,D). In total, 22 compounds show an abnormal kinetic curve with a reduced slope (below the chosen threshold of 3.5) and a reduced difference (< 25000) in all three replicates (Figure 6-3E). It should be noted that some chemicals appear to quench the biosensor fluorescence or show autofluorescence, but the number is relatively small (< 1 %).

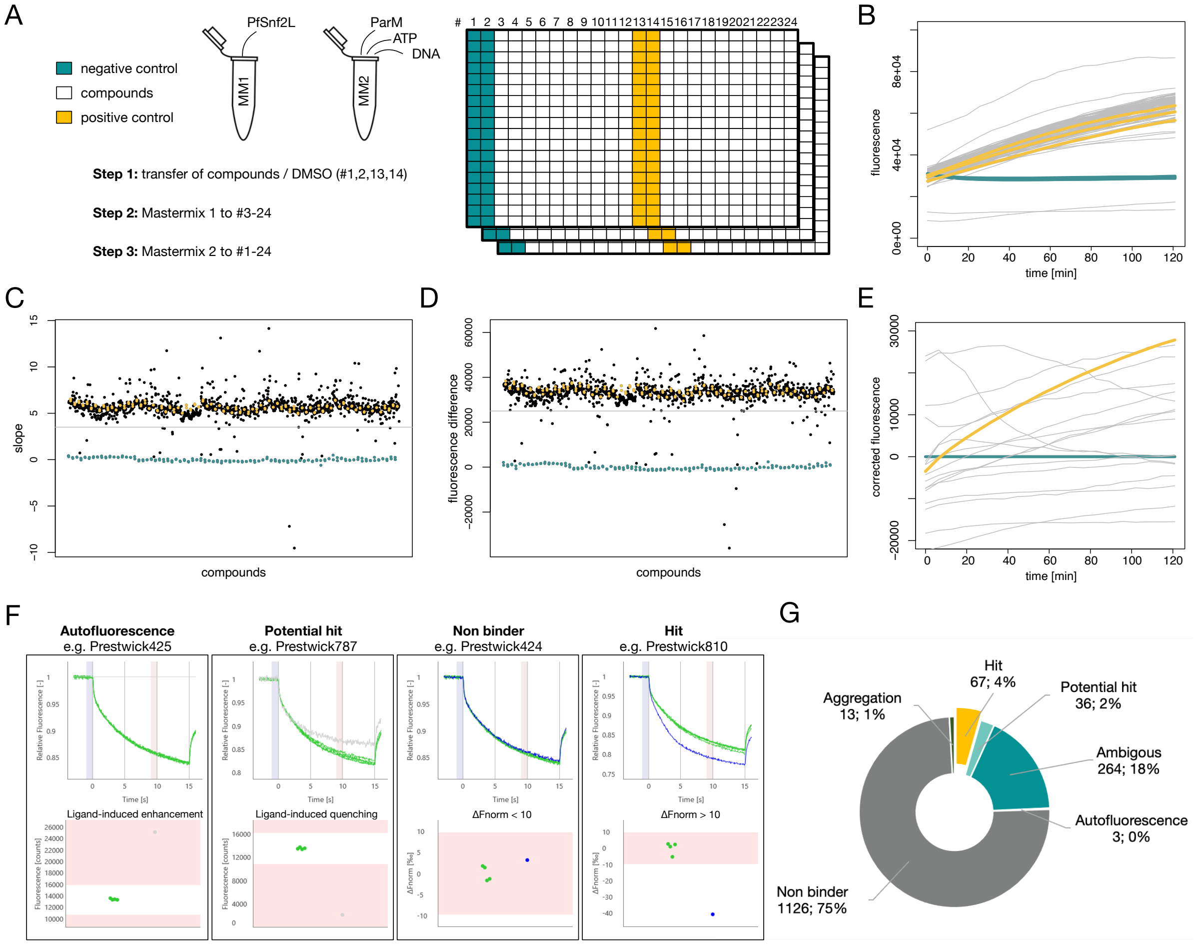

Figure 6-3: High-throughput activity screen and binding screen. A. *Schematic representation of the procedure of activity screen implementation.* ***B.*** *ATPase kinetics of negative controls (no ATPase, petrol, three replicates, mean of each), positive controls (no compound, yellow, three replicates, mean of each) and 100 individual compounds (grey, one representative replicate), not corrected.* ***C.*** *Slope of kinetics in absence (yellow) or presence of 1506 compounds (black). Fluorescence was corrected for negative control (no ATPase, petrol) and slope was calculated as corrected fluorescence / 60 min. Mean of three replicates is shown, grey line indicated inhibition cut-off (slope<3.5).* ***D.*** *Fluorescence difference of kinetics in absence (yellow) or presence of 1506 compounds (black). Fluorescence was corrected for negative control (no ATPase, petrol) and difference was calculated as* $F_{120min} - F_{0min}$*. Mean of three replicates is shown, grey line indicated inhibition cut-off (difference<25000).* ***E.*** *Corrected ATPase kinetics in absence (yellow) and presence of 24 inhibiting compounds (grey), defined as slope<3.5 and difference<25000, and negative control (petrol).* ***F.*** *Categorization criteria of ligands screened for binding to PfSnf2Lcore via Microscale Thermophoresis with exemplary measurements shown. Upper panel shows MST curves in absence (green) and presence of 100 µM compound (grey or blue). Lower panel shows ligand-induced changes of absolute fluorescence in case of autofluorescence and potential hits, and difference of normalized fluorescence (ΔFnorm) in case of non-binding/binding compounds.* ***G.*** *Ligand categories with numbers and proportion in the MST binding screen of 1506 compounds.*

The second assay, Microscale Thermophoresis, which screens for molecular interactions, is based on the movement changes of fluorescently labeled *Pf*Snf2Lcore in a temperature gradient. Therefore, *Pf*Snf2Lcore was fluorescently labeled with NHS-amine labeling and analyzed in MST for fluorescence changes in presence of 100 µM compound in two replicates or DMSO, respectively. This procedure was carried out by the company 2bind. Within this fluorescence-based assay, a few compounds were also identified as autofluorescent (fluorescence counts increase > 25000). 2 % of the chemicals showed ligand-induced quenching (fluorescence counts decrease > 25000), representing potential hits. The rest could be categorized as hits (4 %, $\Delta F_{norm} > 10$), non-binders (75 %, $\Delta F_{norm} < 10$) or ambiguous compounds (18 %, replicates not matching) (Figure 6-3F,G).

The activity screen results were combined with the binding screen results to select compounds for the *in vitro* validation (Table 6-1). Of the 22 compounds that affected *Pf*Snf2Lcore activity, only two were non-binders in the binding screen. The rest mainly fell into the categories of hit, potential hit or ambiguous, indicating good agreement of the two tests. For further validation, compounds with autofluorescence or a low inhibitory effect when looking at the kinetic curve in the ADP biosensor screen were excluded. With one exception for financial reasons (Prestw-NAT-0114), twelve promising inhibitors were purchased and analyzed for their impact on protein stability and remodeling activity.

Table 6-1: List of 22 hits identified in the activity screen *including their observed effects on ATPase activity and their categorization in the binding screen. Compounds picked for further in vitro validation and their effect on PfSnf2Lcore stability and PfSnf2L remodeling activity are shown right. Prestw-1472 - as a showcase compound in further figures - is marked yellow.*

	High-throughput screening		***In vitro* validation**	
Compound	**activity screen**	**binding screen**	**stability screen**	**remodeling**
Prestw-777	autofluorescence	ambiguous		
Prestw-925	autofluorescence	aggregation		
Prestw-705	autofluorescence	ambiguous		
Prestw-438	autofluorescence	hit		
Prestw-487	autofluorescence	hit		
Prestw-787	autofluorescence	potential hit		
Prestw-425	quenching	autofluorescence	destabilization	no inhibition
Prestw-NAT-0103	quenching	potential hit	destabilization	inhibition
Prestw-809	low inhibition	non binder	no effect	no inhibition
Prestw-708	low inhibition	ambiguous		
Prestw-306	low inhibition	ambiguous		
Prestw-227	low inhibition	ambiguous		
Prestw-1472	inhibition	ambiguous	destabilization	inhibition
Prestw-1189	inhibition	ambiguous	destabilization	inhibition
Prestw-1224	inhibition	hit	no effect	no inhibition
Prestw-NAT-0114	inhibition	ambiguous		
Prestw-740	inhibition	hit	destabilization	no inhibition
Prestw-136	strong inhibition	ambiguous	no effect	no inhibition
Prestw-1364	strong inhibition	hit	destabilization	inhibition
Prestw-370	strong inhibition	hit	destabilization	inhibition
Prestw-1506	strong inhibition	non binder	no effect	no inhibition
Prestw-202	strong inhibition	potential hit	destabilization	inhibition

6.1.3 Validation of screening hits

Differential scanning fluorimetry (nanoDSF) is a method for determining protein stability by measuring fluorescence changes of intrinsic tryptophan and tyrosine residues upon thermal unfolding. Since this method requires relatively large amounts of target proteins, it has been evaluated as unsuitable for high-throughput screening, but suitable for the validation step.

*Pf*Snf2Lcore (4 µM) was analyzed in presence of 1/10/100/1000 µM compounds in duplicates. An exemplary melting curve of Prestw-1472 shows an unchanged T_M value of *Pf*Snf2Lcore at low concentration, but a reduced T_M value at 10 µM (Figure 6-4B). In total, eight out of twelve promising inhibitors were found to destabilize the protein, further emphasizing the molecular interaction (Figure 6-4A).

All twelve promising cendidates were tested in a remodeling assay with full-length *Pf*Snf2L for a potential inhibitory effect. The inhibition by the showcase compound Prestw-1472 can be seen by the fact that no nucleosome remodeling takes place in presence of high inhibitor concentrations (Figure 6-4D). Quantification of the initial nucleosome band shows a clear concentration-dependent inhibitory effect on nucleosome remodeling for six of the eight compounds (Figure 6-4C). The four chemicals that do not affect protein stability also did not impair remodeling at high concentrations (500 µM tested, not shown).

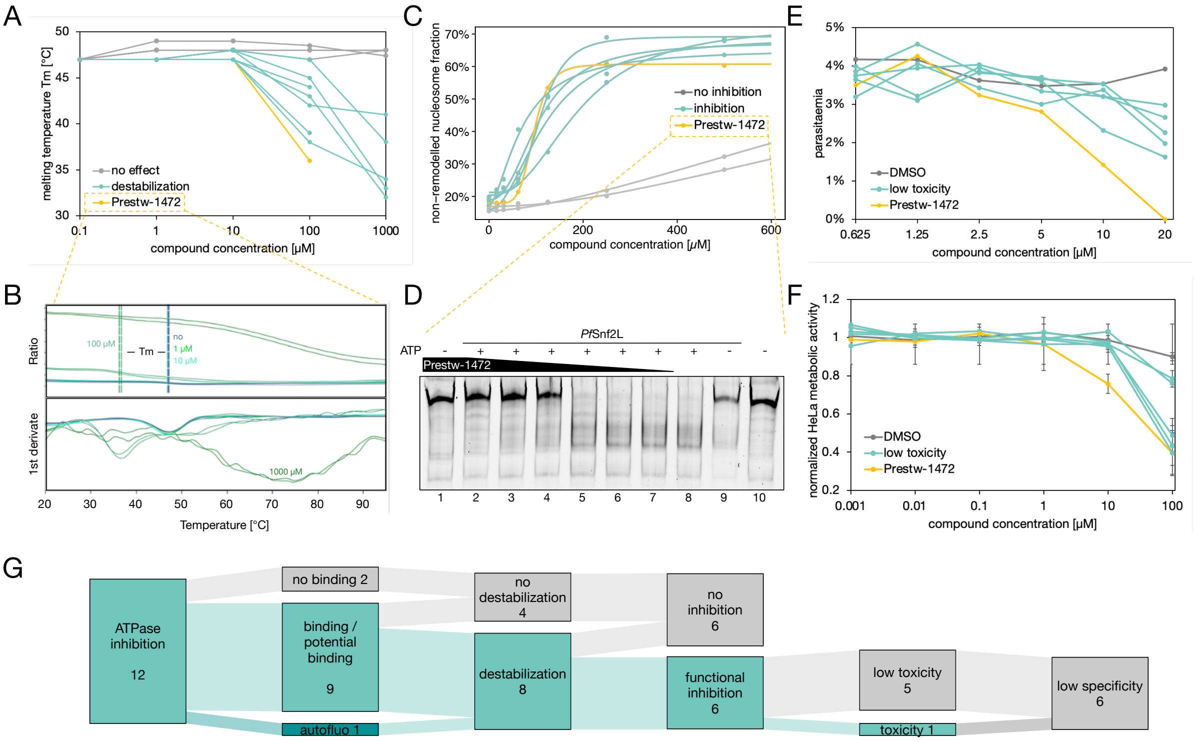

Figure 6-4: In vitro and in vivo validation of twelve screening hits. Each line represents one compound, colored for the respective effect (no effect – grey, effect – turquoise, Prestw-1472 – yellow). ***A.*** *Dose-dependent effect of twelve hit compounds on melting temperature of PfSnf2Lcore measured in nanoDSF, mean of two replicates shown.* ***B.*** *Exemplary melting curves of PfSnf2Lcore in presence of Prestw-1472 (1/10/100/1000 µM), fluorescence ratio and its 1st derivate displayed and determined T_M marked.* ***C.*** *Dose-dependent effect of eight hit compounds on chromatin remodeling activity of PfSnf2L. Gel band intensities were quantified, and the non-remodelled nucleosome fraction was calculated (initial band intensity/total intensity). Dose response model (four-parameter log-logistic models) was fitted.* ***D.*** *Exemplary chromatin remodeling assay of PfSnf2L in absence (lane 8) and presence of 500-16 µM Prestw-1472 (lane 2-7). Lane 9 serves as no ATP control and lane 1 (500 µM Prestw-1472 only) shows its effect on the nucleosome (lane 10).* ***E.*** *Dose-dependent toxicity of six hit compounds and DMSO on Plasmodium falciparum measured as parasitemia after 72 h.* ***F.*** *Dose-dependent toxicity of six hit compounds and DMSO on HeLa cells measured as metabolic activity after 72 h via XTT assay, mean and SD of two replicates shown.* ***G.*** *Summary of screening process starting with twelve hits from the PfSnf2L activity screen resulting in one toxic, but unspecific compound.*

After four steps of screening based on different *in vitro* assays, a library of 1506 compounds exposed six promising hits, that functionally inhibit *Pf*Snf2L (Figure 6-4G). These candidates were tested for toxicity on *Plasmodium falciparum*. One of the six compounds – Prestw-1472 – efficiently kills parasites at a concentration of 10 µM, as reflected by a drastically reduced parasitemia after 72 h (Figure 6-4E). The remaining five compounds show only low toxicity. Potential antimalarial drugs must meet the requirements of specificity for *Plasmodium falciparum* and that there is no toxicity for human cells. To get a first impression of toxicity against human cells, HeLa cells were exposed to the six candidates in a concentration-dependent manner. The viability of the HeLa cells was quantified by measuring their metabolic activity after 72 hours using the XTT assay (Figure 6-4F). Prestw-1472, the most toxic compound for parasites, also affects the viability of HeLa cells at 10 µM. In summary, the screening process of 1506 chemicals resulted in a set of twelve promising hits, which were further reduced in multiple validation steps (Figure 6-4G). *In vivo* validation resulted in one remaining hit compound. Since a relatively high concentration is required for a toxic effect, and the specificity for *Plasmodium falciparum* could not be confirmed, this chemical was not further characterized.

6.1.4 Screening of second library with optimized pipeline

The inhibitor screen described in the previous section proves the concept that a targeted *in vitro* screen can yield in a toxic compound, even though the potency of the compound is not sufficiently high. The experience gained from the first screen was used to screen another library – *Selleck Bioactive Compound Library* – containing 2645 chemicals. A slightly modified screening pipeline was applied (Figure 6-5A): Since the ADP biosensor assay was found to be the best predictor of inhibition in a high-throughput context, the entire library was analyzed with this assay only. The screen was implemented and analyzed as described (6.1.2)

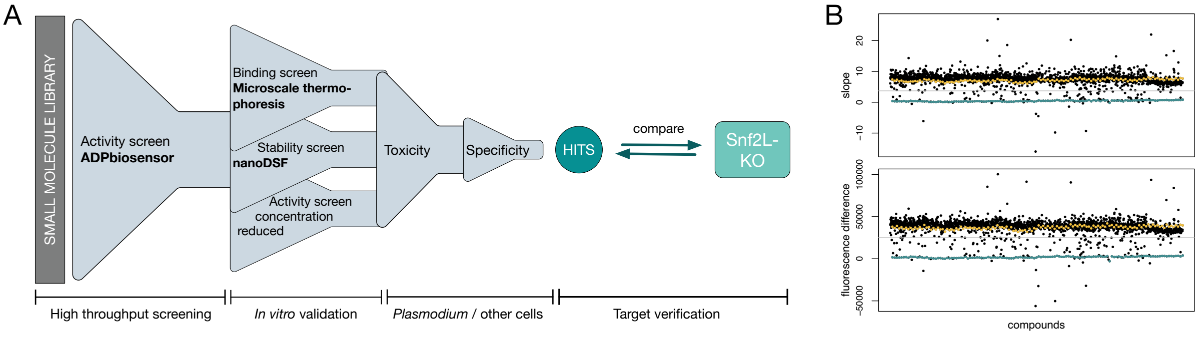

*Figure 6-5: **Screening of 2nd library containing 2645 chemicals. A.** Adjusted PfSnf2L inhibitor screening pipeline with the ADP biosensor assay for high-throughput screening and further methods for hit validation and target verification. **B.** Slope and fluorescence difference of kinetics in absence (yellow) or presence of 2645 compounds (grey) as described in Figure 6-3C/D. Mean of two replicates is shown, grey lines indicated inhibition cutoff (slope=3.7, difference=25000).*

with a compound concentration of 100 µM in duplicates. The analysis revealed 105 potentially inhibiting compounds, which were cherry-picked for *in vitro* validation (Figure 6-5B). The *in vitro* validation comprises three parallel strategies - analysis of binding to *Pf*Snf2Lcore, effect on *Pf*Snf2Lcore stability and dose-dependent ATPase inhibition. The selected candidates were automatically spotted onto suitable destination plates with volumes corresponding to the final concentrations – 100 µM for binding, stability, activity and 10 µM for activity assay. The validation assays were performed in duplicates as described for the initial screen (0) and the results are summarized in Figure 6-6A. The effects in the three different experiments were scored as strong (yellow) / moderate (turquoise) / low (petrol). Nine compounds showed a strong effect in all three approaches and were therefore considered as most promising.

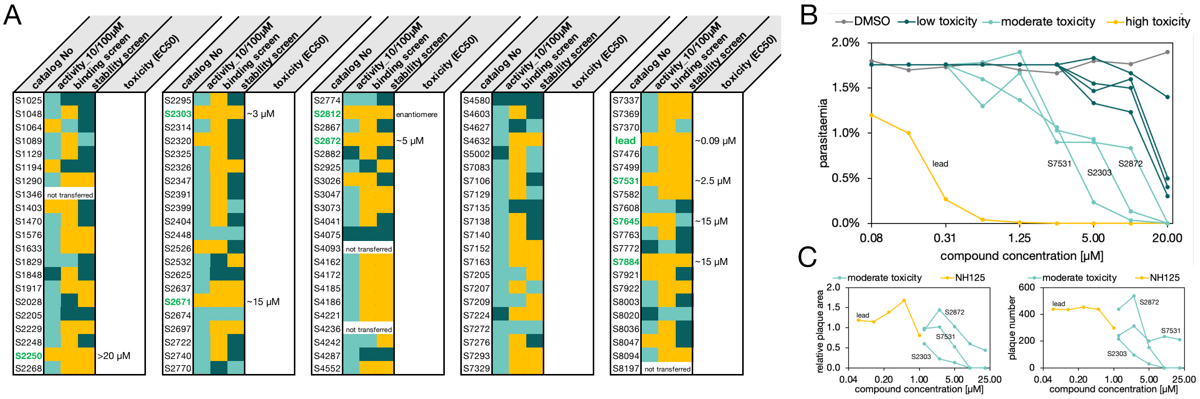

Figure 6-6: In vitro and in vivo validation of 105 hits. A. *Summary of in vitro validation of 105 hits comprising PfSnf2Lcore stability, PfSnf2Lcore binding, and dose-dependent ATPase screen. The effects were assessed as strong (yellow) / moderate (turquoise) / low (petrol) with following criteria: activity screen – inhibition at 10 µM / inhibition at 100 µM / no inhibition. Binding screen – hit or potential hit / aggregation or ambiguous / non-binder. Stability screen –* $\Delta T_M > 2$ *°C /* $\Delta T_M < 2$ *°C /* $\Delta T_M < 0.2$ *°C. Compounds with 3 x yellow (marked green) were chosen for further in vivo validation and their approximate EC50 values are noted.* ***B.*** *Dose-dependent toxicity of eight hit compounds and DMSO on Plasmodium falciparum measured as parasitemia after 72 h. Coloring indicates toxicity assessment.* ***C.*** *Dose-dependent toxicity of four hit compounds on Toxoplasma gondii measured as relative plaque area and plaque number after six days, coloring as in B.*

Like after the first screening process, the most promising candidates obtained from the second screen were purchased and analyzed for toxicity. One compound, S2812, was excluded because it was identified as an enantiomer of S2303. The remaining eight chemicals were tested for their toxicity to *Plasmodium falciparum.* The analogously performed screen revealed a toxic effect for most of the compounds, four of which exhibiting low potency, three moderate potency and one very high potency (Figure 6-6B). The latter is referred to as "lead compound”. To address the specificity, another apicomplexan parasite was tested. Treatment of *Toxoplasma gondii* shows toxicity in the micromolar range for the four most potent compounds (Figure 6-6C). EC50 values were estimated from the plaque assay by measuring number and relative area of parasite plaques (example described in 6.1.5). The difference between Plasmodium EC50 (<0.1 µM) and Toxoplasma EC50 (>1 µM) of the lead compound indicates a specific toxicity, or at least a specificity in its potency.

6.1.5 Characterization of the lead compound

One inhibitor of *Pf*Snf2L identified in the second screen – the lead compound - was found to have a high drug efficacy, as it is highly toxic to *Plasmodium falciparum.* A detailed characterization of the chemical and its effect on the parasite was initiated. Multiple replicates of drug treatment and quantification of parasitemia after 72 h revealed an EC50 value of ~ 90 nM for *Plasmodium falciparum* (Figure 6-7B, upper panel). This corresponds to a relatively high potency, especially in comparison with the active concentration in the *in vitro* characterization. In a dose-response assay monitoring ATPase activity, the lead compound was found to inhibit *Pf*Snf2L in the low micromolar range with an IC50 of ~ 10 µM (Figure 6-7A). With that, the *in vivo* potency is even higher (by a factor of ~100) than the *in vitro* potency under the conditions tested. However, toxicity and specificity are the key criteria for

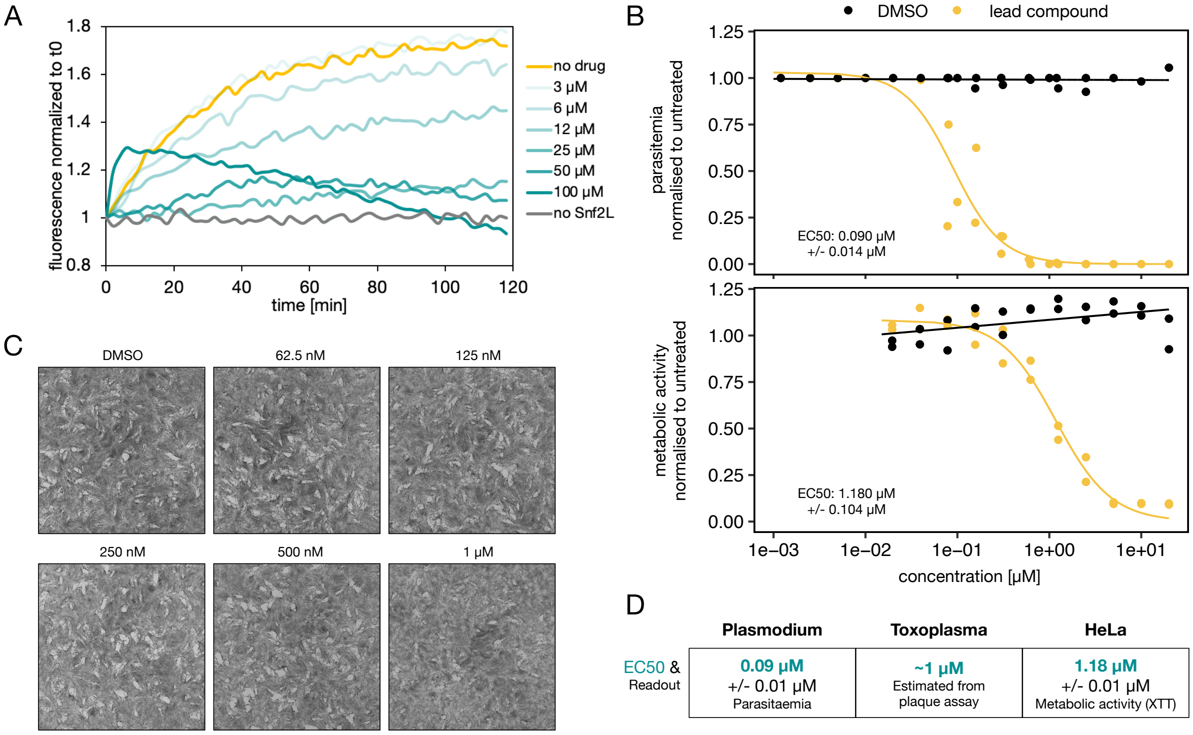

	Plasmodium	Toxoplasma	HeLa
EC50 & Readout	**0.09 µM** +/- 0.01 µM Parasitaemia	**~1 µM** Estimated from plaque assay	**1.18 µM** +/- 0.01 µM Metabolic activity (XTT)

Figure 6-7: Potency of lead compound. A. *ATP hydrolysis kinetic of PfSnf2L in presence of drug in varying concentrations (turquoise shades) with fluorescence normalized to t0. PfSnf2L (+DMSO) in absence of drug (yellow) serves positive control, samples without ATPase (grey) as negative control.* ***B.*** *Toxicity for Plasmodium falciparum shown as parasitemia after 72 hours in presence of varying concentration of drug or DMSO correspondingly of three independent experiments, normalized to untreated parasitemia (upper panel). Toxicity for HeLa cells shown as metabolic activity (monitored by XTT assay) in presence of varying concentration of drug or DMSO correspondingly of two independent experiments, normalized to untreated. EC50 was determined by fitting dose response model (three-parameter log-logistic model) and is indicated.* ***C.*** *Toxicity for Toxoplasma gondii shown as exemplary plaque assay of parasite infected human foreskin fibroblasts incubated for seven days before fixation and staining. Parasite plaques appear as bright areas.* ***D.*** *Toxicity of lead compound expressed by EC50 values on HeLa/Plasmodium/Toxoplasma cells from B/C and the corresponding readout method.*

drug development. The specificity of the lead compound was evaluated by exposure to *Toxoplasma gondii* as another representative of apicomplexan parasites and HeLa as a representative of human cells. Toxoplasma toxicity was estimated from plaque assay, where replicating parasites typically form white plaques when cultivated motionless in host cells for one week. A replication defect due to toxicity would affect the size and number of plaques. Drug treatment didn't lead to impaired plaque formation below a concentration of 1 µM (Figure 6-7C). HeLa cells were also cultured in media with increasing drug concentrations. Cell viability was determined by the XTT assay, which monitors metabolic activity, as was done for previous compounds (Figure 6-7B, lower panel). For both type of cells, an approximate EC50 value of 1 µM could be derived. This suggests that the lead compound is mildly toxic to other than Plasmodium cells, probably to most cell types. However, there appears to be a ~10-fold difference in potency (Figure 6-7D). These observations regarding its toxicity still leave open the question of how the drug affects parasite viability and what consequences treatment entails in detail.

The impact of drug treatment on parasite development was investigated using unmodified 3D7 strains. The observed drug effects were then compared to the previously detected phenotype upon *Pf*Snf2L-KO (5.1.3, 5.1.4). As already indicated by the toxicity assay, the severity of drug treatment effect varies with drug concentration (Figure 6-8A). When a synchronous parasite culture of early trophozoites (24 hpi) is treated with a low drug concentration (0.1 µM), the parasitemia is not reduced for the first 48 h and the composition of parasite stages does not change. The first effects appear after one cycle, when the number of viable parasites decreases, and development of the remaining parasites is impaired. 0.3 µM drug exposure leads to an arrest in ring stage of the following cycle and the parasites begin to die after ~24 hours. At 1 µM drug exposure, schizogony is immediately impaired and no viable parasites can be detected after 25 hours. A complete knockout mediated by inducible gene excision is most comparable to the fast-acting inhibition seen at high concentrations. Therefore, the effect of 1 µM lead compound on different parasite stages was analyzed by starting the treatment at 0 hpi (early ring) or 24 hpi (early trophozoite). As seen in the Giemsa-stained blood smears, parasite development is impaired in both cases compared to the untreated samples (Figure 6-8B). The developmental defect seems to be slightly more severe with early treatment, but both conditions show impaired replication as the parasites have difficulty undergoing schizogony. This suggests that this step in the parasite cycle is critical and highly sensitive to the lead compound. Quantification of nuclei in schizonts (46 hpi) emphasizes the replication defect, as treated parasites accomplished nuclear division to a lesser extent (Figure 6-8, right panel). The fact, that multi-nucleated parasites are visible, suggests that replication is still possible but slowed down. This agrees very well with the observed phenotype of *Pf*Snf2L-KO, indicating that the drug targets *Pf*Snf2L *in vivo* and thus phenocopies the knockout effect.

Detailed transcriptomic analysis was performed to analyze whether drug exposure also causes transcriptomic changes as it was seen in *Pf*Snf2L-KO (5.1.4). In a comparable setup, the parasites were tightly synchronized and treated with 1 µM drug or DMSO respectively. mRNA was isolated after 20 / 25 / 35 hours and sequenced to follow the transcriptomic changes over time (Figure 6-8C). Principal component analysis (PCA) of the whole transcriptome – plotted onto the reference transcriptome over the whole cycle (from 5.1.4) – shows the normal trajectory of untreated parasites. The drug-treated parasites, on the other hand, show a delayed development, as they progress more slowly. At 20 hpi there is hardly any difference, while 25 hpi the treated parasites are already lagging behind, and distance increases for 35 hpi. Again, the drug-dependent transcriptomic delay was observed alike in the *Pf*Snf2L-KO transcriptome with a very similar PCA upon late KO-induction (Figure 5-10B). Looking at the sampling times in both experimental setups, a faster effect is seen with inhibition (~25 hours) than with knockout (~48 hours). This difference is likely explainable by the time lag due to gene excision, subsequent downregulation of *Pf*Snf2L transcription and

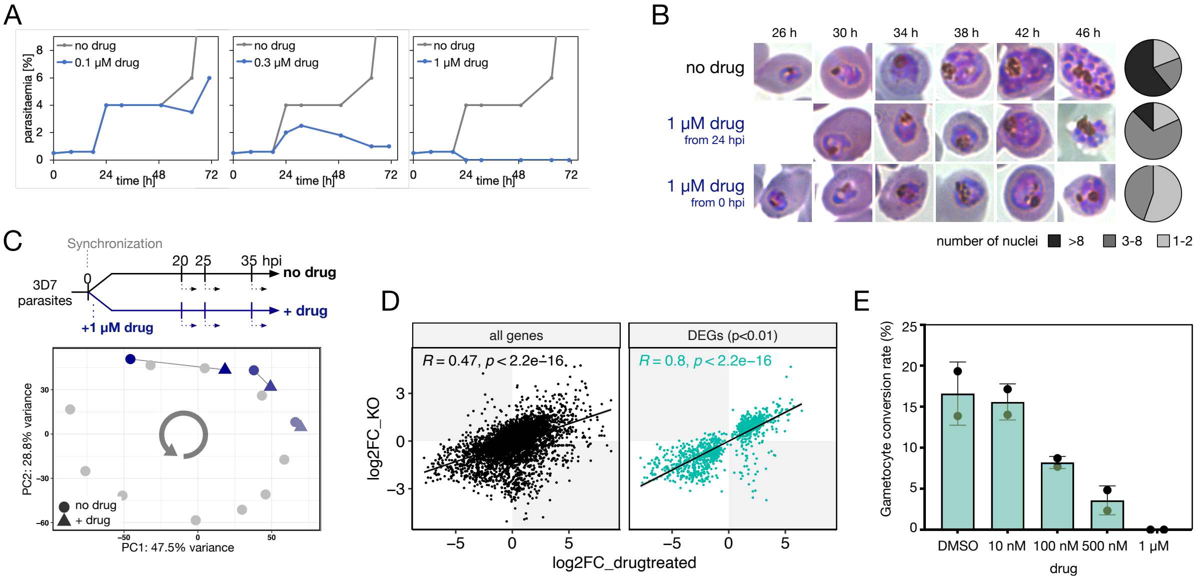

Figure 6-8: Developmental defect of P. falciparum upon lead compound treatment. A. *Growth curve assay of synchronized parasites, starting with early trophozoite stage (24 hpi), in absence (grey) and presence of 0.1 µM / 0.3 µM / 1 µM drug (blue) over 72 h. One representative of two replicates shown.* ***B.*** *Representative Giemsa-stained blood smears of parasites cultured in presence of 1 µM drug started from 0/24 hpi with quantification of nuclei in schizonts harvested 46 hpi (n>80 each, right panel).* ***C.*** *Scheme of drug treatment and RNA extraction timing (upper panel). Principal component analysis of whole transcriptome data of parasites as shown (blue) plus reference transcriptome (grey) as in Figure 5-10B. Pool of three biological replicates shown.* ***D.*** *Pearson correlation between gene expression changes upon late PfSnf2L-KO (+60 h, Figure 5-10) and upon drug treatment (+35 h) of all genes (left)/genes showing a significant change over both time course experiments (p<0.01) (right).* ***E.*** *Gametocyte conversion rate upon one day treatment with the lead compound of varying concentration and DMSO respectively. Mean ± SD of two independent experiments is shown.*

translation and *Pf*Snf2L protein turnover. Comparing the expression of all genes in KO and in drug-treated parasites, a clear correlation can be seen (Figure 6-8D). KO-upregulated genes tend to be upregulated upon drug treatment and the same is true for down regulated genes. Looking only at significantly differentially expressed genes across the three timepoints ($p<0.01$), this correlation is even more pronounced, with an R-value of 0.8. The high correlation in transcriptomic changes upon drug exposure and *Pf*Snf2L-KO can be seen as very strong indication of *Pf*Snf2L being the direct target of the lead compound.

Beside the strong impact on erythrocytic development, the lead compound was also found to inhibit gametocyte formation. The expression changes of gametocyte-specific genes in *Pf*Snf2L-KO RNA-Seq already indicated a function of *Pf*Snf2L in gametocyte formation (Figure 5-11). A gametocyte induction assay performed with one-day drug treatment during induction, revealed a clear defect in gametocyte formation (Figure 6-8E). As shown by the gametocyte conversion rate (gametocytemia on day 8 / parasitemia on day 2), parasites are unable to form mature gametocytes when treated with 1 µM drug. Lower concentrations clearly impair the gametocyte conversion rate compared to the DMSO control. This suggests that *Pf*Snf2L has an important function either in gametocyte commitment or in gametocyte development. This cannot be conclusively clarified within this assay, but exposure to the lead compound prevents the sexual conversion of *Plasmodium falciparum* parasites, most likely by inhibiting *Pf*Snf2L.

6.2 DISCUSSION

Evaluation of screening procedure

Screening for *Pf*Snf2L inhibitors directed against the ATPase activity resulted in compounds that are toxic to *Plasmodium falciparum.* The multistep screening pipeline was successfully established, as reflected by a not too high hit rate and an efficient pipeline to identify true positive hits. A library of ~1500 compounds yielded 22 putative hits after high-throughput screening, which were reduced to six after *in vitro* validation and ended in one toxic compound. The second screen starting with ~2500 compounds resulted in eight *in vitro* inhibitors, four of which exhibit toxicity to parasites. Moreover, one highly potent and specific inhibitor was identified among them. The second screen was further optimized based on the experience from the first screen. The central readout of both screens is the *in vitro* ATPase activity of *Pf*Snf2Lcore based on an ADP biosensor method.

Screening for ATPase activity *in vitro* has been previously considered as a useful application since ATP hydrolysis is required for protein function and many enzymes and ATP turnover can be easily measured. So far, these screens have mainly been based on other technologies. It is common to couple ADP generation to another enzymatic reaction that delivers substrates for a peroxidase reaction to enable fluorescent readout (Wigle and Singleton, 2007). Other ATPase detection methods are for example RNA-based biosensors, immunodetection of nucleotides or the use of fluorescently-labeled nucleotides (Kleman-Leyer et al., 2009; Su et al., 2016; Webb and Corrie, 2001). In contrast to these technologies, the ADP biosensor system with fluorescently labeled ParM offers the advantage of using target proteins and ligands in their physiological form without labeling or modification. Furthermore, it is a direct method to measure ADP concentration in real time and is therefore very suitable for monitoring *Pf*Snf2L activity. Nevertheless, the setup has some limitations: The assay is only useful for enzymes with relatively high ATPase activity. Attempts to perform the screen with *Hs*Snf2L failed because this enzyme has a ~6-10-fold reduced ATP hydrolysis rate. To measure an inhibitory effect on less active enzymes, higher ATPase and higher ParM concentrations are required.

Another notable side effect of the APD biosensor screen is the fact, that it also screens for inhibitors of ParM. When the biosensor molecule is inhibited, fluorescence enhancement by ADP binding is prevented. Therefore, ParM inhibition and ATPase inhibition result in a similar readout. To test for this bias, the twelve potential hits from screen 1 were analyzed for ParM interference independently. Fluorescence was measured in the absence of an ATPase to detect compound-induced changes. In addition, the compounds were tested for ParM interaction in MST assays. Only for four of the twelve compounds an interaction with ParM could be ruled out. The other eight chemicals showed signs of binding to ParM or altered fluorescence signals, enhancement or quenching (not shown). These false-positive hits cannot be prevented in the ADP biosensor screen but emphasize the importance of complementary assays based on different biophysical principles.

Although microscale thermophoresis has been shown to be a valuable technique for measuring molecular interactions, we found the ADP biosensor assay to be more efficient for *Pf*Snf2L screening (Jerabek-Willemsen et al., 2014; Zillner et al., 2012). The short measurement time, easy handling and low consumption of material make it a useful and easily implementable tool (Bartoschik et al., 2017). It has been used in several drug development studies, but only for validation of potential hits rather than for large-scale screens (Bartoschik et al., 2017; Linke et al., 2016; Zimmermann et al., 2022). MST screening is expected to identify a larger number of interactors that do not necessarily affect enzyme function. Accordingly, it reveals more false positive hits compared to the direct screening for enzymatic inhibition. As a complementary method, the MST measurement eliminates compounds that interfere with ParM instead of the target protein. As a primary screening technique, MST has some limitations depending on the target molecule or protein (Rainard et al., 2018): Proteins with low stability tend to appear in a mixed population of correctly folded / misfolded / unfolded proteins, which affects the diffusion behavior in the temperature gradient. The protein of interest in this case, *Pf*Snf2L, was also shown to be not very stable, which could cause issues. Related to protein stability, the fluorescent labeling procedure required for this method – NHS-amine labeling in this study – can influence stability as well as intra-/ intermolecular binding. Furthermore, a binding reference molecule is highly recommended for unambiguous interpretation of molecular interactions in MST and any other screening system. In the case of *Pf*Snf2L, the lack of known binding partners or binding small molecule, which would be even better, forced us to perform the screen without a positive control. The only known interactor, ATP, was tried to be establish as a reference measurement, but failed to show a consistent binding effect in MST at feasible concentrations. Moreover, the design of a single-point screen using only one concentration of compound logically comes at the expense of reliability. The number of ambiguous results (18 %) in the first screen of this study confirms this problem, which could be circumvented by measuring dose response curves. For large libraries, this would be an enormous effort. Evaluating all the advantages and disadvantages, Microscale Thermophoresis is a useful biophysical technique for validating high-throughput hits. Hence, the screening strategy was adapted for the second screen. There, MST provides orthogonal evidence of target engagement in combination with nano Differential Scanning Fluorimetry.

The nanoDSF method has been used in drug screening before and has also been shown to be suitable in our setup (Clark et al., 2015). Due to the high amounts of protein, that are required to obtain sufficient intrinsic tryptophan/tyrosine fluorescence, it is more applicable for hit validation than for high-throughput screening. The remodeling assay represents a good method for functional validation of hit compounds. Since nucleosome remodeling is the key function of CREs, inhibition of this activity is most meaningful. Throughout the whole screening process, the core protein was used as target molecule. This makes it even more important to validate the hits in the context of the full-length protein. For a larger number of compounds, however, the remodeling assay is time-consuming and labor-intensive.

The composition of the applied screening pipeline targeting *Pf*Snf2L has the potential to be upscaled to larger compound libraries containing up to millions of molecules. Generation of required substrates as well as the infrastructure of assay implementation is expected to be manageable also for larger scales. The screens performed in this study serve primarily as proof-of-principle to demonstrate that *in vitro* based screens combining different biophysical technologies lead to actual toxic compounds.

Target identification of the lead compound

Not to be neglected, the screen proves the druggability of plasmodial chromatin remodeling enzymes, specifically *Pf*Snf2L. Epigenetic enzymes in *Plasmodium falciparum* have previously been reported to be good drug targets (Coetzee et al., 2020; Sen et al., 2020). In cancer therapy, targeting the catalytic activity of epigenetic regulators is already used (Foss et al., 2011; Garcia-Manero and Fenaux, 2011; Vardiman, 2006), and great efforts are bbeing made to develop new potent inhibitors of this class of enzymes (Dawson and Kouzarides, 2012; Sbardella, 2019). So far, the inhibition of CREs by small molecules has only been investigated in cancer research attempting to develop new therapeutic strategies (Jagani et al., 2019; Papillon et al., 2018). The functional and sequence divergence of *Plasmodium falciparum* CREs suggests that they may also be good antimalarial drug target. The *in vitro* screen described is a directed molecular approach targeting *Pf*Snf2L and the obtained hits are shown to target this enzyme. Despite having evidence of *in vitro Pf*Snf2L inhibition, the resulting compounds cannot be excluded to have off-target effects when applied to the parasites. Consequently, the high toxicity of the lead compound could potentially be caused by inhibiting other targets or processes. The observed difference between *in vitro* and *in vivo* potency (by a factor of 100) could be due to additional target inhibition. On the other hand, this effect could also be caused by suboptimal *in vitro* conditions or promiscuous drug action, differences in target turnover, etc. (Jansson-Löfmark et al., 2020).

The lead compound is known to be a potent and selective inhibitor of eukaryotic elongation factor 2 kinase (eEF-2K/CaMKIII), which can induce eEF2 phosphorylation. Because most enzymes, including elongation factor 2 kinase, are also highly divergent in *Plasmodium falciparum*, there is no certainty, that the drug acts on *Pf*EF-2K. However, this organism also possesses many kinases or ATPases, that could potentially be inhibited. Contrary to this possibility, the detailed characterization of the treated parasites revealed an effect on parasites very similar to the knockout of *Pf*Snf2L. In particular, the high correlation of transcriptomic data suggests *Pf*Snf2L to be the primary target of the lead compound, also in the cellular context. Even more direct evidence was sought by attempting to develop resistance against the drug. By culturing the parasites on low drug concentration for months, they were provoked to become resistant. Subsequent genotyping should reveal resistance mutations and potentially identify *Pf*Snf2L as the target. Since the generation of resistant parasites failed, the location of resistance-inducing mutations was obsolete. More importantly here, resistance does not appear to be easily established, emphasizing the toxicity and the drug potential of the lead compound.

In the future, efforts will be made to further prove the direct interaction of the chemical and *Pf*Snf2L and to identify the detailed interaction site. A nearby path to elucidate the intermolecular interaction is structural approaches. So far, no attempt has been made to resolve the structure of *Pf*Snf2L, but the ability to recombinantly express and purify the protein opens the possibility to perform cryo-electron microscopy or X-ray crystallography. Another promising method is Nuclear magnetic resonance (NMR) spectroscopy, not only to study macromolecular interactions but also in the field of drug development. It is used as a tool to identify small molecule binding and for hit-to-lead optimization (Harner et al., 2013). As a future goal, NMR-spectroscopy can be used to study the interaction between *Pf*Snf2L and compound, to identify the binding site and to potentially enable drug optimization.

Prospects for hit-to-lead drug optimization

The search for therapeutic compounds does not end with the completion of a high-throughput screen. Drug discovery in mechanistic enzymology involves numerous steps, before compounds are considered for advancement into clinical phases (Holdgate et al., 2018): The initial step is to develop an assay, where understanding the target biochemistry and designing a suitable screening strategy are essential. This is followed by a primary screening, where hit compounds are identified and evaluated using orthogonal approaches. In the third step, hit-to-lead, the promising ligands are characterized in detail. Finally, the mechanism of inhibition is clarified during lead optimization including the collection of binding site information. For *Pf*Snf2L inhibition, the first three steps have been completed, while the elucidation of the detailed mechanism is still pending and will be attempted in the future.

Hit and lead criteria for antimalarial drugs were defined by experts from the Medicines for Malaria Venture, the Drugs for Neglected Diseases initiative, and the TB Alliance, together with representatives from the Bill & Melinda Gates Foundation (Katsuno et al., 2015). Validated hits should meet the required potency EC50 < 1 µM and 10-fold selectivity for Plasmodium over mammalian cells. For early lead compounds, a potency of < 100 nM and 100-fold selectivity is suggested. Applying these criteria, the identified compound is a validated hit, that has the potential to be further improved from hit to lead. To achieve this improvement, structure-based design is probably the most powerful strategy. As the example of a CRE inhibitor shows, a 100-fold improvement in potency was achieved with just a few cycles of design and synthesis, (Drouin et al., 2015). Once structural information about the compound's binding to *Pf*Snf2L is available, computational approaches can be applied to optimize the drug *in silico*. By modifying individual chemical groups, the potency and specificity of the identified lead compound can be increased.

In summary, the functional divergence of *Pf*Snf2L revealed by *in vitro* characterization provided the basis to specifically target the enzyme with antimalarial drugs. A customized drug screen resulted in a validated inhibitor of *Pf*Snf2L that was shown to be toxic and specific for *Plasmodium falciparum* parasites. With further optimization, it can be developed into a potent and specific inhibitor of *Pf*Snf2L and could one day potentially be applied as an antimalarial drug. In combination with knockout studies *in vivo*, it helped to elucidate the function of *Pf*Snf2L. The findings of this study provide new insights into the complex epigenetic gene regulation of the parasite representing a valuable addition to current knowledge. Further investigations building on this may unravel still existing mysteries of the complex regulation of the deadly malaria parasite. The demonstrated druggability of *Pf*Snf2L and the exemplary inhibitor screen provide a promising starting point for targeting chromatin remodeling enzymes in the ongoing fight against *Plasmodium falciparum*.

7 MATERIAL AND METHODS

7.1 Technical devices

Table 7-1: Overview of technical devices

Description	Application	Supplier
3-16K centrifuge	Centrifuge	Sigma
BAS-MS 2040	Imagaing Plate	Fujifilm Holdings Corporation
Biorupter ® Standard	Sonifier	Diagenode
Branson Sonifier 250D	Sonifier	Emerson Electric Co
Centrifuge 5415 R	Centrifuge	Eppendorf AG
EnVision Nexus	Multimode Microplate Reader	PerkinElmer
EPS301	Electrophoresis power supply	Amersham Biosciences
PowerPac Basic Power Supply	Electrophoresis power supply	BioRad
FastGene B/G	LED Transilluminator	Nippon Genetics
GEL iX20 Imager	Imager	Intas Science Imaging
Incubator	For bacteria/insect/mammalian cells	Memmert / Binder
L-28	Testtube rotator	Labinco B.V.
Mastercycler X50s	Thermal cycler	Eppendorf
Monolith NT.115pico	Microscale Thermophoresis	NanoTemper Technologies
MR Hei-Standard	Magnetic Stirrer	Heidolph
Nanodrop ND-1000	Spectrophotometer	Peqlab Biotechnologies
Qubit 2.0	Fluorometer	Invitrogen
PeqStar	Thermal cycler	Peqlab Biotechnologies
Perfection V700	Photo Scanner	Seiko Epson Corporation
pH meter	pH meter	Knick
Pipetboy	Pipette controller	Eppendorf
Pipetteman Neo pipettes	Pipette controller	Gilson
Polymax 1040	Platform shaker	Heidolph
Prometheus NT.48	nanoDSF	NanoTemper Technologies
Pumpdrive 5001	Peristaltic pump	Heidolph
Purelab Ultra	Water purification system	ELGA LabWaters VWS
REAX Top	Vortexer	Heidolph
Shaker incubator		HT Infors
Tabletop centrifuge	Centrifuge	Roth
Tecan infinite F500	Microplate reader	Tecan
Thermomixer comfort	Thermomixer	Eppendorf AG
Tritec KBP 6151	Plasmodium Incubator	Tritec
Typhoon FLA 9500	Fluorescence Reader	Fujifilm Holdings Corporation
LAS-3000 image reader	Chemoluminescence Reader	Fujifilm Holdings Corporation
Odyssey® imaging system	Fluorescence Reader	LiCOR Biosciences
DOS-20M	Orbital shaker	ELMI
BIO-PRINT 3000	UV Transluminator / Imager	Vilber, Lourmat
Kendro HS18 HS 18	Laminar Flow Hood Plasmodium	Heraeus
HB 2472 K GS	Laminar Flow Hood insect	Heraeus
Herasafe KS12	Laminar Flow Hood HeLA	Thermo Fisher
Mini Submarine Electrophoresis Unit	Agarose gel chambers	Tarsons
Mini-PROTEAN Tetra Cell	Electrophoresis system	BioRad
Mini Trans-Blot Cell	WetTank blotting system	BioRad
Self-print	Electrophoresis chamber	
Mikro 200 R	Microliter centrifuge	Hettich
Centrifuge 5910 R	Centrifuge	Eppendorf
4D-Nucleofector System	Nucleofection	Lonza
Leica DMi8 Widefield	Microscope	Leica Microsystems
4200 TapeStation System	Automated electrophoresis platform	Agilent Technologies
Multidrop Combi system	Reagent Dispenser	Thermo Fisher

7.2 Software tools

Table 7-2: Overview of software tools

Software	Application	Supplier
Bcl2fastq	Conversion Software	Illumina
BioanalyzeR 0.10.0	TapeStation visualization	https://github.com/jwfoley/bioanalyzeR
Bowtie2_v2.4.2/2.3.5	Mapping ChIP-Seq/MNase-Seq	(Langmead and Salzberg, 2012)
deeptool_v3.3.2/3.5.0	Preprocessing sequencing data	(Ramírez et al., 2016)
DESeq2	Differential expression analysis	(Liao et al., 2014; Love et al., 2014)
DANPOS	Nucleosome calling	custom version, based on DANPOS3 (Chen et al., 2013)
DEGreport	differential expression analyses	(Pantano, 2022)
Epson Scan	Scanning software	Seiko Epson Corporation
Excel	Spreadsheet program	Microsoft Corporation
FastQC 0.11.8	Mapping quality control	(Andrews, Simon, n.d.)
Geneious v11.1.5	*In silico* cloning & alignment tool	Biomatters
gffread 0.12.1	Convert annotation	(Pertea and Pertea, 2020)
ggpubr	Data visualization package	(Kassambara, 2022)
i-control	Microplate Reader Software	Tecan
IGV v2.11.0	Integrative Genomics Viewer	(Robinson et al., 2011)
ImageJ2 v 2.9.0	Image processing program	(open source)
Leica Application Suite X (LAS X)	Life Science Microscope Software	Leica Microsystems
LI-COR Image Studio	Image acquisition software	LI-COR Biosciences
MACS2_ v2.1.1.2	Peak calling ChIP-Seq	(Zhang et al., 2008)
NCBI Blast	Comparative alignment tool	NCBI
multiqc 1.9	preprocessing sequencing data	(Ewels et al., 2016)
Multigauge V3.1	LAS reader viewer software	Fujifilm Holdings Corporation
Nucleosome Dynamics	Nucleosome analysis tool	(Buitrago et al., 2019)
OrthoDB v11	Orthology database	(Kuznetsov et al., 2023)
P. falciparum 3D7 genome v3.0	(plasmoDB.org, release 52,)	(Aurrecoechea et al., 2009)
PlasmoDB/VEuPathDB	Plasmodium database	(Amos et al., 2022)
PR.ThermControl	nanoDSF control software	nanoTemper Technologies
qualimap 2.2.2d	preprocessing sequencing data	(Okonechnikov et al., 2016)
R 4.1.1	statistical software	(R Core Team, 2022)
RSubread/FeatureCounts 2.12.2	Read count calculation	(Liao et al., 2019, 2014)
samtools 1.9/1.12	Preprocessing sequencing data	(Li et al., 2009)
Skewer 0.2.2	Trimming MNase-Seq	(Jiang et al., 2014)
snakemake 5.32.0	Pipeline implementation	(Mölder et al., 2021)
STAR 2.7.9a	Mapping RNA-Seq	(Dobin et al., 2013)
TapeStation software 5.1	Control/analysis software	Agilent
tidyverse	Data transformation package	(Wickham et al., 2019)
topGO	enrichment analysis for Gene Ontology (GO) terms	(Alexa and Rahnenfuhrer, 2022)
trimmomatic v0.39	Trimming RNA-Seq	(Bolger et al., 2014)
Typhoon FLA 9500 control software	Scanning software	Fujifilm Holdings Corporation
VICTOR Nivo v4.0	Multimode Plate Reader Software	PerkinElmer
VisionCapt 15.0	Imaging software	Vilber Lourmat

7.3 Chemicals and consumables

Table 7-3: Overview of chemicals and consumables

Name	Supplier
1.5 ml and 2 ml reaction tubes	Sarstedt
15 ml and 50 ml tubes	Sarstedt
Acetic acid	Fluka
Agarose	Invitrogen
Amersham Protran Western blotting membranes, nitrocellulose	Sigma
Ampicillin	Roth
Ammonium acetate	Merck
Ammonium hydroxide (NH_4OH)	Merck
Ammonium persulfate	Roth

AMPure XP Reagent	Beckman coulter
Aprotinin	Sigma
Adenosine diphosphate (ADP)	Sigma
Adenosine triphosphate (ATP)	Sigma
[γ-32P]-ATP	Hartman Analytics
Bacto ager	BD Biosciences
Bacto tryptone	BD Biosciences
Bacto yeast extract	BD Biosciences
Benzamidine hydrochloride hydrate	Sigma
Blood – Vollblut human	Blutspendedienst BRK
Boric acid	Babochem. International
Bradford reagent	BioRad
Bromphenol blue	Merck
Bovine serum albumin (BSA)	Sigma
β-Mercaptoethanol (β-ME)	Roth
Calcium chloride ($CaCl_2$)	Roth
Chamaleon Duo, Protein ladder	LiCOR
Citric acid	Merck
cOmplete, EDTA-free; protease inhibitor cocktail (PIC)	Roche
Compound2	(Taylor et al., 2010)
Coomassie Brilliant Blue G-250	Roth
Cytiva Sera-Mag SpeedBeads	Thermo Fisher
D-sorbitol	Sigma
Deoxycholic acid sodium salt (DOC)	Sigma
Dextrose	Sigma
Dithiothreitol (DTT)	Sigma
Dimethylsulfoxid (DMSO)	Merck
Disuccinimidyl glutarate (DSG)	Sigma
DMEM	Sigma
dNTPs	New England Biolabs
Dulbecco′s Phosphate Buffered Saline (PBS)	Sigma
DynaMag™-2 Magnet	Invitrogen
Ethylenediaminetetraacetic acid (EDTA)	Merck
Ethylene glycol-bis(β-aminoethylether)-N,N,N′,N′-tetraacetic acid (EGTA)	Sigma
Ethidium bromide	Roth
Ethanol (EtOH) tech., p.a.	Sigma
Fetal bovine serum (FBS)	BioSell / Gibco
Formaldehyde, 37 %	Merck
Formic acid	Merck
G-418 solution	Roche
Gel cassettes 1 mm	Life Technologies
GeneRuler 1 kb Plus DNA ladder	Fermentas
Gentamycine	Sigma
Glutaraldehyde 50 %, EM grade	Science Service
Glycerin 99 %	Roth
Glycine	Sigma
Glycogen	Roche
Hemacolor Rapid Staining of blood smear – colour reagent red	Merck
Hemacolor Rapid Staining of blood smear – colour reagent blue	Merck
Hepes	VWR
Igepal CA-630	Sigma
Immersol 518 N	Zeiss
Imidazole	Roth
Isopropanol p.a.	VWR
Kanamycin	Roth
L-glutamine	Sigma
Laboratory Film	Parafilm
Leupeptin	Roth
Lithium chloride (LiCl)	Sigma
Low binding 1.5 ml reaction tubes	Sarstedt
Magnesium chloride (Mg_2Cl)	Merck
Methanol, p.a. (MeOH)	VWR
Microplate, 384 well, *PP*, small volume	Greiner

Microplate, 384 well, PS, µCLEAR	Greiner
Microscope cover glasses, 24x40 mm	Superior Marienfeld
Microscope slides Menzel Gläser	Thermo Fisher
Mini Protean TGX Gels 4-20 %, 10 well	Biorad
Mounting Medium with DAPI	Abcam, Ab104139
µ-slide 8 well glass bottom	Idibi GmbH
N,N,N',N'-Tetramethylethylendiamin (TEMED)	Roth
nanoDSF Grade Standard Capillaries	NanoTemper
Ni-NTA agarose	Qiagen
Orange G	Sigma
PageRuler Plus prestained protein ladder	Fermentas
PAP Pen Liquid Blocker	Newcomersupply
Pasteur pipettes	VWR
PBS 10x, pH 7,4	Thermo Fisher
PCR reaction tubes 0.2 ml	Biozym
Percoll, pH 8.5-9.5	Sigma
Paraformaldehyde 32%, EM Grade (PFA)	Science Service
PEG-8000	Promega
Pepstatin A	Roth
Pierce Anti-HA magnetic beads	Thermo Fisher
Pierce Protein G magnetic beads	Thermo Fisher
Pierce Protease inhibitor Mix tablets, EDTA free (PIC)	Thermo Fisher
PIPES	Roth
Pipette tips	Sarstedt
Plastic cuvettes	Sarstedt
Pluronic	Sigma
Phenylmethylsulfonylfluorid (PMSF)	Roth
Potassium chloride (KCl)	Labochem. International
Prestwick small molecule library (Prestwick Chemical Library® + Prestwick Phytochemical Library)	Prestwick
Prestw-136 Astemizole	Biomol
Prestw-202 Tiratricol, 3,3',5-triiodothyroacetic acid	ABCR
Prestw-370 Benzbromarone	Biomol
Prestw-425 Chicago sky blue 6B	ABCR
Prestw-705 Methyl benzethonium chloride	ABCR
Prestw-740 Ebselen	ABCR
Prestw-777 Alexidine dihydrochloride	Biomol
Prestw-809 Dichlorphenamide	Biomol
Prestw-1189 Montelukast	ABCR
Prestw-1224 Anthralin	ABCR
Prestw-1472 Hexachlorophene	Biomol
Prestw-1506 Mizolastine	ABCR
Prestw-NAT-0103 Myricetin	Biomol
Rapamycin	Sigma
Rotiphorese Gel 30	Roth
RPMI 1640 with AlbuMAX-II	Gibco
[REDACTED] - lead compound *	Biomol
S2250 (-)-Epigallocatechin Gallate	Biomol
S2303 gossypol-Acetic acid	ABCR
S2671 AS-252424	Biomol
S2872 GW5074	Biomol
S7531 UMI-77	Biomol
S7645 Pilaralisib (XL147)	Biomol
S7884 AMI-1	Biomol
Saponin	Sigma
Selleck Bioactive Compound Library	Selleck Chemicals, Cat.No.L1700
Serological pipettes 2 ml, 5 ml, 10 ml, 25 ml, 50 ml	Sarstedt
Sf900 II SFM	Gibco
Silver nitrate ($AgNO_3$)	Roth
Skimmed milk	dm
Slide-A-Lyze MINI Dialysis Devices, 10K MWCO	Thermo Fisher
Sodium chloride (NaCl)	Fisher chemicals
Sodium hydroxide (NaOH)	VWR

Sodium dodecylsulfate (SDS)	Roth
Sucrose	Sigma
SYBR Safe DNA Gel Stain	Invitrogen
Tetracycline	Sigma
Tissue culture flask 175 cm^2 plug seal cap	Corning
Tissue culture flask 175 cm^2 Vent	Sarstedt
Tissue culture flask 25 cm^2 VENT screw cap	TPP
Tissue culture flask 175/25 cm^2 VENT screw cap	TPP
Tissue culture plates 6/12/24/96-well	TPP/Sarstedt
PEI-Cellulose F plates	Merck
Tris	Roth
Triton-X100	Roth
Tween 20	Sigma
Whatman chromatography paper	Sigma
WR99210	Jacobus Pharmaceutical Co
X-Gal (5-Bromo-4-chloro-3-indolyl-β-D-galactopyranosid	Sigma
X-tremeGENE	Roche
1 % O_2, 5 % CO_2, 94 % N_2	Riessner Gase

*The name of the chemical has been redacted due to pending patent. For information, see Prof. Dr. Längst.

7.4 Buffers, solutions, media

Table 7-4: Standard buffers and solutions

Buffer	Composition
TBE buffer	90 mM Tris, 90 mM Boric acid, 2 mM EDTA
TE buffer	10 mM Tris-HCl pH 7.6, 1 mM EDTA
DNA loading dye 10 x	50 mM Tris-HCl pH 7.6, 10 mM EDTA, 50 % glycerol, 0.05 % bromphenol blue (w/v)
Orange G loading dye 10 x	10 mM EDTA, 50 % glycerol, 0.05 % Orange G (w/v)
Lämmli buffer 6 x	350 mM Tris-HCl pH 6.8, 10 % SDS (w/v), 5 % β-ME (v/v)
OrangeG SDS loading buffer 4x	62 mM Tris pH 6.5, 25 % glycerol, 2 % SDS, 0.2 M DTT, 0.05 % Orange G
SDS-PAGE upper tris buffer 4x	0.5 M Tris-HCl pH 6.8, 0.4 % SDS (w/v)
SDS-PAGE lower tris buffer 4x	1.5 M Tris-HCl pH 8.8, 0.4 % SDS (w/v)
SDS running buffer	200 mM Glycine, 25 mM Tris, 0.1 % SDS (w/v)
Coomassie staining solution	50 % MeOH, 10 % Acetic acid, 0.25 % Coomassie Brilliant Blue R250 (w/v)
Silver stain fixing solution	50 % MeOH, 12 % Acetic acid, 0.019 % Formaldehyde
Silver stain solution A	0.8 % $AgNO_3$ (w/v), 0.45 % NH_4OH, 0.075 % NaOH
Silver stain solution B	0.005 % Citric acid, 0.019 % Formaldehyde
Silver stain stop solution	45 % MeOH, 10 % acetic acid
Western blot transfer buffer	25 mM Tris pH 8.3, 192 mM glycine, 12 % MeOH, 0.02 % SDS
High salt buffer	10 mM Tris-HCl pH 7.6, 2 M NaCl, 1 mM EDTA, 1 mM β-ME, 0.05 % Igepal CA-630
Low salt buffer	10 mM Tris-HCl pH 7.6, 50 mM NaCl, 1 mM EDTA, 1 mM β-ME, 0.05 % Igepal CA-630
PI mix	2 µg/ml Aprotinin, 10 µM Leupeptin, 0.4 mM PMSF, 0.9 mM Benzamidine, 1 µM Pepstatin
Lysis buffer	20 mM Tris-HCl pH 7.6, 1.5 mM $MgCl_2$, 0.5 mM EGTA, 500 mM KCl, 10 mM Imidazole, 0.1 % Igepal CA-630, 0.01 % β-ME, 10 % Glycerol, PI mix
Wash buffer	20 mM Tris-HCl pH 7.6, 1.5 mM $MgCl_2$, 0.5 mM EGTA, 500 mM KCl, 20 mM Imidazole, 0.1 % Igepal CA-630, 0.01 % β-ME, 10 % Glycerol, PI mix
Elution buffer	20 mM Tris-HCl pH 7.6, 1.5 mM $MgCl_2$, 0.5 mM EGTA, 500 mM KCl, 250 mM Imidazole, 0.1 % Igepal CA-630, 0.01 % β-ME, 10 % Glycerol, PI mix
In vitro buffer	20 mM Tris pH 7.6, 100 mM KCl, 1.5 mM $MgCl_2$, 0.5 mM EGTA, 10 % glycerol
Biosensor buffer	10 mM Tris pH 8.6, 1.5 mM $MgCl_2$, 100 mM KCl, 0.01 % Pluronic
PBS-T	PBS, 0.2 % Tween 20
Freezing solution	28 % glycerol, 3 % sorbitol (w/v), 0.65 % NaCl (w/v)
Thawing solution	0.9 % NaCl, 2 % dextrose
Synchronization solution	70 % Percoll (90 %), 20 % RPMI media, 1x PBS

PHEM buffer	30 mM PIPES pH 7.2, 2.5 mM $MgCl_2$, 35 mM KCl, 5 mM EGTA, 10 mM Hepes
Swelling buffer	20 mM HEPES pH 7.9, 10 mM KCl, 0.1 mM EDTA, 0.1 mM EGTA, 1 mM DTT, PIC
extraction buffer I	20 mM Hepes, 400 mM KCl, 1 mM EDTA, 1 mM DTT, PIC
extraction buffer II	20 mM Hepes, 800 mM KCl, 1 mM EDTA, 1 mM DTT, PIC
RIPA150 buffer	150 mM NaCl, 50 mM Tris-HCl pH 7.4, 1 mM EDTA, 1 % Igepal CA-630, PIC
RIPA50 buffer	50 mM NaCl, 50 mM Tris-HCl pH 7.4, 1 mM EDTA, 1 % Igepal CA-630, PIC
ChIP sonication buffer	50 mM Tris pH 8, 1% SDS, 10 mM EDTA, PIC
ChIP incubation buffer	12.5 mM Hepes pH 7.4, 0.6 % Triton-X100, 95 mM NaCl, 0.6 mM EDTA, 0.3 mM EGTA
ChIP wash buffer I	20 mM Hepes pH 7.4, 0.1% SDS, 0.1% DOC, 1% Triton-X100, 1 mM EDTA, 0.5 mM EGTA
ChIP wash buffer II	ChIP wash buffer I + 500 mM NaCl
ChIP wash buffer III	20 mM Hepes pH 7.4, 250 mM LiCl, 0.5% DOC, 0.5% Igepal CA-630, 1 mM EDTA, 0.5 mM EGTA
ChIP wash buffer IV	20 mM Hepes pH 7.41 mM EDTA, 0.5 mM EGTA
MNase digestion buffer	50 mM Tris pH 7.4, 4 mM $MgCl_2$, 1 mM $CaCl_2$, 0.075 % Igepal CA-630, 1 mM DTT, PIC
MNase stopping solution	2 % Triton-X100, 0.6 % SDS, 300 mM NaCl, 6 mM EDTA, PIC
18 % SPRI beads	0.3 % Sera-Mag beads, 18 % PEG-8000, 1 M, NaCl, 10 mM Tris-HCl pH 8.0, 1 mM EDTA, 0.05 % Tween-20, acc. to MT Gansauge, MPI

Table 7-5: Composition of media

Media	Composition (w/v)
LB_0 medium	1 % Bacto tryptone, 0.5 % Bacto yeast extract, 1 % NaCl
LB agar plates	LB medium, 2 % Agar
SOB medium	2 % Bacto tryptone, 0.5 % Bacto yeast extract, 0.05 % NaCl, 0.125 % KCl, 10 mM $MgCl_2$
Sf21 media	Sf900 II SFM
RPMI medium	RPMI 1640 with AlbuMAX-II, 2.5 mM L-glutamine, 25 µg/ml gentamycin
HeLa medium	DMEM with 10 % FBS
Toxoplasma medium	DMEM with 10 % FBS, 4 mM L-glutamate, 20µg/ml gentamicin

7.5 Kits

Table 7-6: Overview of used kits

Kit	Supplier
Phusion® High-Fidelity PCR Kit	Finnzyme
QIAEX® Gel extraction Kit	Qiagen
QIAprep Spin Miniprep Kit	Qiagen
Plasmid Plus Midi Kit	Qiagen
PureLink™HiPure Plasmid Maxiprep Kit	Invitrogen
DNeasy Blood and Tissue kit	Qiagen
Quick-RNA Whole Blood	Zymo Research
Monolith Protein Labeling Kit RED-NHS	Nanotemper technologies
BM Chemiluminescence Blotting Substrate (POD)	Roche
Amaxa™ P3 primary cell 4D-Nucleofector™ X Kit L	Lonza
EXTRACTME DNA CLEAN-UP MICRO SPIN kit	Blirt
High Sensitivity RNA ScreenTape Analysis	Agilent
High Sensitivity DNA ScreenTape Analysis	Agilent
NEBNext ultra II library prep kit	New England Biolabs
Illumina Stranded mRNA Prep Ligation	Illumina
Qubit dsDNA HS Assay Kits	Thermo Fisher
Cell Proliferation Kit II-XTT	Sigma

7.6 Nucleic acids

7.6.1 Oligonucleotides

Table 7-7: Overview of oligonucleotides

oligo	used for	Sequence (5' – 3')
0-NPS-for	NPS template generation	GATCCAGAATCCTGGTGCTGAG
6-NPS-for	NPS template generation	GGCCGCCCTGGAGAATC
29-NPS-for	NPS template generation	GTTATGTGATGGACCCTATACGC
40-NPS-for	NPS template generation	GCCCTTCTCGGGTTATGTGAT
60-NPS-for	NPS template generation	CCGCCAGTGTGCTGGAATTC
77-NPS-for	NPS template generation	ATCTTTTGAGGTCCGGTTCTTT
NPS-0-rev	NPS template generation	TAGCTGTATATATCTGACACATG (-Cy3/-Cy5)
NPS-47-rev	NPS template generation	GCGTATAGGGTCCATCACATAACC (-Cy5)
NPS-29-rev	NPS template generation	GTCGCTGTTCAATACATGCAC (-Cy5)
NPS-77-rev	NPS template generation	GTACAGAGAGGGAGAGTCACAAAAC (-Cy3/-Cy5)
20bp-DNA	DNA EMSA	TCTTAACGCGTGGACGATTCC -Cy5
25bp-DNA	DNA EMSA	TCTAACGCGTGGAATCGTCCCCTTG -Cy5
35bp-DNA	DNA EMSA	TGCGGAATCGTCTAACGCGTGGAATCGTCCCCTTG -Cy5
60bp-DNA	DNA EMSA	TGCGGAATCGTCTAACGCGTGGAATCGTCCGATTGAGGTCGCGATCTCGAATCACGGTGC -Cy5
Mut1	Mutagenesis KR + NTR	CAAATCATTTGTATATTAATTAAAATACTATA
Mut2	Mutagenesis KR + NTR	TTCAGCAGTGACCACAGCTC
Mut3	Mutagenesis KR	GGTTTGCAGTGTTCGACCCAGACC
Mut4	Mutagenesis KR	GTCTGGGTCGAACACTGCAAACCATC
Mut5	Mutagenesis NTR	GGGCATTCATTTTCAGACGTTGACCTGCCAGGAAGTGGGTATAACG
Mut6	Mutagenesis NTR	CGTCTGAAAATGAATGCCCAGATGAAAAGCTCCAAAAAAGGTCGCCATCGGAAGACCGAAAAAGAAGAGGATGAGGAGCTGCTGAAAGACGCC
Mut7	Mutagenesis *Pf*Snf2Lcore	CCAAG*CCATGG*ACCGTGCCC
Mut8	Mutagenesis *Pf*Snf2Lcore	CCTTCCAGG*GCATGC*TCAGTGATGATGGTGATGGTGGCTAGAATCCTCTTCATCCGTGC
Mut9	Mutagenesis *Hs*Snf2Lcore	CTCGAG*CCATGG*CCTAAATCTGAAAAGGAAATGGACCC
Mut10	Mutagenesis *Hs*Snf2Lcore	GGTACC*GCATGC*TCAGTGGTGATGGTGATGATGTAGAGAAGACTCTCCCATTTTTTGCAGG
Geno1	Genotyping *Pf*Snf2L	GCCAATGAATATTAATGGTACG
Geno2	Genotyping *Pf*Snf2L	GTTTTCCTTCTTCAATCTTGGC
Geno3	Genotyping *Pf*Snf2L	CGAATTCTCTTTTTTTAATCTAGG
Geno4	Genotyping *Pf*Snf2P	GAAAAAGTAAAACAACCATCCATTC
Geno5	Genotyping *Pf*Snf2P	CAAGATGTTCATCAACTTAGTC
Geno6	Genotyping *Pf*Snf2P	GTCACATAGAATGTTCATAAGC
Geno7	Genotyping	CGATTCTATTAACAAGGGTATC

7.6.2 Plasmids

Table 7-8: Overview of plasmids and sequences

Plasmid	Description	Resistance	Source
pFL	Polyhedrin and p10 gene promoter, MCS1 + 2	Amp	Imre Berger
pFL-*Pf*Snf2L	N-Flag *Pf*Snf2L aa250-1425 10xHis in pFL	Amp, Gem	Elisabeth Silberhorn
pFL-*Pf*Snf2L-KR	N-Flag *Pf*Snf2L-KR aa250-1425 10xHis in pFL	Amp, Gem	This work
pFL-*Pf*Snf2L-NTRmut	N-Flag *Pf*Snf2L-NTRmut aa250-1425 10xHis in pFL	Amp, Gem	This work
pFL-*Pf*Snf2Lcore	N-Flag *Pf*Snf2L aa246 - 843 6xHis in pFL	Amp, Gem	This work
pFL-*Hs*Snf2Lcore	*Hs*Snf2L aa79-715 6xHis in pFL	Amp, Gem	This work
pT11	Yeast rDNA	Amp	Joachim Griesenbeck
pUC18 12 x 601	12 repeats of 601 NPS sequence	Amp	Josef Exler
pPCRScript_slo1-gla75	dimeric nucleosome positioning sequence NPS1 with rDNA and hsp70 DNA flanking	Amp	Sloning BioTechnology
TOPO-II-1x601	Topo with 1x 601 NPS sequence	Kan	Elisabeth Silberhorn

pT2A-X-cKO	gGEM backbone with skip peptide T2A followed by Neomycin resistance gene, loxP site, gfp gene and PbDT terminator, additional hDHFR gene under *Pf*CAM promoter	Amp	Birnbaum et al. 2017
pT2A-Snf2L-cKO	*Pf*Snf2L-KO plasmid: pT2A-X-cKO with *Pf*Snf2L-homology box, artificial intron with loxP site, recodonized C-terminus, 3x HA tag	Amp	This work
pT2A-Snf2P-cKO	*Pf*Snf2P-KO plasmid: pT2A-X-cKO with *Pf*Snf2P-homology box, artificial intron with loxP site, recodonized C-terminus, 3x HA tag	Amp	This work

7.7 Enzymes and polypeptides

7.7.1 Peptides, Proteins and Enzymes

Table 7-9: Overview of peptides, proteins and enzymes

Peptide / Protein / Enzymes	Source
Histone H4 (8-25-WC)	AnaSpec
Gg octamers	Purified from chicken erythrocytes
Bt octamers	Purified from calf thymus
Hs octamers	recombinant, Elisabeth Silberhorn
Hs octamers H4dNaa1-24	recombinant, Elisabeth Silberhorn
Pf canonical octamers	recombinant, Elisabeth Silberhorn
Pf variant octamers H2A.Z/B.Z	recombinant, Elisabeth Silberhorn
Benzonase	Sigma Aldrich
DNaseI	New England Biolabs
Exonuclease III	New England Biolabs
Micrococcal nuclease	Worthington Biochemicals Corporation
Phusion® DNA polymerase	Finnzyme
Proteinase K	Sigma / ZymoResearch
Q5 High-Fidelity DNA Polymerase	New England Biolabs
Restriction enzymes	New England Biolabs
T4 DNA ligase	New England Biolabs
Taq Polymerase	Elisabeth Silberhorn
TMR-maleimide-labeled ParM	Elisabeth Silberhorn

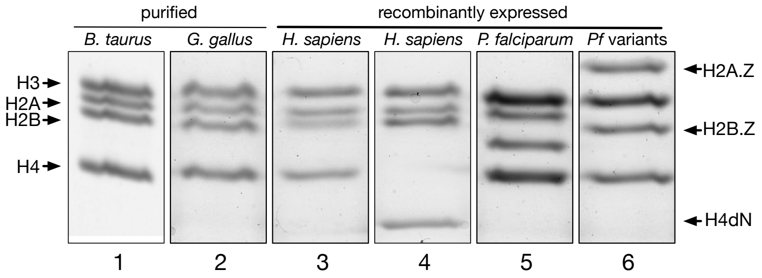

Figure 7-1: Purified and recombinant histone octamers. *1 µg of all used octamers were separated in a 17 % SDS gel and the gel was stained with coomassie blue. Names and positions of individual histones are indicated.*

7.7.2 Antibodies and dyes

Table 7-10: Overview of antibodies

Antibodies/Dye	dilution	Source
rat anti-HA, monoclonal (clone3F10)	IFA (1:500), WB (1:2000)	Roche, cat11867423001
mouse anti-Enolase	WB (1:1000)	Prof GK Jarori, TIFR
rabbit anti-Gap45	IFA (1:500),	Jones et al. 2006
rabbit anti-Ama1	IFA (1:500),	Collins et al. 2009
mouse anti-RESA	WB (1:20000)	Robin Anders, La Trobe University
rabbit anti-Rex1	WB (1:50000)	Dr. T Spielmann, BNITM
rabbit anti-Rex3	IFA (1:500), WB (1:5000)	Dr. T Spielmann, BNITM
rabbit anti-SBP1	IFA (1:2000), WB (1:5000)	Dr. T Spielmann, BNITM
mouse anti-Mahrp1	IFA (1:2000), WB (1:5000)	Dr. N Brancucci, SwissTPH
Goat anti-Mouse IgG (H+L) Alexa Fluor 488	IFA (1:1000)	Thermo Fisher, A11001
Goat anti-Rat IgG Alexa Fluor 488	IFA (1:1000)	Thermo Fisher, A11006
Goat anti-Rabbit IgG Alexa Fluor 488	IFA (1:1000)	Thermo Fisher, A32731
Abberior STAR 580, goat anti-mouse IgG	IFA (1:1000)	Abberior ST580-1001
Abberior STAR 580, goat anti-rabbit IgG	IFA (1:1000)	Abberior ST580-1002
Abberior STAR 635P, goat anti-mouse IgG	IFA (1:1000)	Abberior ST635P-1001
Abberior STAR 635P, goat anti-rabbit IgG	IFA (1:1000)	Abberior ST635P-1002
IRDye680RD Donkey anti-Rabbit IgG	WB (1:10000)	LI-COR Biosciences, 925-68073
IRDye800CW Donkey anti-Mouse IgG	WB (1:10000)	LI-COR Biosciences, 925-32212
IRDye800CW Goat anti-Rat IgG	WB (1:10000)	LI-COR Biosciences, 925-32219
Goat IgG anti-Rat IgG (L)-HRPO	WB (1:10000)	Dianova, 112-035-175
Phalloidin-iFluor 594 Reagent	0.1x	Abcam, ab176757

7.8 Organisms

Table 7-11: Overview of prokaryotic and eukaryotic cell lines

Cell line	Description
E. coli DH5alpha	*Escherichia coli* cell line for plasmid propagation
E. coli XL1 blue	*Escherichia coli* cell line for plasmid propagation, blue/white screening
E. coli DH10Bac EM YFP	*Escherichia coli* cell line for baculovirus propagation
Sf21	Insect cell line (*Spodoptera frugiperda)* for protein expression
3D7	Parasite cell line (*Plasmodium falciparum)*
3D7-DiCre	DiCre-expressing 3D7 parasite line
3D7-*PfSnf2L-HA-cKO*	3D7-DiCre line with *Pf*Snf2L endogenous tag, conditional KO system
3D7-*PfSnf2P-HA-cKO*	3D7-DiCre line with *Pf*Snf2P endogenous tag, conditional KO system
*Tg*RHΔHX	*Toxoplasma gondii* tachyzoites, RHΔHX
HFF-1	human foreskin fibroblasts - ATCC, SCRC-1041
HeLa cells	Human cervical carcinoma cells - ATCC, CCL-2

7.9 Experimental procedures

7.9.1 Phylogenetic analysis and multiple sequence alignments

The core helicase-like regions were trimmed according to Flaus et al. spanning from 50 amino acids N-terminal to helicase motif I to 50 amino acids C-terminal of helicase motif VI. Exact regions of individual CREs used for phylogenetic analysis are listed in Appendix 2. Phylogenetic trees were generated using *Geneious Tree Builder* (Geneious software 11.1.5*)*: Global alignment with free end gaps, Blosum62 as Cost Matrix, Jukes-Cantor Distance Model, Method Neighbor-Joining, Gap open penalty 10 and Gap extension penalty 0.2. For multiple sequence alignments, *Geneious Alignmen*t was used with the same parameters, but Gap open penalty 20 and 5 refinement iterations. Pairwise identity within and between Metazoa/Apicomplexa was calculated from multiple sequence alignments and kernel smoothing with a bandwidth of 80 was applied.

7.9.2 Working with DNA

Preparation of DNA - amplification of plasmids in *Escherichia coli* bacteria, purification, concentration determination, restriction enzyme digestion, ligation of DNA fragments, analysis of DNA on agarose and polyacrylamide gels, and amplification of the DNA by the polymerase chain reaction (PCR) - was performed according to the standard protocols (Sambrook and Russell, 2001).

DNA amplification

For amplification, chemically competent DH5alpha cells were heat-shock transformed with purified plasmid DNA or ligation reaction (5 min on ice – 1 min at 42 °C – 5 min on ice). After 30-60 min in LB_0 media, transformed cells were grown over night on agar cell containing the respective antibiotics at 37 °C (ampicillin – 100 µg/ml, kanamycin – 50 µg/ml, gentamycin – 10 µg/ml, tetracyclin 12.5 µg/ml). Cultures inoculated with a single colony from agar plates was grown over night at 37 °C in selective media and plasmid DNA was purified using the Plasmid Prep Kits from Qiagen (Mini, Midi) or Invitrogen (Maxi) according to manufacturer's recommendations. Amplification of linear fragments was performed with three-step PCR optimized for the respective application. Composition and protocols are specified in the respective section.

DNA purification

For purification, DNA was precipitated by addition of 0.5 reaction volumes 7.5 M ammonium acetate (pH 7.8), 2 µg glycogen and 0.8 volumes of isopropanol or 2 volumes of 100 % ice-cold EtOH. DNA was precipitated (30 min, 4 °C, 13000 g) and washed twice with 70 % EtOH.

DNA was eluted generally with TE buffer and stored at – 20 °C, concentration and purity were determined by absorbance measurement using a NanoDrop ND1000 spectrometer or Qubit Fluorometer.

Agarose gel electrophoresis

DNA fragments were analyzed by agarose gel electrophoresis using 0.8-2 % agarose gels in 1x TBE buffer, supplemented with 0.01 % SYBR Safe. Gels were run in 1 x TBE under constant voltage of 100-120 V and scanned with UV light for visualization. Isolation of DNA fragments from agarose gels was performed using the Qiagen Gel Extraction Kit.

Native polyacrylamide gel electrophoresis

For DNA and nucleosome analysis, native polyacrylamide gel electrophoresis (PAGE) was performed in 0.4x TBE and at 100 V. Prior to the run, the gel was pre-run for 20-30 min at 60-80 V. For visualization of unlabeled DNA, the gel was stained in 0.4x TBE containing ethidium bromide (0.75 µg/ml) for 15 min and washed twice with water. Stained gels were scanned with a UV transilluminator, and gels with fluorescently labeled DNA were scanned with the Typhoon FLA-9500.

7.9.3 Working with proteins

Proteins were purified and analyzed according to standard protocols (Sambrook and Russell, 2001). In general, proteins were stored at -80 °C and kept on ice before starting an experiment. Protein concentrations were determined using the colorimetric assay described by Bradford (Bradford, 1976).

SDS-polyacrylamide gel electrophoresis

SDS-polyacrylamide gel electrophoresis (SDS-PAGE) was used to determine quality and quantity of proteins. For recombinant proteins, 6 – 17 % SDS polyacrylamide gels were prepared in gel cassettes with separating gel and stacking gel (Table 7-12). Protein samples were mixed with Laemmli buffer, heat-denatured at 95 °C for 5 min and loaded onto the gel together with a protein ladder. Proteins were separated at 40 mA for 30-60 min using SDS running buffer. Parasite extracts and pulldown samples were heat-denatured in OrangeG SDS loading buffer (similar principle as Laemmli buffer) and separated on 4-20 % gradient SDS gels at 160 V. Proteins were stained with Coomassie staining solution for 15 min and de-stained by multiple wash steps in water. For alternative silver staining, gels were fixed in fixing solution for 1 h, incubated in 50 % EtOH for 20 min and washed twice with water. After 15 min incubation in freshly prepared staining solution A, the gel was rinsed with water and incubated in staining solution B until proper staining was visible. After rinsing in water, reaction was stopped by incubation in stop solution for 10 min.

Table 7-12: Composition of SDS gels

Reagent	5 % stacking	6 % separating	17 % separating
Acryl-Bisacrylamide (30 % / 0.8 %)	0.25 ml	1.2 ml	3.4 ml
H_2O	0.87 ml	3.26 ml	1.06 ml
4 x lower Tris buffer		1.5 ml	1.5 ml
4 x upper Tris buffer	0.38 ml		
20 % ammonium persulfate	7.5 µl	30 µl	30 µl
TEMED	1.5 µl	6 µl	6 µl

Western blot analysis

For western blot analysis, SDS-PAGE separated proteins were transferred onto a nitrocellulose membrane prior to immunoblotting. After membrane activation for 5 min in MeOH, the membrane and the unstained gel were equilibrated in transfer buffer for 20 min. Between two layers of Whatman paper, protein transfer from gel to membrane was performed for 90 min at 400 mA in a wet-tank system. After 1 h blocking in 5 % skim milk in PBS-T, the membrane was incubated with primary antibody in 5 % milk for 1-3 h at room temperature. After three washes in PBS-T, 1 h incubation with secondary antibody in PBS-T followed, before the membrane was washed three times in PBS-T and PBS again. Fluorophore-conjugated immunoblotting was visualized with the Odyssey imaging system, HRP-conjugated antibodies with the LAS-3000 reader using the BM chemoluminescence Kit according to manufacturer's recommendations.

7.9.4 Cloning of DNA constructs

Cloning and mutagenesis for recombinant CRE-expression

*Pf*Snf2L (aa250-1426) was sequence-optimized with the addition of a C-terminal 10xHis-Tag, ordered as a synthetic gene (IDT), and cloned into pFL plasmid by Elisabeth Silberhorn. CRE mutants – *Pf*Snf2L-KR and *Pf*Snf2L-NTRmut – were generated by site directed mutagenesis following an overlapping PCR strategy. In a first round of PCR, two fragments were amplified with primers introducing the respective mutation (KR: Mut1+Mut3, Mut2+Mut4; NTR: Mut1+Mut5, Mut2+Mut6). In a second PCR step, both amplified and purified fragments were combined and overlapped using the flanking primers Mut1+Mut2. The obtained product was precipitated, digested with AgeI/NheI, and eluted from agarose gels. Subsequently, it was ligated in the accordingly digested pFL-*Pf*Snf2L plasmid according to manufacturer's recommendation.

*Pf*Snf2L and *Hs*Snf2L truncations were generated by PCR using primers Mut7+Mut8 and primers Mut9+Mut10, respectively. After purifying the obtained DNA fragments via EtOH precipitation, they were digested with SphI/NcoI, as were pFL-*Pf*Snf2L and pFL. All required fragments were eluted from agarose gel and the *Pf*Snf2L-truncation fragment was ligated into pFL-*Pf*Snf2L, *Hs*Snf2L-truncation fragment was ligated into pFL. Correct mutagenesis was verified by DNA sequencing. Mutagenesis PCR was performed using the Phusion High-Fidelity PCR Kit and adjusted from following protocol (Table 7-13):

Table 7-13: Composition and protocol of PCR reaction for CRE mutagenesis PCR

Reagent	Concentration	Cycle step	Temp	Time	Cycles
Oligos	0.25 µM	Initial denaturation	90 °C	5 min	
dNTP	200 µM	denaturation	90°C	15-30 sec	
Template	100 ng	annealing	54-56 °C	60 sec	30
Phusion	0.02 U/µl	elongation	72 °C	30-120 sec	
1x Phusion buffer	Ad 50 µl	Final elongation	72 °C	5 min	

Cloning of conditional knockout constructs

Two synthetic genes comprising the native nucleotides 995-1894 (PF3D7_1104200) / 2640-3649 (PF3D7_0216000), an artificial intron with loxP site, nucleotides 1895-4278 (PF3D7_1104200) / 3650-5992 (PF3D7_0216000) recodonized and a 3xHA-tag encoding sequence were ordered as synthetic gene (IDT). Digestion with NotI/SalI allowed ligation into the accordingly digested vector pT2A-X-cKO. The resulting plasmids pT2A-Snf2L-cKO/ pT2A-Snf2P-cKO were verified by sequencing.

7.9.5 Preparation of *in vitro* tools

Nucleosome template preparation

DNA templates for mononucleosome assembly were synthesized by PCR. If required, plasmid DNA was digested with restriction enzymes prior to PCR amplification according to manufacturer's recommendation and verified by 1 % agarose gel electrophoresis. PCR was performed with oligonucleotides – optionally labeled with Cy3-/Cy5 – annealing to flanking regions of 147 bp nucleosome positioning sequence (NPS), creating various linker lengths (Table 7-15). Nucleosome template PCR was performed using a lab-made *Thermus aquaticus* (Taq) polymerase and was adjusted for each reaction from following protocol (Table 7-14):

Table 7-14: Composition and protocol of PCR reaction for nucleosome template generation

Reagent	Concentration	Cycle step	Temp	Time	Cycles
Oligos	0.25 µM	Initial denaturation	95 °C	5 min	
dNTP	200 µM	denaturation	95°C	20-40 sec	
Template	1-100 ng	annealing	50-60 °C	20-60 sec	20-30
Labmade Taq	0.02 U/µl	elongation	72 °C	30-60 sec	
1x Taq buffer	Ad 50 µl	Final elongation	72 °C	5 min	

To purify amplified DNA, it was precipitated with isopropanol and purity was ascertained by native PAGE.

Table 7-15: Primer and PCR template used for nucleosome template generation

	Forward primer	Reverse Primer	PCR template
0-NPS-0	0-NPS-for	NPS-0-rev	pPCRScript_slo1-gla75 BglII digested
6-NPS-47	6-NPS-for	NPS-47-rev	pUC18 12x601 NotI digested
29-NPS-0	29-NPS-for	NPS-0-rev	TOPO-II-1x601
40-NPS-0	40-NPS-for	NPS-0-rev	TOPO-II-1x601
60-NPS-0	60-NPS-for	NPS-0-rev	TOPO-II-1x601
29-NPS-29	29-NPS-for	NPS-29-rev	pUC18 12x601 AvaI digested
77-NPS-77	77-NPS-for	NPS-77-rev	pPCRScript_slo1-gla75 BglII digested

Nucleosome reconstitution

Recombinant histones - canonical *Hs/Pf* and variant *Pf* (containing H2A.Z/B.Z) - were expressed, purified and refolded by Elisabeth Silberhorn as previously described (Silberhorn et al., 2016). *Bt* and *Gg* octamers were purified from calf thymus, or chicken blood respectively, as described in (Laybourn and Kadonaga, 1991; Maldonado et al., 2019). Nucleosome assembly was performed via gradient dialysis: Appropriate ratios of histone octamer : DNA were mixed in 40-200 µl high salt buffer supplemented with 200 ng/µl BSA and placed into small dialysis chambers. Starting in a beaker with 300 ml high salt buffer, salt concentration was slowly reduced by pumping in 3 l of low salt buffer. Reconstituted mononucleosomes were analyzed by gel electrophoresis, using 6 % polyacrylamide 0.4 x TBE gels and visualized by fluorescence scanning or ethidium bromide staining. Reconstituted nucleosome arrays on pT11 plasmid DNA were analyzed on a 0.8 % agarose gel and stained with ethidium bromide. Nucleosomes were stored at 4 °C.

Protein expression in insect cells

Chemically competent DH10Bac EM YFP cells were transformed with the respective pFL plasmid and cultured overnight at 37 °C in SOB medium. Distribution on $\text{LB}_{\text{amp, tet, gent, X-Gal-IPTG}}$ plates enabled the selection of positive clones by blue-white screening, which was verified by colony PCR. Bacmid DNA was isolated from one positive clone grown in 2 ml $\text{LB}_{\text{amp, tet, gent, X- Gal-IPTG}}$ using step 1-5 of the Qiagen Plasmid Miniprep kit and subsequent isopropanol precipitation. Bacmid DNA was dissolved in sterile water and used for transfection of *Spodoptera frugiperda* Sf21 cells.

Sf21 cells were grown as suspension cells without any antibiotic selection in Sf900 II media at 27 °C under rotation (100 rpm). For optimal growth, the cell density was adjusted once a day to remain between 0.5 - 2 x 10^6 cells/ml. 2/3 of the isolated bacmid in 220 µl media was incubated for 10 min with pre-mixed 10 µl X-tremeGENE solution in 100 µl media. This solution was added in duplicates to 10^6 cells in six-well plates and incubated for 48 h without shaking before changing media. Transfection efficiency was checked microscopically by YFP expression and thus, green fluorescence. 96 h after transfection, supernatant was harvested as initial virus V_0 and further propagated to obtain a higher virus titer.

3 x 50 ml Sf21 cultures with 0.6 x 10^6 cells/ml were infected with 10/50/250 µl V_0 and incubated for two more days after they reached growth arrest. V_1 containing supernatant was harvested and stored at 4 °C. In the case of *Hs*Snf2L, pre-prepared baculovirus V_1 encoding the CRE with an N-terminal 6xHis tag was used (LV#068, Josef Exler). The optimal virus amount and harvesting timepoint for protein expression was determined in a test expression. Levels of recombinant protein in cell pellets were analyzed by SDS-PAGE. Determined infection conditions were used for large-scale expression of 200-800 ml Sf21 cultures and cell pellets were snap frozen in liquid nitrogen and stored at -80 °C.

Protein purification

During protein purification, all steps were performed at 4 °C and buffers and solutions were pre-chilled on ice. Pellets of ~10^9 cells were resuspended in 10 ml lysis buffer, sonified with the Branson Sonifier 150D using the small tip (50% duty cycle/level 4, 5x 15'' on/off) and centrifuged (30 min, 4 °C, 10000 rpm). The supernatant was incubated with equilibrated Ni-NTA beads (150 µl slurry volume) and agitated on a rotating wheel for three hours. Beads were pelleted (5 min, 4 °C, 200 rpm), 90 % of the supernatant was discarded and the rest was loaded with the beads onto a 1 ml mini column. Solvent was allowed to flow through by gravity and beads were washed with a total of 8 column volumes of wash buffer in multiple washing steps. For elution of recombinant proteins, beads were incubated three times with 80 µl elution buffer for 30 min and elution fractions were collected. Purity was analyzed by SDS-PAGE, appropriate fractions were pooled, and protein concentration was determined. Protein aliquots were snap-frozen and stored at -80 °C.

7.9.6 *In vitro* functional assays

Nucleosome binding and remodeling assays

Electromobility shift assays (EMSAs) were performed by incubating *in vitro* reconstituted nucleosomes in 10 µl in-vitro buffer supplemented with 200 ng/µl BSA for 60 min at 30 °C in absence/presence of recombinantly expressed CRE (0.02-1.5 µM). Competitive binding assays used 15-20 nM of each nucleosome, non-labeled binding assays used 120 nM nucleosome, chromatin EMSAs used 2 µg *in vitro* reconstituted chromatin and DNA EMSAs used 20 nM of each DNA. Nucleosomes were analyzed by 6 % native PAGE and visualized by fluorescence scanning or ethidium bromide staining.

Remodeling assays were performed accordingly in absence and presence of 1 mM ATP. Reactions were stopped after 60 min (unless otherwise noted) by addition of 1 µg competitor plasmid DNA and nucleosome positions were analyzed via 6 % native PAGE.

For concentration-dependent inhibition analysis, the described assay was performed in presence/absence of hit compounds at various concentrations (16-600 µM).

For quantitative analysis of the EMSA, band intensity of the unbound nucleosome was quantified, corrected for background, and normalized to maximum signal. Remodeling activity was quantified by dividing the initial band intensity by the total nucleosome band intensity (= non-remodelled nucleosome fraction).

End point ATPase assay

ATPase activity was analyzed by incubation of CRE (130-700 nM) in in-vitro buffer together with 500 µM ATP and 0.2 µCi ^{32}P-γ-ATP for 40 min at 30°C. Potential stimulation was addressed by adding mononucleosomes various compositions (60-350 nM), nucleosomal array (*Bt*-oct on 100 ng pT11), pT11 DNA + H4 tail peptide (100 ng + 5 µM), plasmid or linear DNA (100-200 ng), H4tail (5 µM), En3 RNA (30 ng). ATP hydrolysis was previously tested to be independent of substrate amounts as well as nucleosome composition – octamer of different organisms and DNA sequence. The assay was performed in three technical replicates and chemical ATP hydrolysis was measured in a control sample without CRE. After incubation, released ^{32}P-γ phosphate was separated from non-hydrolyzed ^{32}P-γ-ATP by thin layer chromatography on PEI-Cellulose F plates [mobile phase: 50% acetic acid, 0.5 mM LiCl]. A phosphor screen was exposed to the dried plate for 16 h, then scanned and signal intensities were quantified. The hydrolysis rate (P_i/total) was calculated, corrected for chemical hydrolysis. For comparison of different CREs, it was normalized to protein concentration. For stimulation analysis, the fraction of maximal hydrolysis (x/max) or stimulation factor (x/non-stimulated) was calculated.

ATPase kinetic assay

ATPase kinetics of CREs were measured using 0.2 µM TMR-maleimide-labeled ParM and 125 µM ATP in 20 µl biosensor buffer. 0.4 µM *Pf*Snf2L/*Hs*Snf2L were analyzed in duplicates in absence/presence of substrates (50 ng DNA + 2.5 µM H4 tail per reaction). Immediately after mixing in a glass-bottom µCLEAR microplate, fluorescence measurement was started in a Tecan plate reader at 2 min intervals for 120 min at 28 °C. ATP-induced background fluorescence was measured kinetically in absence of ATPase and used for fluorescence curve correction. For quantification of ATPase rate, the linear segment of normalized fluorescence was analyzed with simple linear regression.

For titration of reaction components, the fluorescence enhancement factor was calculated as $\text{fluo}_{\text{end}}/\text{fluo}_{\text{start}}$. For concentration-dependent inhibition analysis, the described assay was performed in presence/absence of lead compound in varying concentrations (3-100 µM). Signal was additionally normalized to timepoint 0 to account for compound autofluorescence.

7.9.7 Culturing and transfection of parasites

P. falciparum parasites were cultured according to standard procedures in human red blood cells (RBCs) in RPMI 1640 with Albumax supplemented with L-glutamine and gentamycin under oxygen-reduced conditions (1 % O_2, 5 % CO_2, 94 % N_2) at 37 °C. Prior to infection, human blood was sedimented (7 min, 4 °C, 2630 g), plasma and leukocytes were removed, and red blood cells were washed with cold media and stored at 4 °C for up to 4 weeks. Parasites were maintained in culture with a hematocrit of 1-5 % and with parasitemia below 5 %. Media was changed at least every 72 h and parasitemia was regularly monitored in thin blood smears on Microscope slides stained with Giemsa (3 sec in MeOH, 3 sec in Hemacolor red, 30 sec in Hemacolor blue). Transgenic parasites expressing hDHFR are cultured constantly in media containing WR99210 (2.5 nM). For parasite freezing, 350 µl of blood containing mainly ring stage parasites was added to 700 µl freezing solution and stored in liquid nitrogen. For thawing, 100 µl 12 % NaCl was added to the vial, before slowly adding 5 ml 1.6 % NaCl and then 5 ml thawing solution. Infected cells were sedimented (by default 3 min, 21 °C, 695 g) and transferred to a new culture with 200 µl fresh blood. Media was changed daily for three days, before respective drug was supplemented.

Synchronization of parasites

Tight synchronization of parasites was adapted from (Blackman, 1995): 10 ml prewarmed synchronization solution was overlaid with a culture of predominantly late stages (~2 ml blood in 7.5 ml) and centrifuged (11 min, 22 °C, 260 g). The interface containing schizonts was washed with media and then incubated for 1-2 h with new 2 ml red blood cells in 50 ml media under agitation. Subsequently, another round of Percoll gradient centrifugation was performed as described and the remaining schizonts in the interface were removed. Infected RBCs were treated with 8 ml 5 % sorbitol at 37 °C for 10 min in order to lyse late-stage parasites and washed with media before being returned to culture.

Transfection of parasites

For transfection of parasites (Amaxa™ P3 primary cell 4D-Nucleofector™ X Kit), 20 µg DNA in 100 µl of the supplied transfection solution P3 was added to purified schizonts. The mixture was transferred into a Lonza cuvette and transfection was initiated (pulse code: FP158). Schizonts were rapidly returned to 2 ml prewarmed culture with 15 % hematocrit and agitated for 45 min. Then, media was added and changed for new WR99210-containing media for the next three days to select for successful transfection. Once resistant parasites were established, after 2-3 weeks, they were cryopreserved in liquid nitrogen and further selected for genomic integration with G418 (400 µg/ml for *Pf*Snf2L-cKO, 200 µg/ml *Pf*Snf2P-cKO parasites). Individual clones were isolated using limiting dilution of drug-resistant parasites (Thomas et al., 2016). A culture with 1 % parasitemia was diluted 1:400 in well A1 of a 96-well plate. The parasites were diluted row-wise and column-wise 1:5 in media with RBCs to statistically obtain single or no parasites per well. The number of parasites per well was estimated based on plaque formation and individual clones were picked and returned to culture.

Parasite genotyping

For genotyping of transgenic parasite clones, genomic DNA was isolated using the DNeasy Blood and Tissue kit. Genotyping PCR was performed with Q5 DNA Polymerase and the respective primers (*Pf*Snf2L-integrant: Geno1+Geno2, *Pf*Snf2L-wildtype: Geno1+Geno3, *Pf*Snf2L-KO: Geno1+Geno7, *Pf*Snf2L-integrant: Geno4+Geno5, *Pf*Snf2L-wildtype: Geno4+Geno6, *Pf*Snf2L-KO: Geno4+Geno7) adjusted from following protocol (Table 7-16):

Table 7-16: Composition and protocol of PCR reaction for genotyping

Reagent	Concentration	Cycle step	Temp	Time	Cycles
Oligos	0.25 µM	Initial denaturation	94 °C	1 min	
dNTP	200 µM	denaturation	94 °C	15 sec	25-30
gDNA	100 ng	annealing	52 °C	15 sec	
Q5-pol	0.02 U/µl	elongation	68 °C	60-120 sec	
1x Q5 buffer	Ad 25 µl	Final elongation	68 °C	5 min	

Amplification of genotyping fragments was analyzed via agarose gel electrophoresis.

7.9.8 Parasite fractionation

For fractionation, ~10^9 infected RBCs containing mixed parasite stages were harvested (3 min, 4 °C, 695 g) and resuspended in 0.1% saponin in PBS with PIC for RBC lysis. After 5 min, parasites were separated by centrifugation (10 min, 4 °C, 5000 g) and washed in PBS+PIC. For preparation of nuclei, parasites were resuspended in swelling buffer and incubated 15 min on ice. IGEPAL 630 was added to a final concentration of 0.65 % and after 1 min on ice, nuclei were pelleted (10 min, 4 °C, 2500 g). The cytoplasm fraction was collected, and nuclei were washed with swelling buffer. Nuclei were then treated with 50 U DNaseI in 250 µl supplied DNaseI buffer for 10 min at 37 °C, before the reaction was stopped with 5 mM EDTA. After centrifugation (10 min, 4 °C, 2500 g), the supernatant containing soluble molecules was collected as nucleoplasm fraction. The pellet was washed again with 250 µl swelling buffer (wash fraction). Hardly soluble proteins were released with 250 µl extraction buffer I for 1 h under constant agitation at 4 °C and separated by centrifugation (30 min, 4 °C, 5000 g). Another extraction step followed with extraction buffer II accordingly. Insoluble proteins were extracted with 2 % SDS in 10 mM Tris-HCl, pH 8.0 for 30 min rotating at 4 °C (5 min, 4 °C, 13000 g). All fractions were collected and 10 % was analyzed by SDS-PAGE. Remaining samples were stored at -80 °C for downstream analysis.

As an alternative to DNaseI treatment, nuclei were treated with 50 U benzonase in RIPA150 buffer for 10 min at room temperature. For nuclear protein extraction, KCl was added to 0.4 M, incubated for 30 min at room temperature and insoluble fraction was removed by centrifugation (30 min, 4 °C, 5000 g).

7.9.9 KO induction and phenotyping of parasite reproduction

KO induction

One clone per transgenic parasite line verified by genotyping PCR was used for further phenotyping. Conditional DiCre-mediated recombination between loxP sites was induced as described (Collins et al., 2013). Asynchronous or tightly synchronized parasite cultures were split in half and incubated for 4 h in media containing 100 nM rapamycin or 0.2 % DMSO, respectively. After washing with media, they were returned to drug-free culture. Gene excision was confirmed 24 / 48 h after KO induction by genotyping PCR (7.9.7). For *Pf*Snf2L, efficient knockout was also verified on mRNA level by RNA sequencing (7.9.13) and on protein level by western blot. Therefore, infected RBCs were pelleted and lysed with 0.1 % saponin as described (7.9.8). Parasites were heat-denatured and whole cell extract was analyzed by SDS-PAGE and subsequent immunoblotting (7.9.3).

Parasite growth assay

Parasite growth was determined by microscopic counting of parasites from Giemsa-stained thin blood films and expressed as percentage parasitemia (% infected RBCs/RBCs). At least 5000 erythrocytes were counted per sample and parasite growth was quantified in at least two biological replicates. Growth was monitored continuously after KO induction for *Pf*Snf2L-cKO parasites and correspondingly for 3D7 parasites with persistent drug-treatment.

Parasite reproduction

Equal numbers of mature schizonts from DMSO/rapamycin-treated cultures were Percoll-purified. They were resuspended in media containing 1 % hematocrit and cultured for 2 h at 37 °C. Parasitemia of newly invaded rings was subsequently quantified by microscopy of Giemsa-stained thin blood films. At least 100 parasites were counted per sample and reproduction rate was quantified in two biological replicates.

Quantification of nuclei

The number of nuclei was quantified by microscopy of DAPI-stained parasites. Parasites at schizont stage (~46 hpi) were fixed as described for IFA (7.9.10) and mounted in DAPI-containing mounting solution. A Leica DMi8 Widefield microscope was used for imaging and counting the number of visible nuclei per parasite, as least for 100 parasites per sample. The exact number of nuclei was visualized or binned in 1-2 / 3-8 / 9-15 / >16 nuclei. Reproduction was quantified for *Pf*Snf2L-cKO parasites upon KO induction and correspondinglyfor 3D7 parasites with persistent drug-treatment.

7.9.10 Imaging assays for phenotyping of cellular structures

Live imaging of parasite egress

Live imaging of parasite egress was performed as described (Das et al., 2017). Therefore, equal numbers of mature schizonts from DMSO/rapamycin-treated cultures were Percoll-purified. For further maturation under prevention of egress, schizonts were incubated for 2-3 h in media supplemented with 2 µM compound2. Compound2 is a specific protein kinase PKG inhibitor that prevents parasite rupture (Taylor et al., 2010). Compound2 was washed off prior to video microscopy, and schizonts were immediately resuspended in warm media and placed into a glass bottom microscopy chamber. The chamber was transferred to a temperature-controlled microscope stage at 37 °C on a Leica DMi8 Widefield microscope. Images were routinely collected in DIC channel at 3.5 sec intervals, beginning 6 min after compound2 was washed off, for a total of 20 min. Parasites were classified as “normal egress” or “clustered merozoites” 15 sec post red blood cell rupture. For analysis of the host cell cytoskeleton, the assay was performed accordingly using media supplemented with 0.1x phalloidin 594 Conjugate during live imaging. Staining of RBC actin could be monitored by additional image acquisition in the fluorescence channel. RBC ghost location was categorized as “distant ghost”, “merozoites attached” or “complete overlap” 40 sec after egress start. Egress videos were collected in three technical replicates, alternating noKO and iKO, and at least two biological replicates.

Immunofluorescence assays (IFA)

For immunofluorescence assay, thin smears of infected red blood cells or purified schizonts were prepared on glass slides. After drying and framing with a hydrophobic pen, parasites were fixed for 30 min in 4 % PFA/0.0075 % glutaraldehyde in PBS. Cells were permeabilized with 0.1 % Triton-X100/PBS for 10 min, washed and blocked for >1 h in 4 % BSA/PBS. Antigens were labeled with 60-100 µl suitable primary antibodies in 4 % BSA/PBS as listed in Table 7-10 overnight in a humidity chamber at 4 °C. After washing in PBS, 60-100 µl secondary fluorophore-conjugated antibody diluted in 4 % BSA/PBS was applied onto the cells. After 45-60 min in a light-protected humidity-chamber, slides were washed in PBS and dried. DAPI-containing mounting solution was added, a cover glass was placed onto the cells and sealed. IFA slides were stored at 4 °C until imaging. For image acquisition, Leica DMi8

Widefield microscope with the respective fluorescence channels and LasX software was used. Image processing and quantification was performed with software ImageJ2 v2.9.0. All images presented are representative; all IFAs were repeated at least twice with similar results. It should be noted that the transfected construct in *Pf*Snf2L-HA-cKO generation contains a GFP-encoding gene. However, no endogenous GFP fluorescence was detectable in an IFA experiment without antibody (data not shown). Therefore, all detected signals can be attributed to used fluorophore-conjugated antibodies.

For quantification of IFA images, parasite contours were automatically detected with a customized ImageJ Macro using an enlarged mask based on the DAPI signal. Within the obtained mask, the total signal intensity was measured in all channels. All images and all channels were corrected for background signal from a manually selected blank region. Where schizont parasites are analyzed, a minimal DAPI signal was set by visual inspection to exclude early-stage parasites with fewer nuclei. Where noKO and iKO parasites were mixed, anti-HA signal was used to assign individual parasites to noKO or iKO. Based on the intensity distribution, a threshold was chosen that best separated the two populations. Automatically detected parasites were manually checked.

Transmission Electron Microscopy (TEM)

iRBCs were washed in PHEM buffer and fixed for 1 hour in a solution containing 2.5 % glutaraldehyde, 4 % formaldehyde, 4 % sucrose in 0.1 M PHEM buffer.

All further steps were performed by Andreas Klingl (LMU) and colleagues: Cells were postfixed in 1 % OsO_4 plus 0.8 % ferrocyanide and 5 mM $CaCl_2$ in 0.1 M cacodylate buffer for 1 hour, washed twice in cacodylate buffer (10 min, 1 h) and double-distilled water (5 min, 15 min), respectively and dehydrated in a graded acetone series which included *en bloc* staining with 1 % uranyl acetate in the 20 % step. The cells were finally embedded in Epon812 epoxy resin to enable ultrathin sectioning. To carry out electron microscopy, the ultrathin sections were post-stained with 1 % lead citrate for 2 min. Transmission electron microscopy was carried out using either a Zeiss EM 912 (Zeiss AG, Oberkochen, Germany), set to an acceleration voltage of 80 kV, operated in the zero-loss mode and equipped with a 2k x 2k slow-scan CCD camera (TRS Tröndle Restlichtverstärkersysteme, Moorenweis, Germany) or a JEOL F200 (JEOL, Freising, Germany), operated at 200 kV equipped with a XAROSA 20 mega pixel CMOS camera (EMSIS, Münster, Germany.)

7.9.11 Co-immunoprecipitation, mass spectrometry and data analysis

For Co-immunoprecipitation (CoIP) experiments, nuclei of *Pf*Snf2L-HA and 3D7 parasites containing mixed stages were prepared and treated with DNaseI or benzonase as described

(7.9.8). The obtained DNaseI-/ benzonase-treated nucleoplasm fractions were used as input. These input fractions were analyzed for DNA fragment size using agarose gel electrophoresis. The DNaseI-treated input was diluted in 2.5 volumes RIPA150 buffer, the benzonase-treated input in 2.5 volumes RIPA50 buffer. Subsequently, they were incubated overnight at 4 °C under constant agitation with equilibrated anti-HA magnetic beads. Using a magnetic rack, beads were pelleted and washed three times with 400 µl RIPA150 buffer for 10 min. Three more washing steps with 50 mM Tris-HCl pH 8 followed, before beads were transferred into a clean tube, dried, and stored at -20 °C. Collected fractions (input, flowthrough, beads) were analyzed on 4-20 % SDS-PAGE in duplicates. One gel was silver-stained, and the duplicate version was probed anti-HA in western blot. Co-immunoprecipitation was performed for both nuclease conditions in three biological replicates, for *Pf*Snf2L-HA and 3D7 parasites each, and used for LC-MS/MS analysis of co-immunoprecipitated proteins.

All further steps were performed by the Protein Analysis Unit (ZfP, LMU): Beads were incubated with 10 ng/µL trypsin in 1 M urea/50 mM NH_4HCO_3 for 30 min, washed with 50 mM NH_4HCO_3, and the supernatant digested overnight in presence of 1 mM DTT. Digested peptides were alkylated and desalted prior to LC–MS analysis. For LC–MS/MS purposes, desalted peptides were injected in an Ultimate 3000 RSLCnano system (Thermo Fisher), separated in a 15-cm analytical column (75 µm ID with ReproSil-Pur C18-AQ 2.4 µm from Dr. Maisch) with a 50-min gradient from 4 % to 40 % acetonitrile in 0.1 % formic acid. The effluent from the HPLC was directly electrosprayed into a QexactiveHF (Thermo Fisher) operated in data dependent mode to automatically switch between full scan MS and MS/MS acquisition. Survey full scan MS spectra (from m/z 350 to 1,600) were acquired with resolution R = 60,000 at m/z 400 (AGC target of 3×10^6). The 10 most intense peptide ions with charge states between 2 and 5 were sequentially isolated to a target value of 1×10^5 and fragmented at 30 % normalized collision energy. Typical mass spectrometric conditions were as follows: spray voltage, 1.5 kV; heated capillary temperature, 275 °C; ion selection threshold, 33.000 counts.

MaxQuant 1.6.14.0 was used to identify proteins and quantify by iBAQ with the following parameters: Database Uniprot_UP000001450_Plasmodiumfalciparum_20201007.fasta; MS tol, 10 ppm; MS/MS tol, 20 ppm Da; PSM FDR, 0.01; Protein FDR, 0.01 min; Peptide Length, 7; Variable modifications, Oxidation (M), Acetyl (Protein N-term); Fixed modifications, Carbamidomethyl (C); Peptides for protein quantitation, razor and unique; Min. peptides, 1; Min. ratio count, 2. MaxQuant iBAQ values were log2 transformed, missing values implemented with 8. Ribosomal proteins and hits detected with only 1 peptide were excluded. Identified proteins were considered as interaction partners of the bait, if $\log_2$(Snf2L-

3HA) – $\log_2$(3D7) > 3 or $\log_2$(Snf2L-3HA) – $\log_2$(3D7) > 2 & FDR <0.05. The mass spectrometry proteomics data have been deposited to the ProteomeXchange Consortium via the PRIDE partner repository with the dataset identifier PXD041155.

7.9.12 Chromatin-immunoprecipitation-Sequencing (ChIP-Seq) and data analysis

For Chromatin-immunoprecipitation experiments, mixed stage *Pf*Snf2L-HA parasites were grown to ~5 % parasitemia, and two different crosslinking conditions were applied. For formaldehyde crosslinking, parasites were incubated in media supplemented with 1 % formaldehyde for 15 min at 37 °C under rotation. For additional disuccinimidyl glutarate (DSG) fixation, parasites were pre-incubated in 2 mM DSG for 30 min at 37 °C, before formaldehyde crosslinking was performed accordingly. To stop crosslinking, glycine was added to the culture to a final concentration of 0.125 M. Red blood cells were lysed with saponin, centrifuged (15 min, 4 °C, 11000 g) and washed multiple times with PBS+PIC. Parasite nuclei were prepared as described (7.9.8). The obtained nuclei (~6 x 10^8) were resuspended in 250 µl sonication buffer and sonicated for 20 cycles of 30 sec ON/OFF (high). 50 µl were saved as input control, the rest was added to 9 volumes incubation buffer. Half was incubated overnight at 4 °C under rotation with anti-HA magnetic beads (30 µl slurry) and one half with Protein G magnetic beads without antibodies coupled (30 µl slurry). Magnetic beads were successively washed with 400 µl wash buffer I / wash buffer I / wash buffer II / wash buffer III / wash buffer IV / wash buffer IV for 5 min each. After 20 min incubation in 200 µl 1 % SDS/0.1 M $NaHCO_3$ at room temperature, the elutant was separated from beads and supplemented with 1 M NaCl for de-crosslinking at 55 °C for > 6 h. Input was de-crosslinked accordingly. 2 µl of supplied proteinase K was added, incubated for 10 min and subsequently, DNA was purified using the DNA CLEAN-UP MICRO SPIN kit. Input, αHA-ChIP and control-ChIP samples were analyzed for DNA fragment size and concentration using the 4200 TapeStation System. ChIP experiment was performed for both crosslinking conditions in three biological replicates each and used sequencing analysis of co-immunoprecipitated DNA. 2 ng of each sample was used for NEBNEXT ultra II library preparation as manufacturer recommends, and quality of library was tested with TapeStation technology. Libraries from all input samples, all ChIP samples and two exemplar control samples were sequenced on the Illumina NextSeq 500 Sequencing System. Sequenced reads (2x42bp bp, paired-end, 10-20 Mio reads/sample) were trimmed with bcl2fastq and mapped to *P. falciparum* 3D7 genome v3.0 using Bowtie2. Preprocessing and mapping quality control was done with FastQC, samtools and deeptool, peaks were called using MACS2 with a false discovery rate (FDR) of 0.05.

7.9.13 RNA-Sequencing (RNA-Seq) and data analysis

For detailed transcriptome analysis, *Pf*Snf2L-HA-cKO were synchronized within a one-hour window and KO was induced as described (7.9.9) either at early ring stage (1-5 hpi) or at late early trophozoite stage (24-28 hpi). iRBCs were harvested in five-hour-intervals and total RNA was isolated using Whole Blood Quick RNA kit according to the manufacturer's protocol. RNA isolation of 3D7 parasites 20/25/35 hours drug-treated/non-treated was performed accordingly.

RNA quality was checked using 4200 TapeStation System and 300 ng were used as input for Illumina Stranded mRNA Prep Ligation. Libraries were sequenced on the Illumina NextSeq 2000 Sequencing System. Sequencing data processing and data analysis was performed by Simon Holzinger: Sequenced reads (2x57bp bp, paired-end, ~20 Mio reads/sample) were trimmed with trimmomatic v0.39 and mapped to *P. falciparum* 3D7 genome v3.0 using STAR 2.7.9a. PlasmoDB annotation was converted to GTF-format with gffread 0.12.1. Preprocessing and mapping quality control was done with FastQC 0.11.8, qualimap 2.2.2d, samtools 1.12 and multiqc 1.9. The pipeline was implemented with snakemake 5.32.0 and is available at https://github.com/SimHolz/Watzlowik_et_al_2023. RSubread/FeatureCounts 2.12.2 was utilized to calculate read counts, while differential expression analysis was performed by DESeq2 adjusted P-value <0.05 as significance cutoff. Further analysis and visualization were done in R using tidyverse and ggpubr. GO term enrichment analysis was performed using topGP with Fisher-test, redundancy-reduced, Enrichment defined as -log10(defaultKS) >2. noKO samples t0-t45 were defined as reference transcriptome and coefficient of variation per gene was calculated by standard deviation/mean x 100 across reference transcriptome. For expression quantile calculation transcript per millions (TPM) normalization of reference transcriptome was used. DEGreport was used for clustering. RNA-Seq-based cell cycle progression was estimated in R by comparing the normalized expression values of each sample to the RNA-Seq data from (Painter et al., 2018) using the statistical model previously described (Lemieux et al., 2009). Estimation of *Pf*Snf2L knockout efficacy was done by mapping reads to the sequence of the recodonized transfected Snf2L gene and counting reads mapped to the Snf2L$_{\text{recodon}}$ part of the gene which is disintegrated upon knockout induction. RNA-Seq data were submitted to Gene Expression Omnibus database (accession number GSE228949).

7.9.14 MNase-Sequencing (MNase-Seq) and data analysis

For chromatin phenotyping, micrococcal nuclease digestion and subsequent sequencing of noKO/iKO chromatin was performed. *Pf*Snf2L-HA-cKO were synchronized within a two-hour window and KO was induced as described (7.9.9) either at early ring stage (1-5 hpi) or at late early trophozoite stage (24-28 hpi). 45 hours post KO induction, parasites were crosslinked with formaldehyde and nuclei were prepared as described in 7.9.12. Nuclei were resuspended in 75 µl digestion buffer with 0.75 U Micrococcal nuclease and 50 U Exonuclease III. Each sample was aliquoted in 3 x 25 µl and incubated for 2.5 / 5 / 10 min at 37 °C under agitation (low/mid/high digestion), before the reaction was stopped by adding 25 µl stopping solution and placed at 4 °C. De-crosslinking was performed at 45 °C overnight after adjusting to 1 % SDS / 0.1 M $NaHCO_3$ / 0.5 M NaCl. Proteins were digested by addition of 40 µg of Proteinase K (Zymo Research) and incubation for 1 h at 55 °C. Subsequently, DNA was isolated using DNA CLEAN-UP MICRO SPIN kit as the manufacturer recommends. Digestion efficacy of extracted DNA fragments was analyzed with TapeStation 4200 System and DNA size distribution (molarity) was visualized using BioanalyzeR. For low digested samples, DNA fragments >700 bp were removed using 0.75 x SPRI beads, no size-selection step was applied for high digested samples.

1 ng of high/low digested samples was used as input for NEBNext Ultra II DNA library prep kit, according to manufacturer's protocol. Libraries were sequenced on the Illumina NextSeq 2000 Sequencing System. Sequencing data processing and data analysis was performed by Simon Holzinger: Sequenced reads (2x65 bp, paired-end, ~20 Mio reads/sample) were trimmed with skewer 0.2.2, and subsequently mapped to *P. falciparum* 3D7 genome v3.0 (plasmoDB.org, release 52) using Bowtie2 2.3.5 with "--very-sensitive --no-discordant --no-mixed --no-unal" options. Mapped fragments were filtered with deeptools 3.5.0 for a mapping quality of at least 20, a fragment size between 75 -175 bp and proper read pairs. The remaining fragments were used for nucleosome calling with DANPOS. Quality control was done with FastQC 0.11.8, qualimap 2.2.2d, samtools 1.12 and multiqc 1.9. Further analysis was done with R etc. The pipeline was implemented with snakemake 5.32.0 and is available at https://github.com/SimHolz/Watzlowik_et_al_2023. MNase-Seq data were submitted to Gene Expression Omnibus database (accession number GSE228949).

MNase-Seq data analysis details

MNase-Sequencing of schizont stage chromatin +/- *Pf*Snf2L-cKO was performed in triplicates, MNase-Sequencing of late ring stage chromatin +/- *Pf*Snf2L-cKO in duplicates.

DANPOS: Replicate bam files were put into a single directory respectively to be recognized as a single dataset by DANPOS. Nucleosome calling was performed with the following command: python3 danpos.py dpos <Input> -o <outDir> -m 1 -c 51137214 --extend 73 -a 1 -jd 100 -e 1 -z 20 -s 1. For comparison and differential nucleosome positioning of two datasets, the two inputs are separated by ":" like "iKO_0h_high/:noKO_0h_high/".

The differential nucleosome positioning results were adjusted with a custom R script using simulated random nucleosome positions and Benjamini Hochberg Procedure to calculate FDR values and loess-smoothing for improved dyad position calling.

DYNAMICs: Among the nucleosomes obtained from differential nucleosomes analysis in late ring stage, the following were defined as dynamically changed: Adjusted FDR values (-log10 transformed for occupancy and fuzziness changes, not transformed for shifts) were normalized to maximum change and ranked and slope=1 was defined as cutoff. Cutoff values were extracted and applied for differential schizont stage nucleosomes. Among dynamic nucleosomes, only the ones within the 20 % best-positioned nucleosomes in both stages were considered.

Gene part assignment: Dynamic nucleosomes identified as described above were assigned to gene parts obtained from PlasmoDB annotation with a minimum overlap of 99 bp: 5’UTR, protein-coding (= CDS), 3’UTR, intergenic (= no feature assigned), others (= introns, pseudogenes, snoRNA, ncRNA, tRNA, snRNA, rRNA).

Profiles: The transcriptional landmark sites (TSS, AUG, STOP, TTS) were extracted from PlasmoDB annotation for each gene on chromosome 1-14, only one site per gene considered. Occupancy profiles were obtained by aligning the coverage 1000 bp upstream and downstream of the mark for all available replicates and averaging. The corresponding GC-content around landmarks was aligned, averaged, and smoothed accordingly. Occupancy profiles around +1 nucleosome were created analogously.

Nucleosome Dynamics Suite: BAM files were used as input for Nucleosome Dynamics program suite, utilizing the readBam, nucleR and txstart function. nucleR was run with “--type paired --fragmentLen 175 --thresholdPercentage 50” in addition to default parameters and txstart with “--p1.max.downstream 100” in addition to default parameters.

NFR Width: Distance between +1 and -1 nucleosome as detected by the nucleosome dynamics txstart function was used as NFR width estimation.

+1 Nucleosome Annotation: BAM files of replicates of noKO_24h_high and noKO_0h_high were merged respectively and used as input for Nucleosome Dynamics program suite, The 3’-end of the resulting gff from txstart was used as +1 nucleosome dyad annotation.

Mean Fuzziness change calculation: Promoter regions were defined as 1000 bp upstream and 1000 bp downstream of the +1 nucleosomes identified via Nucleosome Dynamics program suite. All called nucleosomes with a minimum overlap of 75 bp with the promoter region were averaged. Mean fuzziness scores were subtracted (iKO-noKO). Only promoters harboring at least six called nucleosomes were considered.

7.9.15 High throughput screening implementation and data analysis

ADP biosensor screen

The screening of *Pf*Snf2Lcore inhibition by presence of compounds was analyzed by kinetic ATPase measurement (7.9.6). The measurement was performed in 20 µl biosensor buffer containing 0.2 µM TMR-maleimide-labeled ParM, 125 µM ATP, 10 ng/µl pT11 DNA and 0.2 µM recombinantly expressed *Pf*Snf2Lcore. To prevent ATP hydrolysis prior to measurement, the components were mixed in two master mixes (MM) and added in following order: 200 nl compound in DMSO or DMSO alone were transferred to glass-bottom µCLEAR microplates using automatic acoustic droplet ejection, performed by the Fraunhofer Institute for Toxicology and Experimental Medicine (ITEM). 10 µl MM1 containing *Pf*Snf2Lcore in biosensor buffer (or buffer only for noATPase control) were transferred to each well using the Multidrop Combi system. Subsequently, 10 µl MM2 containing all other components were added accordingly. After rapid mixing and spinning, measurements were immediately started in an EnVision fluorescence reader. The following measurement parameters were applied: excitation wavelength: 550 nm, emission wavelength 590 nm, temperature: room temperature, time interval: 6 min, duration 120 min. All 1506 chemicals of the *Prestwick small molecule library* were measured in triplicates at three different days. An automated plate stacker allowed five plates to be measured in parallel, with all compounds and controls on each plate. The 2645 chemicals of the *Selleck Bioactive Compound Library* were measured accordingly in duplicates. The 105 cherry-picked chemicals of the second screen were measured in two different concentrations (10 µM / 100 µM) in duplicates using the same setup.

The fluorescence values for each compound and each timepoint were corrected for the mean ATPase-absent value of the corresponding replicate and the obtained kinetic curve was analyzed for two parameters: The slope of the curve within the first 60 min was calculated by fitting a linear model (threshold = 3.5 (1^{st}) / 3.7 (2^{nd})), as well as the difference between end and start point (F_{120}-F_0, threshold = 25000). All compounds showing a kinetic curve below both thresholds were considered as *Pf*Snf2Lcore ATPase inhibiting chemicals.

The dose-dependent ATPase inhibition of cherry-picked chemicals was scored for each compound as strong inhibition (at 10 µM), moderate inhibition (at 100 µM) or no inhibition.

MST measurement

The screening of compound binding to *Pf*Snf2Lcore via Microscale thermophoresis was performed by the company 2bind (Biopark, Regensburg): Recombinantly expressed *Pf*Snf2Lcore was labeled with NHS-DY647P1 using the Monolith Protein RED-NHS Labeling

Kit. All 1506 chemicals of *Prestwick small molecule library* and 105 cherry-picked chemicals of the *Selleck Bioactive Compound Library* were measured in duplicates. The measurement was performed in 10 µl of 20 mM Tris pH 8.6 / 1.5 mM $MgCl_2$ / 0.5 mM EGTA / 100 mM KCl / 0.01 % Pluronic, and following measurement parameters were applied:

Device: Monolith NT.115pico, MSTpower: medium, ExcitationPower: 20 %, ColdRegion: -1-0 s, HotRegion: 9-10 s, Temperature: 25 °C, Target: *Pf*Snf2Lcore NHS-DY647P1-labeled, Target concentration: 5 nM, Ligand concentration: 100 µM / DMSO 1 %

For evaluation of target binding, values were calculated as follows and cutoff criteria applied: for compounds/DMSO F_{norm} [‰] = F_{hot}/F_{cold}; ΔF_{norm}= F_{norm}(compound)- F_{norm}(DMSO); Autofluorescence (ligand-induced enhancement): F_{cold} >110 % of F_{cold}(DMSO); potential hit (ligand-induced quenching): $F_{cold} < 90$ % of F_{cold}(DMSO); binder: $\Delta F_{norm} >$ 3x SD of F_{norm}(DMSO); non-binder: $\Delta F_{norm} <$ 3x SD of F_{norm}(DMSO); ambiguous: different classification in replicates. The *Pf*Snf2Lcore binding probability of cherry-picked chemicals was scored for each compound as strong (hit or potential hit), moderate (aggregation or ambiguous), or no binding (non-binder).

nanoDSF measurement

The screening of (de-)stabilization of *Pf*Snf2Lcore by presence of compounds was analyzed using differential scanning fluorimetry (nanoDSF). The measurement was performed in 10 µl of 20 mM Tris pH 8.6 / 1.5 mM $MgCl_2$ / 0.5 mM EGTA / 100 mM KCl containing 4 µM recombinantly expressed *Pf*Snf2Lcore. Twelve hit compounds of the *Prestwick small molecule library* were measured in various concentration (1000 / 100 / 10 / 1 µM), while the 105 cherry-picked chemicals of the *Selleck Bioactive Compound Library* were measured in 100 µM, each in duplicates. A destabilizing effect on *Pf*Snf2Lcore by corresponding DMSO concentrations could be excluded for up to 1 % (= 100 µM) and proven as minimal for 10 % (= 1 mM). Following measurement parameters were applied:

Device: Prometheus NT.48, Capillaries: nanoDSF Grade Standard Capillaries, LEDexcitation: 80 %, Temperature 20-95 °C, simultaneous scanning of 330 nm and 350 nm fluorescence. The ratio of fluorescence F_{350nm}/F_{330nm} is calculated over temperature, and the first derivate operation gives the melting temperature T_M (where 50 % of the protein is unfolded) as a maximum/minimum.

*Pf*Snf2Lcore destabilization of cherry-picked chemicals was scored for each compound as strong ($\Delta T_M > 2$ °C), moderate ($\Delta T_M < 2$ °C), or no destabilization ($\Delta T_M < 0.2$ °C).

7.9.16 Toxicity assay

***Plasmodium falciparum* toxicity**

Toxicity to *Plasmodium falciparum* was determined by culturing 3D7 parasites in presence of hit compounds at various concentrations (0.08-20 µM). After 72 hours, thin blood films were prepared, Giemsa-stained and parasitemia was quantified. EC50 values were estimated for compounds with the lead compound as an exception. To assess toxicity, the lead compound was tested in three independent replicates, normalized to parasitemia when untreated and the EC50 value was obtained by fitting a dose response model using a three-parameter log-logistic model.

***Toxoplasma gondii* toxicity**

Toxicity to Toxoplasma was tested by Matthew Gow (Meissner Lab, LMU) using a plaque assay: *T. gondii* tachyzoites were generally passaged onto human foreskin fibroblast (HFF-1) monolayers at 37°C and 5 % CO_2 in DMEM with 10 % fetal bovine serum (FBS), 4mM L-glutamate, 20µg/ml gentamicin. To analyze toxicity of hit compounds, 1000 *T. gondii* tachyzoites inoculated onto HFF-1 were treated with drug/DMSO at various concentrations (0.06-20 µM). After 6 days, the HFF-1 monolayer was washed in PBS, fixed with 4 % PFA for 20 min and stained with Giemsa-staining solutions. Plaque formation serves as a measure for parasite proliferation. Using the Leica DMi8 Widefield Microscope, number of plaques and relative area was quantified and EC50 values were estimated.

Human HeLa cell toxicity

Toxicity to human cells was representatively tested on highly proliferating HeLa cells. HeLa cells were grown in DMEM containing 2 mM GlutaMAX-I supplemented with 10 % FBS without antibiotics and maintained under constant conditions of 37 °C and 5 % CO_2. To analyze drug toxicity, 5000 cells per well were seeded in a 96-well plate and treated for 48 h with drug at various concentrations (0.02-20 µM) and DMSO, respectively. Subsequently, metabolic activity was monitored using the Cell Proliferation Kit II-XTT according to manufacturer's recommendatiosn. After 4 h incubation with substrates, the absorbance was measured in a plate reader, A_{490nm}-A_{620nm} was calculated and normalized to untreated. The EC50 value was obtained by fitting a dose response model using a three-parameter log-logistic model.

7.9.17 Gametocyte induction and quantification

Gametocyte induction and quantification was performed by Ritwik Singhal (Llinás Lab, PennState University): Tightly synchronized trophozoites (24 - 28 hpi) at 2 % parasitemia were grown in minimal fatty acid (mFA) media and drug / DMSO for 22 – 24 hours before returning to complete media (without drug / DMSO). mFA media was prepared by supplementing incomplete RPMI-1640 (complete medium without AlbuMAX II) with 0.39 % fatty acid-free bovine serum albumin (BSA, Sigma-Aldrich), 30 µM oleic acid (Sigma-Aldrich), and 30 µM palmitic acid (Sigma-Aldrich) (Brancucci et al., 2017). On day 2, parasitemia was quantified using Giemsa-stained blood smears and 20 U/mL heparin was added to the cultures to prevent parasite re-invasion. Heparin-containing complete media was replaced daily for the remainder of the assay until quantification of gametocytemia on day 8 by Giemsa-staining. The gametocyte conversion rate (GCR) was calculated as GCR = (Gametocytemia on Day 8/Parasitemia on Day 2)*100. GCR assays were performed in biological duplicates, each consisting of two technical replicates.

8 REFERENCES

Abel, S., Le Roch, K.G., 2019. The role of epigenetics and chromatin structure in transcriptional regulation in malaria parasites. Briefings in Functional Genomics. https://doi.org/10.1093/bfgp/elz005

Abkarian, M., Massiera, G., Berry, L., Roques, M., Braun-Breton, C., 2011. A novel mechanism for egress of malarial parasites from red blood cells. Blood 117, 4118–4124. https://doi.org/10.1182/blood-2010-08-299883

Adjalley, S.-H., Chabbert, C.D., Klaus, B., Pelechano, V., Steinmetz, L.M., 2016. Landscape and Dynamics of Transcription Initiation in the Malaria Parasite Plasmodium falciparum. Cell Rep 14, 2463–2475. https://doi.org/10.1016/j.celrep.2016.02.025

Alexa, A., Rahnenfuhrer, J., 2022. topGO: Enrichment Analysis for Gene Ontology.

Alvarez, D.R., Ospina, A., Barwell, T., Zheng, B., Dey, A., Li, C., Basu, S., Shi, X., Kadri, S., Chakrabarti, K., 2021. The RNA structurome in the asexual blood stages of malaria pathogen *plasmodium falciparum*. RNA Biology 18, 2480–2497. https://doi.org/10.1080/15476286.2021.1926747

Aly, A.S.I., Vaughan, A.M., Kappe, S.H.I., 2009. Malaria parasite development in the mosquito and infection of the mammalian host. Annu Rev Microbiol 63, 195–221. https://doi.org/10.1146/annurev.micro.091208.073403

Amos, B., Aurrecoechea, C., Barba, M., Barreto, A., Basenko, E.Y., Bażant, W., Belnap, R., Blevins, A.S., Böhme, U., Brestelli, J., Brunk, B.P., Caddick, M., Callan, D., Campbell, L., Christensen, M.B., Christophides, G.K., Crouch, K., Davis, K., DeBarry, J., Doherty, R., Duan, Y., Dunn, M., Falke, D., Fisher, S., Flicek, P., Fox, B., Gajria, B., Giraldo-Calderón, G.I., Harb, O.S., Harper, E., Hertz-Fowler, C., Hickman, M.J., Howington, C., Hu, S., Humphrey, J., Iodice, J., Jones, A., Judkins, J., Kelly, S.A., Kissinger, J.C., Kwon, D.K., Lamoureux, K., Lawson, D., Li, W., Lies, K., Lodha, D., Long, J., MacCallum, R.M., Maslen, G., McDowell, M.A., Nabrzyski, J., Roos, D.S., Rund, S.S.C., Schulman, S.W., Shanmugasundram, A., Sitnik, V., Spruill, D., Starns, D., Stoeckert, C.J., Tomko, S.S., Wang, H., Warrenfeltz, S., Wieck, R., Wilkinson, P.A., Xu, L., Zheng, J., 2022. VEuPathDB: the eukaryotic pathogen, vector and host bioinformatics resource center. Nucleic Acids Research 50, D898–D911. https://doi.org/10.1093/nar/gkab929

Andrews, Simon, n.d. FastQC - A Quality Control Tool for High Throughput Sequence Data.

Arnot, D.E., Ronander, E., Bengtsson, D.C., 2011. The progression of the intra-erythrocytic cell cycle of Plasmodium falciparum and the role of the centriolar plaques in asynchronous mitotic division during schizogony. International Journal for Parasitology 41, 71–80. https://doi.org/10.1016/j.ijpara.2010.07.012

Ast, G., 2004. How did alternative splicing evolve? Nat Rev Genet 5, 773–782. https://doi.org/10.1038/nrg1451

Aurrecoechea, C., Brestelli, J., Brunk, B.P., Dommer, J., Fischer, S., Gajria, B., Gao, X., Gingle, A., Grant, G., Harb, O.S., Heiges, M., Innamorato, F., Iodice, J., Kissinger, J.C., Kraemer, E., Li, W., Miller, J.A., Nayak, V., Pennington, C., Pinney, D.F., Roos, D.S., Ross, C., Stoeckert, C.J., Treatman, C., Wang, H., 2009. PlasmoDB: A Functional Genomic Database for Malaria Parasites. Nucleic Acids Research 37, D539-543. https://doi.org/10.1093/nar/gkn814

Ay, F., Bunnik, E.M., Varoquaux, N., Bol, S.M., Prudhomme, J., Vert, J.-P., Noble, W.S., Le Roch, K.G., 2014. Three-dimensional modeling of the P. falciparum genome during the erythrocytic cycle reveals a strong connection between genome architecture and gene expression. Genome Res. 24, 974–988. https://doi.org/10.1101/gr.169417.113

Ay, F., Bunnik, E.M., Varoquaux, N., Vert, J.-P., Noble, W.S., Le Roch, K.G., 2015. Multiple dimensions of epigenetic gene regulation in the malaria parasite Plasmodium falciparum: gene regulation via histone modifications, nucleosome positioning and nuclear architecture in P. falciparum. Bioessays 37, 182–194. https://doi.org/10.1002/bies.201400145

Balaji, S., Babu, M.M., Iyer, L.M., Aravind, L., 2005. Discovery of the principal specific transcription factors of Apicomplexa and their implication for the evolution of the AP2-integrase DNA binding domains. Nucleic Acids Res. 33, 3994–4006. https://doi.org/10.1093/nar/gki709

Baldi, S., Jain, D.S., Harpprecht, L., Zabel, A., Scheibe, M., Butter, F., Straub, T., Becker, P.B., 2018. Genome-wide Rules of Nucleosome Phasing in Drosophila. Mol Cell 72, 661-672.e4. https://doi.org/10.1016/j.molcel.2018.09.032

Bártfai, R., Hoeijmakers, W.A.M., Salcedo-Amaya, A.M., Smits, A.H., Janssen-Megens, E., Kaan, A., Treeck, M., Gilberger, T.-W., Françoijs, K.-J., Stunnenberg, H.G., 2010. H2A.Z demarcates intergenic regions of the plasmodium falciparum epigenome that are dynamically marked by H3K9ac and H3K4me3. PLoS Pathog. 6, e1001223. https://doi.org/10.1371/journal.ppat.1001223

Bartholomew, B., 2014a. Regulating the Chromatin Landscape: Structural and Mechanistic Perspectives. Annual Review of Biochemistry 83, 671–696. https://doi.org/10.1146/annurev-biochem-051810-093157

Bartholomew, B., 2014b. ISWI chromatin remodeling: one primary actor or a coordinated effort? Current Opinion in Structural Biology 24, 150–155. https://doi.org/10.1016/j.sbi.2014.01.010

Bartoschik, T., Maschberger, M., Feoli, A., André, T., Baaske, P., Duhr, S., Breitsprecher, D., 2017. Microscale Thermophoresis in Drug Discovery, in: Huddler, D., Zartler, E.R. (Eds.), Applied Biophysics for Drug Discovery. John Wiley & Sons, Ltd, Chichester, UK, pp. 73–92. https://doi.org/10.1002/9781119099512.ch5

Baumgarten, S., Bryant, J., 2022. Chromatin structure can introduce systematic biases in genome-wide analyses of Plasmodium falciparum. Open Res Europe 2, 75. https://doi.org/10.12688/openreseurope.14836.2

Baxevanis, A.D., Landsman, D., 1998. Histone Sequence Database: new histone fold family members. Nucleic Acids Res. 26, 372–375. https://doi.org/10.1093/nar/26.1.372

Becker, P.B., Workman, J.L., 2013. Nucleosome Remodeling and Epigenetics. Cold Spring Harbor Perspectives in Biology 5, a017905–a017905. https://doi.org/10.1101/cshperspect.a017905

Birnbaum, J., Flemming, S., Reichard, N., Soares, A.B., Mesén-Ramírez, P., Jonscher, E., Bergmann, B., Spielmann, T., 2017. A genetic system to study Plasmodium falciparum protein function. Nature Methods 14, 450–456. https://doi.org/10.1038/nmeth.4223

Bischoff, E., Vaquero, C., 2010. In silico and biological survey of transcription-associated proteins implicated in the transcriptional machinery during the erythrocytic development of Plasmodium falciparum. BMC Genomics 11, 34. https://doi.org/10.1186/1471-2164-11-34

Blackman, M.J., 1995. Chapter 11: Purification of Plasmodium falciparum Merozoites for Analysis of the Processing of Merozoite Surface Protein-1, in: Methods in Cell Biology. Elsevier, pp. 213–220. https://doi.org/10.1016/S0091-679X(08)61853-1

Boddey, J.A., Cowman, A.F., 2013. *Plasmodium* Nesting: Remaking the Erythrocyte from the Inside Out. Annu. Rev. Microbiol. 67, 243–269. https://doi.org/10.1146/annurev-micro-092412-155730

Böhme, U., Otto, T.D., Sanders, M., Newbold, C.I., Berriman, M., 2019. Progression of the canonical reference malaria parasite genome from 2002-2019. Wellcome Open Res 4, 58. https://doi.org/10.12688/wellcomeopenres.15194.2

Bolger, A.M., Lohse, M., Usadel, B., 2014. Trimmomatic: A Flexible Trimmer for Illumina Sequence Data. Bioinformatics (Oxford, England) 30, 2114–2120. https://doi.org/10.1093/bioinformatics/btu170

Bowen, N.J., Fujita, N., Kajita, M., Wade, P.A., 2004. Mi-2/NuRD: multiple complexes for many purposes. Biochim Biophys Acta 1677, 52–57. https://doi.org/10.1016/j.bbaexp.2003.10.010

Bozdech, Z., Llinás, M., Pulliam, B.L., Wong, E.D., Zhu, J., DeRisi, J.L., 2003. The transcriptome of the intraerythrocytic developmental cycle of Plasmodium falciparum. PLoS Biol. 1, E5. https://doi.org/10.1371/journal.pbio.0000005

Bradford, M.M., 1976. A rapid and sensitive method for the quantitation of microgram quantities of protein utilizing the principle of protein-dye binding. Anal Biochem 72, 248–254. https://doi.org/10.1006/abio.1976.9999

Brancucci, N.M.B., Bertschi, N.L., Zhu, L., Niederwieser, I., Chin, W.H., Wampfler, R., Freymond, C., Rottmann, M., Felger, I., Bozdech, Z., Voss, T.S., 2014. Heterochromatin protein 1 secures survival and transmission of malaria parasites. Cell Host Microbe 16, 165–176. https://doi.org/10.1016/j.chom.2014.07.004

Brancucci, N.M.B., Gerdt, J.P., Wang, C., De Niz, M., Philip, N., Adapa, S.R., Zhang, M., Hitz, E., Niederwieser, I., Boltryk, S.D., Laffitte, M.-C., Clark, M.A., Grüring, C., Ravel, D., Blancke Soares, A., Demas, A., Bopp, S., Rubio-Ruiz, B., Conejo-Garcia, A., Wirth, D.F., Gendaszewska-Darmach, E., Duraisingh, M.T., Adams, J.H., Voss, T.S., Waters, A.P., Jiang, R.H.Y., Clardy, J., Marti, M., 2017. Lysophosphatidylcholine Regulates Sexual Stage Differentiation in the Human Malaria Parasite Plasmodium falciparum. Cell 171, 1532-1544.e15. https://doi.org/10.1016/j.cell.2017.10.020

Brockelman, C.R., 1982. Conditions favoring gametocytogenesis in the continuous culture of Plasmodium falciparum. J Protozool 29, 454–458. https://doi.org/10.1111/j.1550-7408.1982.tb05432.x

Bryant, J.M., Baumgarten, S., Dingli, F., Loew, D., Sinha, A., Claës, A., Preiser, P.R., Dedon, P.C., Scherf, A., 2020. Exploring the virulence gene interactome with CRISPR / DC as9 in the human malaria parasite. Molecular Systems Biology 16. https://doi.org/10.15252/msb.20209569

Buitrago, D., Codó, L., Illa, R., de Jorge, P., Battistini, F., Flores, O., Bayarri, G., Royo, R., Del Pino, M., Heath, S., Hospital, A., Gelpí, J.L., Heath, I.B., Orozco, M., 2019. Nucleosome Dynamics: a new tool for the dynamic analysis of nucleosome positioning. Nucleic Acids Research 47, 9511–9523. https://doi.org/10.1093/nar/gkz759

Bunnik, E.M., Chung, D.-W.D., Hamilton, M., Ponts, N., Saraf, A., Prudhomme, J., Florens, L., Le Roch, K.G., 2013. Polysome profiling reveals translational control of gene expression in the human malaria parasite Plasmodium falciparum. Genome Biol. 14, R128. https://doi.org/10.1186/gb-2013-14-11-r128

Bunnik, E.M., Polishko, A., Prudhomme, J., Ponts, N., Gill, S.S., Lonardi, S., Le Roch, K.G., 2014. DNA-encoded nucleosome occupancy is associated with transcription levels in the human malaria parasite Plasmodium falciparum. BMC Genomics 15, 347. https://doi.org/10.1186/1471-2164-15-347

Button-Simons, K.A., Kumar, S., Carmago, N., Haile, M.T., Jett, C., Checkley, L.A., Kennedy, S.Y., Pinapati, R.S., Shoue, D.A., McDew-White, M., Li, X., Nosten, F.H., Kappe, S.H., Anderson, T.J.C., Romero-Severson, J., Ferdig, M.T., Emrich, S.J., Vaughan, A.M., Cheeseman, I.H., 2021. The power and promise of genetic mapping from Plasmodium falciparum crosses utilizing human liver-chimeric mice. Commun Biol 4, 734. https://doi.org/10.1038/s42003-021-02210-1

Campbell, T.L., De Silva, E.K., Olszewski, K.L., Elemento, O., Llinás, M., 2010. Identification and genome-wide prediction of DNA binding specificities for the ApiAP2 family of regulators from the malaria parasite. PLoS Pathog. 6, e1001165. https://doi.org/10.1371/journal.ppat.1001165

Carninci, P., Sandelin, A., Lenhard, B., Katayama, S., Shimokawa, K., Ponjavic, J., Semple, C.A.M., Taylor, M.S., Engström, P.G., Frith, M.C., Forrest, A.R.R., Alkema, W.B., Tan, S.L., Plessy, C., Kodzius, R., Ravasi, T., Kasukawa, T., Fukuda, S., Kanamori-Katayama, M., Kitazume, Y., Kawaji, H., Kai, C., Nakamura, M., Konno, H., Nakano, K., Mottagui-Tabar, S., Arner, P., Chesi, A., Gustincich, S., Persichetti, F., Suzuki, H., Grimmond, S.M., Wells, C.A., Orlando, V., Wahlestedt, C., Liu, E.T., Harbers, M., Kawai, J., Bajic, V.B., Hume, D.A., Hayashizaki, Y., 2006. Genome-wide analysis of mammalian promoter architecture and evolution. Nat Genet 38, 626–635. https://doi.org/10.1038/ng1789

Chappell, L., Ross, P., Orchard, L., Russell, T.J., Otto, T.D., Berriman, M., Rayner, J.C., Llinás, M., 2020. Refining the transcriptome of the human malaria parasite Plasmodium falciparum using amplification-free RNA-seq. BMC Genomics 21, 395. https://doi.org/10.1186/s12864-020-06787-5

Chen, K., Xi, Y., Pan, X., Li, Z., Kaestner, K., Tyler, J., Dent, S., He, X., Li, W., 2013. DANPOS: Dynamic Analysis of Nucleosome Position and Occupancy by Sequencing. Genome Research 23, 341–351. https://doi.org/10.1101/gr.142067.112

Chereji, R.V., Kan, T.-W., Grudniewska, M.K., Romashchenko, A.V., Berezikov, E., Zhimulev, I.F., Guryev, V., Morozov, A.V., Moshkin, Y.M., 2016. Genome-wide profiling of nucleosome sensitivity and chromatin accessibility in Drosophila melanogaster. Nucleic Acids Res 44, 1036–1051. https://doi.org/10.1093/nar/gkv978

Chittori, S., Hong, J., Bai, Y., Subramaniam, S., 2019. Structure of the primed state of the ATPase domain of chromatin remodeling factor ISWI bound to the nucleosome. Nucleic Acids Research 47, 9400–9409. https://doi.org/10.1093/nar/gkz670

Clapier, C.R., Cairns, B.R., 2012. Regulation of ISWI involves inhibitory modules antagonized by nucleosomal epitopes. Nature 492, 280–284. https://doi.org/10.1038/nature11625

Clapier, C.R., Iwasa, J., Cairns, B.R., Peterson, C.L., 2017. Mechanisms of action and regulation of ATP-dependent chromatin-remodelling complexes. Nature Reviews Molecular Cell Biology 18, 407–422. https://doi.org/10.1038/nrm.2017.26

Clark, P.G.K., Vieira, L.C.C., Tallant, C., Fedorov, O., Singleton, D.C., Rogers, C.M., Monteiro, O.P., Bennett, J.M., Baronio, R., Müller, S., Daniels, D.L., Méndez, J., Knapp, S., Brennan, P.E., Dixon, D.J., 2015. LP99: Discovery and Synthesis of the First Selective BRD7/9 Bromodomain Inhibitor. Angew Chem Int Ed Engl 54, 6217–6221. https://doi.org/10.1002/anie.201501394

Coetzee, N., Sidoli, S., van Biljon, R., Painter, H., Llinás, M., Garcia, B.A., Birkholtz, L.-M., 2017. Quantitative chromatin proteomics reveals a dynamic histone post-translational modification landscape that defines asexual and sexual Plasmodium falciparum parasites. Scientific Reports 7. https://doi.org/10.1038/s41598-017-00687-7

Coetzee, N., von Grüning, H., Opperman, D., van der Watt, M., Reader, J., Birkholtz, L.-M., 2020. Epigenetic inhibitors target multiple stages of Plasmodium falciparum parasites. Sci Rep 10, 2355. https://doi.org/10.1038/s41598-020-59298-4

Collins, C.R., Das, S., Wong, E.H., Andenmatten, N., Stallmach, R., Hackett, F., Herman, J.-P., Müller, S., Meissner, M., Blackman, M.J., 2013. Robust inducible Cre recombinase activity in the human malaria parasite *Plasmodium falciparum* enables efficient gene deletion within a single asexual erythrocytic growth cycle: Conditional Cre in the human malaria parasite. Molecular Microbiology 88, 687–701. https://doi.org/10.1111/mmi.12206

Corona, D.F.V., Siriaco, G., Armstrong, J.A., Snarskaya, N., McClymont, S.A., Scott, M.P., Tamkun, J.W., 2007. ISWI Regulates Higher-Order Chromatin Structure and Histone H1 Assembly In Vivo. PLoS Biol 5, e232. https://doi.org/10.1371/journal.pbio.0050232

Coulson, R.M.R., Hall, N., Ouzounis, C.A., 2004. Comparative genomics of transcriptional control in the human malaria parasite Plasmodium falciparum. Genome Res. 14, 1548–1554. https://doi.org/10.1101/gr.2218604

Cowman, A.F., Crabb, B.S., 2006. Invasion of Red Blood Cells by Malaria Parasites. Cell 124, 755–766. https://doi.org/10.1016/j.cell.2006.02.006

Croken, M.M., Nardelli, S.C., Kim, K., 2012. Chromatin modifications, epigenetics, and how protozoan parasites regulate their lives. Trends in Parasitology 28, 202–213. https://doi.org/10.1016/j.pt.2012.02.009

Cui, Long, Miao, J., Furuya, T., Li, X., Su, X., Cui, Liwang, 2007. PfGCN5-mediated histone H3 acetylation plays a key role in gene expression in Plasmodium falciparum. Eukaryotic Cell 6, 1219–1227. https://doi.org/10.1128/EC.00062-07

Dang, W., Bartholomew, B., 2007. Domain Architecture of the Catalytic Subunit in the ISW2-Nucleosome Complex. Molecular and Cellular Biology 27, 8306–8317. https://doi.org/10.1128/MCB.01351-07

Dao, H.T., Dul, B.E., Dann, G.P., Liszczak, G.P., Muir, T.W., 2020. A basic motif anchoring ISWI to nucleosome acidic patch regulates nucleosome spacing. Nat Chem Biol 16, 134–142. https://doi.org/10.1038/s41589-019-0413-4

Das, S., Lemgruber, L., Tay, C.L., Baum, J., Meissner, M., 2017. Multiple essential functions of Plasmodium falciparum actin-1 during malaria blood-stage development. BMC Biology 15. https://doi.org/10.1186/s12915-017-0406-2

Dawson, M.A., Kouzarides, T., 2012. Cancer Epigenetics: From Mechanism to Therapy. Cell 150, 12–27. https://doi.org/10.1016/j.cell.2012.06.013

de Koning-Ward, T.F., Dixon, M.W.A., Tilley, L., Gilson, P.R., 2016. Plasmodium species: master renovators of their host cells. Nat Rev Microbiol 14, 494–507. https://doi.org/10.1038/nrmicro.2016.79

de Koning-Ward, T.F., Gilson, P.R., Crabb, B.S., 2015. Advances in molecular genetic systems in malaria. Nature Reviews Microbiology 13, 373–387. https://doi.org/10.1038/nrmicro3450

Dechassa, M.L., Sabri, A., Pondugula, S., Kassabov, S.R., Chatterjee, N., Kladde, M.P., Bartholomew, B., 2010. SWI/SNF Has Intrinsic Nucleosome Disassembly Activity that Is Dependent on Adjacent Nucleosomes. Molecular Cell 38, 590–602. https://doi.org/10.1016/j.molcel.2010.02.040

Diermeier, S., Kolovos, P., Heizinger, L., Schwartz, U., Georgomanolis, T., Zirkel, A., Wedemann, G., Grosveld, F., Knoch, T.A., Merkl, R., Cook, P.R., Längst, G., Papantonis, A., 2014. TNFα signalling primes chromatin for NF-κB binding and induces rapid and widespread nucleosome repositioning. Genome Biol 15, 536. https://doi.org/10.1186/s13059-014-0536-6

Dimova, D., Nackerdien, Z., Furgeson, S., Eguchi, S., Osley, M.A., 1999. A role for transcriptional repressors in targeting the yeast Swi/Snf complex. Mol Cell 4, 75–83. https://doi.org/10.1016/s1097-2765(00)80189-6

Dobin, A., Davis, C.A., Schlesinger, F., Drenkow, J., Zaleski, C., Jha, S., Batut, P., Chaisson, M., Gingeras, T.R., 2013. STAR: Ultrafast Universal RNA-seq Aligner. Bioinformatics (Oxford, England) 29, 15–21. https://doi.org/10.1093/bioinformatics/bts635

Drouin, L., McGrath, S., Vidler, L.R., Chaikuad, A., Monteiro, O., Tallant, C., Philpott, M., Rogers, C., Fedorov, O., Liu, M., Akhtar, W., Hayes, A., Raynaud, F., Müller, S., Knapp, S., Hoelder, S., 2015. Structure enabled design of BAZ2-ICR, a chemical probe targeting the bromodomains of BAZ2A and BAZ2B. J Med Chem 58, 2553–2559. https://doi.org/10.1021/jm501963e

Eappen, A.G., Li, T., Marquette, M., Chakravarty, S., Kc, N., Zanghi, G., Hoffman, B.U., Hettiarachchi, H., Patil, A., Abebe, Y., Tran, C., Yossef, A.A., McWilliams, I., Morrison, R.D., Rathakrishnan, A., Inbar, E., Aly, A.S.I., De La Vega, P., Belmonte, M., Sedegah, M., Wai, T., Campo, J.J., King, H., Kappe, S.H.I., Li, M., Billingsley, P.F., Sim, B.K.L., Hoffman, S.L., 2022. In vitro production of infectious Plasmodium falciparum sporozoites. Nature 612, 534–539. https://doi.org/10.1038/s41586-022-05466-7

Erdel, F., Krug, J., Längst, G., Rippe, K., 2011. Targeting chromatin remodelers: signals and search mechanisms. Biochim Biophys Acta 1809, 497–508. https://doi.org/10.1016/j.bbagrm.2011.06.005

Ewels, P., Magnusson, M., Lundin, S., Käller, M., 2016. MultiQC: Summarize Analysis Results for Multiple Tools and Samples in a Single Report. Bioinformatics (Oxford, England) 32, 3047–3048. https://doi.org/10.1093/bioinformatics/btw354

Fan, Q., An, L., Cui, L., 2004. Plasmodium falciparum histone acetyltransferase, a yeast GCN5 homologue involved in chromatin remodeling. Eukaryotic Cell 3, 264–276.

Filarsky, M., Fraschka, S.A., Niederwieser, I., Brancucci, N.M.B., Carrington, E., Carrió, E., Moes, S., Jenoe, P., Bártfai, R., Voss, T.S., 2018. GDV1 induces sexual commitment of malaria parasites by antagonizing HP1-dependent gene silencing. Science 359, 1259–1263. https://doi.org/10.1126/science.aan6042

Flaus, A., 2006. Identification of multiple distinct Snf2 subfamilies with conserved structural motifs. Nucleic Acids Research 34, 2887–2905. https://doi.org/10.1093/nar/gkl295

Foss, F.M., Zinzani, P.L., Vose, J.M., Gascoyne, R.D., Rosen, S.T., Tobinai, K., 2011. Peripheral T-cell lymphoma. Blood 117, 6756–6767. https://doi.org/10.1182/blood-2010-05-231548

Francis, W.R., Wörheide, G., 2017. Similar Ratios of Introns to Intergenic Sequence across Animal Genomes. Genome Biol Evol 9, 1582–1598. https://doi.org/10.1093/gbe/evx103

Fraschka, S.A.-K., Henderson, R.W.M., Bártfai, R., 2016. H3.3 demarcates GC-rich coding and subtelomeric regions and serves as potential memory mark for virulence gene expression in Plasmodium falciparum. Sci Rep 6, 31965. https://doi.org/10.1038/srep31965

Fry, C.J., Peterson, C.L., 2001. Chromatin remodeling enzymes: who’s on first? Curr Biol 11, R185-197. https://doi.org/10.1016/s0960-9822(01)00090-2

Fyodorov, D.V., Kadonaga, J.T., 2002. Binding of Acf1 to DNA involves a WAC motif and is important for ACF-mediated chromatin assembly. Mol Cell Biol 22, 6344–6353. https://doi.org/10.1128/MCB.22.18.6344-6353.2002

Garcia-Manero, G., Fenaux, P., 2011. Hypomethylating Agents and Other Novel Strategies in Myelodysplastic Syndromes. JCO 29, 516–523. https://doi.org/10.1200/JCO.2010.31.0854

Gardner, M.J., Hall, N., Fung, E., White, O., Berriman, M., Hyman, R.W., Carlton, J.M., Pain, A., Nelson, K.E., Bowman, S., Paulsen, I.T., James, K., Eisen, J.A., Rutherford, K., Salzberg, S.L., Craig, A., Kyes, S., Chan, M.-S., Nene, V., Shallom, S.J., Suh, B., Peterson, J., Angiuoli, S., Pertea, M., Allen, J., Selengut, J., Haft, D., Mather, M.W., Vaidya, A.B., Martin, D.M.A., Fairlamb, A.H., Fraunholz, M.J., Roos, D.S., Ralph, S.A., McFadden, G.I., Cummings, L.M., Subramanian, G.M., Mungall, C., Venter, J.C., Carucci, D.J., Hoffman, S.L., Newbold, C., Davis, R.W., Fraser, C.M., Barrell, B., 2002. Genome sequence of the human malaria parasite Plasmodium falciparum. Nature 419, 498–511. https://doi.org/10.1038/nature01097

Glenister, F.K., Coppel, R.L., Cowman, A.F., Mohandas, N., Cooke, B.M., 2002. Contribution of parasite proteins to altered mechanical properties of malaria-infected red blood cells. Blood 99, 1060–1063. https://doi.org/10.1182/blood.v99.3.1060

Grüne, T., Brzeski, J., Eberharter, A., Clapier, C.R., Corona, D.F.V., Becker, P.B., Müller, C.W., 2003. Crystal Structure and Functional Analysis of a Nucleosome Recognition Module of the Remodeling Factor ISWI. Molecular Cell 12, 449–460. https://doi.org/10.1016/S1097-2765(03)00273-9

Gupta, M.K., Agarawal, M., Banu, K., Reddy, K.S., Gaur, D., Dhar, S.K., 2018. Role of Chromatin assembly factor 1 in DNA replication of Plasmodium falciparum. Biochemical and Biophysical Research Communications 495, 1285–1291. https://doi.org/10.1016/j.bbrc.2017.11.131

Hahn, S., Young, E.T., 2011. Transcriptional Regulation in *Saccharomyces cerevisiae*: Transcription Factor Regulation and Function, Mechanisms of Initiation, and Roles of Activators and Coactivators. Genetics 189, 705–736. https://doi.org/10.1534/genetics.111.127019

Haldar, K., Bhattacharjee, S., Safeukui, I., 2018. Drug resistance in Plasmodium. Nature Reviews Microbiology 16, 156–170. https://doi.org/10.1038/nrmicro.2017.161

Harada, A., Kimura, H., Ohkawa, Y., 2021. Recent advances in single-cell epigenomics. Current Opinion in Structural Biology 71, 116–122. https://doi.org/10.1016/j.sbi.2021.06.010

Harner, M.J., Frank, A.O., Fesik, S.W., 2013. Fragment-based drug discovery using NMR spectroscopy. J Biomol NMR 56, 65–75. https://doi.org/10.1007/s10858-013-9740-z

Harrer, N., Schindler, C.E.M., Bruetzel, L.K., Forné, I., Ludwigsen, J., Imhof, A., Zacharias, M., Lipfert, J., Mueller-Planitz, F., 2018. Structural Architecture of the Nucleosome Remodeler ISWI Determined from Cross-Linking, Mass Spectrometry, SAXS, and Modeling. Structure 26, 282-294.e6. https://doi.org/10.1016/j.str.2017.12.015

Heyer, W.-D., Li, X., Rolfsmeier, M., Zhang, X.-P., 2006. Rad54: the Swiss Army knife of homologous recombination? Nucleic Acids Research 34, 4115–4125. https://doi.org/10.1093/nar/gkl481

Hoeijmakers, W.A.M., Flueck, C., Françoijs, K.-J., Smits, A.H., Wetzel, J., Volz, J.C., Cowman, A.F., Voss, T., Stunnenberg, H.G., Bártfai, R., 2012. Plasmodium falciparum centromeres display a unique epigenetic makeup and cluster prior to and during schizogony. Cell. Microbiol. 14, 1391–1401. https://doi.org/10.1111/j.1462-5822.2012.01803.x

Hoeijmakers, W.A.M., Salcedo-Amaya, A.M., Smits, A.H., Françoijs, K.-J., Treeck, M., Gilberger, T.-W., Stunnenberg, H.G., Bártfai, R., 2013. H2A.Z/H2B.Z double-variant nucleosomes inhabit the AT-rich promoter regions of the Plasmodium falciparum genome. Mol. Microbiol. 87, 1061–1073. https://doi.org/10.1111/mmi.12151

Hoffmeister, H., Fuchs, A., Erdel, F., Pinz, S., Gröbner-Ferreira, R., Bruckmann, A., Deutzmann, R., Schwartz, U., Maldonado, R., Huber, C., Dendorfer, A.-S., Rippe, K., Längst, G., 2017. CHD3 and CHD4 form distinct NuRD complexes with different yet overlapping functionality. Nucleic Acids Res 45, 10534–10554. https://doi.org/10.1093/nar/gkx711

Holdgate, G.A., Meek, T.D., Grimley, R.L., 2018. Mechanistic enzymology in drug discovery: a fresh perspective. Nat Rev Drug Discov 17, 115–132. https://doi.org/10.1038/nrd.2017.219

Hollin, T., Gupta, M., Lenz, T., Le Roch, K.G., 2020. Dynamic Chromatin Structure and Epigenetics Control the Fate of Malaria Parasites. Trends in Genetics. https://doi.org/10.1016/j.tig.2020.09.003

Horrocks, P., Lanzer, M., 1999. Differences in nucleosome organization over episomally located plasmids coincides with aberrant promoter activity in P. falciparum. Parasitol. Int. 48, 55–61.

Horrocks, P., Wong, E., Russell, K., Emes, R.D., 2009. Control of gene expression in Plasmodium falciparum - ten years on. Mol. Biochem. Parasitol. 164, 9–25. https://doi.org/10.1016/j.molbiopara.2008.11.010

Howick, V.M., Russell, A.J.C., Andrews, T., Heaton, H., Reid, A.J., Natarajan, K., Butungi, H., Metcalf, T., Verzier, L.H., Rayner, J.C., Berriman, M., Herren, J.K., Billker, O., Hemberg, M., Talman, A.M., Lawniczak, M.K.N., 2019. The Malaria Cell Atlas: Single parasite transcriptomes across the complete Plasmodium life cycle. Science 365, eaaw2619. https://doi.org/10.1126/science.aaw2619

Iengar, P., Joshi, N.V., 2009. Identification of putative regulatory motifs in the upstream regions of co-expressed functional groups of genes in Plasmodium falciparum. BMC Genomics 10, 18. https://doi.org/10.1186/1471-2164-10-18

Iwanaga, S., Kaneko, I., Kato, T., Yuda, M., 2012. Identification of an AP2-family protein that is critical for malaria liver stage development. PLoS ONE 7, e47557. https://doi.org/10.1371/journal.pone.0047557

Iyer, L.M., Anantharaman, V., Wolf, M.Y., Aravind, L., 2008. Comparative genomics of transcription factors and chromatin proteins in parasitic protists and other eukaryotes. Int. J. Parasitol. 38, 1–31. https://doi.org/10.1016/j.ijpara.2007.07.018

Jagani, Z., Chenail, G., Xiang, K., Bushold, G., Bhang, H.-E.C., Li, A., Elliott, G., Zhu, J., Vattay, A., Gilbert, T., Bric, A., Kikkawa, R., Dubost, V., Terranova, R., Cantwell, J., Luu, C., Silver, S., Shirley, M., Huet, F., Maher, R., Reece-Hoyes, J., Ruddy, D., Rakiec, D., Korn, J., Russ, C., Ruda, V., Dooley, J., Costa, E., Park, I., Moebitz, H., Nakajima, K., Adair, C.D., Mathieu, S., Ntaganda, R., Smith, T., Farley, D., King, D., Xie, X., Kulathila, R., Hu, T., Pan, X., Ma, Q., Vulic, K., Rago, F., Clarkson, S., Ge, R., Sigoillot, F., Pardee, G., Bagdasarian, L., McLaughlin, M., Haas, K., Weiler, J., Kovats, S., Jaskelioff, M., Apolline-Gerard, M., Beil, J., Naumann, U., Fortin, P., Stegmeier, F.P., Acker, M.G., Williams, J., Meyer, M., Bradner, J.E., Keen, N., Sellers, W.R., Hofmann, F., Engelman, J.A., Stuart, D., Papillon, J.P.N., 2019. In-Depth Characterization and Validation in *BRG1* -Mutant Lung Cancers Define Novel Catalytic Inhibitors of SWI/SNF Chromatin Remodeling (preprint). Cancer Biology. https://doi.org/10.1101/812628

Jansson-Löfmark, R., Hjorth, S., Gabrielsson, J., 2020. Does *In Vitro* Potency Predict Clinically Efficacious Concentrations? Clin. Pharmacol. Ther. 108, 298–305. https://doi.org/10.1002/cpt.1846

Jeninga, M., Quinn, J., Petter, M., 2019. ApiAP2 Transcription Factors in Apicomplexan Parasites. Pathogens 8, 47. https://doi.org/10.3390/pathogens8020047

Jeninga, M.D., Tang, J., Selvarajah, S.A., Maier, A.G., Duffy, M.F., Petter, M., 2023. Plasmodium falciparum gametocytes display global chromatin remodelling during sexual differentiation. BMC Biol 21, 65. https://doi.org/10.1186/s12915-023-01568-4

Jenuwein, T., 2001. Translating the Histone Code. Science 293, 1074–1080. https://doi.org/10.1126/science.1063127

Jerabek-Willemsen, M., André, T., Wanner, R., Roth, H.M., Duhr, S., Baaske, P., Breitsprecher, D., 2014. MicroScale Thermophoresis: Interaction analysis and beyond. Journal of Molecular Structure 1077, 101–113. https://doi.org/10.1016/j.molstruc.2014.03.009

Ji, D.D., Arnot, D.E., 1997. A Plasmodium falciparum homologue of the ATPase subunit of a multi-protein complex involved in chromatin remodelling for transcription. Mol. Biochem. Parasitol. 88, 151–162.

Jiang, H., Lei, R., Ding, S.-W., Zhu, S., 2014. Skewer: A Fast and Accurate Adapter Trimmer for next-Generation Sequencing Paired-End Reads. BMC bioinformatics 15, 182. https://doi.org/10.1186/1471-2105-15-182

Jonsdottir, T.K., Gabriela, M., Crabb, B.S., F de Koning-Ward, T., Gilson, P.R., 2021. Defining the Essential Exportome of the Malaria Parasite. Trends Parasitol 37, 664–675. https://doi.org/10.1016/j.pt.2021.04.009

Josling, G.A., Llinás, M., 2015. Sexual development in Plasmodium parasites: knowing when it's time to commit. Nat Rev Microbiol 13, 573–587. https://doi.org/10.1038/nrmicro3519

Josling, G.A., Petter, M., Oehring, S.C., Gupta, A.P., Dietz, O., Wilson, D.W., Schubert, T., Längst, G., Gilson, P.R., Crabb, B.S., Moes, S., Jenoe, P., Lim, S.W., Brown, G.V., Bozdech, Z., Voss, T.S., Duffy, M.F., 2015. A Plasmodium Falciparum Bromodomain Protein Regulates Invasion Gene Expression. Cell Host Microbe 17, 741–751. https://doi.org/10.1016/j.chom.2015.05.009

Jumper, J., Evans, R., Pritzel, A., Green, T., Figurnov, M., Ronneberger, O., Tunyasuvunakool, K., Bates, R., Žídek, A., Potapenko, A., Bridgland, A., Meyer, C., Kohl, S.A.A., Ballard, A.J., Cowie, A., Romera-Paredes, B., Nikolov, S., Jain, R., Adler, J., Back, T., Petersen, S., Reiman, D., Clancy, E., Zielinski, M., Steinegger, M., Pacholska, M., Berghammer, T., Bodenstein, S., Silver, D., Vinyals, O., Senior, A.W., Kavukcuoglu, K., Kohli, P., Hassabis, D., 2021. Highly accurate protein structure prediction with AlphaFold. Nature 596, 583–589. https://doi.org/10.1038/s41586-021-03819-2

Kafsack, B.F.C., Rovira-Graells, N., Clark, T.G., Bancells, C., Crowley, V.M., Campino, S.G., Williams, A.E., Drought, L.G., Kwiatkowski, D.P., Baker, D.A., Cortés, A., Llinás, M., 2014. A transcriptional switch underlies commitment to sexual development in malaria parasites. Nature 507, 248–252. https://doi.org/10.1038/nature12920

Kagalwala, M.N., Glaus, B.J., Dang, W., Zofall, M., Bartholomew, B., 2004. Topography of the ISW2–nucleosome complex: insights into nucleosome spacing and chromatin remodeling. EMBO J 23, 2092–2104. https://doi.org/10.1038/sj.emboj.7600220

Kamakaka, R.T., 2005. Histone variants: deviants? Genes & Development 19, 295–316. https://doi.org/10.1101/gad.1272805

Kaneko, I., Nishi, T., Iwanaga, S., Yuda, M., 2023. Differentiation of *Plasmodium* male gametocytes is initiated by the recruitment of a chromatin remodeler to a male-specific cis-element. Proc. Natl. Acad. Sci. U.S.A. 120, e2303432120. https://doi.org/10.1073/pnas.2303432120

Kassambara, A., 2022. Ggpubr: “ggplot2” Based Publication Ready Plots.

Katsuno, K., Burrows, J.N., Duncan, K., van Huijsduijnen, R.H., Kaneko, T., Kita, K., Mowbray, C.E., Schmatz, D., Warner, P., Slingsby, B.T., 2015. Hit and lead criteria in drug discovery for infectious diseases of the developing world. Nat Rev Drug Discov 14, 751–758. https://doi.org/10.1038/nrd4683

Kaya-Okur, H.S., Wu, S.J., Codomo, C.A., Pledger, E.S., Bryson, T.D., Henikoff, J.G., Ahmad, K., Henikoff, S., 2019. CUT&Tag for efficient epigenomic profiling of small samples and single cells. Nat Commun 10, 1930. https://doi.org/10.1038/s41467-019-09982-5

Kensche, P.R., Hoeijmakers, W.A.M., Toenhake, C.G., Bras, M., Chappell, L., Berriman, M., Bártfai, R., 2016. The nucleosome landscape of *Plasmodium falciparum* reveals chromatin architecture and dynamics of regulatory sequences. Nucleic Acids Research 44, 2110–2124. https://doi.org/10.1093/nar/gkv1214

Kleman-Leyer, K.M., Klink, T.A., Kopp, A.L., Westermeyer, T.A., Koeff, M.D., Larson, B.R., Worzella, T.J., Pinchard, C.A., van de Kar, S.A.T., Zaman, G.J.R., Hornberg, J.J., Lowery, R.G., 2009. Characterization and optimization of a red-shifted fluorescence polarization ADP detection assay. Assay Drug Dev Technol 7, 56–67. https://doi.org/10.1089/adt.2008.175

Kunzelmann, S., Webb, M.R., 2010. A Fluorescent, Reagentless Biosensor for ADP Based on Tetramethylrhodamine-Labeled ParM. ACS Chemical Biology 5, 415–425. https://doi.org/10.1021/cb9003173

Kunzelmann, S., Webb, M.R., 2009. A Biosensor for Fluorescent Determination of ADP with High Time Resolution. Journal of Biological Chemistry 284, 33130–33138. https://doi.org/10.1074/jbc.M109.047118

Kuznetsov, D., Tegenfeldt, F., Manni, M., Seppey, M., Berkeley, M., Kriventseva, E.V., Zdobnov, E.M., 2023. OrthoDB v11: annotation of orthologs in the widest sampling of organismal diversity. Nucleic Acids Res 51, D445–D451. https://doi.org/10.1093/nar/gkac998

Lai, W.K.M., Pugh, B.F., 2017. Understanding nucleosome dynamics and their links to gene expression and DNA replication. Nat Rev Mol Cell Biol 18, 548–562. https://doi.org/10.1038/nrm.2017.47

Lambert, S.A., Jolma, A., Campitelli, L.F., Das, P.K., Yin, Y., Albu, M., Chen, X., Taipale, J., Hughes, T.R., Weirauch, M.T., 2018. The Human Transcription Factors. Cell 172, 650–665. https://doi.org/10.1016/j.cell.2018.01.029

Langmead, B., Salzberg, S.L., 2012. Fast Gapped-Read Alignment with Bowtie 2. Nature Methods 9, 357–359. https://doi.org/10.1038/nmeth.1923

Längst, G., Becker, P.B., 2001. ISWI Induces Nucleosome Sliding on Nicked DNA. Molecular Cell 8, 1085–1092. https://doi.org/10.1016/S1097-2765(01)00397-5

Längst, G., Manelyte, L., 2015. Chromatin Remodelers: From Function to Dysfunction. Genes 6, 299–324. https://doi.org/10.3390/genes6020299

Laybourn, P.J., Kadonaga, J.T., 1991. Role of nucleosomal cores and histone H1 in regulation of transcription by RNA polymerase II. Science 254, 238–245. https://doi.org/10.1126/science.254.5029.238

Le Roch, K.G., Zhou, Y., Blair, P.L., Grainger, M., Moch, J.K., Haynes, J.D., De La Vega, P., Holder, A.A., Batalov, S., Carucci, D.J., Winzeler, E.A., 2003. Discovery of gene function by expression profiling of the malaria parasite life cycle. Science 301, 1503–1508. https://doi.org/10.1126/science.1087025

Lemieux, J.E., Gomez-Escobar, N., Feller, A., Carret, C., Amambua-Ngwa, A., Pinches, R., Day, F., Kyes, S.A., Conway, D.J., Holmes, C.C., Newbold, C.I., 2009. Statistical estimation of cell-cycle progression and lineage commitment in *Plasmodium falciparum* reveals a homogeneous pattern of transcription in ex vivo culture. Proc. Natl. Acad. Sci. U.S.A. 106, 7559–7564. https://doi.org/10.1073/pnas.0811829106

Leonard, J.D., Narlikar, G.J., 2015. A Nucleotide-Driven Switch Regulates Flanking DNA Length Sensing by a Dimeric Chromatin Remodeler. Molecular Cell 57, 850–859. https://doi.org/10.1016/j.molcel.2015.01.008

Levo, M., Segal, E., 2014. In pursuit of design principles of regulatory sequences. Nature Reviews Genetics 15, 453–468. https://doi.org/10.1038/nrg3684

Li, H., Handsaker, B., Wysoker, A., Fennell, T., Ruan, J., Homer, N., Marth, G., Abecasis, G., Durbin, R., 1000 Genome Project Data Processing Subgroup, 2009. The Sequence Alignment/Map Format and SAMtools. Bioinformatics (Oxford, England) 25, 2078–2079. https://doi.org/10.1093/bioinformatics/btp352

Liao, Y., Smyth, G.K., Shi, W., 2019. The R package Rsubread is easier, faster, cheaper and better for alignment and quantification of RNA sequencing reads. Nucleic Acids Res 47, e47. https://doi.org/10.1093/nar/gkz114

Liao, Y., Smyth, G.K., Shi, W., 2014. featureCounts: an efficient general purpose program for assigning sequence reads to genomic features. Bioinformatics 30, 923–930. https://doi.org/10.1093/bioinformatics/btt656

Lieleg, C., Krietenstein, N., Walker, M., Korber, P., 2015. Nucleosome positioning in yeasts: methods, maps, and mechanisms. Chromosoma 124, 131–151. https://doi.org/10.1007/s00412-014-0501-x

Linke, P., Amaning, K., Maschberger, M., Vallee, F., Steier, V., Baaske, P., Duhr, S., Breitsprecher, D., Rak, A., 2016. An Automated Microscale Thermophoresis Screening Approach for Fragment-Based Lead Discovery. J Biomol Screen 21, 414–421. https://doi.org/10.1177/1087057115618347

Linzweiler, W., Horz, W., 1985. Reconstitution experiments show that sequence-specific histone-DNA interactions are the basis for nucleosome phasing on mouse satellite DNA. Cell 42, 281–290. https://doi.org/10.1016/S0092-8674(85)80123-9

Llorà-Batlle, O., Michel-Todó, L., Witmer, K., Toda, H., Fernández-Becerra, C., Baum, J., Cortés, A., 2020. Conditional expression of PfAP2-G for controlled massive sexual conversion in *Plasmodium falciparum*. Sci. Adv. 6, eaaz5057. https://doi.org/10.1126/sciadv.aaz5057

López-Barragán, M.J., Lemieux, J., Quiñones, M., Williamson, K.C., Molina-Cruz, A., Cui, K., Barillas-Mury, C., Zhao, K., Su, X., 2011. Directional gene expression and antisense transcripts in sexual and asexual stages of Plasmodium falciparum. BMC Genomics 12, 587. https://doi.org/10.1186/1471-2164-12-587

Love, M.I., Huber, W., Anders, S., 2014. Moderated estimation of fold change and dispersion for RNA-seq data with DESeq2. Genome Biol 15, 550. https://doi.org/10.1186/s13059-014-0550-8

Lu, Z., Lin, Z., 2019. Pervasive and dynamic transcription initiation in *Saccharomyces cerevisiae*. Genome Res. 29, 1198–1210. https://doi.org/10.1101/gr.245456.118

Lucius, R., Loos-Frank, B., Lane, R.P., Poulin, R., Roberts, C.W., Grencis, R.K., 2017. The Biology of Parasites. Wiley-VCH Verlag GmbH & Co. KGaA, Weinheim.

Ludwigsen, J., Pfennig, S., Singh, A.K., Schindler, C., Harrer, N., Forné, I., Zacharias, M., Mueller-Planitz, F., 2017. Concerted regulation of ISWI by an autoinhibitory domain and the H4 N-terminal tail. eLife 6. https://doi.org/10.7554/eLife.21477

Lusser, A., Urwin, D.L., Kadonaga, J.T., 2005. Distinct activities of CHD1 and ACF in ATP-dependent chromatin assembly. Nat Struct Mol Biol 12, 160–166. https://doi.org/10.1038/nsmb884

Maier, A.G., Cooke, B.M., Cowman, A.F., Tilley, L., 2009. Malaria parasite proteins that remodel the host erythrocyte. Nat Rev Microbiol 7, 341–354. https://doi.org/10.1038/nrmicro2110

Maier, A.G., Matuschewski, K., Zhang, M., Rug, M., 2019. Plasmodium falciparum. Trends in Parasitology 35, 481–482. https://doi.org/10.1016/j.pt.2018.11.010

Maier, A.G., Rug, M., O'Neill, M.T., Brown, M., Chakravorty, S., Szestak, T., Chesson, J., Wu, Y., Hughes, K., Coppel, R.L., Newbold, C., Beeson, J.G., Craig, A., Crabb, B.S., Cowman, A.F., 2008. Exported proteins required for virulence and rigidity of Plasmodium falciparum-infected human erythrocytes. Cell 134, 48–61. https://doi.org/10.1016/j.cell.2008.04.051

Maldonado, R., Schwartz, U., Silberhorn, E., Längst, G., 2019. Nucleosomes Stabilize ssRNA-dsDNA Triple Helices in Human Cells. Molecular Cell 73, 1243-1254.e6. https://doi.org/10.1016/j.molcel.2019.01.007

Martire, S., Banaszynski, L.A., 2020. The roles of histone variants in fine-tuning chromatin organization and function. Nat Rev Mol Cell Biol 21, 522–541. https://doi.org/10.1038/s41580-020-0262-8

Mbengue, A., Audiger, N., Vialla, E., Dubremetz, J.-F., Braun-Breton, C., 2013. Novel *Plasmodium falciparum* Maurer's clefts protein families implicated in the release of infectious merozoites: Novel *P. falciparum* exported proteins. Molecular Microbiology 88, 425–442. https://doi.org/10.1111/mmi.12193

McGinty, R.K., Tan, S., 2015. Nucleosome Structure and Function. Chem. Rev. 115, 2255–2273. https://doi.org/10.1021/cr500373h

McKnight, J.N., Jenkins, K.R., Nodelman, I.M., Escobar, T., Bowman, G.D., 2011. Extranucleosomal DNA binding directs nucleosome sliding by Chd1. Mol Cell Biol 31, 4746–4759. https://doi.org/10.1128/MCB.05735-11

Meerstein-Kessel, L., Venhuizen, J., Garza, D., Proellochs, N.I., Vos, E.J., Obiero, J.M., Felgner, P.L., Sauerwein, R.W., Peters, M., Yang, A.S.P., Huynen, M.A., 2021. Novel insights from the Plasmodium falciparum sporozoite-specific proteome by probabilistic integration of 26 studies. PLoS Comput Biol 17, e1008067. https://doi.org/10.1371/journal.pcbi.1008067

Mengeritsky, G., Trifonov, E.N., 1983. Nucleotide sequence-directed mapping of the nucleosomes. Nucleic Acids Res 11, 3833–3851. https://doi.org/10.1093/nar/11.11.3833

Miao, J., Fan, Q., Cui, Long, Li, Junsuo, Li, Jianyong, Cui, Liwang, 2006. The malaria parasite Plasmodium falciparum histones: organization, expression, and acetylation. Gene 369, 53–65. https://doi.org/10.1016/j.gene.2005.10.022

Miao, J., Wang, C., Lucky, A.B., Liang, X., Min, H., Adapa, S.R., Jiang, R., Kim, K., Cui, L., 2021. A unique GCN5 histone acetyltransferase complex controls erythrocyte invasion and virulence in the malaria parasite Plasmodium falciparum. PLoS Pathog 17, e1009351. https://doi.org/10.1371/journal.ppat.1009351

Millholland, M.G., Chandramohanadas, R., Pizzarro, A., Wehr, A., Shi, H., Darling, C., Lim, C.T., Greenbaum, D.C., 2011. The malaria parasite progressively dismantles the host erythrocyte cytoskeleton for efficient egress. Mol Cell Proteomics 10, M111.010678. https://doi.org/10.1074/mcp.M111.010678

Mills, J.P., Diez-Silva, M., Quinn, D.J., Dao, M., Lang, M.J., Tan, K.S.W., Lim, C.T., Milon, G., David, P.H., Mercereau-Puijalon, O., Bonnefoy, S., Suresh, S., 2007. Effect of plasmodial RESA protein on deformability of human red blood cells harboring Plasmodium falciparum. Proc Natl Acad Sci U S A 104, 9213–9217. https://doi.org/10.1073/pnas.0703433104

Mito, Y., Henikoff, J.G., Henikoff, S., 2005. Genome-scale profiling of histone H3.3 replacement patterns. Nat Genet 37, 1090–1097. https://doi.org/10.1038/ng1637

Modrzynska, K., Pfander, C., Chappell, L., Yu, L., Suarez, C., Dundas, K., Gomes, A.R., Goulding, D., Rayner, J.C., Choudhary, J., Billker, O., 2017. A Knockout Screen of ApiAP2 Genes Reveals Networks of Interacting Transcriptional Regulators Controlling the Plasmodium Life Cycle. Cell Host & Microbe 21, 11–22. https://doi.org/10.1016/j.chom.2016.12.003

Mölder, F., Jablonski, K.P., Letcher, B., Hall, M.B., Tomkins-Tinch, C.H., Sochat, V., Forster, J., Lee, S., Twardziok, S.O., Kanitz, A., Wilm, A., Holtgrewe, M., Rahmann, S., Nahnsen, S., Köster, J., 2021. Sustainable data analysis with Snakemake. F1000Res 10, 33. https://doi.org/10.12688/f1000research.29032.2

Morrison, A.J., Shen, X., 2009. Chromatin remodelling beyond transcription: the INO80 and SWR1 complexes. Nature Reviews Molecular Cell Biology 10, 373–384. https://doi.org/10.1038/nrm2693

Mueller-Planitz, F., Klinker, H., Ludwigsen, J., Becker, P.B., 2013. The ATPase domain of ISWI is an autonomous nucleosome remodeling machine. Nat Struct Mol Biol 20, 82–89. https://doi.org/10.1038/nsmb.2457

Mundwiler-Pachlatko, E., Beck, H.-P., 2013. Maurer's clefts, the enigma of Plasmodium falciparum. Proceedings of the National Academy of Sciences 110, 19987–19994. https://doi.org/10.1073/pnas.1309247110

Muralidharan, V., Goldberg, D.E., 2013. Asparagine repeats in Plasmodium falciparum proteins: good for nothing? PLoS Pathog 9, e1003488. https://doi.org/10.1371/journal.ppat.1003488

Myant, K., Stancheva, I., 2008. LSH Cooperates with DNA Methyltransferases To Repress Transcription. MCB 28, 215–226. https://doi.org/10.1128/MCB.01073-07

Narlikar, G.J., Fan, H.-Y., Kingston, R.E., 2002. Cooperation between Complexes that Regulate Chromatin Structure and Transcription. Cell 108, 475–487. https://doi.org/10.1016/S0092-8674(02)00654-2

Narlikar, G.J., Sundaramoorthy, R., Owen-Hughes, T., 2013. Mechanisms and Functions of ATP-Dependent Chromatin-Remodeling Enzymes. Cell 154, 490–503. https://doi.org/10.1016/j.cell.2013.07.011

Ngara, M., Palmkvist, M., Sagasser, S., Hjelmqvist, D., Björklund, Å.K., Wahlgren, M., Ankarklev, J., Sandberg, R., 2018. Exploring parasite heterogeneity using single-cell RNA-seq reveals a gene signature among sexual stage Plasmodium falciparum parasites. Experimental Cell Research 371, 130–138. https://doi.org/10.1016/j.yexcr.2018.08.003

Nikitina, T., Wang, D., Gomberg, M., Grigoryev, S.A., Zhurkin, V.B., 2013. Combined micrococcal nuclease and exonuclease III digestion reveals precise positions of the nucleosome core/linker junctions: implications for high-resolution nucleosome mapping. J Mol Biol 425, 1946–1960. https://doi.org/10.1016/j.jmb.2013.02.026

Ocampo, J., Chereji, R.V., Eriksson, P.R., Clark, D.J., 2016. The ISW1 and CHD1 ATP-dependent chromatin remodelers compete to set nucleosome spacing *in vivo*. Nucleic Acids Res 44, 4625–4635. https://doi.org/10.1093/nar/gkw068

Okonechnikov, K., Conesa, A., García-Alcalde, F., 2016. Qualimap 2: Advanced Multi-Sample Quality Control for High-Throughput Sequencing Data. Bioinformatics (Oxford, England) 32, 292–294. https://doi.org/10.1093/bioinformatics/btv566

Oppikofer, M., Bai, T., Gan, Y., Haley, B., Liu, P., Sandoval, W., Ciferri, C., Cochran, A.G., 2017. Expansion of the ISWI chromatin remodeler family with new active complexes. EMBO Rep 18, 1697–1706. https://doi.org/10.15252/embr.201744011

Otto, T.D., Wilinski, D., Assefa, S., Keane, T.M., Sarry, L.R., Böhme, U., Lemieux, J., Barrell, B., Pain, A., Berriman, M., Newbold, C., Llinás, M., 2010. New insights into the blood-stage transcriptome of Plasmodium falciparum using RNA-Seq. Mol. Microbiol. 76, 12–24. https://doi.org/10.1111/j.1365-2958.2009.07026.x

Painter, H.J., Chung, N.C., Sebastian, A., Albert, I., Storey, J.D., Llinás, M., 2018. Genome-wide real-time in vivo transcriptional dynamics during Plasmodium falciparum blood-stage development. Nat Commun 9, 2656. https://doi.org/10.1038/s41467-018-04966-3

Pantano, L., 2022. DEGreport: Report of DEG Analysis.

Papillon, J.P.N., Nakajima, K., Adair, C.D., Hempel, J., Jouk, A.O., Karki, R.G., Mathieu, S., Möbitz, H., Ntaganda, R., Smith, T., Visser, M., Hill, S.E., Hurtado, F.K., Chenail, G., Bhang, H.-E.C., Bric, A., Xiang, K., Bushold, G., Gilbert, T., Vattay, A., Dooley, J., Costa, E.A., Park, I., Li, A., Farley, D., Lounkine, E., Yue, Q.K., Xie, X., Zhu, X., Kulathila, R., King, D., Hu, T., Vulic, K., Cantwell, J., Luu, C., Jagani, Z., 2018. Discovery of Orally Active Inhibitors of Brahma Homolog (BRM)/SMARCA2 ATPase Activity for the Treatment of Brahma Related Gene 1 (BRG1)/SMARCA4-Mutant Cancers. J. Med. Chem. 61, 10155–10172. https://doi.org/10.1021/acs.jmedchem.8b01318

Pertea, G., Pertea, M., 2020. GFF Utilities: GffRead and GffCompare. F1000Res 9, ISCB Comm J-304. https://doi.org/10.12688/f1000research.23297.2

Pesole, G., 2002. UTRdb and UTRsite: specialized databases of sequences and functional elements of 5’ and 3’ untranslated regions of eukaryotic mRNAs. Update 2002. Nucleic Acids Research 30, 335–340. https://doi.org/10.1093/nar/30.1.335

Petter, M., Selvarajah, S.A., Lee, C.C., Chin, W.H., Gupta, A.P., Bozdech, Z., Brown, G.V., Duffy, M.F., 2013. H2A.Z and H2B.Z double-variant nucleosomes define intergenic regions and dynamically occupy var gene promoters in the malaria parasite Plasmodium falciparum. Mol. Microbiol. 87, 1167–1182. https://doi.org/10.1111/mmi.12154

Petty, E., Pillus, L., 2013. Balancing chromatin remodeling and histone modifications in transcription. Trends in Genetics 29, 621–629. https://doi.org/10.1016/j.tig.2013.06.006

Pointner, J., Persson, J., Prasad, P., Norman-Axelsson, U., Strålfors, A., Khorosjutina, O., Krietenstein, N., Peter Svensson, J., Ekwall, K., Korber, P., 2012. CHD1 remodelers regulate nucleosome spacing *in vitro* and align nucleosomal arrays over gene coding regions in *S. pombe*: CHD1 remodelers generate genic arrays in *S. pombe*. The EMBO Journal 31, 4388–4403. https://doi.org/10.1038/emboj.2012.289

Ponts, N., Harris, E.Y., Lonardi, S., Le Roch, K.G., 2011. Nucleosome occupancy at transcription start sites in the human malaria parasite: a hard-wired evolution of virulence? Infect. Genet. Evol. 11, 716–724. https://doi.org/10.1016/j.meegid.2010.08.002

Ponts, N., Harris, E.Y., Prudhomme, J., Wick, I., Eckhardt-Ludka, C., Hicks, G.R., Hardiman, G., Lonardi, S., Le Roch, K.G., 2010. Nucleosome landscape and control of transcription in the human malaria parasite. Genome Res. 20, 228–238. https://doi.org/10.1101/gr.101063.109

Poran, A., Nötzel, C., Aly, O., Mencia-Trinchant, N., Harris, C.T., Guzman, M.L., Hassane, D.C., Elemento, O., Kafsack, B.F.C., 2017. Single-cell RNA sequencing reveals a signature of sexual commitment in malaria parasites. Nature 551, 95–99. https://doi.org/10.1038/nature24280

Prommana, P., Uthaipibull, C., Wongsombat, C., Kamchonwongpaisan, S., Yuthavong, Y., Knuepfer, E., Holder, A.A., Shaw, P.J., 2013. Inducible Knockdown of Plasmodium Gene Expression Using the glmS Ribozyme. PLoS ONE 8, e73783. https://doi.org/10.1371/journal.pone.0073783

Prudêncio, M., Rodriguez, A., Mota, M.M., 2006. The silent path to thousands of merozoites: the Plasmodium liver stage. Nat Rev Microbiol 4, 849–856. https://doi.org/10.1038/nrmicro1529

R Core Team, 2022. R: A Language and Environment for Statistical Computing.

Rainard, J.M., Pandarakalam, G.C., McElroy, S.P., 2018. Using Microscale Thermophoresis to Characterize Hits from High-Throughput Screening: A European Lead Factory Perspective. SLAS Discov 23, 225–241. https://doi.org/10.1177/2472555217744728

Rajapandi, T., 2020. Chaperoning of asparagine repeat-containing proteins in Plasmodium falciparum. J Parasit Dis 44, 687–693. https://doi.org/10.1007/s12639-020-01251-3

Ramírez, F., Ryan, D.P., Grüning, B., Bhardwaj, V., Kilpert, F., Richter, A.S., Heyne, S., Dündar, F., Manke, T., 2016. deepTools2: A next Generation Web Server for Deep-Sequencing Data Analysis. Nucleic Acids Research 44, W160-165. https://doi.org/10.1093/nar/gkw257

Read, D.F., Cook, K., Lu, Y.Y., Le Roch, K., Noble, W., 2019. Predicting gene expression in the human malaria parasite Plasmodium falciparum. bioRxiv. https://doi.org/10.1101/431049

Real, E., Howick, V.M., Dahalan, F.A., Witmer, K., Cudini, J., Andradi-Brown, C., Blight, J., Davidson, M.S., Dogga, S.K., Reid, A.J., Baum, J., Lawniczak, M.K.N., 2021. A single-cell atlas of Plasmodium falciparum transmission through the mosquito. Nat Commun 12, 3196. https://doi.org/10.1038/s41467-021-23434-z

Reece, J.B., Campbell, N.A., 2011. Campbell biology. Benjamin Cummings / Pearson, Boston.

Reid, A.J., Talman, A.M., Bennett, H.M., Gomes, A.R., Sanders, M.J., Illingworth, C.J.R., Billker, O., Berriman, M., Lawniczak, M.K., 2018. Single-cell RNA-seq reveals hidden transcriptional variation in malaria parasites. Elife 7. https://doi.org/10.7554/eLife.33105

Ren, J., Briones, V., Barbour, S., Yu, W., Han, Y., Terashima, M., Muegge, K., 2015. The ATP binding site of the chromatin remodeling homolog Lsh is required for nucleosome density and de novo DNA methylation at repeat sequences. Nucleic Acids Research 43, 1444–1455. https://doi.org/10.1093/nar/gku1371

Rippe, K., Schrader, A., Riede, P., Strohner, R., Lehmann, E., Längst, G., 2007. DNA sequence- and conformation-directed positioning of nucleosomes by chromatin-remodeling complexes. Proc Natl Acad Sci U S A 104, 15635–15640. https://doi.org/10.1073/pnas.0702430104

Robinson, J.T., Thorvaldsdóttir, H., Winckler, W., Guttman, M., Lander, E.S., Getz, G., Mesirov, J.P., 2011. Integrative genomics viewer. Nat Biotechnol 29, 24–26. https://doi.org/10.1038/nbt.1754

Rovira-Graells, N., Gupta, A.P., Planet, E., Crowley, V.M., Mok, S., Ribas de Pouplana, L., Preiser, P.R., Bozdech, Z., Cortés, A., 2012. Transcriptional variation in the malaria parasite Plasmodium falciparum. Genome Res. 22, 925–938. https://doi.org/10.1101/gr.129692.111

Rowley, M.J., Corces, V.G., 2016. The three-dimensional genome: principles and roles of long-distance interactions. Current Opinion in Cell Biology 40, 8–14. https://doi.org/10.1016/j.ceb.2016.01.009

Ruiz, J.L., Tena, J.J., Bancells, C., Cortés, A., Gómez-Skarmeta, J.L., Gómez-Díaz, E., 2018. Characterization of the accessible genome in the human malaria parasite Plasmodium falciparum. Nucleic Acids Research 46, 9414–9431. https://doi.org/10.1093/nar/gky643

Russell, K., Cheng, C.-H., Bizzaro, J.W., Ponts, N., Emes, R.D., Le Roch, K., Marx, K.A., Horrocks, P., 2014. Homopolymer tract organization in the human malarial parasite Plasmodium falciparum and related Apicomplexan parasites. BMC Genomics 15, 848. https://doi.org/10.1186/1471-2164-15-848

Salcedo-Amaya, A.M., van Driel, M.A., Alako, B.T., Trelle, M.B., van den Elzen, A.M.G., Cohen, A.M., Janssen-Megens, E.M., van de Vegte-Bolmer, M., Selzer, R.R., Iniguez, A.L., Green, R.D., Sauerwein, R.W., Jensen, O.N., Stunnenberg, H.G., 2009. Dynamic histone H3 epigenome marking during the intraerythrocytic cycle of Plasmodium falciparum. Proc. Natl. Acad. Sci. U.S.A. 106, 9655–9660. https://doi.org/10.1073/pnas.0902515106

Sambrook, J., Russell, D.W., 2001. Molecular cloning: a laboratory manual, 3rd ed. ed. Cold Spring Harbor Laboratory Press, Cold Spring Harbor, N.Y.

Santos, J.M., Josling, G., Ross, P., Joshi, P., Orchard, L., Campbell, T., Schieler, A., Cristea, I.M., Llinás, M., 2017. Red Blood Cell Invasion by the Malaria Parasite Is Coordinated by the PfAP2-I Transcription Factor. Cell Host Microbe 21, 731-741.e10. https://doi.org/10.1016/j.chom.2017.05.006

Saraf, A., Cervantes, S., Bunnik, E.M., Ponts, N., Sardiu, M.E., Chung, D.-W.D., Prudhomme, J., Varberg, J.M., Wen, Z., Washburn, M.P., Florens, L., Le Roch, K.G., 2016. Dynamic and Combinatorial Landscape of Histone Modifications during the Intraerythrocytic Developmental Cycle of the Malaria Parasite. J. Proteome Res. 15, 2787–2801. https://doi.org/10.1021/acs.jproteome.6b00366

Sato, S., 2021. Plasmodium—a brief introduction to the parasites causing human malaria and their basic biology. J Physiol Anthropol 40, 1. https://doi.org/10.1186/s40101-020-00251-9

Sbardella, G., 2019. Methyl-Readers and Inhibitors, in: Mai, A. (Ed.), Chemical Epigenetics, Topics in Medicinal Chemistry. Springer International Publishing, Cham, pp. 339–399. https://doi.org/10.1007/7355_2019_78

Scherf, A., Lopez-Rubio, J.J., Riviere, L., 2008. Antigenic Variation in *Plasmodium falciparum*. Annu. Rev. Microbiol. 62, 445–470. https://doi.org/10.1146/annurev.micro.61.080706.093134

Schuster, F.L., 2002. Cultivation of plasmodium spp. Clin Microbiol Rev 15, 355–364. https://doi.org/10.1128/CMR.15.3.355-364.2002

Schwartz, U., Németh, A., Diermeier, S., Exler, J.H., Hansch, S., Maldonado, R., Heizinger, L., Merkl, R., Längst, G., 2019. Characterizing the nuclease accessibility of DNA in human cells to map higher order structures of chromatin. Nucleic Acids Research 47, 1239–1254. https://doi.org/10.1093/nar/gky1203

Segal, E., Fondufe-Mittendorf, Y., Chen, L., Thåström, A., Field, Y., Moore, I.K., Wang, J.-P.Z., Widom, J., 2006. A genomic code for nucleosome positioning. Nature 442, 772–778. https://doi.org/10.1038/nature04979

Segal, E., Widom, J., 2009. What controls nucleosome positions? Trends in Genetics 25, 335–343. https://doi.org/10.1016/j.tig.2009.06.002

Sen, U., Nayak, A., Khurana, J., Sharma, D., Gupta, A., 2020. Inhibition of PfMYST Histone Acetyltransferase Activity Blocks Plasmodium falciparum Growth and Survival. Antimicrob Agents Chemother 65, e00953-20. https://doi.org/10.1128/AAC.00953-20

Shaw, P.J., Kaewprommal, P., Wongsombat, C., Ngampiw, C., Taechalertpaisarn, T., Kamchonwongpaisan, S., Tongsima, S., Piriyapongsa, J., 2022. Transcriptomic complexity of the human malaria parasite Plasmodium falciparum revealed by long-read sequencing. PLoS ONE 17, e0276956. https://doi.org/10.1371/journal.pone.0276956

Shaw, P.J., Piriyapongsa, J., Kaewprommal, P., Wongsombat, C., Chaosrikul, C., Teeravajanadet, K., Boonbangyang, M., Uthaipibull, C., Kamchonwongpaisan, S., Tongsima, S., 2021. Identifying transcript 5′ capped ends in *Plasmodium falciparum*. PeerJ 9, e11983. https://doi.org/10.7717/peerj.11983

Sherling, E.S., van Ooij, C., 2016. Host cell remodeling by pathogens: the exomembrane system in *Plasmodium* -infected erythrocytes. FEMS Microbiology Reviews 40, 701–721. https://doi.org/10.1093/femsre/fuw016

Siciliano, G., Costa, G., Suárez-Cortés, P., Valleriani, A., Alano, P., Levashina, E.A., 2020. Critical Steps of Plasmodium falciparum Ookinete Maturation. Front. Microbiol. 11, 269. https://doi.org/10.3389/fmicb.2020.00269

Silberhorn, E., Schwartz, U., Löffler, P., Schmitz, S., Symelka, A., de Koning-Ward, T., Merkl, R., Längst, G., 2016. Plasmodium falciparum Nucleosomes Exhibit Reduced Stability and Lost Sequence Dependent Nucleosome Positioning. PLoS Pathog. 12, e1006080. https://doi.org/10.1371/journal.ppat.1006080

Singh, G.P., Chandra, B.R., Bhattacharya, A., Akhouri, R.R., Singh, S.K., Sharma, A., 2004. Hyper-expansion of asparagines correlates with an abundance of proteins with prion-like domains in Plasmodium falciparum. Mol Biochem Parasitol 137, 307–319. https://doi.org/10.1016/j.molbiopara.2004.05.016

Singh, S., Santos, J.M., Orchard, L.M., Yamada, N., Biljon, R., Painter, H.J., Mahony, S., Llinás, M., 2021. The PfAP2-G2 transcription factor is a critical regulator of gametocyte maturation. Mol Microbiol 115, 1005–1024. https://doi.org/10.1111/mmi.14676

Sinha, A., Hughes, K.R., Modrzynska, K.K., Otto, T.D., Pfander, C., Dickens, N.J., Religa, A.A., Bushell, E., Graham, A.L., Cameron, R., Kafsack, B.F.C., Williams, A.E., Llinas, M., Berriman, M., Billker, O., Waters, A.P., 2014. A cascade of DNA-binding proteins for sexual commitment and development in Plasmodium. Nature 507, 253–257. https://doi.org/10.1038/nature12970

Skene, P.J., Henikoff, S., 2017. An efficient targeted nuclease strategy for high-resolution mapping of DNA binding sites. Elife 6, e21856. https://doi.org/10.7554/eLife.21856

Smolle, M., Venkatesh, S., Gogol, M.M., Li, H., Zhang, Y., Florens, L., Washburn, M.P., Workman, J.L., 2012. Chromatin remodelers Isw1 and Chd1 maintain chromatin structure during transcription by preventing histone exchange. Nat Struct Mol Biol 19, 884–892. https://doi.org/10.1038/nsmb.2312

Spielmann, T., Birnbaum, J., Flemming, S., Reichard, N., Blancke Soares, A., Mesén-Ramírez, P., Jonscher, E., Bergmann, B., Spielmann, T., 2017. Selection linked integration (SLI) for endogenous gene tagging and knock sideways in Plasmodium falciparum parasites. Protocol Exchange. https://doi.org/10.1038/protex.2017.022

Strohner, R., Wachsmuth, M., Dachauer, K., Mazurkiewicz, J., Hochstatter, J., Rippe, K., Längst, G., 2005. A “loop recapture” mechanism for ACF-dependent nucleosome remodeling. Nat Struct Mol Biol 12, 683–690. https://doi.org/10.1038/nsmb966

Su, X., Lane, K.D., Xia, L., Sá, J.M., Wellems, T.E., 2019. *Plasmodium* Genomics and Genetics: New Insights into Malaria Pathogenesis, Drug Resistance, Epidemiology, and Evolution. Clinical Microbiology Reviews 32. https://doi.org/10.1128/CMR.00019-19

Su, Y., Hickey, S.F., Keyser, S.G.L., Hammond, M.C., 2016. *In Vitro* and *In Vivo* Enzyme Activity Screening via RNA-Based Fluorescent Biosensors for *S* -Adenosyl- L -homocysteine (SAH). J. Am. Chem. Soc. 138, 7040–7047. https://doi.org/10.1021/jacs.6b01621

Sullivan, W.J., Monroy, M.A., Bohne, W., Nallani, K.C., Chrivia, J., Yaciuk, P., Smith, C.K., Queener, S.F., 2003. Molecular cloning and characterization of an SRCAP chromatin remodeling homologue in Toxoplasma gondii. Parasitol. Res. 90, 1–8. https://doi.org/10.1007/s00436-002-0814-1

Svejstrup, J.Q., 2003. Rescue of arrested RNA polymerase II complexes. Journal of Cell Science 116, 447–451. https://doi.org/10.1242/jcs.00271

Taylor, H.M., McRobert, L., Grainger, M., Sicard, A., Dluzewski, A.R., Hopp, C.S., Holder, A.A., Baker, D.A., 2010. The malaria parasite cyclic GMP-dependent protein kinase plays a central role in blood-stage schizogony. Eukaryot Cell 9, 37–45. https://doi.org/10.1128/EC.00186-09

Thomas, J.A., Collins, C.R., Das, S., Hackett, F., Graindorge, A., Bell, D., Deu, E., Blackman, M.J., 2016. Development and Application of a Simple Plaque Assay for the Human Malaria Parasite Plasmodium falciparum. PLoS ONE 11, e0157873. https://doi.org/10.1371/journal.pone.0157873

Toenhake, C.G., Bártfai, R., 2019. What functional genomics has taught us about transcriptional regulation in malaria parasites. Briefings in Functional Genomics. https://doi.org/10.1093/bfgp/elz004

Toenhake, C.G., Fraschka, S.A.-K., Vijayabaskar, M.S., Westhead, D.R., van Heeringen, S.J., Bártfai, R., 2018. Chromatin Accessibility-Based Characterization of the Gene Regulatory Network Underlying Plasmodium falciparum Blood-Stage Development. Cell Host Microbe 23, 557-569.e9. https://doi.org/10.1016/j.chom.2018.03.007

Trampuz, A., Jereb, M., Muzlovic, I., Prabhu, R.M., 2003. Clinical review: Severe malaria. Crit Care 7, 315. https://doi.org/10.1186/cc2183

Unk, I., Hajdú, I., Blastyák, A., Haracska, L., 2010. Role of yeast Rad5 and its human orthologs, HLTF and SHPRH in DNA damage tolerance. DNA Repair 9, 257–267. https://doi.org/10.1016/j.dnarep.2009.12.013

Usui, M., Prajapati, S.K., Ayanful-Torgby, R., Acquah, F.K., Cudjoe, E., Kakaney, C., Amponsah, J.A., Obboh, E.K., Reddy, D.K., Barbeau, M.C., Simons, L.M., Czesny, B., Raiciulescu, S., Olsen, C., Abuaku, B.K., Amoah, L.E., Williamson, K.C., 2019. Plasmodium falciparum sexual differentiation in malaria patients is associated with host factors and GDV1-dependent genes. Nat Commun 10, 2140. https://doi.org/10.1038/s41467-019-10172-6

van Biljon, R., van Wyk, R., Painter, H.J., Orchard, L., Reader, J., Niemand, J., Llinás, M., Birkholtz, L.-M., 2019. Hierarchical transcriptional control regulates Plasmodium falciparum sexual differentiation. BMC Genomics 20, 920. https://doi.org/10.1186/s12864-019-6322-9

Vanagas, L., Marisol Contreras, S., Angel, S., 2019. Apicomplexa and Histone Variants: What’s New?, in: Epigenetics and Chromatin [Working Title]. IntechOpen. https://doi.org/10.5772/intechopen.81409

Vannoort, V., Huynen, M., 2006. Combinatorial gene regulation in Plasmodium falciparum. Trends in Genetics 22, 73–78. https://doi.org/10.1016/j.tig.2005.12.002

Vardiman, J.W., 2006. Hematopathological Concepts and Controversies in the Diagnosis and Classification of Myelodysplastic Syndromes. Hematology 2006, 199–204. https://doi.org/10.1182/asheducation-2006.1.199

Vignali, M., Hassan, A.H., Neely, K.E., Workman, J.L., 2000. ATP-dependent chromatin-remodeling complexes. Mol Cell Biol 20, 1899–1910. https://doi.org/10.1128/MCB.20.6.1899-1910.2000

Wang, C., Gibbons, J., Adapa, S.R., Oberstaller, J., Liao, X., Zhang, M., Adams, J.H., Jiang, R.H.Y., 2020. The human malaria parasite genome is configured into thousands of co-expressed linear regulatory units. Journal of Genetics and Genomics. https://doi.org/10.1016/j.jgg.2020.08.005

Watanabe, J., Sasaki, M., Suzuki, Y., Sugano, S., 2002. Analysis of transcriptomes of human malaria parasite Plasmodium falciparum using full-length enriched library: identification of novel genes and diverse transcription start sites of messenger RNAs. Gene 291, 105–113.

Watzlowik, M.T., Das, S., Meissner, M., Längst, G., 2021. Peculiarities of Plasmodium falciparum Gene Regulation and Chromatin Structure. Int J Mol Sci 22, 5168. https://doi.org/10.3390/ijms22105168

Webb, M.R., Corrie, J.E., 2001. Fluorescent coumarin-labeled nucleotides to measure ADP release from actomyosin. Biophys J 81, 1562–1569. https://doi.org/10.1016/S0006-3495(01)75810-9

Westenberger, S.J., Cui, Long, Dharia, N., Winzeler, E., Cui, Liwang, 2009. Genome-wide nucleosome mapping of Plasmodium falciparum reveals histone-rich coding and histone-poor intergenic regions and chromatin remodeling of core and subtelomeric genes. BMC Genomics 10, 610. https://doi.org/10.1186/1471-2164-10-610

Whitehouse, I., Stockdale, C., Flaus, A., Szczelkun, M.D., Owen-Hughes, T., 2003. Evidence for DNA Translocation by the ISWI Chromatin-Remodeling Enzyme. Molecular and Cellular Biology 23, 1935–1945. https://doi.org/10.1128/MCB.23.6.1935-1945.2003

Wickham, H., Averick, M., Bryan, J., Chang, W., McGowan, L.D., François, R., Grolemund, G., Hayes, A., Henry, L., Hester, J., Kuhn, M., Pedersen, T.L., Miller, E., Bache, S.M., Müller, K., Ooms, J., Robinson, D., Seidel, D.P., Spinu, V., Takahashi, K., Vaughan, D., Wilke, C., Woo, K., Yutani, H., 2019. Welcome to the Tidyverse. Journal of Open Source Software 4, 1686. https://doi.org/10.21105/joss.01686

Widom, J., 2001. Role of DNA sequence in nucleosome stability and dynamics. Quart. Rev. Biophys. 34, 269–324. https://doi.org/10.1017/S0033583501003699

Wigle, T.J., Singleton, S.F., 2007. Directed molecular screening for RecA ATPase inhibitors. Bioorg Med Chem Lett 17, 3249–3253. https://doi.org/10.1016/j.bmcl.2007.04.013

World Health Organization, 2022. World malaria report 2022 License: CC BY-NC-SA 3.0 IGO.

Wu, J., Sieglaff, D.H., Gervin, J., Xie, X.S., 2008. Discovering regulatory motifs in the Plasmodium genome using comparative genomics. Bioinformatics 24, 1843–1849. https://doi.org/10.1093/bioinformatics/btn348

Yan, L., Wang, L., Tian, Y., Xia, X., Chen, Z., 2016. Structure and regulation of the chromatin remodeller ISWI. Nature 540, 466–469. https://doi.org/10.1038/nature20590

Yan, L., Wu, H., Li, X., Gao, N., Chen, Z., 2019. Structures of the ISWI–nucleosome complex reveal a conserved mechanism of chromatin remodeling. Nature Structural & Molecular Biology. https://doi.org/10.1038/s41594-019-0199-9

Yeoh, L.M., Lee, V.V., McFadden, G.I., Ralph, S.A., 2019. Alternative Splicing in Apicomplexan Parasites. mBio 10, e02866-18. https://doi.org/10.1128/mBio.02866-18

Young, J.A., Johnson, J.R., Benner, C., Yan, S.F., Chen, K., Le Roch, K.G., Zhou, Y., Winzeler, E.A., 2008. In silico discovery of transcription regulatory elements in Plasmodium falciparum. BMC Genomics 9, 70. https://doi.org/10.1186/1471-2164-9-70

Yuda, M., Kaneko, I., Murata, Y., Iwanaga, S., Nishi, T., 2021. Mechanisms of triggering malaria gametocytogenesis by AP2-G. Parasitology International 84, 102403. https://doi.org/10.1016/j.parint.2021.102403

Zhang, H.-M., Chen, H., Liu, W., Liu, H., Gong, J., Wang, H., Guo, A.-Y., 2012. AnimalTFDB: a comprehensive animal transcription factor database. Nucleic Acids Research 40, D144–D149. https://doi.org/10.1093/nar/gkr965

Zhang, M., Wang, C., Otto, T.D., Oberstaller, J., Liao, X., Adapa, S.R., Udenze, K., Bronner, I.F., Casandra, D., Mayho, M., Brown, J., Li, S., Swanson, J., Rayner, J.C., Jiang, R.H.Y., Adams, J.H., 2018a. Uncovering the essential genes of the human malaria parasite *Plasmodium falciparum* by saturation mutagenesis. Science 360, eaap7847. https://doi.org/10.1126/science.aap7847

Zhang, M., Wang, C., Otto, T.D., Oberstaller, J., Liao, X., Adapa, S.R., Udenze, K., Bronner, I.F., Casandra, D., Mayho, M., Brown, J., Li, S., Swanson, J., Rayner, J.C., Jiang, R.H.Y., Adams, J.H., 2018b. Uncovering the essential genes of the human malaria parasite *Plasmodium falciparum* by saturation mutagenesis. Science 360, eaap7847. https://doi.org/10.1126/science.aap7847

Zhang, Y., Liu, T., Meyer, C.A., Eeckhoute, J., Johnson, D.S., Bernstein, B.E., Nusbaum, C., Myers, R.M., Brown, M., Li, W., Liu, X.S., 2008. Model-based analysis of ChIP-Seq (MACS). Genome Biol 9, R137. https://doi.org/10.1186/gb-2008-9-9-r137

Zhu, F., Farnung, L., Kaasinen, E., Sahu, B., Yin, Y., Wei, B., Dodonova, S.O., Nitta, K.R., Morgunova, E., Taipale, M., Cramer, P., Taipale, J., 2018. The interaction landscape between transcription factors and the nucleosome. Nature 562, 76–81. https://doi.org/10.1038/s41586-018-0549-5

Zillner, K., Jerabek-Willemsen, M., Duhr, S., Braun, D., Längst, G., Baaske, P., 2012. Microscale Thermophoresis as a Sensitive Method to Quantify Protein: Nucleic Acid Interactions in Solution, in: Kaufmann, M., Klinger, C. (Eds.), Functional Genomics, Methods in Molecular Biology. Springer New York, New York, NY, pp. 241–252. https://doi.org/10.1007/978-1-61779-424-7_18

Zilversmit, M.M., Volkman, S.K., DePristo, M.A., Wirth, D.F., Awadalla, P., Hartl, D.L., 2010. Low-complexity regions in Plasmodium falciparum: missing links in the evolution of an extreme genome. Mol Biol Evol 27, 2198–2209. https://doi.org/10.1093/molbev/msq108

Zimmermann, R.A., Schwickert, M., Meidner, J.L., Nidoieva, Z., Helm, M., Schirmeister, T., 2022. An Optimized Microscale Thermophoresis Method for High-Throughput Screening of DNA Methyltransferase 2 Ligands. ACS Pharmacol. Transl. Sci. 5, 1079–1085. https://doi.org/10.1021/acsptsci.2c00175

9 ACKNOLEDGEMENTS

Firstly, I would like to express my gratitude to my supervisor, **Prof. Dr. Gernot Längst**, who has given me this opportunity and who has always provided me scientific support, freedom, and encouragement on this path. I am also extremely grateful to my second mentor **Prof. Dr. Markus Meissner** for the possibility to complete a major part of this work within his department and for all the valuable input and fruitful discussions. Furthermore, I would like to thank my third mentor, **Prof. Dr. Philipp Korber**, for giving me excellent feedback. Special thanks to **Dr. Sujaan Das**, who shared all his knowledge about Plasmodium with me and whom I could consult at any time. I had the pleasure of collaborating with Fraunhofer Institute for Toxicology and Experimental Medicine, 2bind, Protein Analysis Unit (LMU), AG Llinás (PSU) and AG Klingl (LMU).

This endeavor would not have been possible without **Elisabeth Silberhorn**, who created the basis of this work and helped me grow as a scientist and as a person. I would like to extend my sincere thanks to **Simon Holzinger**, who made the world of bioinformatics accessible to me and who accompanied me all these years with more-or-less scientific discussions, proofreading willingness, and extra-laboratory activities. Many thanks should also go to current and former members of **AG Längst,** who had brightened my days and who provided me personal and professional support. Thanks to all members of the **AG Meissner**, who adopted me as one of them and gave me an understanding of parasitology. Thanks to everyone from **Biochemistry III**, I could always go to in need for feel-good atmosphere.

Lastly, I could not have undertaken this journey without the moral support of all these individuals during the very different phases: Thanks to **Nadja** for sharing the joy and suffering of every unimportant assay! Thanks to **Michi** for sitting at the kitchen table for 30 minutes in case I want to talk! Thanks to **Lisa** and **Tanja** for over and over discussing my present and future goals! Thanks to **Michi** for your incessant idealism and motivation, when I didn’t have them! Thanks to **Lisa** for all your support in the last stage and for the infinitely motivating outlook for afterwards! Thanks to my family, especially my parents and my Oma, for putting yourself aside so many times, for making my education possible and for always believing in me!

APPENDIX – SUPPLEMENTARY INFORMATION

Appendix 1: Multiple sequence alignment of ISWI homologues *from Homo sapiens (Hs), Mus musculus (Mm), Xenopus laevis (Xl), Drosophila melanogaster (Dm), Saccharomyces cerevisiae (Sc), Arabidopsis thaliana (At), Cyanidioschyzon merolae (Cm), Phaeodactylum tricornutum (Pt), Plasmodium berghei (Pb), Cryptosporidium parvum (Cp), Neospora caninum (Nc), Toxoplasma gondii (Tg), Trypanosoma cruzi (Tc) and PF3D7_1104200 with predicted domains marked as in B (amino acids in agreement to consensus sequence highlighted by color).*

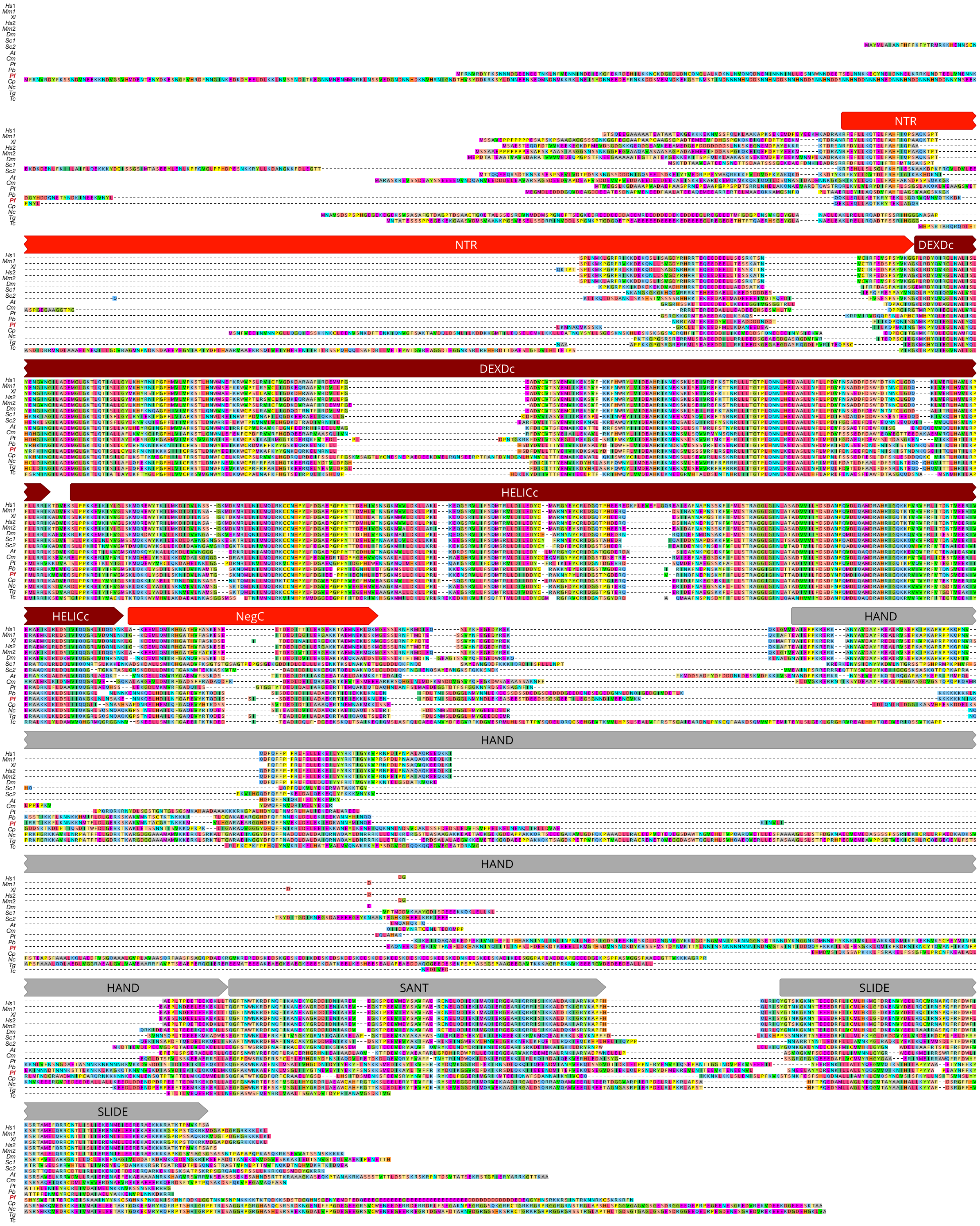

Appendix 2: Sequence used for phylogenetic analysis. *ATPase region was determined by multiple sequence alignment as in Flaus et al. 2006*

Figure	name in tree	species	UniProt ID	ATPase regions (aa)		
5-1A	**dmAtrx**	*Drosophila melanogaster*	Q9GQN5	455-782	897-1070	
5-1A	**dmChd1**	*Drosophila melanogaster*	Q7KU24	528-811	835-987	
5-1A	**dmEtl1**	*Drosophila melanogaster*	Q9VL72	289-586	651-802	
5-1A	**dmIno80**	*Drosophila melanogaster*	Q9VDY1	525-839	1155-1306	
5-1A	**dmISWI**	*Drosophila melanogaster*	Q24368	128-410	430-582	
5-1A	**dmLodestar**	*Drosophila melanogaster*	P34739	439-486	524-804	889-1041
5-1A	**dmMi2**	*Drosophila melanogaster*	O97159	730-1026	1051-1203	
5-1A	**dmMot1**	*Drosophila melanogaster*	Q9VF02	1350-1661	1689-1850	
5-1A	**dmRad54**	*Drosophila melanogaster*	O76460	156-464	497-649	
5-1A	**dmShprh**	*Drosophila melanogaster*	Q9VRV2	160-247	334-1251	
5-1A	**dmSmarcal1**	*Drosophila melanogaster*	Q9VMX6	247-755		
5-1A	**dmSnf2**	*Drosophila melanogaster*	P25439	773-1070	1079-1249	
5-1A	**dmSwr1**	*Drosophila melanogaster*	Q9NDJ2	914-1202	1657-1808	
5-1A	**hsAlc1**	*Homo sapiens*	Q86WJ1	46-327	346-496	
5-1A	**hsArip4**	*Homo sapiens*	Q9Y4B4	263-628	720-889	
5-1A	**hsAtrx**	*Homo sapiens*	P46100	1560-1889	2017-2190	
5-1A	**hsChd1**	*Homo sapiens*	O14646	481-764	787-939	
5-1A	**hsChd7**	*Homo sapiens*	Q9HCK8	811-1100	1132-1284	
5-1A	**hsEP400**	*Homo sapiens*	Q96L91	1091-1373	1897-2048	
5-1A	**hsErcc6**	*Homo sapiens*	Q03468	507-811	838-987	
5-1A	**hsEtl1**	*Homo sapiens*	Q9H4L7	497-787	853-1004	
5-1A	**hsIno80**	*Homo sapiens*	Q9ULG1	518-821	1100-1251	
5-1A	**hsISWI_1**	*Homo sapiens*	P28370	183-649		
5-1A	**hsLodestar**	*Homo sapiens*	Q9UNY4	570-617	641-932	990-1141
5-1A	**hsLsh**	*Homo sapiens*	Q9NRZ9	223-576	598-749	
5-1A	**hsMi2**	*Homo sapiens*	Q12873	736-1034	1059-1211	
5-1A	**hsMot1**	*Homo sapiens*	O14981	1266-1584	1613-1781	
5-1A	**hsRad5**	*Homo sapiens*	Q14527	240-315	477-721	832-987
5-1A	**hsRad54**	*Homo sapiens*	Q92698	153-461	494-646	
5-1A	**hsShprh**	*Homo sapiens*	Q149N8	304-394	715-1661	
5-1A	**hsSmarcal1**	*Homo sapiens*	Q9NZC9	436-954		
5-1A	**hsSnf2**	*Homo sapiens*	P51532	754-1051	1079-1231	
5-1A	**hsSwr1**	*Homo sapiens*	Q6ZRS2	618-906	2042-2193	
5-1A	**scChd1**	*Saccharomyces cerevisiae*	P32657	376-664	694-846	
5-1A	**scErcc6**	*Saccharomyces cerevisiae*	P40352	297-632	650-803	
5-1A	**scEtl1**	*Saccharomyces cerevisiae*	P31380	572-849	948-1100	
5-1A	**scIno80**	*Saccharomyces cerevisiae*	P53115	706-1016	1298-1449	
5-1A	**scISWI_1**	*Saccharomyces cerevisiae*	P38144	196-481	501-653	
5-1A	**scLsh**	*Saccharomyces cerevisiae*	P43610	222-754		
5-1A	**scMot1**	*Saccharomyces cerevisiae*	P32333	1272-1579	1608-1783	
5-1A	**scRad5**	*Saccharomyces cerevisiae*	P32849	437-553	585-847	993-1152
5-1A	**scRad16**	*Saccharomyces cerevisiae*	P31244	184-226	230-772	
5-1A	**scRad54**	*Saccharomyces cerevisiae*	P32863	271-620	654-805	
5-1A	**scRi5-1**	*Saccharomyces cerevisiae*	Q08562	943-990	996-1280	1442-1596
5-1A	**scSnf_1**	*Saccharomyces cerevisiae*	P32597	470-942		
5-1A	**scSwr1**	*Saccharomyces cerevisiae*	Q05471	696-998	1245-1396	
5-1A	**PF3D7_1343400**	*Plasmodium falciparum*	Q8IDQ5	661-705	742-1452	
5-1A	**PF3D7_1104200**	*Plasmodium falciparum*	Q8IIW0	322-777		
5-1A	**PF3D7_1023900**	*Plasmodium falciparum*	Q8IJG6	1296-1764		
5-1A	**PF3D7_0803400**	*Plasmodium falciparum*	Q8IAN4	195-1239		
5-1A	**PF3D7_0624600**	*Plasmodium falciparum*	C6KT82	338-673	1084-1228	
5-1A	**PF3D7_0106000**	*Plasmodium falciparum*	B9ZSI3	1-922		
5-1A	**PF3D7_0216000**	*Plasmodium falciparum*	O96239	884-1485		
5-1A	**PF3D7_0818700**	*Plasmodium falciparum*	C0H4V8	208-1223		
5-1A	**PF3D7_0820000**	*Plasmodium falciparum*	C0H4W3	662-951	1767-1918	
5-1A	**PF3D7_1357500**	*Plasmodium falciparum*	Q8IDD0	353-795		
5-1B	**atISWI**	*Arabidopsis thaliana*	F4JY24	full length		
5-1B	**cmISWI**	*Cyanidioschyzon merolae*	M1VKV9	full length		
5-1B	**cpISWI**	*Cryptosporidium parvum*	Q5CVU2	full length		
5-1B	**dmISWI**	*Drosophila melanogaster*	Q24368	full length		

5-1B	**hsISWI_1**	*Homo sapiens*	P28370	full length
5-1B	**hsISWI_2**	*Homo sapiens*	O60264	full length
5-1B	**mmISWI_1**	*Mus musculus*	Q91ZW3	full length
5-1B	**mmISWI_2**	*Mus musculus*	Q6PGB8	full length
5-1B	**ncISWI**	*Neospora caninum*	F0VIN7	full length
5-1B	**pbISWI**	*Plasmodium bergheii*	A0A509AKD2	full length
5-1B	**ptISWI**	*Phaeodactylum tricornutum*	B7G2T7	full length
5-1B	**scISWI_1**	*Saccharomyces cerevisiae*	P38144	full length
5-1B	**scISWI_2**	*Saccharomyces cerevisiae*	Q08773	full length
5-1B	**tcISWI**	*Trypanosoma cruzii*	Q4CNC6	full length
5-1B	**tgISWI**	*Toxoplasma gondii*	S7V4B2	full length
5-1B	**xlISWI**	*Xenopus laevis*	Q6DFM0	full length
5-1B	**PF3D7_1104200**	*Plasmodium falciparum*	Q8IIW0	full length

***Appendix 3: List of exportome-genes** (Gene IDs) combining predicted (Boddey and Cowman, 2013) and proven (Jonsdottir et al., 2021) exportome*

PF3D7_0401600	**PF3D7_0402100**	**PF3D7_0726100**	**PF3D7_1001700**	**PF3D7_1240300**
PF3D7_0100100	PF3D7_0402200	PF3D7_0726200	PF3D7_1001800	PF3D7_1240400
PF3D7_0101100	PF3D7_0402400	PF3D7_0726700	PF3D7_1001900	PF3D7_1240600
PF3D7_0102200	PF3D7_0404800	PF3D7_0730800	PF3D7_1002000	PF3D7_1240900
PF3D7_0102300	PF3D7_0406100	PF3D7_0730900	PF3D7_1002100	PF3D7_1249900
PF3D7_0102600	PF3D7_0410000	PF3D7_0731100	PF3D7_1007000	PF3D7_1252300
PF3D7_0104200	PF3D7_0412400	PF3D7_0731200	PF3D7_1016300	PF3D7_1252500
PF3D7_0104400	PF3D7_0420900	PF3D7_0731300	PF3D7_1016400	PF3D7_1252700
PF3D7_0106000	PF3D7_0421100	PF3D7_0731800	PF3D7_1016500	PF3D7_1252800
PF3D7_0106100	PF3D7_0421300	PF3D7_0733000	PF3D7_1016600	PF3D7_1252900
PF3D7_0111400	PF3D7_0422000	PF3D7_0800100	PF3D7_1016700	PF3D7_1253000
PF3D7_0112900	PF3D7_0424000	PF3D7_0800300	PF3D7_1016800	PF3D7_1253100
PF3D7_0113000	PF3D7_0424400	PF3D7_0801000	PF3D7_1016900	PF3D7_1253200
PF3D7_0113200	PF3D7_0424500	PF3D7_0807700	PF3D7_1019600	PF3D7_1253300
PF3D7_0113300	PF3D7_0424600	PF3D7_0808600	PF3D7_1031600	PF3D7_1255200
PF3D7_0113400	PF3D7_0424700	PF3D7_0808700	PF3D7_1033000	PF3D7_1300100
PF3D7_0113700	PF3D7_0426000	PF3D7_0809100	PF3D7_1033200	PF3D7_1300200
PF3D7_0114000	PF3D7_0500100	PF3D7_0814100	PF3D7_1034800	PF3D7_1301400
PF3D7_0115700	PF3D7_0500800	PF3D7_0817500	PF3D7_1038500	PF3D7_1301500
PF3D7_0200100	PF3D7_0500900	PF3D7_0822600	PF3D7_1038600	PF3D7_1301700
PF3D7_0201500	PF3D7_0501000	PF3D7_0825300	PF3D7_1038700	PF3D7_1302000
PF3D7_0201600	PF3D7_0501100	PF3D7_0826200	PF3D7_1038800	PF3D7_1303000
PF3D7_0201700	PF3D7_0501200	PF3D7_0830400	PF3D7_1039000	PF3D7_1310500
PF3D7_0201800	PF3D7_0501300	PF3D7_0830500	PF3D7_1039100	PF3D7_1328500
PF3D7_0201900	PF3D7_0505400	PF3D7_0830600	PF3D7_1041300	PF3D7_1330700
PF3D7_0202000	PF3D7_0507300	PF3D7_0830700	PF3D7_1100100	PF3D7_1334300
PF3D7_0202100	PF3D7_0507500	PF3D7_0830900	PF3D7_1100200	PF3D7_1334500
PF3D7_0202200	PF3D7_0515300	PF3D7_0831200	PF3D7_1101500	PF3D7_1334600
PF3D7_0204100	PF3D7_0523400	PF3D7_0831300	PF3D7_1102200	PF3D7_1334700
PF3D7_0207000	PF3D7_0532200	PF3D7_0831400	PF3D7_1102300	PF3D7_1352900
PF3D7_0214000	PF3D7_0532300	PF3D7_0831500	PF3D7_1102500	PF3D7_1353100
PF3D7_0214100	PF3D7_0532400	PF3D7_0831600	PF3D7_1102600	PF3D7_1353200
PF3D7_0219700	PF3D7_0532600	PF3D7_0831800	PF3D7_1104100	PF3D7_1369000
PF3D7_0219800	PF3D7_0533000	PF3D7_0832200	PF3D7_1106100	PF3D7_1370300
PF3D7_0219900	PF3D7_0533100	PF3D7_0833500	PF3D7_1106800	PF3D7_1372100
PF3D7_0220000	PF3D7_0600600	PF3D7_0900100	PF3D7_1108700	PF3D7_1372200
PF3D7_0220100	PF3D7_0601000	PF3D7_0901700	PF3D7_1109900	PF3D7_1372300
PF3D7_0220200	PF3D7_0601500	PF3D7_0902100	PF3D7_1115900	PF3D7_1373500
PF3D7_0220300	PF3D7_0601700	PF3D7_0902200	PF3D7_1121300	PF3D7_1400100
PF3D7_0220400	PF3D7_0601900	PF3D7_0902300	PF3D7_1125000	PF3D7_1401100
PF3D7_0220500	PF3D7_0607200	PF3D7_0902400	PF3D7_1127000	PF3D7_1401200
PF3D7_0220600	PF3D7_0611000	PF3D7_0902500	PF3D7_1133300	PF3D7_1401400
PF3D7_0220700	PF3D7_0617400	PF3D7_0902600	PF3D7_1136500	PF3D7_1401600
PF3D7_0220800	PF3D7_0617600	PF3D7_0902700	PF3D7_1148700	PF3D7_1407800
PF3D7_0221700	PF3D7_0617700	PF3D7_0904900	PF3D7_1148800	PF3D7_1410100
PF3D7_0223500	PF3D7_0623200	PF3D7_0905400	PF3D7_1148900	PF3D7_1419200
PF3D7_0300100	PF3D7_0628400	PF3D7_0908300	PF3D7_1149000	PF3D7_1425900

PF3D7_0301200	PF3D7_0631100	PF3D7_0911900	PF3D7_1149100	PF3D7_1429600
PF3D7_0301300	PF3D7_0631600	PF3D7_0918200	PF3D7_1149200	PF3D7_1430200
PF3D7_0301500	PF3D7_0632500	PF3D7_0923200	PF3D7_1149600	PF3D7_1439000
PF3D7_0301600	PF3D7_0632700	PF3D7_0927900	PF3D7_1200100	PF3D7_1447700
PF3D7_0301700	PF3D7_0632800	PF3D7_0929400	PF3D7_1200500	PF3D7_1448400
PF3D7_0301800	PF3D7_0700100	PF3D7_0935500	PF3D7_1200600	PF3D7_1458000
PF3D7_0302300	PF3D7_0701900	PF3D7_0935700	PF3D7_1200800	PF3D7_1458300
PF3D7_0302500	PF3D7_0702000	PF3D7_0935800	PF3D7_1200900	PF3D7_1464400
PF3D7_0304600	PF3D7_0702100	PF3D7_0935900	PF3D7_1201000	PF3D7_1464600
PF3D7_0310400	PF3D7_0702300	PF3D7_0936000	PF3D7_1201200	PF3D7_1476300
PF3D7_0312400	PF3D7_0702400	PF3D7_0936200	PF3D7_1201400	PF3D7_1476400
PF3D7_0313700	PF3D7_0702500	PF3D7_0936300	PF3D7_1212100	PF3D7_1476600
PF3D7_0314800	PF3D7_0702600	PF3D7_0936400	PF3D7_1219400	PF3D7_1476900
PF3D7_0316300	PF3D7_0709100	PF3D7_0936600	PF3D7_1221700	PF3D7_1477000
PF3D7_0324300	PF3D7_0712400	PF3D7_0936800	PF3D7_1227200	PF3D7_1477300
PF3D7_0324900	PF3D7_0717000	PF3D7_0937000	PF3D7_1229400	PF3D7_1477500
PF3D7_0400100	PF3D7_0718100	PF3D7_0937800	PF3D7_1232000	PF3D7_1477700
PF3D7_0400200	PF3D7_0719800	PF3D7_1000100	PF3D7_1233800	PF3D7_1478000
PF3D7_0401800	PF3D7_0721100	PF3D7_1001400	PF3D7_1237900	PF3D7_1478100
PF3D7_0402000	PF3D7_0725400	PF3D7_1001600	PF3D7_1238000	PF3D7_1478600

Appendix 4: List of stage-specific-genes *(Gene IDs) used for expression change analysis. Genes adapted from following studies (Kessel et al. 2021, López-Barragán 2011) and manually sorted out based on expression data from PlasmoDB*

ookinete-	**sporozoite-**	**gametocyte-specific genes**		
PF3D7_0105700	PF3D7_0104000	PF3D7_0103800	PF3D7_0809700	PF3D7_1207700
PF3D7_0203800	PF3D7_0104100	PF3D7_0105900	PF3D7_0810400	PF3D7_1209800
PF3D7_0209000	PF3D7_0107600	PF3D7_0107000	PF3D7_0810900	PF3D7_1213500
PF3D7_0216000	PF3D7_0207300	PF3D7_0108800	PF3D7_0812600	PF3D7_1214500
PF3D7_0304100	PF3D7_0215200	PF3D7_0109000	PF3D7_0813500	PF3D7_1214900
PF3D7_0309200	PF3D7_0301000	PF3D7_0109400	PF3D7_0825700	PF3D7_1215000
PF3D7_0310100	PF3D7_0304000	PF3D7_0109500	PF3D7_0827200	PF3D7_1216500
PF3D7_0311400	PF3D7_0304600	PF3D7_0109850	PF3D7_0827400	PF3D7_1218900
PF3D7_0315200	PF3D7_0403500	PF3D7_0109950	PF3D7_0830900	PF3D7_1219900
PF3D7_0320400	PF3D7_0404500	PF3D7_0110000	PF3D7_0903800	PF3D7_1220700
PF3D7_0421700	PF3D7_0404600	PF3D7_0203300	PF3D7_0907500	PF3D7_1222600
PF3D7_0513600	PF3D7_0404800	PF3D7_0203400	PF3D7_0907800	PF3D7_1224200
PF3D7_0517200	PF3D7_0405700	PF3D7_0204800	PF3D7_0908300	PF3D7_1231000
PF3D7_0522900	PF3D7_0407600	PF3D7_0205000	PF3D7_0909700	PF3D7_1233800
PF3D7_0523400	PF3D7_0408600	PF3D7_0208800	PF3D7_0912700	PF3D7_1234000
PF3D7_0526600	PF3D7_0408700	PF3D7_0210000	PF3D7_0913800	PF3D7_1234700
PF3D7_0605600	PF3D7_0411400	PF3D7_0210600	PF3D7_0914400	PF3D7_1236800
PF3D7_0611800	PF3D7_0417100	PF3D7_0212000	PF3D7_0916000	PF3D7_1238000
PF3D7_0620000	PF3D7_0418900	PF3D7_0218100	PF3D7_0920500	PF3D7_1242000
PF3D7_0621400	PF3D7_0502100	PF3D7_0303900	PF3D7_0921000	PF3D7_1245000
PF3D7_0628100	PF3D7_0502300	PF3D7_0305600	PF3D7_0922300	PF3D7_1246400
PF3D7_0715200	PF3D7_0511400	PF3D7_0306200	PF3D7_0924600	PF3D7_1247800
PF3D7_0724900	PF3D7_0515500	PF3D7_0308500	PF3D7_0925100	PF3D7_1251300
PF3D7_0729900	PF3D7_0516300	PF3D7_0309100	PF3D7_0925600	PF3D7_1302100
PF3D7_0731300	PF3D7_0518900	PF3D7_0310300	PF3D7_0926400	PF3D7_1310700
PF3D7_0801000	PF3D7_0521300	PF3D7_0311700	PF3D7_0927100	PF3D7_1316700
PF3D7_0801100	PF3D7_0524200	PF3D7_0313200	PF3D7_0927600	PF3D7_1320900
PF3D7_0801300	PF3D7_0615600	PF3D7_0314000	PF3D7_0930000	PF3D7_1321000
PF3D7_0823500	PF3D7_0616000	PF3D7_0314700	PF3D7_0931500	PF3D7_1330500
PF3D7_0829800	PF3D7_0616500	PF3D7_0316100	PF3D7_0932000	PF3D7_1339400
PF3D7_0904200	PF3D7_0717800	PF3D7_0316500	PF3D7_0933200	PF3D7_1340400
PF3D7_0929600	PF3D7_0807700	PF3D7_0317000	PF3D7_0934400	PF3D7_1348400
PF3D7_1005600	PF3D7_0812300	PF3D7_0319100	PF3D7_0936600	PF3D7_1349700
PF3D7_1020100	PF3D7_0814600	PF3D7_0320000	PF3D7_1002800	PF3D7_1350800
PF3D7_1021800	PF3D7_0814700	PF3D7_0320800	PF3D7_1002900	PF3D7_1351600
PF3D7_1036300	PF3D7_0816500	PF3D7_0321400	PF3D7_1004700	PF3D7_1356000

PF3D7_1120700
PF3D7_1139100
PF3D7_1143100
PF3D7_1146800
PF3D7_1147200
PF3D7_1210200
PF3D7_1211000
PF3D7_1233300
PF3D7_1244500
PF3D7_1248400
PF3D7_1250400
PF3D7_1252200
PF3D7_1252400
PF3D7_1301600
PF3D7_1319600
PF3D7_1327300
PF3D7_1358600
PF3D7_1367800
PF3D7_1403100
PF3D7_1404300
PF3D7_1409100
PF3D7_1413700
PF3D7_1420100
PF3D7_1461800
PF3D7_1471600
PF3D7_1471700
PF3D7_1473200
PF3D7_1475500
PF3D7_1478900
PF3D7_1479000
PF3D7_0822700
PF3D7_0828200
PF3D7_0830300
PF3D7_0908200
PF3D7_0916300
PF3D7_0916600
PF3D7_0919300
PF3D7_0919500
PF3D7_1006000
PF3D7_1008600
PF3D7_1020800
PF3D7_1023000
PF3D7_1023800
PF3D7_1024100
PF3D7_1026400
PF3D7_1029700
PF3D7_1131600
PF3D7_1137800
PF3D7_1139600
PF3D7_1139700
PF3D7_1142300
PF3D7_1147000
PF3D7_1147800
PF3D7_1201300
PF3D7_1201700
PF3D7_1207400
PF3D7_1213400
PF3D7_1216600
PF3D7_1219700
PF3D7_1221400
PF3D7_1227300
PF3D7_1230100
PF3D7_1236600
PF3D7_1246900
PF3D7_1302200
PF3D7_1322400
PF3D7_1335900
PF3D7_1342500
PF3D7_1350600
PF3D7_1350900
PF3D7_1354700
PF3D7_1362100
PF3D7_1407600
PF3D7_1407700
PF3D7_1415100
PF3D7_1422900
PF3D7_1442600
PF3D7_1447500
PF3D7_1451400
PF3D7_1456200
PF3D7_1470100
PF3D7_1475400
PF3D7_1476100
PF3D7_0406200
PF3D7_0409700
PF3D7_0413800
PF3D7_0417000
PF3D7_0418800
PF3D7_0422000
PF3D7_0422900
PF3D7_0423000
PF3D7_0423300
PF3D7_0502900
PF3D7_0503000
PF3D7_0504200
PF3D7_0504900
PF3D7_0505600
PF3D7_0505900
PF3D7_0508200
PF3D7_0509700
PF3D7_0510300
PF3D7_0511200
PF3D7_0512000
PF3D7_0512600
PF3D7_0513000
PF3D7_0513100
PF3D7_0513700
PF3D7_0513800
PF3D7_0514500
PF3D7_0516400
PF3D7_0516500
PF3D7_0517800
PF3D7_0518800
PF3D7_0523300
PF3D7_0524600
PF3D7_0525300
PF3D7_0526100
PF3D7_0526400
PF3D7_0528900
PF3D7_0529100
PF3D7_0530800
PF3D7_0532200
PF3D7_0604400
PF3D7_0605300
PF3D7_0606400
PF3D7_0607700
PF3D7_0608600
PF3D7_0611000
PF3D7_0611600
PF3D7_0612500
PF3D7_0613400
PF3D7_0615300
PF3D7_0618500
PF3D7_0618900
PF3D7_0620700
PF3D7_0622700
PF3D7_0624200
PF3D7_0630000
PF3D7_0630400
PF3D7_0707600
PF3D7_0722700
PF3D7_0722800
PF3D7_0728300
PF3D7_0804700
PF3D7_1009100
PF3D7_1009300
PF3D7_1012300
PF3D7_1016900
PF3D7_1017300
PF3D7_1017500
PF3D7_1018400
PF3D7_1019100
PF3D7_1019900
PF3D7_1020200
PF3D7_1020300
PF3D7_1021600
PF3D7_1022900
PF3D7_1023400
PF3D7_1024300
PF3D7_1026100
PF3D7_1027900
PF3D7_1028200
PF3D7_1030900
PF3D7_1031000
PF3D7_1031200
PF3D7_1031700
PF3D7_1031900
PF3D7_1032000
PF3D7_1032500
PF3D7_1033900
PF3D7_1035200
PF3D7_1106100
PF3D7_1106900
PF3D7_1107900
PF3D7_1109100
PF3D7_1112200
PF3D7_1115100
PF3D7_1116500
PF3D7_1118000
PF3D7_1118900
PF3D7_1119100
PF3D7_1119200
PF3D7_1119700
PF3D7_1121000
PF3D7_1124400
PF3D7_1125000
PF3D7_1127500
PF3D7_1127600
PF3D7_1129600
PF3D7_1131100
PF3D7_1131500
PF3D7_1132400
PF3D7_1133100
PF3D7_1135000
PF3D7_1138900
PF3D7_1141100
PF3D7_1141200
PF3D7_1141900
PF3D7_1143600
PF3D7_1144800
PF3D7_1146100
PF3D7_1201600
PF3D7_1203100
PF3D7_1203900
PF3D7_1205700
PF3D7_1356100
PF3D7_1362000
PF3D7_1402200
PF3D7_1403200
PF3D7_1404000
PF3D7_1409400
PF3D7_1410000
PF3D7_1412500
PF3D7_1416900
PF3D7_1420900
PF3D7_1421000
PF3D7_1421400
PF3D7_1421800
PF3D7_1422300
PF3D7_1423400
PF3D7_1423600
PF3D7_1426900
PF3D7_1428800
PF3D7_1429300
PF3D7_1429600
PF3D7_1429700
PF3D7_1430000
PF3D7_1430100
PF3D7_1430900
PF3D7_1431100
PF3D7_1435200
PF3D7_1435600
PF3D7_1438800
PF3D7_1441700
PF3D7_1441800
PF3D7_1444300
PF3D7_1445000
PF3D7_1447800
PF3D7_1448600
PF3D7_1449900
PF3D7_1453500
PF3D7_1454500
PF3D7_1454800
PF3D7_1454900
PF3D7_1459800
PF3D7_1461400
PF3D7_1463000
PF3D7_1465000
PF3D7_1465700
PF3D7_1466000
PF3D7_1466800
PF3D7_1467900
PF3D7_1469700
PF3D7_1469800
PF3D7_1470500
PF3D7_1471500
PF3D7_1471800
PF3D7_1472500
PF3D7_1472800
PF3D7_1472900
PF3D7_1476500
PF3D7_1477400
PF3D7_1478100

APPENDIX – WATZLOWIK ET AL. 2021

International Journal of
Molecular Sciences

MDPI

Review

Peculiarities of *Plasmodium falciparum* Gene Regulation and Chromatin Structure

Maria Theresia Watzlowik [1], Sujaan Das [2], Markus Meissner [2] and Gernot Längst [1,*]

[1] Department of Biochemistry, Genetics and Microbiology, Biochemistry III, University of Regensburg, Universitätsstr. 31, 93053 Regensburg, Germany; Maria-theresia.watzlowik@ur.de
[2] Faculty of Veterinary Medicine, Chair of Experimental Parasitology, Ludwig-Maximilian-University, Munich, Lena-Christ-Str. 48, 82152 Martinsried-Planegg, Germany; Sujaan.Das@para.vetmed.uni-muenchen.de (S.D.); Markus.Meissner@para.vetmed.uni-muenchen.de (M.M.)
* Correspondence: gernot.laengst@ur.de

Abstract: The highly complex life cycle of the human malaria parasite, *Plasmodium falciparum*, is based on an orchestrated and tightly regulated gene expression program. In general, eukaryotic transcription regulation is determined by a combination of sequence-specific transcription factors binding to regulatory DNA elements and the packaging of DNA into chromatin as an additional layer. The accessibility of regulatory DNA elements is controlled by the nucleosome occupancy and changes of their positions by an active process called nucleosome remodeling. These epigenetic mechanisms are poorly explored in *P. falciparum*. The parasite genome is characterized by an extraordinarily high AT-content and the distinct architecture of functional elements, and chromatin-related proteins also exhibit high sequence divergence compared to other eukaryotes. Together with the distinct biochemical properties of nucleosomes, these features suggest substantial differences in chromatin-dependent regulation. Here, we highlight the peculiarities of epigenetic mechanisms in *P. falciparum*, addressing chromatin structure and dynamics with respect to their impact on transcriptional control. We focus on the specialized chromatin remodeling enzymes and discuss their essential function in *P. falciparum* gene regulation.

Keywords: chromatin; epigenetics; *Plasmodium falciparum*; nucleosome; nucleosome remodeling; transcription regulation; chromatin structure

check for updates

Citation: Watzlowik, M.T.; Das, S.; Meissner, M.; Längst, G. Peculiarities of *Plasmodium falciparum* Gene Regulation and Chromatin Structure. *Int. J. Mol. Sci.* **2021**, 22, 5168. https://doi.org/10.3390/ijms22105168

Academic Editor: Tobias Straub

Received: 16 April 2021
Accepted: 10 May 2021
Published: 13 May 2021

1. Introduction

Plasmodium falciparum, a unicellular eukaryotic parasite, causes the most severe and deadly form of the human disease malaria. In 2019, 229 million cases of malaria infection with about 409,000 deaths were reported, mainly affecting children under the age of five [1]. Malaria is still a major threat for humans and the situation may become worse as parasites increasingly develop resistance to the frontline choice of treatment, artimisinin-based combinational therapy, just as resistance to other effective drugs has emerged [2]. There is an urgent need for new antimalarial drugs, but this requires better understanding of the physiological, biochemical and pathological mechanisms of the parasite. In particular, the chromatin landscape and the epigenetic mechanisms are exceptionally different in *Plasmodium*, representing a potential drug target. Here, we review the specific features of *Plasmodium falciparum* chromatin structure.

Plasmodium spp.—together with other parasites such as *Toxoplasma*—belong to the phylum of Apicomplexa, which evolutionarily separated from the human line about 800–1000 million years ago [3]. The *Plasmodium* life cycle is complex, including two different hosts, with an asexual reproduction phase in humans and sexual reproduction in mosquitos of the genus *Anopheles* [4]. In humans, *Plasmodium* exists in intra- and extracellular forms and is capable of invading various cell types, including hepatocytes and erythrocytes. The parasite undergoes asexual reproduction and sexual commitment in the human host, leading to the differentiation of male and female gametocytes, which are taken up by a mosquito bite for the completion of sexual reproduction. This versatile multistage life cycle is tightly regulated with defined sets of proteins being concertedly expressed in specific phases of the life cycle. The underlying regulatory mechanisms of this highly orchestrated gene expression program in *Plasmodium falciparum* are poorly understood.

As a common principle, gene regulation in eukaryotes involves regulation on many levels, starting with controlling DNA accessibility within chromatin, followed by transcriptional control, post-transcriptional regulation, translational control, protein stability and activity, and additional mechanisms [5]. In this review, we will focus on *Plasmodium falciparum* chromatin structure and dynamics, reviewing its contribution to the regulation of gene expression and comparing it to other eukaryotes.

2. DNA-Based Features

2.1. Genome and Gene Architecture

The complete *Plasmodium falciparum* (*Pf*) genome sequence was determined in the year 2002 [6] and consists of 23.3 million base pairs, organized in 14 chromosomes plus 6 kb mitochondrial and 34 kb apicoplast DNA located in the respective cytoplasmic organelles [7]. The parasite genome features one of the most AT-rich eukaryotic genomes with an overall AT-content of 80.7% and within intergenic regions and introns of up to 95% [8]. Due to the high AT-content, the genome contains numerous low-complexity regions, simple sequence repeats and a skewed codon usage bias. It comprises a total number of 5280 protein-coding genes as well as 158 pseudogenes and 103 annotated noncoding RNAs [9]. At least 4557 of the 5280 genes are transcribed and expressed in a complex pattern depending on the life cycle stage [10], requiring a complex regulatory network.

In general, the *Pf* genome exhibits typical eukaryotic features, with genes consisting of exons and introns separated by intergenic regions. But gene architecture clearly differs from other unicellular eukaryotes by an increased mean gene length of 2300 bp (vs. 1400 bp in *Saccharomyces*), an increased mean exon length of 949 bp (typically 200–300 bp in all eukaryotes) and a markedly large proportion of genes larger than 4000 bp. The sizes of introns and intergenic region usually correlate linearly with the genome size [11]. With regard to genome size, *Pf* displays unusually large intergenic regions (mean of 1700 bp) and introns with an average length of 180 bp, which is rather long for protists but very short in comparison to higher eukaryotes [6].

2.2. Regulatory DNA Elements

Like other eukaryotes, *Pf* genes exhibit the characteristic bipartite structures of *cis*-regulatory regions with enhancer elements and basal promotors required for the recruitment of RNA polymerase II to the transcription start site (TSS) (reviewed in [12,13]). Most TSSs are relatively distant to the first exon, resulting in mRNAs with exceptionally long 5′ untranslated regions, with an average of 346 nt [14], when compared to human mRNA (~150 nt) [15]. The presence of antisense transcripts indicates the existence of bidirectional promotors with multiple shared or separate regulatory elements including the presence of multiple clusters of TSSs within a single gene locus [16]. Thus, genome-wide mapping of TSSs revealed highly diverse sets of start sites that are far more variable than those of human genes. Core promotors exhibit sequence motifs directing TSS selection and promotor strength, such as local changes in GC-content and homopolymeric nucleotide stretches (reviewed in [13]). Early on it was shown that the packaging of the promotor DNA into nucleosomes and alterations in nucleosome positioning and histone composition also influence gene activity [17–19], as will be described below.

Applying in silico approaches and algorithms, numerous putative *cis*-regulatory motifs could be predicted [20–22], and a few of them were experimentally validated [23]. These elements act as enhancers or silencers, as known for other eukaryotes, but *Pf* possesses an extraordinarily high number of such elements (4–5 per gene) sharing no sequence similarity with those of other eukaryotic organisms. Recent studies showed that the majority of the plasmodial genome is organized in regulatory units containing multiple genes and multiple regulatory elements with coordinated activity, rather than a one-on-one allocation of *cis*-regulator elements to their neighboring genes [24].

2.3. Trans–Acting Factors

The principle of gene expression regulation is based on the binding of specific transcription factors (TF) to *cis*-regulatory motifs. Surprisingly, only 73 TFs were identified in *Pf* having more than 5000 genes. This is far below the numbers in yeast (~170 TFs for 5400 genes) and human cells (>1500 TFs for 20,000 genes) [25–27]. In addition, most of the major families of eukaryotic TFs, such as homeodomains, basic leucine zipper, GATA fingers, nuclear hormone receptor and FKH domains, could not be identified through a homology search [28]. The *Pf* transcription factors can be grouped into eight helix-turn-helix proteins, 37 C2H2-type zinc fingers and one β-scaffold factor, but all exhibit only low conservation across different *Plasmodium* species [13,25]. Moreover, Apicomplexa possess a novel category of TFs, the ApiAP2 family, which are presumably the main regulators of transcription in the parasite life cycle [29,30].

Most of the 27 members of the ApiAP2 family were shown to exhibit sequence-specific DNA-binding [31,32]. Some of the *Pf* ApiAP2s or orthologs were shown to be essential and to drive transcriptional regulation at different stages of the life cycle [13], [33]: For example, AP2-L plays a critical role in liver-stage development [34]; AP2-G was identified to be the master regulator of gametocytogenesis [35]; AP2-I is relevant for invasion gene activation [36]; AP2-O activates gene expression in ookinetes [37], while gene expression in liver-infecting sporozoites is regulated by AP2-Sp [38]. Still the question remains, how such a low number of factors is sufficient to coordinate the complex gene expression profile of more than 5000 genes. It was suggested that TFs act in a combinatorial fashion and may exhibit pleiotropic functionality [33,39,40]. Alternatively, they might interact with additional regulatory proteins [36,41], or undergo post-transcriptional modification like other epigenetic regulators [42–44].

The interplay between *cis*-acting elements and *trans*-acting factors is strongly influenced by the packaging of the genomic DNA into chromatin. Nucleosome positioning and dynamics control the accessibility of the regulatory DNA elements for the *trans*-acting factors, as histones would mask the binding sites and inhibit DNA sequence recognition. Therefore, nucleosome-positioning plays an essential role, and well-defined chromatin architectures can be observed at regulatory regions. At gene promoters, positioned nucleosomes (+1) just downstream of the TSS can be observed, and the promoter region directly upstream is generally depleted of nucleosomes [18]. Such a structure is compatible with the binding of transcription factors, and changes to this chromatin structure would substantially affect gene activity. Genome-wide profiling using ATAC-seq identified such accessible DNA regions, mainly located in 5′-intergenic regions, overlapping with annotated and predicted *cis*-regulatory elements. These accessible regulatory regions correlate overall with high mRNA levels of the associated genes [45,46], revealing the binding of *trans*-activating factors to these sites. The direct effect of transcription-factor binding to transcriptional regulation was proven, but it is unclear how chromatin structure and nucleosome dynamics additionally affect and regulate the access of the *trans*-acting factors to their binding sites. Chromatin dynamics and nucleosome positioning may be a consequence of transcription-factor binding or represent a preceding event regulated by chromatin-remodeling enzymes that determine DNA accessibility.

3. Chromatin features

3.1. Pf Nucleosomes and Their Special Properties

Nucleosomes are the basic packaging unit of chromatin, consisting of a histone octamer associated with 147 base pairs of DNA wrapped around the proteins in 1.65 turns. The octamer consists typically of the four canonical histones H2A, H2B, H3 and H4, which are—due to their central function in DNA packaging—highly conserved in sequence throughout eukaryotic evolution [47]. For example, *Arabidopsis thaliana* H3 and human H3 differ in only two amino acids [48]. However, *Pf* histones show an extraordinarily high divergence with sequence identities of only 64%, 68%, 93% and 92% between human and *Pf* H2A, H2B, H3 and H4 respectively. The fifth histone H1, usually linking nucleosomes and promoting higher order structure, is not present in *Pf* [6].

In accordance with the diverging sequence of histones, plasmodial nucleosomes exhibit distinct biochemical properties when compared to human nucleosomes (see Figure 1). The *Pf* nucleosome exhibits reduced stability, weaker binding of H2A and H2B and has intriguingly lost the capability of DNA sequence-dependent nucleosome positioning [49].

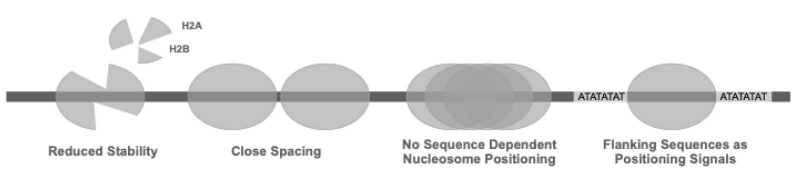

Figure 1. Schematic representation of distinct nucleosome properties in *P. falciparum*. In comparison with human nucleosomes, *Pf* nucleosomes exhibit reduced stability and short spacing between nucleosomes, and positioning is rather independent of internal DNA sequence but is determined by flanking sequence motifs.

Since DNA is not a flexible polymer but a rather rigid molecule with a persistence length of 150 bp, a deviation from this defined DNA structure would require bending energy [50]. In the context of a nucleosome, the DNA molecule has to be highly bent in order to enable wrapping around the histone octamer. The required bending energy is compensated by establishing about 400 direct and indirect ionic interactions and H-bridges between the DNA and the histones [51]. As GC and AT base pairs do not have exactly the same size and geometry, sequence composition does affect DNA structure by inducing bents and kinks with specific sequence motifs. Repetition of such motifs every 10 bp would induce directed DNA curvature that mimics the folding around the histone octamer, requiring less bending energy for nucleosome formation and thus, representing the preferential binding sites of nucleosomes [52]. It is a general eukaryotic principle that the genome sequence codes for a basic chromatin architecture with the base-pair sequence favoring nucleosome positioning and occupancy at specific sites [53–55]. In vitro and in vivo studies showed that nucleosome positions are in part determined by intrinsic DNA features [54]. The GC-content and the frequency of polyA-stretches and certain dinucleotide repeats turned out to be critical determinants for nucleosome positioning and occupancy and, therefore, impact the overall regulation of gene expression [56].

However, the AT-rich plasmodial genome sequence deviates substantially from other eukaryotes with respect to sequence motifs, and likewise *Pf* nucleosomes do not obey the classical sequence-dependent positioning rules [49]. The typical 10 bp periodicity of anti-phased A/T and G/C dinucleotides in nucleosomal DNA [57] is only weakly detectable in *P. falciparum* [18], [58]. The shifted nucleotide-ratio in the *Pf* genome creates a very different basis for chromatin structure, and *Pf* histones show deviating affinities when forming nucleosomes. Nucleosome positioning analysis in *Pf* revealed a significant number of positioned nucleosomes in vivo, mainly located at or in the vicinity of regulatory regions, as expected for their regulatory role in determining DNA accessibility. This raises the question of the mechanisms being responsible for nucleosome positioning in vivo, even though the *Pf* histone octamer does not recognize the underlying sequence code. There are numerous mechanisms that can still contribute to nucleosome positioning in *Pf*, including DNA binding factors, statistical positioning of neighboring nucleosomes by a constant DNA linker length and chromatin-remodeling factors that move and position nucleosomes [59]. For *Pf* nucleosomes it was shown that AT-repeat sequences in the DNA linker regions are sufficient to position nucleosomes. This presents a novel signal and mechanism for nucleosome positioning and suggests that histone linkers may interact with the linker DNA, thereby contributing to nucleosome positioning. Crystal structures of *Pf* nucleosomes are not available so far, but in silico modeling based on human nucleosomes suggests an overall similar nucleosome core structure with only a few divergent amino acids in the histone–DNA interacting regions [49]. The majority of sequence variation is located in the flexible histone tail regions, whose likely contribution to nucleosome positioning has not been proven yet. The fact is that *Pf* nucleosomes show decreased nucleosome stability overall, with weaker binding of H2A/H2B-dimer within the octamer, and an attenuated histone–DNA interaction increases the mobility of nucleosomes on DNA. The hypothesis that altered nucleosome properties evolved as an adaptation to the AT-rich plasmodial genome could be rejected. In vitro and in vivo data show that *Pf* histones like other eukaryotic histones bind preferentially to GC-rich over AT-rich DNA [49].

Besides the differences in nucleosomal properties, the nucleosome repeat length is highly divergent as well when compared to other eukaryotes. With a repeat length of 155 bp, the spacing of the nucleosome cores is maintained by DNA linkers with only 8 bp. Short nucleosome spacing is an intrinsic biochemical property of the *Pf* nucleosome, which can be observed in vitro and is maintained also in vivo [49,60]. The mean linker length in eukaryotes is significantly longer, varying from 20 to 75 bp depending on species and cell type [61]. Such short linker lengths, as found in *Plasmodium*, were shown to inhibit the folding of the nucleosome array into compact higher order structures of chromatin. The absence of higher-order chromatin structure correlates well with the assumption that *Pf* chromatin exhibits high accessibility [49,62–64]. The extremely short linker length and unusual chromatin compaction are putative consequences of the exceptional nature of DNA composition and histone properties in *Pf*.

3.2. Histone Variation

In addition to canonical histones, eukaryotes express histone variants throughout the cell cycle, which differ in amino acid sequence. Sequence variation occurs predominantly in the (N-)terminal histone tails and leads to novel and different sites of post-translational modifications, potentially impacting their function and interaction with chromatin-modifying enzymes [65]. Among eukaryotic species, different sets of variant histones are prevalent, with some ubiquitous variants having specialized functions in DNA repair (H2A.X), transcription activation (H2A.Z), kinetochore formation (CenH3) and transcription in general (H3.3) [66].

In *P. falciparum*, a homologue of the universally present H2A.Z was identified, but no H2A.X. Surprisingly, Apicomplexa additionally express an unusual H2B variant histone, called H2B.Z, whose function is still unclear. Genome-wide profiling revealed similar binding sites of *Pf*H2A.Z and *Pf*H2B.Z and coimmunoprecipitation experiments confirmed the existence of nucleosomes containing both H2A.Z and H2B.Z in the same octamer [67,68]. This observation is shared with studies in other Apicomplexa, including *Toxoplasma gondii*, indicating a role in the regulation of gene expression (reviewed in [69]).

Histones H3.3 and CenH3, the two universal variants replacing histone H3, are present in *P. falciparum*, although they have not been characterized in detail. Histone H3.3 has eight amino acids substitutions compared to canonical H3 (one amino acid exchanged in human H3.3) and is believed to preferentially bind GC-rich repetitive regions, independent of transcriptional activity, potentially contributing to the regulation of *var* gene expression and immune evasion [70]. The second H3 variant, CenH3, is enriched at AT-rich sequences of the centromere and is implicated in chromosome segregation [70,71].

Histones are the target for post-translational modifications (PTMs), mainly comprising acetylation, methylation and phosphorylation of the histone amino termini, which alter histone properties and their interactions with DNA and chromatin proteins, affecting the functionality of the underlying DNA. The combinatorial nature and functional impact of these epigenetic modifications are defined as the "histones code" amplifying the information content and plasticity of chromatin with respect to the regulation of all DNA-dependent processes [72,73]. Here too, *P. falciparum* exhibits striking differences to other eukaryotes with an unusually large proportion of constitutively acetylated histones and a high number (500) of identified PTMs, including several novel modifications specific to *Plasmodium* or Apicomplexa [72,74,75]. A recent study showed, that a few universally eukaryotic PTMs, initially proposed to be absent in *P. falciparum*, are tightly regulated, and their presence is limited to specific life cycle stages [76]. The presence of some dynamic PTMs peaking in particular stages, such as H3K4 and H3K27 modifications, emphasize their contribution to gene-expression regulation throughout stage development [72,76,77].

3.3. Nucleosome Occupancy and Dynamics In Vivo

Nucleosomal distribution on DNA is described by the terms "nucleosome occupancy" and "nucleosome positioning": Occupancy describes the probability with which a certain base pair is covered by a nucleosome, while nucleosome positioning is a measure of the probability of a given base pair to serve as start, dyad or end position of a nucleosome [78].

The reduced stability and loss of sequence-dependent positioning of plasmodial nucleosomes in vitro is reflected by the genome-wide analysis of chromatin structure in vivo. In *Pf*, large genomic regions lack positioned nucleosomes or even appear to lack histone octamers on DNA at all. Several studies have addressed the nucleosomal landscape in *P. falciparum*, using Sonication-ChIP, MNase-ChIP, MNase-Seq and other methods, such as ATAC-seq and FAIRE, to detect nucleosome-free regions [18,45,46,58,79–81]. In summary, these studies show higher nucleosome density in heterochromatin, but contradicting experimental results were obtained regarding nucleosome occupancy in genic or intergenic regions. This review focuses on describing the nucleosomal landscape. For this, we largely exclude the description of FAIRE- and ATAC-seq experiments, as these methods monitor accessible DNA regions, not nucleosomal architecture. Recent studies addressing human and *Drosophila* chromatin have revealed the existence of nucleosomes with different stability [64,82] and, in order to assess all nucleosomes on DNA, appropriate protocols have been established. It was shown that partial MNase digestion of chromatin with still intact di- and tri-nucleosome fragments improves the overall sequencing coverage of nucleosomal DNA and avoids the loss of MNase-sensitive nucleosomes that are preferentially located at regulatory regions [64,82]. Taking into account these recent insights, we focus on experimental data that omit MNase digestion bias, in order to provide a clearer overview of *Plasmodium falciparum* chromatin structure. The only study so far using limited MNase digestion conditions was performed by Kensche and colleagues [18].

Intriguingly, the transcriptional unit of a typical gene in *P. falciparum* is framed by positioned nucleosomes upstream and downstream of the coding region (see Figure 2), resulting in the covering of regulatory regions and functional elements in the genome by positioned nucleosomes. A positioned +1 nucleosome can be mapped right at the TSS next to an upstream nucleosome-depleted region (NDR) of variable size and a detectable -1 nucleosome upstream of the NDR. This is a common pattern in eukaryotes, albeit the clarity and effectiveness of nucleosome positioning at these sites appear to be relaxed. The width of the NDR varies between individual *Pf* core promotors with a tendency of larger NDRs being associated with higher transcription levels. Positioned nucleosomes can also be detected at start and stop codons, as well as at splicing sites, which are relatively static throughout the life cycle. Nucleosomes positioned at start/stop codons may occur solely because of the increased GC-content of coding sequences, whereas those at exon–intron boundaries might be actively positioned to allow recruitment of post-transcriptional machineries. Overall, these observations suggest that nucleosome positions somehow highlight transcriptionally relevant landmarks, but positioning is less stringent and more fuzzy when compared to other eukaryotes. The MNase-seq data also indicated the typical 10 bp periodicity signal for AA/TT-dinucleotide driven nucleosome positioning in genic and intergenic regions, suggesting it is an additional, albeit less pronounced, feature of nucleosome positioning in *Plasmodium*. Kensche and colleagues suggest this much fuzzier pattern to be a global effect originating in the merging of multiple genes displaying different nucleosome patterns. Alternatively, the fuzziness could be a local consequence of the divergent stability and positioning properties of *Pf* nucleosomes within individual genes and thus, point to a distinct chromatin organization [49].

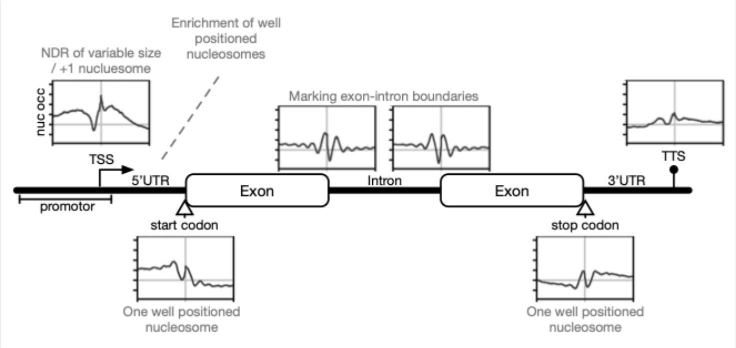

Figure 2. Schematic illustration of a typical gene with transcriptional landmark sites and corresponding plasmodial nucleosome positioning. The nucleosome profiles show the average MNase-seq occupancy normalized by gDNA aligned to the respective gene element combining eight time-points throughout the erythrocytic cycle according to [18]. Functional gene elements are designated, transcription start/stop is indicated arrow-/circle-tipped above the gene, translation start/stop codons are marked by arrows below the gene.

Comparative analysis of nucleosome-positioning dynamics at different life cycle stages shows that most nucleosomes in the transcriptional unit are static and nondynamic, indicating no gross changes of chromatin structure with variable gene expression. However, upstream promotor regions show significant changes in nucleosome occupancy levels during the life cycle, correlating with changes in gene transcription. With increasing transcriptional activity, nucleosome-depleted regions appear, which may be related to the formation of the RNA polymerase II initiation complexes. Accordingly, gene repression correlates with dynamic increases in nucleosome levels inhibiting transcription initiation [18,58,80]. The data suggest local changes in nucleosome occupancy around specific DNA motifs within these 5′ intergenic region being indicative of transcription factor binding, whereas global chromatin structure stays unaltered throughout the life cycle [18].

Studies mapping the genomic localization of nucleosomes containing the histone variants H2A.Z and H2B.Z identified them in the intergenic regions of euchromatin domains, particularly enriched at gene promotors [19,67–69]. The variant nucleosome levels do not change during the life cycle, suggesting that they permanently mark promotors and regulatory regions. The transcriptional activation of the heterochromatic *var* genes represents an exception to this rule, as the H2A.Z/B.Z levels at these promoters correlate with increased transcription level [68]. Moreover, the histone variant *Pf*H3.3 is preferentially located at euchromatic coding and subtelomeric repetitive sequences unrelated to transcription, whereas in other eukaryotes H3.3 is incorporated at sites of active transcription [83]. Interestingly, *Pf*H3.3 incorporation was also found at promotors of poised and active (but not inactive) *var* genes pointing to its putative contribution to epigenetic memory in *var* gene expression [70].

Not only the histone variant distribution, but also the occupancy and positioning of *Pf* nucleosomes in general do not quite follow known eukaryotic principles. The highly divergent underlying determinants—DNA and histone properties—seem to shape a very different chromatin landscape in *Plasmodium falciparum*, and potential novel mechanisms may have evolved to allow for the tightly regulated gene expression program in the parasite.

3.4. Chromatin Density and Nuclear Organization

Progressing through the erythrocytic life cycle, major changes in nucleosome occupancy were reported, obtained via high MNase digestion and Hi-C techniques [58,79,84]: the ring stages exhibit high nucleosome occupancy, whereas a depletion of nucleosomes was observed in the trophozoite stage, potentially opening chromatin for transcription and DNA replication. In the following schizont stage, nucleosome occupancy increases again, correlating with chromatin compaction for merozoite differentiation and egress. The chromatin structure in gametocytes was found to be relatively open. These global changes in chromatin accessibility within the life cycle are specific to *P. falciparum* and have not been reported to a comparable extent in any other eukaryote.

Nuclear organization is proposed to be another epigenetic layer contributing to gene expression regulation using mechanisms such as rearrangement of chromosomes, locus repositioning and heterochromatic silencing [85]. Various studies have attempted to unveil the three-dimensional nuclear organization of *Plasmodium falciparum* using chromosome conformation capture techniques (reviewed in [85,86]). One characteristic of *P. falciparum* is the absence of chromosome territories supporting the presence of a relatively accessible chromatin structure. Although clustering for certain genomic domains, such as heterochromatin foci, telomeres and ribosomal DNA, could be shown, no pronounced chromosome condensation comparable to other eukaryotes was observed [87].

4. Epigenetic Regulation of Transcriptional Activity

As described in the previous sections, gene transcription is impacted by a combination of epigenetic features shaping the chromatin landscape: the main determinants are the variations of nucleosome occupancy and nucleosome positioning at specific DNA elements and histone variants, in addition to the dynamic histone PTMs as well as higher-order chromatin structures. Furthermore, long noncoding RNAs [88,89] have been suggested to contribute to gene regulation by serving as modular scaffolds and targeting modules that recruit chromatin-modifying enzymes to specific loci [90,91]. Finally, the driving force is the accessibility of promotors and enhancers within chromatin—implemented by correct nucleosome positioning—for transcription-factor binding and the initiation of complex formation [92].

Genome-wide MNase-seq [18] and ATAC-seq data [46] confirm this principle in *P. falciparum*: Kensche and colleagues identified 4821 dynamic nucleosomes with 80 percent being located in euchromatic intergenic regions, mainly at promotors. The dynamics of these nucleosomes clearly correlate with temporal transcriptional activity of the downstream gene. Toenhake and colleagues identified 4035 accessible regions, whereof 90 percent are located in intergenic regions. The majority was found to be associated with one or more putative promotors and to correlate in accessibility score with abundance of the downstream gene product.

For some genes with high transcriptional variation, the epigenetic mechanisms were investigated in more detail (reviewed in [85]): the group of invasion genes was found to exist in an activated state caused by an interplay of the transcription factor AP2-I with the bromodomain-binding protein BDP1 binding to H3K9ac [93]. A repressed state in contrast—extensively studied on the example of *var* genes—is maintained by heterochromatin protein HP1, histone deacetylase HDA2 and the histone lysine methyltransferase SET2 and marked by H3K9me3 rendering these genes heterochromatic [94–97]. Furthermore, a chromatin-remodeling enzyme [PF3D7_0624600] and sirtuin proteins influence chromatin condensation [98,99], and the incorporation of noncoding RNAs complement the *var* gene-switching mechanism by silencing the gene locus via its sense—activating via its antisense—lncRNA [90,100]. Sexual commitment is known to be regulated by the epigenetic cascade starting with Ap2-G expression being repressed by HP1, which is evicted upon gametocyte development 1 (GDV1) association to heterochromatin, and GDV1 itself is controlled by the *gdv1* antisense RNA [35,97,101,102].

These examples illustrate the multilayered nature of epigenetic regulation, but concomitant nucleosome occupancy and positioning were hardly taken into consideration. However, in all of the described processes, nucleosome occupancy determines any interactions with the underlying DNA locus and certainly contributes to the unveiled regulatory mechanism. The importance of nucleosome occupancy was highlighted in a machine-learning model, wherein the relevance of individual epigenetic features in relation to the entirety of transcription regulation was assessed [77]: a collection of genomic and epigenomic data sets including information about transcription factor binding motifs, patterns of covalent histone modifications, nucleosome occupancy, GC content and global 3D genome architecture were analyzed for their prevalence in high-/low-expression genes. This kind of comparative analysis emphasizes the relevance of histone modifications, nucleosome occupancy and 3D chromatin architecture and suggests transcription-factor binding to be less important for transcription regulation.

5. Chromatin Remodeling Enzymes

All DNA-dependent processes require dynamic changes in chromatin organization to exert their DNA specific activities. For this, eukaryotic cells have developed numerous enzymes that change the organization of DNA packaging [103]. Chromatin-remodeling enzymes alter chromatin structure by moving nucleosomes, while chromatin modifiers leave their chemical marks on chromatin to change the physicochemical properties of the chromatin fiber or to target protein/RNA complexes to specific genomic loci. The high variability of global and local chromatin packaging states and the numerous chromatin modifications associated with different functional processes, demonstrate the superordinate role of chromatin proteins in eukaryotic cells. On that account, it is important to study this emerging field in *Plasmodium falciparum*, as the fundamental differences between chromatin proteins in humans and *Plasmodium* will provide new insights into the evolution and mechanisms of chromatin dynamics and may reveal new therapeutic options.

In a comparative genomics study, the evolution of transcription factors, chromatin-modifying and -remodeling enzymes in parasitic protists was reconstructed [104]: Intriguingly, chromatin proteins evolved over millions of years in independent eukaryotic lineages through the proliferation of paralogous families and acquisition of novel domain architectures, leading to an enormous variety and to highly diverse sets of enzymes. Some chromatin-modifying enzymes have been identified in *Plasmodium falciparum* (detailed review in [105]). In this review we will focus on the evolution and mechanisms of chromatin-remodeling enzymes.

Remodeling enzymes and the large multiprotein complexes they form exert a direct ATP-dependent effect on nucleosomes. The enzymes alter histone–DNA interactions, resulting in the eviction, exchange and assembly of individual histones or histone octamers, changing the structure and stability of nucleosomes or the movement of histone octamers on DNA to reposition nucleosomes (reviewed in [43,106]). In order to disrupt the very stable interaction between histones and DNA, these enzymes couple their activity to ATP hydrolysis. A highly conserved ATPase module is conserved within all chromatin-remodeling enzymes, which is split into a Snf2_N and a helicase C domain, separated by a P-loop. The enzymes generally exhibit several additional protein domains, determining their specificity in substrate recognition and interaction with other proteins or RNA to form a variety of protein complexes [107].

The essential molecular function of this enzyme family is the movement of nucleosomes in order to provide accessibility to certain DNA regions. However, the exact regulatory mechanisms of this process—with respect to which nucleosomes are recognized to be moved and what is the target position—have not been completely uncovered. There is some evidence of “high affinity” and “low affinity” nucleosomes representing a putative mechanism or at least one aspect of defining reaction educts and products [108]. Therefore, multiple factors, such as the recognition of DNA sequences and structures, nucleosome composition and histone PTMs, play a crucial role. The specificity of remodeling machines depends furthermore on the central motor protein as well as the composition of all the associated complex subunits dramatically changing the responsiveness to various substrates and recruiting mechanisms. [43,106]. In human and mouse cells, it was estimated that over 1000 different chromatin-remodeling complexes with distinct functions may exist. Their cell-type-specific combination and dosage probably determines the cell-type-specific chromatin architecture, the gene-expression network and the responsiveness to specific signaling pathways in the cell [43,106,108–110]. To name an example, Snf2H—one of the 53 remodeling enzymes in humans—was biochemically purified in 18 different multiprotein complexes emphasizing the complexity of the "remodeling code" [111].

The functionally different subfamilies of SWI/SNF ATPases are grouped by the homology of the helicase region according to Flaus et al. (indicated by coloring in Figure 3) [112]: Starting with the Snf2-like group, the ISWI subfamily is mainly responsible for nucleosome repositioning, playing a role in nucleosome stabilization and higher-order structure [113,114]. In contrast, Snf2 enzymes have a more disruptive effect on nucleosomes, and Lsh proteins are associated with transcription silencing, cooperating with methyltransferases [115–117]. Chd proteins, comprising the Chd1, Mi-2 and Chd7 subfamilies, possess specific nucleosome remodeling activities and are characterized by their additional chromodomain. They are involved in processes like chromatin assembly nucleosome spacing [118,119] or function as regulators of gene expression in functionally distinct complexes [120,121]. The principal functions of the Swr1-like group—identifiable by the divided helicase domain and HSA domain—include histone eviction and the exchange of variants [122]. Rad54-like proteins seem to change DNA topology and alter nucleosomal accessibility [123], while Rad5/16 is involved in DNA repair pathways using its characteristic RING finger domain [124]. The SSO1652-like family does not directly alter nucleosome structure but is proposed to interact with transcription factors and is recruited to DNA lesions [115–117,125]. Last, a function for the distant group has not yet been determined. This selective overview indicates the functional diversity between the subfamilies of enzymes that depend on the highly conserved ATPase domain in combination with the additional complex subunits. The interplay of all these complexes in the cell organizes the nucleosomal landscape in a complex manner and, with this, the accessibility of regulatory DNA elements. Regulation of nucleosome positioning, keeping nucleosomes over regulatory sites—OFF state—or moving them next to the binding sites of regulatory factor—ON state configuration—likely determines local gene activity states. This mechanism can be paraphrased as "barcoding" the nucleosome landscape and highlights the essential role of remodeling enzymes in regulation and cellular differentiation [126].

Hidden Markov model (HMM) profile studies in *P. falciparum* revealed 10 genes encoding putative SWI2/SNF2 ATPases [12] and sharing similarities within the several subgroups, but with particularly low conservation when compared to other eukaryotes. According to evolutionary studies of Iyer and colleagues, remodeling enzymes had their origins in the bacteriophage replication system, and thereafter, a set of six enzymes with conserved domain architecture was suggested to be present in the last eukaryotic common ancestor (LECA) (Figure 3, left panel) [104]. During evolution, prior to the origin of kinetoplasts and then chromalveolates, new families of remodeling enzymes evolved with precursors of the Rad5/16 group, distant group, ALC1, Lsh and Etl1. Early on, the apicomplexan line evolved ten chromatin remodelers, whereof eight proteins could be allocated in the evolutionary model of Iyer and colleagues, based on homology search and domain architecture (Figure 3, mid panel). Higher eukaryotes developed a huge variety of SWI2/SNF2 ATPases starting from a few ancient types, e.g. leading to more than 50 in human cells (Figure 3, right panel) [112]. In comparison, *P. falciparum* possesses a limited set of 10 enzymes, only one per family, and therefore lacks the typical redundancy seen in higher eukaryotes, suggesting that these enzymes perform essential tasks in the cell. This fundamental difference in numbers between human cells and *P. falciparum* is accompanied in highly divergent domain architectures. Some domains such as PhD, Chromo and SANT domains, could be identified at very low stringency in sequence comparison but with no indication of their specific functions in *Pf*.

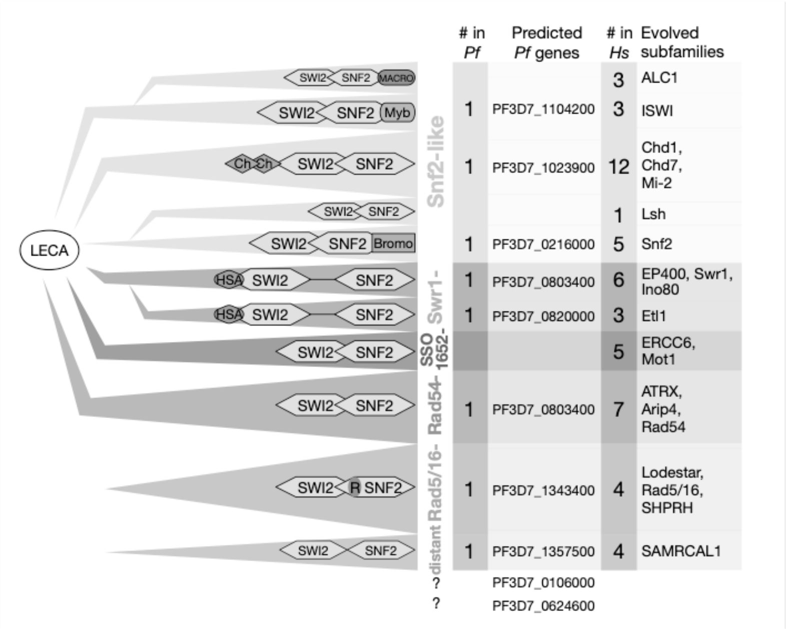

Figure 3. Evolutionary and phylogenetic development of SW2I/SNF2 ATPases. The evolution of SWI2/SNF2 starting from last eukaryotic common ancestor (LECA), according to [104], with triangles grouping together multiple subfamilies and their conserved domain architecture illustrated (left panel). Grouping of subfamilies and their names, according to [112], are indicated by coloring. SWI2-/SNF2-encoding genes in *P. falciparum*—wherever possible—were allocated to the categorization. Numbers of prevalent proteins for *P. falciparum* and *H. sapiens*, as well as names of further evolved subfamilies, are provided. Domain names: Ch = Chromo, R = RING, HAS = helicase/SANT-associated.

The individual remodeling enzymes in *P. falciparum*, and Apicomplexa in general, remain poorly characterized so far. In a pioneering study, Ji and Arnot identified and classified the first SWI2/SNF2 enzyme (Snf2L) with approximately 60% sequence homology to the ATPase domain of the yeast ISWI remodeler [127]. Since then, only a few studies addressed apicomplexan remodelers [98,128]. A genome-wide mutagenesis screen proposed one of the plasmodial remodelers to be essential and another two as putatively essential in asexual blood stages [9]. The authors suggest that the rest are not crucial for parasite fitness, not precluding the possibility of significant roles in chromatin organization.

In general, perhaps with the exception of Chd1, all chromatin-remodeling enzymes are part of large multiprotein complexes with characteristic binding partners that link the enzymes to chromatin modifiers, chromatin and DNA binding motifs and alter the functionality of the complexes [109]. Interestingly, homology searches did not retrieve a single homologue of these proteins in *P. falciparum*. This astonishing lack of known interactors in combination with the reduced number and high divergence in sequence indicates that the chromatin-remodeling system in *Plasmodium* differs from known mechanisms in higher eukaryotes.

6. Potential Regulatory Network

As elaborated in the previous sections, *Plasmodium falciparum* chromatin is unusual in many respects, from the reduced number of transcription factors to high nucleosome dynamics and the divergent chromatin-remodeling enzymes/complexes. Therefore, we hypothesize that *P. falciparum* possesses a highly regulated but distinct chromatin system when compared to other eukaryotes. Here we address how these differences may affect the regulatory network and the transcriptional program throughout the parasite life cycle (Figure 4).

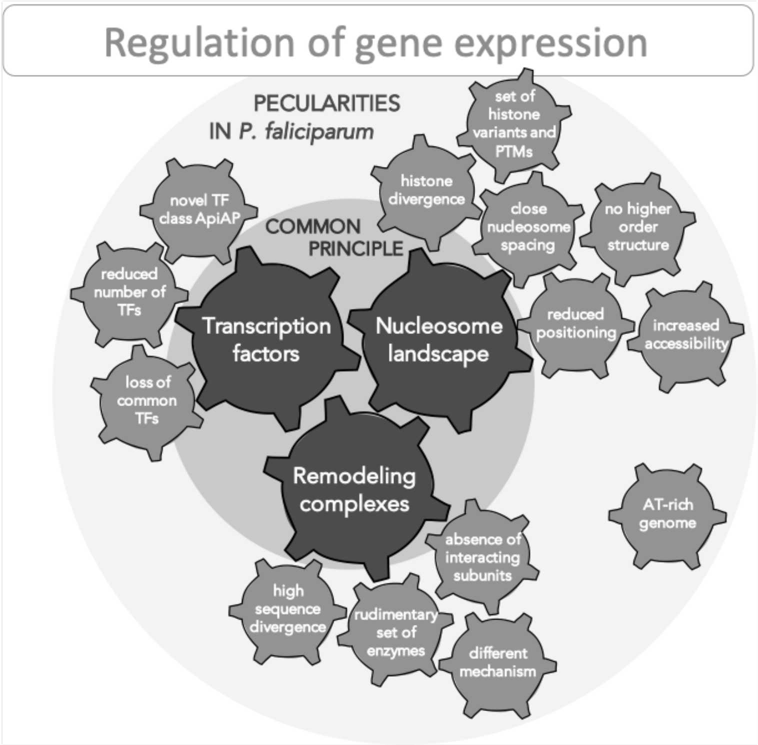

Figure 4. Schematic representation of the regulatory network of gene expression, with peculiar features in *P. falciparum* that affect the common principles.

One crucial parameter for transcription regulation is the nucleosome landscape, which was investigated in several studies within the last few years. Conclusively, these studies point out a highly dynamic chromatin structure and atypical nucleosome features in *P. falciparum* [18,49,79]. The overall *Pf* chromatin was found to have a more open structure; the spacing of nucleosomes is surprisingly short; it is not organized in defined higher-order structures, and the nucleosomes themselves show reduced stability and lost capacity for sequence-dependent positioning (see Sections 3.1 and 3.4). It is not known what exactly causes these altered nucleosome properties, but the extraordinary AT-rich genome and the extraordinarily high sequence divergence of *Pf* histones might interoperate to form this particular chromatin structure.

However, the applied methodology of chromatin analysis in *Plasmodium* parasites and the interpretation of the results is still a matter of discussion. On one hand, the AT-rich nature of the DNA is known to bias sequencing techniques [129]. On the other hand, the parasite rapidly moving through its highly different life cycle stages also blur the clarity of the observations. The fuzziness of *Pf* nucleosomal landscapes might be the consequence of highly unstable nucleosomes but could also represent the dynamic nature of chromatin in this organism. A strictly regulated but rapidly changing nucleosomal landscape is hard to capture precisely with the available techniques so far.

The second pillar of transcriptional regulation is formed by transcription factors and their interaction with *cis*-acting regulatory elements. The set of TFs that exist in *P. falciparum* was identified and characterized to some extent within the last few years, and the binding motifs and binding sites for many of them were identified. For the binding of certain transcription factors, such as Api2-G or Api2-O, defined downstream effects on the transcriptome were observed [32]. Since only a reduced number of TFs, primarily members of the ApiAP2 family were found, their relevance in gene-expression control is questionable. In any case, the mechanism of *trans*-regulatory factors is closely linked to the nucleosome landscape, since the accessibility of binding regions is an essential prerequisite for factor binding [92,130]. Therefore, promotor regions need to be nucleosome-depleted to enable TF binding. A detailed analysis of nucleosome positioning relative to TF binding regions would give us important information about the hierarchy of coaction between those two levels of regulation. Is the DNA region around the binding motif permanently nucleosome-depleted and thus accessible for TF-binding? If not, which mechanisms are responsible for uncovering these regions? Are some of the transcription factors pioneer factors that are capable of recognizing nucleosome-occupied motifs and subsequently recruiting chromatin-remodeling activities? These questions about specificity, recruitment and the order of events are important open issues in the field.

We propose that, for transcription regulation in *Plasmodium falciparum*, the chromatin-remodeling machinery is a third crucial determinant, strongly interlinked with the binding of transcription factors to DNA. As DNA properties explain the nucleosomal landscape only in part, active movement and positioning by remodelers has a high impact on nucleosome positioning and thus, on gene expression regulation [43,106,131]: remodeling complexes are recruited to target genes by transcription factors, RNA polymerases and elongation factors to promote or block transcription initiation and elongation by rearranging nucleosomes. They are the engines that both block (repression) or enable (activation) access to a gene through movement, positioning and the eviction/insertion of nucleosomes, depending on the specific type of remodeling enzyme at this locus. Remodeling complexes may barcode the genome in each stage of the life cycle, meaning that they establish a nucleosome-positioning landscape that allows the binding of certain factors and, conversely, restricts accessibility for other factors. Current investigations attempt to decipher this “remodeling code” and address the questions of how genomic loci are specifically recognized and how these enzymes are regulated. Which features determine the affinity to individual nucleosomes, serving as parameter for locus-specific nucleosome positioning? Another question is what is within the scope of function of the motor protein itself and what features are mediated by complex subunits? Looking at one level above, the regulation of remodeling enzymes themselves need to be investigated; it is presumed to occur in three different ways: control takes place (a) via recruiting to the correct target site by sensing the histone code or other factors [43]; (b) via adjustment of enzyme activity, e.g., by post-transcriptional protein-modification or ncRNAs [91]; or (c) by changing associated subunits and thus, conferring different activities to the complex (reviewed in [106]).

How remodeling enzymes pave the way for transcription-factor and polymerase binding and how they are regulated is completely unexplored in *P. falciparum*. Based on the reduced number of identified *Pf* enzymes with high sequence divergence and the absence of any known interacting subunits, as there are in higher eukaryotes, we expect functional divergence. We propose that *Pf* remodeling complexes—closely linked with the nucleosome landscape and transcription-factor binding—build a complex regulatory network exhibiting major differences in comparison to other eukaryotes. The decryption of this system is indispensable to understanding the mechanism of transcription regulation in the parasite and will provide new insights and novel approaches for fighting malaria.

Author Contributions: Writing—original draft preparation, M.T.W. and G.L.; writing—review and editing, M.T.W., S.D., M.M. and G.L.; funding acquisition, G.L. All authors have read and agreed to the published version of the manuscript.

Funding: This research was funded by Deutsche Forschungsgemeinschaft (SFB960).

Conflicts of Interest: The authors declare no conflict of interest.

References

1. World Health Organization. *World Malaria Report 2020: 20 Years of Global Progress and Challenges*; WHO: Geneva, Switzerland, 2020.
2. Haldar, K.; Bhattacharjee, S.; Safeukui, I. Drug resistance in Plasmodium. *Nat. Rev. Genet.* **2018**, *16*, 156–170. [CrossRef] [PubMed]
3. Douzery, E.J.P.; Snell, E.A.; Bapteste, E.; Delsuc, F.; Philippe, H. The timing of eukaryotic evolution: Does a relaxed molecular clock reconcile proteins and fossils? *Proc. Natl. Acad. Sci. USA* **2004**, *101*, 15386–15391. [CrossRef] [PubMed]
4. Sinka, M.E.; Bangs, M.J.; Manguin, S.; Rubio-Palis, Y.; Chareonviriyaphap, T.; Coetzee, M.; Mbogo, C.M.; Hemingway, J.; Patil, A.P.; Temperley, W.H.; et al. A global map of dominant malaria vectors. *Parasites Vectors* **2012**, *5*, 69. [CrossRef]
5. Reece, J.B.; Campbell, N.A. *Campbell Biology*; Benjamin Cummings/Pearson: Boston, MA, USA, 2011.
6. Gardner, M.J.; Hall, N.; Fung, E.; White, O.; Berriman, M.; Hyman, R.W.; Carlton, J.M.; Pain, A.; Nelson, K.E.; Bowman, S.; et al. Genome sequence of the human malaria parasite *Plasmodium falciparum*. *Nat. Cell Biol.* **2002**, *419*, 498–511. [CrossRef] [PubMed]
7. Böhme, U.; Otto, T.D.; Sanders, M.; Newbold, C.I.; Berriman, M. Progression of the canonical reference malaria parasite genome from 2002–2019. *Wellcome Open Res.* **2019**, *4*, 58. [CrossRef]
8. Su, X.-Z.; Lane, K.D.; Xia, L.; Sá, J.M.; Wellems, T.E. PlasmodiumGenomics and Genetics: New Insights into Malaria Pathogenesis, Drug Resistance, Epidemiology, and Evolution. *Clin. Microbiol. Rev.* **2019**, *32*. [CrossRef] [PubMed]
9. Zhang, M.; Wang, C.; Otto, T.D.; Oberstaller, J.; Liao, X.; Adapa, S.R.; Udenze, K.; Bronner, I.F.; Casandra, D.; Mayho, M.; et al. Uncovering the essential genes of the human malaria parasite *Plasmodium falciparum* by saturation mutagenesis. *Science* **2018**, *360*, eaap7847. [CrossRef]
10. Le Roch, K.G.; Zhou, Y.; Blair, P.L.; Grainger, M.; Moch, J.K.; Haynes, J.D.; De La Vega, P.; Holder, A.A.; Batalov, S.; Carucci, D.J.; et al. Discovery of Gene Function by Expression Profiling of the Malaria Parasite Life Cycle. *Science* **2003**, *301*, 1503–1508. [CrossRef]
11. Francis, W.R.; Wörheide, G. Similar Ratios of Introns to Intergenic Sequence across Animal Genomes. *Genome Biol. Evol.* **2017**, *9*, 1582–1598. [CrossRef]
12. Horrocks, P.; Wong, E.; Russell, K.; Emes, R.D. Control of gene expression in *Plasmodium falciparum*—Ten years on. *Mol. Biochem. Parasitol.* **2009**, *164*, 9–25. [CrossRef]
13. Toenhake, C.G.; Bártfai, R. What functional genomics has taught us about transcriptional regulation in malaria parasites. *Brief. Funct. Genom.* **2019**, *18*, 290–301. [CrossRef] [PubMed]
14. Watanabe, J.; Sasaki, M.; Suzuki, Y.; Sugano, S. Analysis of transcriptomes of human malaria parasite Plasmodium falci-parum using full-length enriched library: Identification of novel genes and diverse transcription start sites of messenger RNAs. *Gene* **2002**, *291*, 105–113. [CrossRef]
15. Pesole, G. UTRdb and UTRsite: Specialized databases of sequences and functional elements of 5′ and 3′ untranslated regions of eukaryotic mRNAs. Update 2002. *Nucleic Acids Res.* **2002**, *30*, 335–340. [CrossRef]
16. Adjalley, S.H.; Chabbert, C.D.; Klaus, B.; Pelechano, V.; Steinmetz, L.M. Landscape and Dynamics of Transcription Initiation in the Malaria Parasite *Plasmodium falciparum*. *Cell Rep.* **2016**, *14*, 2463–2475. [CrossRef] [PubMed]
17. Horrocks, P.; Lanzer, M. Differences in nucleosome organization over episomally located plasmids coincides with aber-rant promoter activity in *P. falciparum*. *Parasitol. Int.* **1999**, *48*, 55–61. [CrossRef]
18. Kensche, P.R.; Hoeijmakers, W.A.M.; Toenhake, C.G.; Bras, M.; Chappell, L.; Berriman, M.; Bártfai, R. The nucleosome landscape of *Plasmodium falciparum* reveals chromatin architecture and dynamics of regulatory sequences. *Nucleic Acids Res.* **2016**, *44*, 2110–2124. [CrossRef] [PubMed]
19. Bártfai, R.; Hoeijmakers, W.A.M.; Salcedo-Amaya, A.M.; Smits, A.H.; Janssen-Megens, E.; Kaan, A.; Treeck, M.; Gilberger, T.-W.; Françoijs, K.-J.; Stunnenberg, H.G. H2A.Z Demarcates Intergenic Regions of the *Plasmodium falciparum* Epigenome That Are Dynamically Marked by H3K9ac and H3K4me3. *PLoS Pathog.* **2010**, *6*, e1001223. [CrossRef] [PubMed]
20. Iengar, P.; Joshi, N. Identification of putative regulatory motifs in the upstream regions of co-expressed functional groups of genes in *Plasmodium falciparum*. *BMC Genom.* **2009**, *10*, 18. [CrossRef]
21. Wu, J.; Sieglaff, D.H.; Gervin, J.; Xie, X.S. Discovering regulatory motifs in the Plasmodium genome using comparative genomics. *Bioinformatics* **2008**, *24*, 1843–1849. [CrossRef]
22. Young, J.A.; Johnson, J.R.; Benner, C.; Yan, S.F.; Chen, K.; Le Roch, K.G.; Zhou, Y.; Winzeler, E.A. In silico discovery of transcription regulatory elements in *Plasmodium falciparum*. *BMC Genom.* **2008**, *9*, 1–21. [CrossRef]
23. Ubhe, S.; Rawat, M.; Verma, S.; Anamika, K.; Karmodiya, K. Genome-wide identification of novel intergenic enhancer-like elements: Implications in the regulation of transcription in *Plasmodium falciparum*. *BMC Genom.* **2017**, *18*, 1–16. [CrossRef]
24. Wang, C.; Gibbons, J.; Adapa, S.R.; Oberstaller, J.; Liao, X.; Zhang, M.; Adams, J.H.; Jiang, R.H. The human malaria parasite genome is configured into thousands of coexpressed linear regulatory units. *J. Genet. Genom.* **2020**, *47*, 513–521. [CrossRef] [PubMed]
25. Bischoff, E.; Vaquero, C. In silico and biological survey of transcription-associated proteins implicated in the transcriptional machinery during the erythrocytic development of *Plasmodium falciparum*. *BMC Genom.* **2010**, *11*, 34. [CrossRef] [PubMed]
26. Hahn, S.; Young, E.T. Transcriptional Regulation in Saccharomyces cerevisiae: Transcription Factor Regulation and Function, Mechanisms of Initiation, and Roles of Activators and Coactivators. *Genetics* **2011**, *189*, 705–736. [CrossRef] [PubMed]
27. Zhang, H.-M.; Chen, H.; Liu, W.; Liu, H.; Gong, J.; Wang, H.; Guo, A.-Y. AnimalTFDB: A comprehensive animal transcription factor database. *Nucleic Acids Res.* **2011**, *40*, D144–D149. [CrossRef] [PubMed]

28. Lambert, S.A.; Jolma, A.; Campitelli, L.F.; Das, P.K.; Yin, Y.; Albu, M.; Chen, X.; Taipale, J.; Hughes, T.R.; Weirauch, M.T. The Human Transcription Factors. *Cell* **2018**, *172*, 650–665. [CrossRef] [PubMed]
29. Balaji, S. Discovery of the principal specific transcription factors of Apicomplexa and their implication for the evolution of the AP2-integrase DNA binding domains. *Nucleic Acids Res.* **2005**, *33*, 3994–4006. [CrossRef] [PubMed]
30. Coulson, R.M.; Hall, N.; Ouzounis, C.A. Comparative Genomics of Transcriptional Control in the Human Malaria Parasite *Plasmodium falciparum*. *Genome Res.* **2004**, *14*, 1548–1554. [CrossRef]
31. Campbell, T.L.; De Silva, E.K.; Olszewski, K.L.; Elemento, O.; Llinás, M. Identification and Genome-Wide Prediction of DNA Binding Specificities for the ApiAP2 Family of Regulators from the Malaria Parasite. *PLoS Pathog.* **2010**, *6*, e1001165. [CrossRef]
32. Jeninga, M.D.; Quinn, J.E.; Petter, M. ApiAP2 Transcription Factors in Apicomplexan Parasites. *Pathogens* **2019**, *8*, 47. [CrossRef]
33. Modrzynska, K.; Pfander, C.; Chappell, L.; Yu, L.; Suarez, C.; Dundas, K.; Gomes, A.R.; Goulding, D.; Rayner, J.C.; Choudhary, J.; et al. A Knockout Screen of ApiAP2 Genes Reveals Networks of Interacting Transcriptional Regulators Controlling the Plasmodium Life Cycle. *Cell Host Microbe* **2017**, *21*, 11–22. [CrossRef]
34. Iwanaga, S.; Kaneko, I.; Kato, T.; Yuda, M. Identification of an AP2-family Protein That Is Critical for Malaria Liver Stage Development. *PLoS ONE* **2012**, *7*, e47557. [CrossRef]
35. Kafsack, B.F.C.; Rovira-Graells, N.; Clark, T.G.; Bancells, C.; Crowley, V.M.; Campino, S.G.; Williams, A.E.; Drought, L.G.; Kwiatkowski, D.P.; Baker, D.A.; et al. A transcriptional switch underlies commitment to sexual development in malaria parasites. *Nat. Cell Biol.* **2014**, *507*, 248–252. [CrossRef] [PubMed]
36. Santos, J.M.; Josling, G.; Ross, P.; Joshi, P.; Orchard, L.; Campbell, T.; Schieler, A.; Cristea, I.M.; Llinás, M. Red Blood Cell Invasion by the Malaria Parasite Is Coordinated by the PfAP2-I Transcription Factor. *Cell Host Microbe* **2017**, *21*, 731–741.e10. [CrossRef] [PubMed]
37. Yuda, M.; Iwanaga, S.; Shigenobu, S.; Mair, G.R.; Janse, C.J.; Waters, A.P.; Kato, T.; Kaneko, I. Identification of a transcription factor in the mosquito-invasive stage of malaria parasites. *Mol. Microbiol.* **2009**, *71*, 1402–1414. [CrossRef]
38. Yuda, M.; Iwanaga, S.; Shigenobu, S.; Kato, T.; Kaneko, I. Transcription factor AP2-Sp and its target genes in malarial sporozoites. *Mol. Microbiol.* **2010**, *75*, 854–863. [CrossRef] [PubMed]
39. Russell, K.; Cheng, C.-H.; Bizzaro, J.W.; Ponts, N.; Emes, R.D.; Le Roch, K.G.; Marx, K.A.; Horrocks, P. Homopolymer tract organization in the human malarial parasite *Plasmodium falciparum* and related Apicomplexan parasites. *BMC Genom.* **2014**, *15*, 1–17. [CrossRef]
40. Van Noort, V.; Huynen, M. Combinatorial gene regulation in *Plasmodium falciparum*. *Trends Genet.* **2006**, *22*, 73–78. [CrossRef]
41. Levo, M.; Segal, E. In pursuit of design principles of regulatory sequences. *Nat. Rev. Genet.* **2014**, *15*, 453–468. [CrossRef]
42. Cobbold, S.A.; Santos, J.M.; Ochoa, A.; Perlman, D.H.; Llinas, M. Proteome-wide analysis reveals widespread lysine acetylation of major protein complexes in the malaria parasite. *Sci. Rep.* **2016**, *6*, 19722. [CrossRef]
43. Becker, P.B.; Workman, J.L. Nucleosome Remodeling and Epigenetics. *Cold Spring Harb. Perspect. Biol.* **2013**, *5*, a017905. [CrossRef]
44. Sales-Gil, R.; Vagnarelli, P. How HP1 Post-Translational Modifications Regulate Heterochromatin Formation and Maintenance. *Cells* **2020**, *9*, 1460. [CrossRef] [PubMed]
45. Ruiz, J.L.; Tena, J.J.; Bancells, C.; Cortés, A.; Gómez-Skarmeta, J.L.; Gómez-Díaz, E. Characterization of the accessible genome in the human malaria parasite *Plasmodium falciparum*. *Nucleic Acids Res.* **2018**, *46*, 9414–9431. [CrossRef] [PubMed]
46. Toenhake, C.G.; Fraschka, S.A.-K.; Vijayabaskar, M.S.; Westhead, D.R.; van Heeringen, S.J.; Bártfai, R. Chromatin Accessibility-Based Characterization of the Gene Regulatory Network Underlying *Plasmodium falciparum* Blood-Stage Development. *Cell Host Microbe* **2018**, *23*, 557–569.e9. [CrossRef] [PubMed]
47. Baxevanis, A. Histone Sequence Database: New histone fold family members. *Nucleic Acids Res.* **1998**, *26*, 372–375. [CrossRef] [PubMed]
48. Marinov, G.K.; Lynch, M. Conservation and divergence of the histone code in nucleomorphs. *Biol. Direct* **2016**, *11*, 18. [CrossRef]
49. Silberhorn, E.; Schwartz, U.; Löffler, P.; Schmitz, S.; Symelka, A.; De Koning-Ward, T.; Merkl, R.; Längst, G. *Plasmodium falciparum* Nucleosomes Exhibit Reduced Stability and Lost Sequence Dependent Nucleosome Positioning. *PLoS Pathog.* **2016**, *12*, e1006080. [CrossRef]
50. Hagerman, P.J. Flexibility of DNA. *Annu. Rev. Biophys. Biophys. Chem.* **1988**, *17*, 265–286. [CrossRef]
51. Richmond, T.J.; Davey, C.A. The structure of DNA in the nucleosome core. *Nat. Cell Biol.* **2003**, *423*, 145–150. [CrossRef]
52. Widom, J. Role of DNA sequence in nucleosome stability and dynamics. *Q. Rev. Biophys.* **2001**, *34*, 269–324. [CrossRef]
53. Linzweiler, W.; Hörz, W. Reconstitution experiments show that sequence-specific histone-DNA interactions are the basis for nucleosome phasing on mouse satellite DNA. *Cell* **1985**, *42*, 281–290. [CrossRef]
54. Segal, E.; Fondufe-Mittendorf, Y.; Chen, L.; Thåström, A.; Field, Y.; Moore, I.K.; Wang, J.-P.Z.; Widom, J. A genomic code for nucleosome positioning. *Nat. Cell Biol.* **2006**, *442*, 772–778. [CrossRef] [PubMed]
55. Mengeritsky, G.; Trifonov, E.N. Nucleotide sequence-directed mapping of the nucleosomes. *Nucleic Acids Res.* **1983**, *11*, 3833–3851. [CrossRef] [PubMed]
56. Tillo, D.; Hughes, T.R. G+C content dominates intrinsic nucleosome occupancy. *BMC Bioinform.* **2009**, *10*, 442. [CrossRef] [PubMed]
57. Cui, F.; Zhurkin, V.B. Structure-based Analysis of DNA Sequence Patterns Guiding Nucleosome Positioningin vitro. *J. Biomol. Struct. Dyn.* **2010**, *27*, 821–841. [CrossRef] [PubMed]

58. Bunnik, E.M.; Polishko, A.; Prudhomme, J.; Ponts, N.; Gill, S.S.; Lonardi, S.; Le Roch, K.G. DNA-encoded nucleosome occupancy is associated with transcription levels in the human malaria parasite *Plasmodium falciparum*. *BMC Genom.* **2014**, *15*, 1–15. [CrossRef]
59. Lieleg, C.; Krietenstein, N.; Walker, M.; Korber, P. Nucleosome positioning in yeasts: Methods, maps, and mechanisms. *Chromosoma* **2015**, *124*, 131–151. [CrossRef]
60. Lanzer, M.; Wertheimer, S.P.; De Bruin, D.; Ravetch, J.V. Chromatin structure determines the sites of chromosome breakages in *Plasmodium falciparum*. *Nucleic Acids Res.* **1994**, *22*, 3099–3103. [CrossRef]
61. Woodcock, C.L.; Ghosh, R.P. Chromatin Higher-order Structure and Dynamics. *Cold Spring Harb. Perspect. Biol.* **2010**, *2*, a000596. [CrossRef]
62. Correll, S.J.; Schubert, M.H.; Grigoryev, S.A. Short nucleosome repeats impose rotational modulations on chromatin fibre folding. *EMBO J.* **2012**, *31*, 2416–2426. [CrossRef]
63. Perišić, O.; Collepardo-Guevara, R.; Schlick, T. Modeling Studies of Chromatin Fiber Structure as a Function of DNA Linker Length. *J. Mol. Biol.* **2010**, *403*, 777–802. [CrossRef] [PubMed]
64. Schwartz, U.; Németh, A.; Diermeier, S.; Exler, J.H.; Hansch, S.; Maldonado, R.; Heizinger, L.; Merkl, R.; Längst, G. Characterizing the nuclease accessibility of DNA in human cells to map higher order structures of chromatin. *Nucleic Acids Res.* **2019**, *47*, 1239–1254. [CrossRef] [PubMed]
65. Miao, J.; Fan, Q.; Cui, L.; Li, J.; Li, J.; Cui, L. The malaria parasite *Plasmodium falciparum* histones: Organization, expression, and acetylation. *Gene* **2006**, *369*, 53–65. [CrossRef] [PubMed]
66. Kamakaka, R.T. Histone variants: Deviants? *Genes Dev.* **2005**, *19*, 295–316. [CrossRef] [PubMed]
67. Hoeijmakers, W.A.M.; Salcedo-Amaya, A.M.; Smits, A.H.; Françoijs, K.; Treeck, M.; Gilberger, T.; Stunnenberg, H.G.; Bártfai, R. H2A.Z/H2B.Z double-variant nucleosomes inhabit the AT -rich promoter regions of the P lasmodium falciparum genome. *Mol. Microbiol.* **2013**, *87*, 1061–1073. [CrossRef] [PubMed]
68. Petter, M.; Selvarajah, S.A.; Lee, C.C.; Chin, W.H.; Gupta, A.P.; Bozdech, Z.; Brown, G.V.; Duffy, M.F. H2A.Z and H2B.Z double-variant nucleosomes define intergenic regions and dynamically occupyvargene promoters in the malaria parasite *Plasmodium falciparum*. *Mol. Microbiol.* **2013**, *87*, 1167–1182. [CrossRef] [PubMed]
69. Vanagas, L.; Contreras, S.M.; Angel, S.O. Apicomplexa and Histone Variants: What's New? In *Chromatin and Epigenetics*; Logie, C., Knoch, T.A., Eds.; IntechOpen: London, UK, 2020; ISBN 978-1-78984-493-1.
70. Fraschka, S.A.-K.; Henderson, R.W.M.; Bártfai, R. H3.3 demarcates GC-rich coding and subtelomeric regions and serves as potential memory mark for virulence gene expression in *Plasmodium falciparum*. *Sci. Rep.* **2016**, *6*, 31965. [CrossRef]
71. Hoeijmakers, W.A.M.; Flueck, C.; Françoijs, K.-J.; Smits, A.H.; Wetzel, J.; Volz, J.C.; Cowman, A.F.; Voss, T.; Stunnenberg, H.G.; Bártfai, R. *Plasmodium falciparum* centromeres display a unique epigenetic makeup and cluster prior to and during schizogony. *Cell. Microbiol.* **2012**, *14*, 1391–1401. [CrossRef]
72. Ay, F.; Bunnik, E.M.; Varoquaux, N.; Vert, J.-P.; Noble, W.S.; Le Roch, K.G. Multiple dimensions of epigenetic gene regulation in the malaria parasite *Plasmodium falciparum*. *BioEssays* **2015**, *37*, 182–194. [CrossRef]
73. Jenuwein, T.; Allis, C.D. Translating the Histone Code. *Science* **2001**, *293*, 1074–1080. [CrossRef] [PubMed]
74. Saraf, A.; Cervantes, S.; Bunnik, E.M.; Ponts, N.; Sardiu, M.E.; Chung, D.-W.D.; Prudhomme, J.; Varberg, J.M.; Wen, Z.; Washburn, M.P.; et al. Dynamic and Combinatorial Landscape of Histone Modifications during the Intraerythrocytic Developmental Cycle of the Malaria Parasite. *J. Proteome Res.* **2016**, *15*, 2787–2801. [CrossRef] [PubMed]
75. Salcedo-Amaya, A.M.; van Driel, M.A.; Alako, B.T.; Trelle, M.B.; Elzen, A.M.G.V.D.; Cohen, A.M.; Janssen-Megens, E.M.; van de Vegte-Bolmer, M.; Selzer, R.R.; Iniguez, A.L.; et al. Dynamic histone H3 epigenome marking during the intraerythrocytic cycle of *Plasmodium falciparum*. *Proc. Natl. Acad. Sci. USA* **2009**, *106*, 9655–9660. [CrossRef] [PubMed]
76. Coetzee, N.; Sidoli, S.; Van Biljon, R.; Painter, H.; Llinás, M.; Garcia, B.A.; Birkholtz, L.-M. Quantitative chromatin proteomics reveals a dynamic histone post-translational modification landscape that defines asexual and sexual *Plasmodium falciparum* parasites. *Sci. Rep.* **2017**, *7*, 1–12. [CrossRef] [PubMed]
77. Read, D.F.; Lu, Y.Y.; Cook, K.; Le Roch, K.; Noble, W.S. Predicting gene expression in the human malaria parasite Plasmo-dium falciparum. *bioRxiv* **2019**, 431049. [CrossRef]
78. Segal, E.; Widom, J. What controls nucleosome positions? *Trends Genet.* **2009**, *25*, 335–343. [CrossRef]
79. Ponts, N.; Harris, E.Y.; Prudhomme, J.; Wick, I.; Eckhardt-Ludka, C.; Hicks, G.R.; Hardiman, G.; Lonardi, S.; Le Roch, K.G. Nucleosome landscape and control of transcription in the human malaria parasite. *Genome Res.* **2010**, *20*, 228–238. [CrossRef]
80. Ponts, N.; Harris, E.Y.; Lonardi, S.; Le Roch, K.G. Nucleosome occupancy at transcription start sites in the human malaria parasite: A hard-wired evolution of virulence? *Infect. Genet. Evol.* **2011**, *11*, 716–724. [CrossRef]
81. Westenberger, S.J.; Cui, L.; Dharia, N.; Winzeler, E.; Cui, L. Genome-wide nucleosome mapping of *Plasmodium falciparum* reveals histone-rich coding and histone-poor intergenic regions and chromatin remodeling of core and subtelomeric genes. *BMC Genom.* **2009**, *10*, 610–617. [CrossRef]
82. Chereji, R.V.; Kan, T.-W.; Grudniewska, M.K.; Romashchenko, A.V.; Berezikov, E.; Zhimulev, I.F.; Guryev, V.; Morozov, A.V.; Moshkin, Y.M. Genome-wide profiling of nucleosome sensitivity and chromatin accessibility in Drosophila melanogaster. *Nucleic Acids Res.* **2015**, *44*, 1036–1051. [CrossRef]
83. Mito, Y.; Henikoff, J.G.; Henikoff, S. Genome-scale profiling of histone H3.3 replacement patterns. *Nat. Genet.* **2005**, *37*, 1090–1097. [CrossRef]

84. Ay, F.; Bunnik, E.M.; Varoquaux, N.; Bol, S.M.; Prudhomme, J.; Vert, J.-P.; Noble, W.S.; Le Roch, K.G. Three-dimensional modeling of the P. falciparum genome during the erythrocytic cycle reveals a strong connection between genome architecture and gene expression. *Genome Res.* **2014**, *24*, 974–988. [CrossRef] [PubMed]
85. Abel, S.; Le Roch, K.G. The role of epigenetics and chromatin structure in transcriptional regulation in malaria parasites. *Brief. Funct. Genom.* **2019**, *18*, 302–313. [CrossRef] [PubMed]
86. Hollin, T.; Gupta, M.; Lenz, T.; Le Roch, K.G. Dynamic Chromatin Structure and Epigenetics Control the Fate of Malaria Parasites. *Trends Genet.* **2021**, *37*, 73–85. [CrossRef]
87. Rowley, M.J.; Corces, V.G. The three-dimensional genome: Principles and roles of long-distance interactions. *Curr. Opin. Cell Biol.* **2016**, *40*, 8–14. [CrossRef] [PubMed]
88. Broadbent, K.M.; Broadbent, J.C.; Ribacke, U.; Wirth, D.F.; Rinn, J.L.; Sabeti, P.C. Strand-specific RNA sequencing in *Plasmodium falciparum* malaria identifies developmentally regulated long non-coding RNA and circular RNA. *BMC Genom.* **2015**, *16*, 1–22. [CrossRef]
89. Yin, S.; Fan, Y.; He, X.; Wei, G.; Wen, Y.; Zhao, Y.; Shi, M.; Wei, J.; Chen, H.; Han, J.; et al. The cryptic unstable transcripts are associated with developmentally regulated gene expression in blood-stage *Plasmodium falciparum*. *RNA Biol.* **2020**, *17*, 828–842. [CrossRef]
90. Amit-Avraham, I.; Pozner, G.; Eshar, S.; Fastman, Y.; Kolevzon, N.; Yavin, E.; Dzikowski, R. Antisense long noncoding RNAs regulate var gene activation in the malaria parasite *Plasmodium falciparum*. *Proc. Natl. Acad. Sci. USA* **2015**, *112*, E982–E991. [CrossRef]
91. Rinn, J.L.; Chang, H.Y. Genome Regulation by Long Noncoding RNAs. *Annu. Rev. Biochem.* **2012**, *81*, 145–166. [CrossRef]
92. Zhu, F.; Farnung, L.; Kaasinen, E.; Sahu, B.; Yin, Y.; Wei, B.; Dodonova, S.O.; Nitta, K.R.; Morgunova, E.; Taipale, M.; et al. The interaction landscape between transcription factors and the nucleosome. *Nat. Cell Biol.* **2018**, *562*, 76–81. [CrossRef]
93. Cortés, A.; Carret, C.; Kaneko, O.; Lim, B.Y.S.Y.; Ivens, A.; Holder, A.A. Epigenetic Silencing of *Plasmodium falciparum* Genes Linked to Erythrocyte Invasion. *PLoS Pathog.* **2007**, *3*, e107. [CrossRef]
94. Jiang, L.; Mu, J.; Zhang, Q.; Ni, T.; Srinivasan, P.; Rayavara, K.; Yang, W.; Turner, L.; Lavstsen, T.; Theander, T.G.; et al. PfSETvs methylation of histone H3K36 represses virulence genes in *Plasmodium falciparum*. *Nat. Cell Biol.* **2013**, *499*, 223–227. [CrossRef] [PubMed]
95. Ukaegbu, U.E.; Kishore, S.P.; Kwiatkowski, D.L.; Pandarinath, C.; Dahan-Pasternak, N.; Dzikowski, R.; Deitsch, K.W. Recruitment of PfSET2 by RNA Polymerase II to Variant Antigen Encoding Loci Contributes to Antigenic Variation in P. falciparum. *PLoS Pathog.* **2014**, *10*, e1003854. [CrossRef] [PubMed]
96. Coleman, B.I.; Skillman, K.M.; Jiang, R.H.; Childs, L.M.; Altenhofen, L.M.; Ganter, M.; Leung, Y.; Goldowitz, I.; Kafsack, B.F.; Marti, M.; et al. A *Plasmodium falciparum* Histone Deacetylase Regulates Antigenic Variation and Gametocyte Conversion. *Cell Host Microbe* **2014**, *16*, 177–186. [CrossRef] [PubMed]
97. Brancucci, N.M.; Bertschi, N.L.; Zhu, L.; Niederwieser, I.; Chin, W.H.; Wampfler, R.; Freymond, C.; Rottmann, M.; Felger, I.; Bozdech, Z.; et al. Heterochromatin Protein 1 Secures Survival and Transmission of Malaria Parasites. *Cell Host Microbe* **2014**, *16*, 165–176. [CrossRef]
98. Bryant, J.M.; Baumgarten, S.; Dingli, F.; Loew, D.; Sinha, A.; Claës, A.; Preiser, P.R.; Dedon, P.C.; Scherf, A. Exploring the virulence gene interactome with CRISPR/dC as9 in the human malaria parasite. *Mol. Syst. Biol.* **2020**, *16*, e9569. [CrossRef]
99. Merrick, C.J.; Jiang, R.H.Y.; Skillman, K.M.; Samarakoon, U.; Moore, R.M.; Dzikowski, R.; Ferdig, M.T.; Duraisingh, M.T. Functional Analysis of Sirtuin Genes in Multiple *Plasmodium falciparum* Strains. *PLoS ONE* **2015**, *10*, e0118865. [CrossRef]
100. Epp, C.; Li, F.; Howitt, C.A.; Chookajorn, T.; Deitsch, K.W. Chromatin associated sense and antisense noncoding RNAs are transcribed from the var gene family of virulence genes of the malaria parasite *Plasmodium falciparum*. *RNA* **2008**, *15*, 116–127. [CrossRef]
101. Filarsky, M.; Fraschka, S.A.; Niederwieser, I.; Brancucci, N.M.B.; Carrington, E.; Carrió, E.; Moes, S.; Jenoe, P.; Bártfai, R.; Voss, T.S. GDV1 induces sexual commitment of malaria parasites by antagonizing HP1-dependent gene silencing. *Science* **2018**, *359*, 1259–1263. [CrossRef]
102. Sinha, A.; Hughes, K.R.; Modrzynska, K.K.; Otto, T.D.; Pfander, C.; Dickens, N.J.; Religa, A.A.; Bushell, E.; Graham, A.L.; Cameron, R.; et al. A cascade of DNA-binding proteins for sexual commitment and development in Plasmodium. *Nat. Cell Biol.* **2014**, *507*, 253–257. [CrossRef]
103. Narlikar, G.J.; Fan, H.-Y.; Kingston, R.E. Cooperation between Complexes that Regulate Chromatin Structure and Transcription. *Cell* **2002**, *108*, 475–487. [CrossRef]
104. Iyer, L.M.; Anantharaman, V.; Wolf, M.Y.; Aravind, L. Comparative genomics of transcription factors and chromatin proteins in parasitic protists and other eukaryotes. *Int. J. Parasitol.* **2008**, *38*, 1–31. [CrossRef] [PubMed]
105. Croken, M.M.; Nardelli, S.C.; Kim, K. Chromatin modifications, epigenetics, and how protozoan parasites regulate their lives. *Trends Parasitol.* **2012**, *28*, 202–213. [CrossRef]
106. Bartholomew, B. Regulating the Chromatin Landscape: Structural and Mechanistic Perspectives. *Annu. Rev. Biochem.* **2014**, *83*, 671–696. [CrossRef] [PubMed]
107. Erdel, F.; Krug, J.; Längst, G.; Rippe, K. Targeting chromatin remodelers: Signals and search mechanisms. *Biochim. Biophys. Acta (BBA) Bioenerg.* **2011**, *1809*, 497–508. [CrossRef]

108. Rippe, K.; Schrader, A.; Riede, P.; Strohner, R.; Lehmann, E.; Langst, G. DNA sequence- and conformation-directed positioning of nucleosomes by chromatin-remodeling complexes. *Proc. Natl. Acad. Sci. USA* **2007**, *104*, 15635–15640. [CrossRef] [PubMed]
109. Clapier, C.R.; Iwasa, J.; Cairns, B.R.; Peterson, C.L. Mechanisms of action and regulation of ATP-dependent chromatin-remodelling complexes. *Nat. Rev. Mol. Cell Biol.* **2017**, *18*, 407–422. [CrossRef] [PubMed]
110. Narlikar, G.J.; Sundaramoorthy, R.; Owen-Hughes, T. Mechanisms and Functions of ATP-Dependent Chromatin-Remodeling Enzymes. *Cell* **2013**, *154*, 490–503. [CrossRef]
111. Oppikofer, M.; Bai, T.; Gan, Y.; Haley, B.; Liu, P.; Sandoval, W.; Ciferri, C.; Cochran, A.G. Expansion of the ISWI chromatin remodeler family with new active complexes. *EMBO Rep.* **2017**, *18*, 1697–1706. [CrossRef] [PubMed]
112. Flaus, A. Identification of multiple distinct Snf2 subfamilies with conserved structural motifs. *Nucleic Acids Res.* **2006**, *34*, 2887–2905. [CrossRef]
113. Corona, D.F.V.; Siriaco, G.; Armstrong, J.A.; Snarskaya, N.; McClymont, S.A.; Scott, M.P.; Tamkun, J.W. ISWI Regulates Higher-Order Chromatin Structure and Histone H1 Assembly In Vivo. *PLoS Biol.* **2007**, *5*, e232. [CrossRef]
114. Strohner, R.; Wachsmuth, M.; Dachauer, K.; Mazurkiewicz, J.; Hochstatter, J.; Rippe, K.; Längst, G. A 'loop recapture' mechanism for ACF-dependent nucleosome remodeling. *Nat. Struct. Mol. Biol.* **2005**, *12*, 683–690. [CrossRef] [PubMed]
115. Dechassa, M.L.; Sabri, A.; Pondugula, S.; Kassabov, S.R.; Chatterjee, N.; Kladde, M.P.; Bartholomew, B. SWI/SNF Has Intrinsic Nucleosome Disassembly Activity that Is Dependent on Adjacent Nucleosomes. *Mol. Cell* **2010**, *38*, 590–602. [CrossRef]
116. Ren, J.; Briones, V.; Barbour, S.; Yu, W.; Han, Y.; Terashima, M.; Muegge, K. The ATP binding site of the chromatin remodeling homolog Lsh is required for nucleosome density and de novo DNA methylation at repeat sequences. *Nucleic Acids Res.* **2015**, *43*, 1444–1455. [CrossRef] [PubMed]
117. Myant, K.; Stancheva, I. LSH Cooperates with DNA Methyltransferases to Repress Transcription. *Mol. Cell. Biol.* **2007**, *28*, 215–226. [CrossRef] [PubMed]
118. Ocampo, J.; Chereji, R.V.; Eriksson, P.R.; Clark, D.J. The ISW1 and CHD1 ATP-dependent chromatin remodelers compete to set nucleosome spacingin vivo. *Nucleic Acids Res.* **2016**, *44*, 4625–4635. [CrossRef] [PubMed]
119. Pointner, J.; Persson, J.; Prasad, P.; Norman-Axelsson, U.; Strålfors, A.; Khorosjutina, O.; Krietenstein, N.; Svensson, J.P.; Ekwall, K.; Korber, P. CHD1 remodelers regulate nucleosome spacingin vitroand align nucleosomal arrays over gene coding regions inS. pombe. *EMBO J.* **2012**, *31*, 4388–4403. [CrossRef]
120. Hoffmeister, H.; Fuchs, A.; Erdel, F.; Pinz, S.; Gröbner-Ferreira, R.; Bruckmann, A.; Deutzmann, R.; Schwartz, U.; Maldonado, R.; Huber, C.; et al. CHD3 and CHD4 form distinct NuRD complexes with different yet overlapping functionality. *Nucleic Acids Res.* **2017**, *45*, 10534–10554. [CrossRef]
121. Bowen, N.J.; Fujita, N.; Kajita, M.; Wade, P.A. Mi-2/NuRD: Multiple complexes for many purposes. *Biochim. Biophys. Acta (BBA) Gene Struct. Expr.* **2004**, *1677*, 52–57. [CrossRef]
122. Morrison, A.J.; Shen, X. Chromatin remodelling beyond transcription: The INO80 and SWR1 complexes. *Nat. Rev. Mol. Cell Biol.* **2009**, *10*, 373–384. [CrossRef]
123. Heyer, W.-D.; Li, X.; Rolfsmeier, M.; Zhang, X.-P. Rad54: The Swiss Army knife of homologous recombination? *Nucleic Acids Res.* **2006**, *34*, 4115–4125. [CrossRef]
124. Unk, I.; Hajdú, I.; Blastyák, A.; Haracska, L. Role of yeast Rad5 and its human orthologs, HLTF and SHPRH in DNA damage tolerance. *DNA Repair* **2010**, *9*, 257–267. [CrossRef] [PubMed]
125. Svejstrup, J.Q. Rescue of arrested RNA polymerase II complexes. *J. Cell Sci.* **2003**, *116*, 447–451. [CrossRef]
126. Diermeier, S.; Kolovos, P.; Heizinger, L.; Schwartz, U.; Georgomanolis, T.; Zirkel, A.; Wedemann, G.; Grosveld, F.; Knoch, T.A.; Merkl, R.; et al. TNFα signalling primes chromatin for NF-κB binding and induces rapid and widespread nucleosome repositioning. *Genome Biol.* **2014**, *15*, 1–13. [CrossRef]
127. Ji, D.D.; Arnot, D.E. A *Plasmodium falciparum* homologue of the ATPase subunit of a multi-protein complex involved in chromatin remodelling for transcription. *Mol. Biochem. Parasitol.* **1997**, *88*, 151–162. [CrossRef]
128. Sullivan, W.J.; Monroy, M.A.; Bohne, W.; Nallani, K.C.; Chrivia, J.; Yaciuk, P.; Smith, C.K.; Queener, S.F. Molecular cloning and characterization of an SRCAP chromatin remodeling homologue in Toxoplasma gondii. *Parasitol. Res.* **2003**, *90*, 1–8. [CrossRef]
129. Dabney, J.; Meyer, M. Length and GC-biases during sequencing library amplification: A comparison of various polymerase-buffer systems with ancient and modern DNA sequencing libraries. *Biotechniques* **2012**, *52*, 87–94. [CrossRef] [PubMed]
130. Spitz, F.; Furlong, E.E.M. Transcription factors: From enhancer binding to developmental control. *Nat. Rev. Genet.* **2012**, *13*, 613–626. [CrossRef]
131. Kubik, S.; O'Duibhir, E.; de Jonge, W.J.; Mattarocci, S.; Albert, B.; Falcone, J.-L.; Bruzzone, M.J.; Holstege, F.C.; Shore, D. Sequence-Directed Action of RSC Remodeler and General Regulatory Factors Modulates +1 Nucleosome Position to Facilitate Transcription. *Mol. Cell* **2018**, *71*, 89–102.e5. [CrossRef] [PubMed]

APPENDIX – MANUSCRIPT IN PREPARATION

Current version prior to submission (as at 31/05/23)

*Pf*Snf2L - an epigenetic coordinator of blood cycle expression timing and gametocyte formation in *Plasmodium falciparum*

Maria Watzlowik[1], Sujaan Das[3], Simon Holzinger[1], Elisabeth Silberhorn[1], Ritwik Singhal[2], Victoria Bonnell[2], Matthew Gow[3], Andreas Klingl[4], Manuel Llinás[2], Markus Meissner[3,*], Gernot Längst[1,*]

1 Regensburg Center for Biochemistry (RCB), University of Regensburg, 93053 Regensburg, Germany.
2 Department of Biochemistry and Molecular Biology, Pennsylvania State University, State College, Pennsylvania, United States of America,
3 Experimental Parasitology, Faculty of Veterinary Medicine, Ludwig-Maximilians-Universität, Munich, Germany
4 Plant Development, Ludwig-Maximilians-University Munich, Planegg-Martinsried, 82152, Germany
* Corresponding authors: Gernot Längst (gernot.laengst@ur.de) and Markus Meissner (markus.meissner@lmu.de)

Findings

- *Pf*Snf2L is an ATP-dependent ISWI-like nucleosome remodeling enzyme
- *Pf*Snf2L shapes the promoter architecture of stage-specific genes and is essential for parasite development (in the intraerythrocytic life cycle).
- *Pf*Snf2L globally controls just-in-time transcription regulation and specifically represses gametocyte-specific gene expression.
- An identified toxic inhibitor phenocopies *Pf*Snf2L-KO and prevents gametocyte formation.

Abstract

The complex life cycle of the malaria parasite *Plasmodium falciparum (Pf)* and the accompanying transcriptional variation is only explained in part by stage-specific transcription factors like the ApiAP2 family, as these factors are strongly under-represented in *Pf* [1–5]. Global and local changes in chromatin structure during life cycle progression suggest the contribution of epigenetic mechanisms as a critical mechanism for fine-tuning gene regulation during malaria parasite development [6–12]. *Pf* chromatin is largely unexplored and is distinct from other eukaryotes in many respects. This is likely to accommodate the highly A/T-rich genome which averages over 90% in non-coding regions, the highest of any known eukaryote [13]. We characterized PF3D7_1104200 (P*f*Snf2L), an ATPase-containing protein that is related to ISWI-type chromatin remodeling enzymes (CREs). Using a conditional knockout system, we demonstrate that *Pf*Snf2L is essential for parasite development, globally controls just-in-time transcription regulation, and specifically represses gametocyte-specific gene expression. Characterization of the enzymatic activity *in vitro*, combined with mapping chromatin organization *in vivo* revealed that *Pf*Snf2L shapes the promoter architecture of stage-specific genes through its nucleosome remodeling activity, thereby influencing gene activation and repression. The unique properties of the Plasmodium Snf2L allowed screening and identification of a specific inhibitor that specifically kills the parasite, phenocopies the loss of correct gene expression timing, and inhibits the formation of gametocytes.

Main part

The chromatin structure at promoters restricts or enables transcription factor access, representing a crucial mechanism for gene expression regulation in eukaryotes. Histone octamers positioned on DNA are a major obstacle for sequence-specific DNA binding factors, and epigenetic mechanisms such as site-specific DNA/ histone modification or RNA-mediated processes additionally regulate accessibility [14–16]. Furthermore, the maintenance and re-establishment of chromatin upon transcription elongation or DNA replication requires a molecular machinery for nucleosome assembly, positioning and spacing[15,17,18]. Chromatin remodeling enzymes (CREs) are ATP-dependent enzymes exerting movement, disruption or assembly of nucleosomes, the exchange of histones for variants, or generally altering chromatin structure to control access to DNA in chromatin [19–21]. Histone CREs and their associated proteins are highly conserved across eukaryotes. In comparison to human cells, which have evolved 53 SWI/SNF enzymes, allowing for the formation of more than 1000 distinct remodeling complexes [22,23], *Plasmodium falciparum* only encodes for 10 putative enzymes with no subfamily-specific redundancy and lacking the typical CRE complex subunits. Furthermore, this parasite exhibits an extraordinarily high AT-content of >80% and highly divergent histones, suggesting different mechanisms of chromatin organization.

Here we explore the functional role of the Plasmodium *Pf*Snf2L (PF3D7_1104200) which is closely related to the ATP-dependent ISWI subfamily of CREs [24]. *Pf*Snf2L has only 30% homology to the human Snf2L (Fig. S1A-B) containing a relatively conserved ATPase region, although no additional conservation in the auto-regulatory and substrate-binding domains could be detected (Fig. 1A). *Pf*Snf2L also contains several large asparagine-rich insertions (Fig. S1C-D), which could impede its predicted activity as a nucleosome remodeling machine. Using recombinantly purified *Pf*Snf2L, we found that it exhibits specific binding to nucleosomes containing a DNA linker (Fig. S2A-E) and performs ATP-dependent histone octamer movement along the DNA (Fig. 1B). Furthermore, the enzyme is capable of assembling nucleosomes in an ATP-independent manner from histone-DNA-aggregates to well-positioned and movable octamers on DNA (Fig1. C-D). These activities classify *Pf*Snf2L as an active ISWI-like CRE, irrespective of the lack of remodeler-specific domains [25–27] (Figs. 1D, S1F).

Endogenous C-terminal tagging of *Pf*Snf2L revealed its expression in all asexual blood stages of 3D7 parasites, peaking in late ring/trophozoite stage (Figs. S3A, S4A-B). Immunofluorescence analysis showed its nuclear localization, being unevenly distributed in the nucleoplasm with spots of local enrichment (Fig. 1E). *Pf*Snf2L-immunoprecipitation combined with LC-MS/MS analysis identified a list of specific protein interactors with a strong link to chromatin organization (Fig. S3C-D, Table_S1). We detected 21 Apicomplexan- or Plasmodium-specific proteins, among them several uncharacterized proteins. Neither the IP experiment nor *in silico* attempts identified orthologues of characteristic subunits of ISWI-type complexes in *Pf*, pointing towards the existence of novel divergent CRE complexes. Some interactors are also associated with transcription regulation and chromatin assembly, remodeling, and organization (Fig. 1F). For example, the FACT-complex plays an important role in nucleosome assembly during transcription elongation [28], while CAF- and NAP-proteins function in replication-coupled assembly [29]. Other likely interactors are one or more versions of the GCN5 complex, as multiple GCN5 complex subunits were detected in the *Pf*Snf2L-IP and an interaction between *Pf*Snf2L with tagged Gcn5 was reported previously [30]. The results suggest a role for *Pf*Snf2L in nucleosome assembly and the chromatin-dependent regulation of gene expression [30–33].

To explore the biological function of *Pf*Snf2L in parasites, we used an inducible dimerizable Cre-lox (DiCre)-mediated gene excision system[34]. The knockout (KO) was verified at the DNA, mRNA and protein level 46 hours after induction, being highly efficient (> 95 % induction rate) (Fig. S4B-E). Early induction of KO – 0 hours post invasion (hpi) – results in reduced parasitemia, major developmental defects and impaired replication in the second cycle. Late induction of *Pf*Snf2L KO (24 hpi) caused a similar, but delayed effect (Fig. 2A-B). The reduced cycle transition upon early KO was a consequence of defects in merozoite release during host cell exit, as shown by live imaging (video), resulting in a reduced rate of newly infected red blood cells (RBCs). Until egress, the numbers of nuclei, schizont segmentation, cytogenesis and invasion organelle formation remained unaffected (Fig. S5). Staining of the host cells during egress revealed, that the RBC ghost often remains attached to egressed merozoites after induction of the KO (iKO), while merozoites without KO induction (noKO) appear distant from ruptured host cells (video,Fig. S5H). The parasite is known to actively modify the RBC properties by exporting proteins (such as EMP3-, REX-, RESA-proteins), suggesting that this process is affected upon early *Pf*Snf2L-KO [35]. Taken together, we found that *Pf*Snf2L plays an essential role in parasite survival and development during the asexual blood stages.

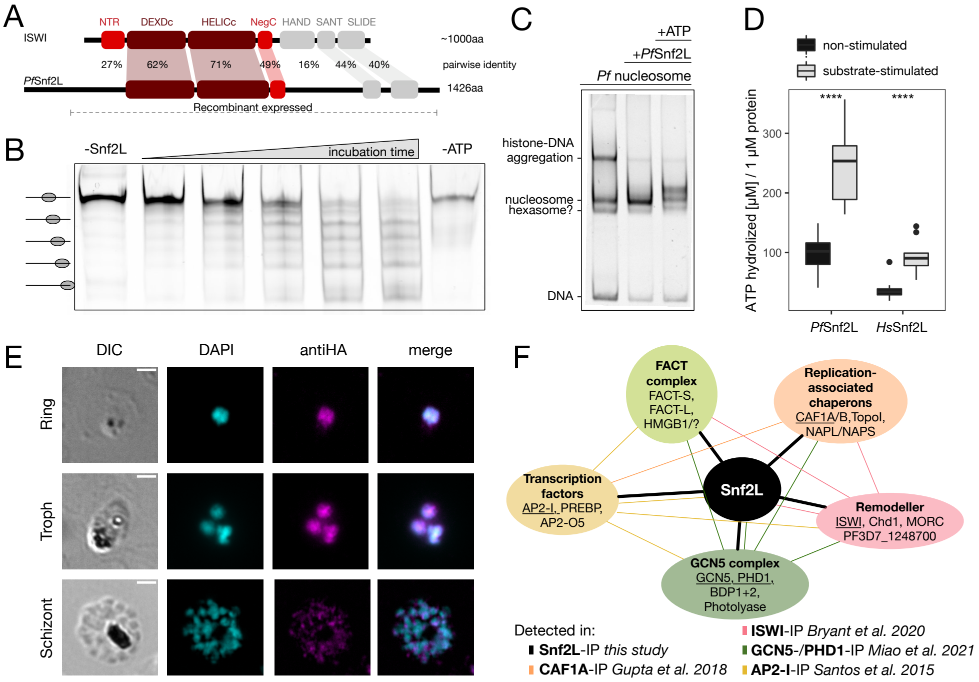

Fig. 1: Identification and enzymatic activity of a divergent ISWI-type chromatin remodeler and its interactors
A. ISWI domain architecture with ATPase region (dark red), autoregulatory domains (light red) and HAND-SANT-SLIDE (grey) and partly conservation in PfSnf2L. B. Chromatin remodeling activity: Representative gel of time-limited remodeling assay on centered-positioned nucleosomes (Bt/77-NPS-77-Cy5). Relative positions of nucleosomes indicated (uncropped Figure see Fig. S2F). C. Assembly activity: Representative gel of nucleosome re-assembly (canonical Pf/6-NPS-47) by PfSnf2L. D. Substrate-dependent ATPase activity: Boxplot showing non-stimulated / nucleosome stimulated ATP hydrolysis rate / enzyme for n=18/n=10 independent experiments. E. Snf2L-HA colocalization IFAs in asexual blood stages, representative images. (DIC: differential interference contrast, DAPI: 4',6-diamidino-2-phenylindole, scale bar: 2 µm). F. PfSnf2L interaction network with selected proteins identified in Snf2L-IP LC-MS/MS of unsynchronized Snf2L-HA vs. 3D7 parasites and additional interactions detected in complementary IP experiments (underlined) with corresponding colors. (For a comprehensive list and interaction criteria see Table_S1.)

To determine whether the drastic developmental effects were caused by perturbation of the parasite chromatin landscape, we used MNase digestion and sequencing of schizont/late ring chromatin +/- Snf2L-KO (Fig. 2C,D). The MNase-Seq method allows detection of individual nucleosome positions and in addition, monitoring of changes in the general accessibility of chromatin [36] (Schwartz et al. 2019). MNase digestion kinetics at schizont stage shows no detectable effect in chromatin accessibility, with noKO and iKO having a similar time-dependent DNA length pattern. However, after invasion, in the late ring stage, the chromatin of iKO parasites is more nuclease-accessible than in noKO parasites, releasing mono-nucleosomal DNA after shorter reaction times. Therefore, the loss of *Pf*Snf2L induces a global opening of chromatin at the ring stage.

To analyze the local chromatin structure and individual nucleosome positions, noKO and iKO chromatin – digested to a similar degree – were analyzed in schizont and ring stages. Only minor changes of the nucleosome maps could be observed in schizonts (<1 % Fig. S6B). However, we found substantial changes in nucleosome positioning in late rings (exemplary tracks shown, criteria see Fig. S6A), where roughly 20 % of the well-positioned nucleosomes were dynamically altered, exhibiting changes in occupancy, fuzziness, or positioning. Dynamic changes occurred preferentially in the 5'UTR and intergenic regions (Fig. 2E). Those regions are associated with regulatory processes, comprising promoters with a highly defined chromatin architecture.

Drastic changes of the chromatin structure at regulatory elements upon *Pf*Snf2L-KO suggest effects on gene expression that may lead to the observed developmental defects. Transcriptomic analysis of highly synchronous cultures revealed a delay in gene expression regulation of KO-parasites (for experimental timing see Fig. S7A). Genes normally activated at specific stages are delayed in activation, and genes turning off also exhibit a later onset of repression in iKO (Fig. S7C). These changes in timing fidelity globally slowed down the circular trajectory of gene expression in the erythrocyte

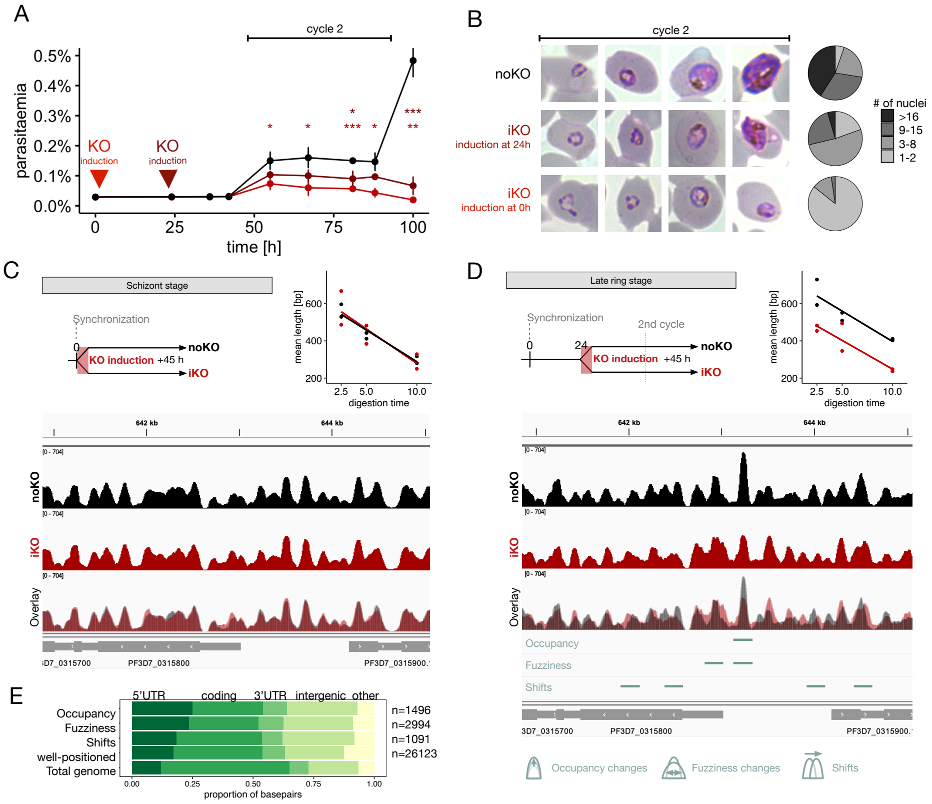

Fig. 2: Snf2L-KO leads to alteration in ring stage chromatin preventing parasite development and survival
*__A.__ Growth curve assay of synchronized Snf2L-HA-KO parasites not-induced (black), induced at 24 hpi (dark red), induced at 0 hpi (light red), Mean ± SD is shown, significance is indicated (two-tailed Student's t-test, unpaired, ns p>0.05, * p<0.05, ** p<0.01, ***p<0.005). __B.__ Representative Giemsa-stained blood smears of parasites as in A and quantification of nuclei in noKO/iKO0 schizonts harvested 46 hpi of cycle 2 (n=100 each). __C/D.__ Scheme of KO induction and chromatin extraction timing at schizont stage (C) / late ring stage (D) and digestion kinetics showing concentration-weighted mean DNA length of tapestation D1000 electrophoresis for MNase digested chromatin of corresponding noKO (black) /iKO (red) samples. Lower panels display exemplary coverage plots of MNase-seq fragments including nucleosome dynamics (criteria see Fig. S5C). Regions shown is chr3:641000–645000, genes are indicated in grey. __E.__ Category, numbers, and localization of nucleosome dynamics in iKO/noKO at late ring stage, assigned to gene section annotations relative to base pairs.*

life cycle of the parasites, with the first effects visible 4approx. one cycle (40 h) post KO induction (Figs. 3A, S7B). In total, 75 % of the genes are differentially expressed (DEG) in at least one time point, with about 200 DEGs at schizont stage and 4approx. 2000 genes affected in ring and trophozoite stages (Fig. 3B). The numbers as well as the enriched GO Terms show that *Pf*Snf2L-KO does not affect expression of specific gene categories. However, a loss of *Pf*Snf2L impacts genes undergoing activation or repression at the respective developmental stage of the parasites. This suggests that *Pf*Snf2L is globally required to maintain the timing of the regulation of the parasite transcriptome. The gene expression changes are also consistent with the phenotype of delayed cell cycle progression and suggest a functional basis for the observed host cell exit defect. The few DEGs at schizont stage comprise numerous exported proteins, among them all EPF3/4 proteins – a conserved multigene family, whose collective knockdown was previously shown to result in inefficient merozoite release, similar to the iKO of *Pf*Snf2L [37]. Interestingly, genes expressed outside of the asexual blood stages are upregulated in early rings, where they should widely be silenced (Figs. 3D, S7D). Among the mis-activated genes are numerous gametocyte-specific genes (Table_S1). This indicates that *Pf*Snf2L may play a role in commitment to sexual differentiation. In previous transcriptomic studies of gametocytogenesis, *Pf*Snf2L as well as ISWI (*Pf*3D7_0624600) were identified as likely upstream regulators of sexual commitment [38,39]. We find that these gametocyte-specific genes tend to be upregulated in early stages upon *Pf*Snf2L-KO and are mostly downregulated in trophozoite stage (Fig. S6D). Interestingly, several known epigenetic regulators of sexual commitment are dysregulated (Fig. S6E). The detailed mechanism of how *Pf*Snf2L impacts the silencing of clonally variant and gametocyte-specific

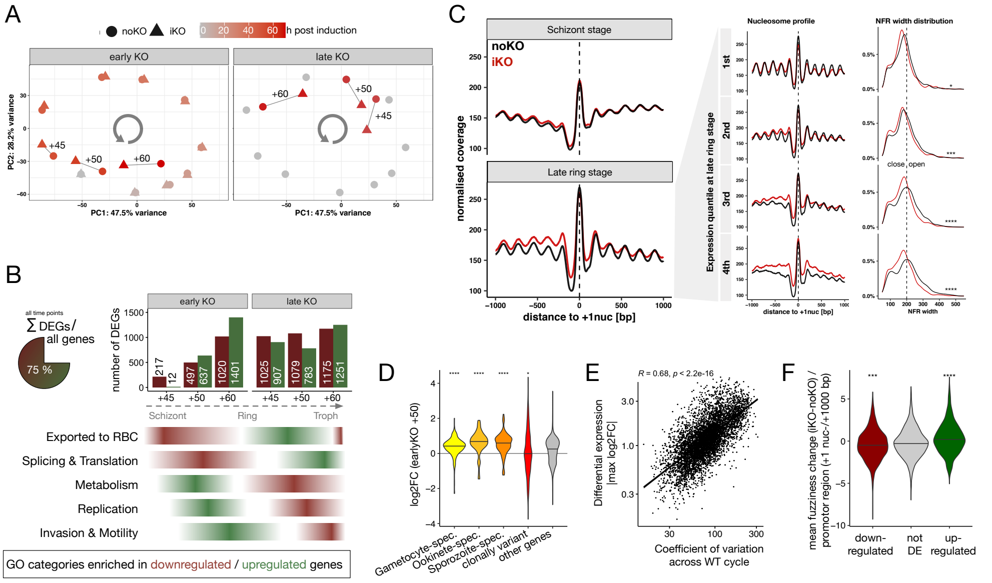

Fig. 3: PfSnf2L is critical for global just-in-time transcription by shaping promoter architecture of stage-specific genes
A. *Principal component analysis of whole RNAseq data of highly synchronous noKO (circle) / iKO (triangle) parasites at different time points (45 h / 50 h / 60 h) post early (left) or late KO induction (right). Pool of three biological replicates shown.* ***B.*** *Summation (left) and timed numbers (right) of differentially expressed genes (DEGs) in iKO/noKO parasites as in A and superordinate GO categories enriched in DEGs based on GO Term Enrichment analysis.* ***C.*** *Average MNase-seq occupancy profiles of iKO/noKO around +1 nucleosome (based on on txstart from nucleosome dynamics) at schizont stage / late ring stage, with latter profile and NFR width distribution differentiated by gene expression quantiles (TPM) at late ring stage* ***D.*** *DE of genes grouped by their stage-specific expression (gene categorization see Table_S2)* ***E.*** *Pearson correlation between the maximal differential expression of each gene and its expression variation across cycle in the reference transcriptome.* ***F.*** *Difference of mean fuzziness score of all nucleosomes within region +/- 1000 bp arround +1 nucleosome for each gene with more than 6 nucleosomes called (iKO-noKO) over differential expression. (two-tailed Student's t-test, unpaired, ns p>0.05, * p<0.05, ** p<0.01, ***p<0.005, ****p>0.001)*

genes, as well as the chronological order of transcription factor recruitment, histone modifying enzymes and CREs remains unsolved. However, we find that *Pf*Snf2L is one of the key organizers of the nucleosomal landscape at gene promoter and its activity is decisive for precise timing of transcription activation/repression throughout the asexual and sexual intraerythrocytic stages of *Plasmodium falciparum* development.

Gene expression regulation occurs on multiple regulatory levels including transcriptional control, splicing, and RNA degradation, but varies for each gene. However, promoter architecture universally determines transcription with positioned nucleosomes around a nucleosome-free region (NFR) controlling the accessibility for DNA binding factors and polymerase [15]. By analyzing the aligned nucleosome profiles around promoter regions, we found many genome-wide differences upon KO at late ring stage (Fig. S6C). Due to stage-dependent variation in transcription start site (TSS) usage and therefore a documented variability in TSS annotation, we used an alternative chromatin-based method to determine the start of transcription in our data. Using NucDyn [40] to define the first well-positioned nucleosome downstream as the +1 nucleosome of promoters we determined changes in the chromatin structure and the accessibility of the regions immediately upstream of the transcription start site (Fig. 3C). The subdivision of the data into gene expression quantiles reveals less defined nucleosome positioning for highly expressed genes (4th quantile) due to *Pf*Snf2L-KO. Furthermore, nucleosome-free regions tend to be longer and likely more accessible with increased expression in the noKO samples, but not in iKO, suggesting that a loss in *Pf*Snf2L results in a closure of the NFR. As the correlation between gene expression and promoter architecture is disturbed in the KO, we suggest that *Pf*Snf2L plays a crucial role in opening and maintaining an active promoter structure. This relation is further supported by the observation that genes that undergo strong activation and repression during the cycle – notably clonally variant genes[41] – are most strongly affected by the absence of *Pf*Snf2L (Fig. 3D,E). In addition, increased mRNA abundance in KO coincides with a loss in nucleosome positioning at promoter regions, shown by increased nucleosome fuzziness, and the opposite effect for downregulated genes (Fig. 3F). Supporting these results, ISWI-type CREs in other organisms have been shown to facilitate transcription initiation by enhancing the accessibility of trans-acting factors to chromatin regions upstream of the +1 nucleosomes, to [42]. *Pf*Snf2L has also been demonstrated to interact with transcription factors and the Gcn5-complex [30,43], and deletion of the GCN5/PHD1 domain results in a delay in developmental progression, with reduced cycle transition and upregulation of non-blood stage-specific genes [30] as seen for *Pf*Snf2L-KO.

The essentiality of *Pf*Snf2L to the malaria parasite in asexual stages, combined with its high sequence divergence from the human enzymes suggests that the protein may serve as a potential drug target. Based on its enzymatic activity, a small molecule library was screened for inhibition and binding of the ATPase domain of the recombinant protein. The screening pipeline (Fig. 4A) combined an ATPase activity screen, followed by biophysical analysis of protein small molecule interactions and *in vitro* nucleosome remodeling assays. Efficient inhibitors were validated *in vivo*, and toxicity and specificity of the compounds were assessed. The anti-plasmodial chemical compound with the most pronounced effect was XXX (Figs. S8A, 4C). Exposure to this compound mimics the *Pf*Snf2L-KO phenotype, exhibiting a similar developmental delay as shown by Giemsa staining and in time-resolved transcriptomic analysis (Fig. 4B,D). Treatment of synchronized parasites with 1 μM of XXX for 20/25/35 h and the subsequent RNA sequencing show a very high and significant correlation of DEGs when compared to the KO transcriptome analysis (Fig. 4E). Furthermore, drug treatment for one day during gametocyte induction, dramatically decreased the gametocyte conversion rate in a dose dependent manner, strongly emphasizing the proposed function of *Pf*Snf2L in sexual commitment (Fig. 4F). Whereas other epigenetic modifiers, Had2 and Gcn5, were previously proposed to control the frequency of sexual conversion by maintaining the asexual transcription program, our data suggests that *Pf*Snf2L has an antagonistic function [30,44].

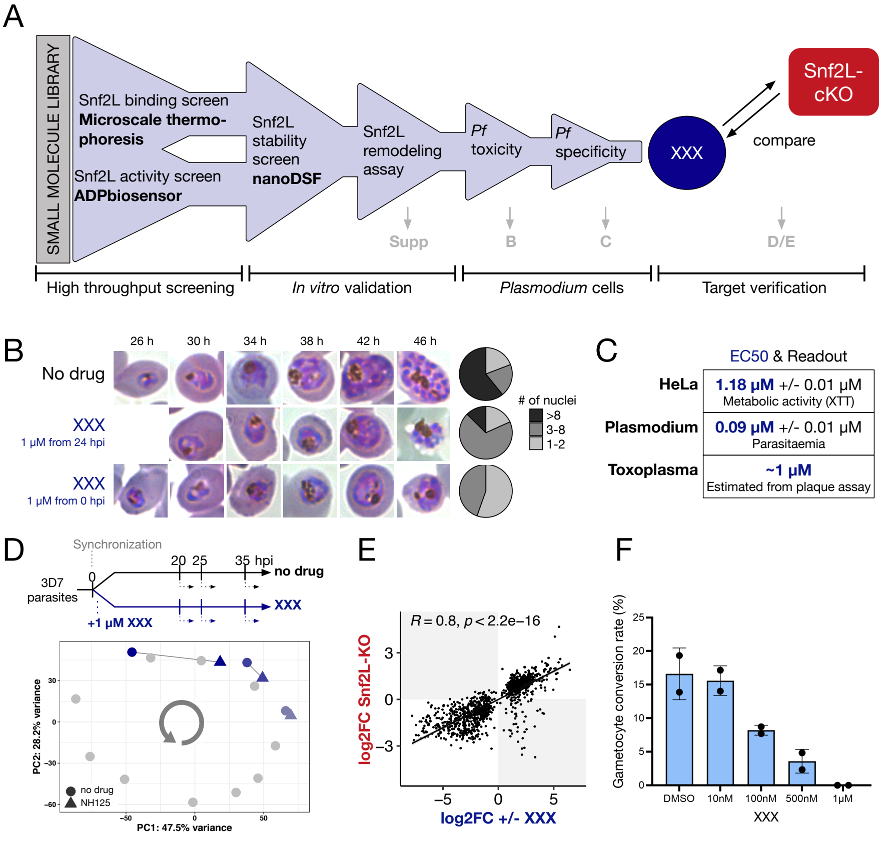

Fig. 4: An in vitro inhibitor screen targeting Snf2L resulted in a toxic compound with phenocopying effect
A. *Inhibitor screening pipeline* ***B.*** *Representative Giemsa-stained blood smears of parasites cultured in media with 1 µM XXX started from 0/24 hpi and quantification of nuclei in schizonts harvested 46 hpi (n>80 each).* ***C.*** *Toxicity of XXX expressed by EC50 values on HeLa/Plasmodium/Toxoplasma cells and the corresponding readout method.* ***D.*** *Scheme of drug treatment and RNA extraction timing (left). Principal component analysis of whole transcriptome data of parasites as described in D plus reference transcriptome (grey) as in Fig. 3A (right). Pool of three biological replicates shown.* ***E.*** *Pearson correlation between DE upon late Snf2L-KO (+60) and DE upon XXX treatment (+35) of each gene showing a significant change over both timecourse experiments (p<0.01).* ***F.*** *Gametocyte conversion rate upon 1 day treatment with XXX.*

Our study has shown that *Pf*Snf2L, is an ATP-dependent ISWI-like nucleosome remodeler, being essential for the development of the parasite. While ISWI-CREs in other eukaryotes function mainly in nucleosome spacing, *Pf*Snf2L is responsible for shaping the promoters of stage-specific genes and controls just-in-time transcription regulation globally. The distinct domain architecture, dissimilar interaction network, and functional differences of *Pf*Snf2L suggest a specialized mode of action for Plasmodium CREs. *Pf*Snf2L essential role in coordinating the orchestrated transcriptional program and its sequence divergence from other eukaryotic CREs, makes it a potential drug target. Disrupting its activity dramatically interferes with the intraerythrocytic cycle progression and gametogenesis, proving it as a new class of promising epigenetic drugs to target malaria.

Supplement Figures:

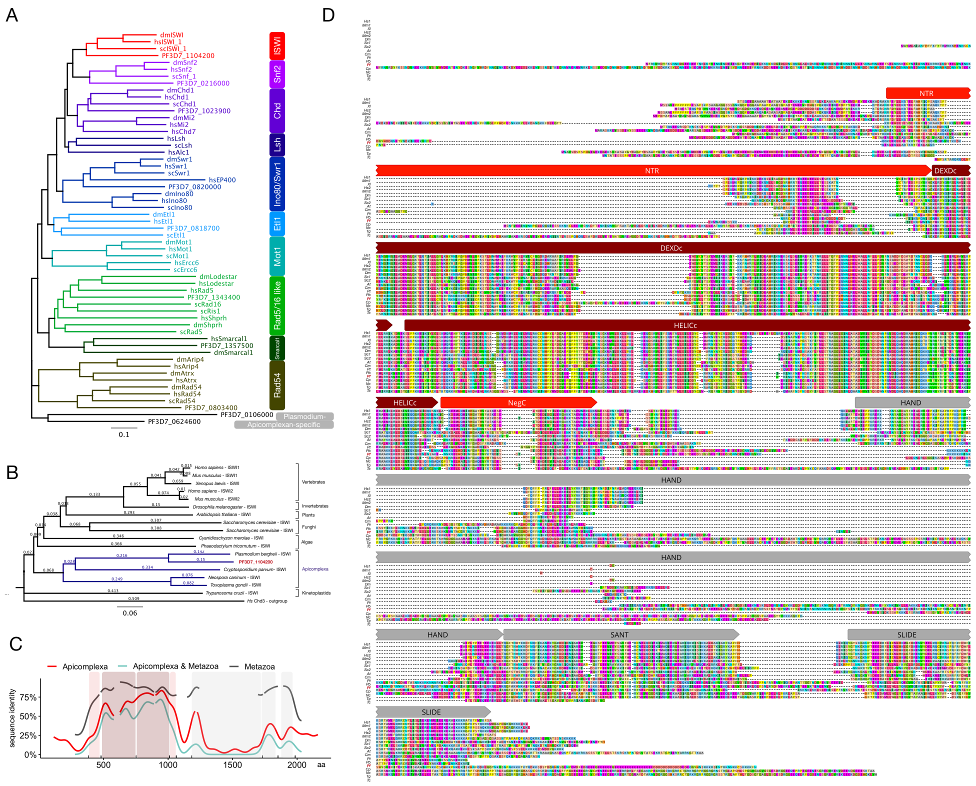

Supplement Figure 1: in silico analysis

A. *Phylogenetic analysis of the helicase region with subfamily representatives of Hs, Dm and Sc and predicted Pf SWI2/SNF2-ATPases (list see Table_S3), coloring represents SWI/SNF subgroups according to* [23]*.* ***B.*** *Rooted phylogenetic tree of the full length ISWI homologues from different organisms representing eukaryotic (sub-) kingdoms with Apicomplexa highlighted (blue) and HsChd3 as outgroup. Numbers indicating substitutions per site.* ***C.*** *Pairwise identity among metazoanISWI, apicomplexanISWI and between them based on multiple sequence alignment (Fig. S1D), gaps represent insertions, coloring represent predicted domains.* ***D.*** *Multiple sequence alignment of ISWI homologues from Hs, Mm, Xl, Dm, Sc, At, Cm, Pt, Pb, Cp, Nc, Tg, Tc and PF3D7_1104200 with predicted domains (amino acids in agreement to consensus sequence highlighted by color).*

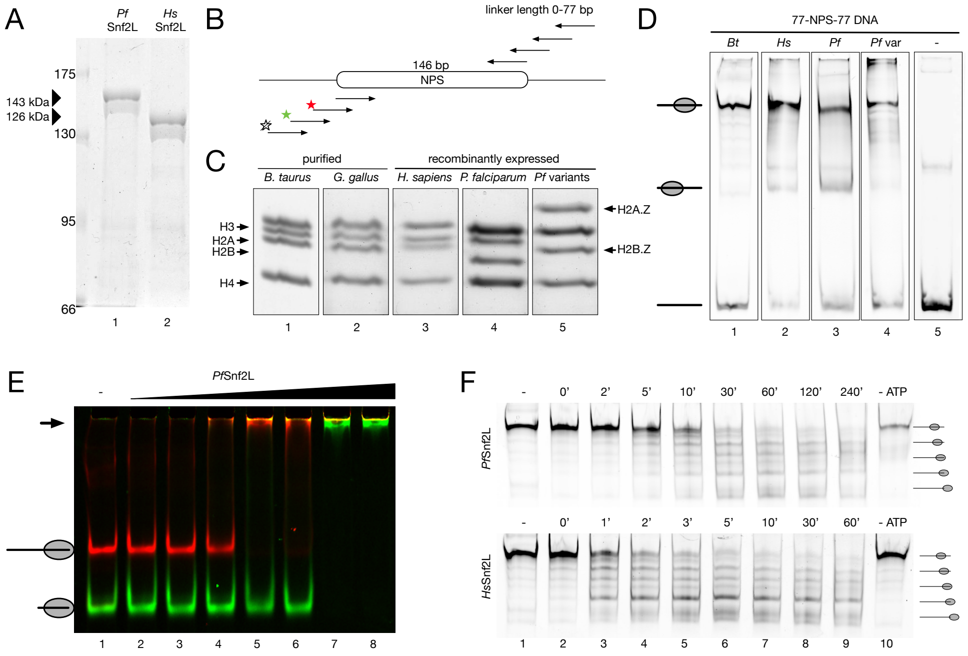

Supplement Figure 2: in vitro

A. *SDS-PAGE (6 %, Coomassie-stained) of remodeling enzymes, recombinantly expressed in SF21 cells and purified via affinity chromatography. Expected protein band and its size is indicated.* ***B.*** *Schematic representation of DNA template generation for nucleosome assembly containing various linker length and fluorescence labelling (stars) implemented via PCR. NPS: nucleosome positioning sequence.* ***C.*** *SDS-PAGE (15%, Coomassie-stained) of histone octamer preparation of purified or recombinantly expressed origin.* ***D.*** *Native PAGE with reconstituted nucleosomes on Cy5-labelled 77-NPS-77 DNA (lane 5) using following octamer-DNA ratios: Bt (1.4:1), Hs (1.5:1), canonical Pf (1.4:1) and variant Pf (0.9:1). Relative position of nucleosome and DNA are indicated.* ***E.*** *Linker-dependent nucleosome binding was analyzed in a competitive binding assay with PfSnf2L-titration (0.02-0.6 µM) to an equimolar mixture of Gg/6-NPS-47-Cy5 (red) and Gg/0-NPS-0-Cy3 (green) nucleosomes and subsequent analysis via native PAGE. Merged channels are shown with nucleosome positions and shift products (arrow) indicated.* ***F.*** *Comprehensive gel of time-limited chromatin remodeling assay on centered-positioned nucleosomes (Bt/77-NPS-77-Cy5) of PfSnf2L as in Fig. 1B and HsSnf2L in comparison. Relative positions of nucleosomes indicated.*

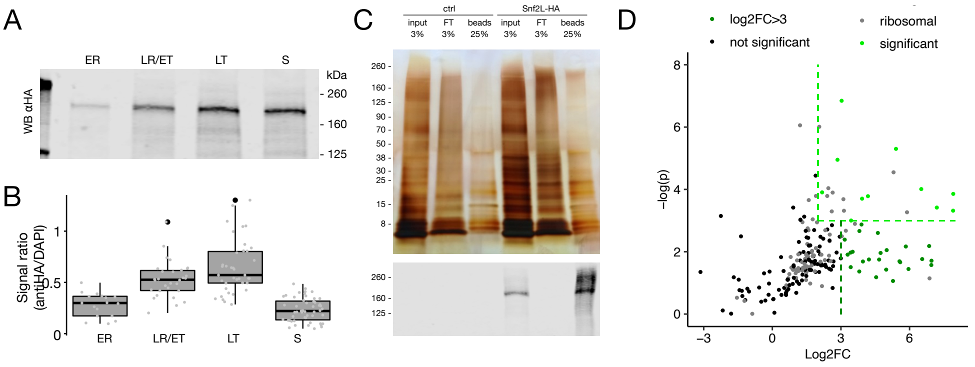

Supplement Figure 3: in vivo

A*. Western blot analysis of Snf2L levels using antiHA antibody on whole cell extract of synchronized Snf2L-HA expressing parasites harvested after 11/22/33/44 hpi (equal number of iRBCs loaded on 4-20 % SDS-PAGE).* ***B.*** *Quantification of IFA signal as in A. For 178 parasites in four different stages, antiHA and DAPI signal intensities were measured, corrected for background and antiHA/DAPI signal ratio for single parasites is shown as boxplot.* ***C.*** *antiHA-IP samples of one representative experiment - input, flowthrough (FT) and beads - obtained from 3D7 and Snf2L-HA parasites were analyzed on 4-20% SDS-PAGE and silver-stained (upper panel), probed with antiHA antibody on western blot (lower panel).* ***D****. Scatterplot of Snf2L-IP LC-MS/MS results showing -log(p-value) of a two-sided t.test over log2FC(IP/ctrl): significantly enriched (light green), highly enriched (dark green), ribosomal proteins (grey), rest (black).*

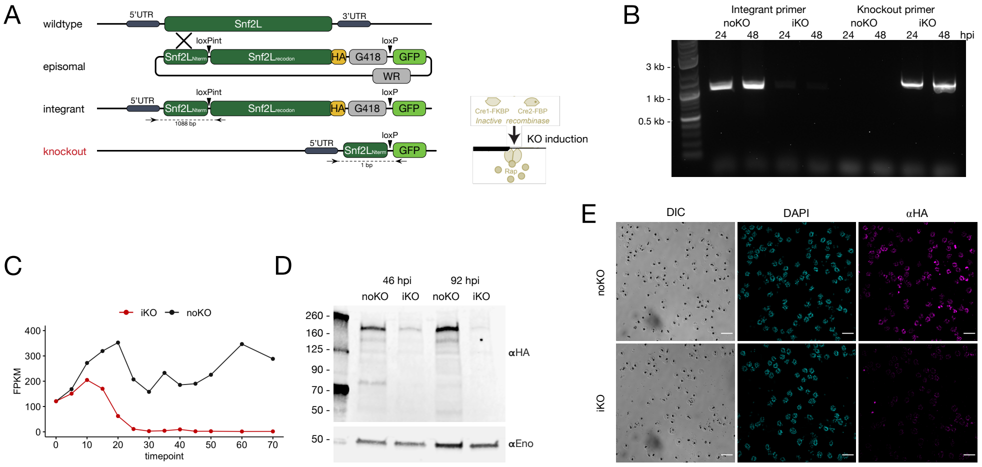

Supplement Figure 4: Conditional Snf2L-Knockout strategy and efficacy

A. *Schematic representation for generation of transgenic Snf2L-HA-KO parasites. Transfection of DiCre-expressing parasite line with the plasmid leads to endogenous integration of the Snf2L-cassette containing recodonized and C-terminally HA-tagged Snf2L flanked by loxP sites. Upon rapamycin addition, the catalytically active part of the Snf2L locus is excised. Abbreviations. Rap: rapamycin, UTR: untranslated region, Nterm: N-terminal, recodon: recodonized, loxPint: artificial intron with loxP site, G418/WR: resistance genes, GFP: green-fluorescent protein.* ***B.*** *Validation of Snf2L-knockout on DNA level by genotyping PCR 24/48 h post KO induction with primers indicated in A.* ***C.*** *mRNA levels of* Snf2L$_{recodon}$ *upon KO induction in synchronized parasites obtained by RNAseq in one representative replicate of three.* ***D.*** *Western blot analysis of Snf2L levels with antiHA antibody in whole cell extracts with and without rapamycin one/two cycles after induction, antiEnolase as loading control.* ***E.*** *Immunofluorescence analysis of schizont stage parasites one cycle after KO induction with antiHA antibody and DAPI (scale bar: 20 µm).*

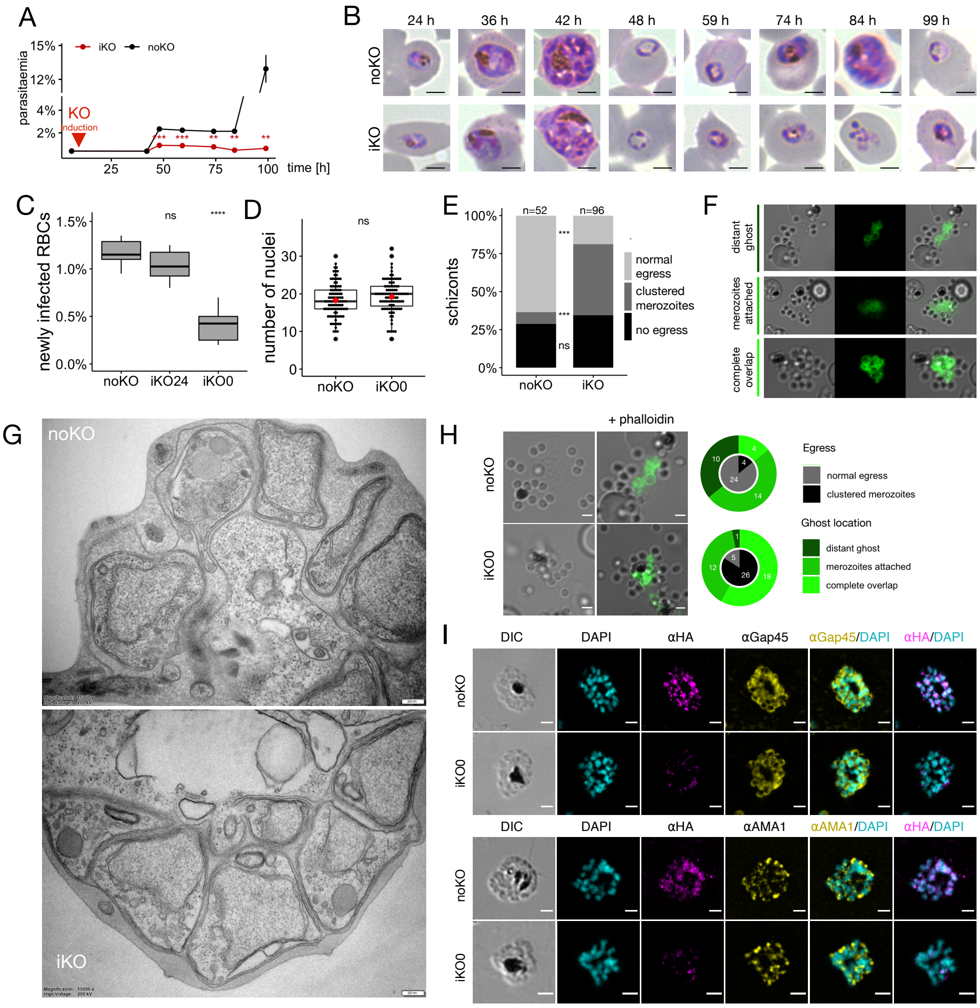

Supplement Figure 5: Snf2L-KO and its downstream effects in second cycle

A. *Growth curve assay of synchronized Snf2L-HA-KO parasites not-induced (black), induced at ring stage (red), (Mean ± SD).* ***B.*** *Representative Giemsa-stained blood smears of parasites as in A.* ***C.*** *Reproduction rate of noKO/iKO24/iKO0 schizonts (46 hpi) after 2 h with fresh RBCs ($n_{parasites}$>100 each).* ***D.*** *Quantification of nuclei in noKO /iKO0 parasites 46 hpi (two-tailed Student's t-test, unpaired, ns p>0.05, * p<0.05, ** p<0.01, ***p<0.005)* ***E.*** *Quantification of egress phenotype 46 h after induction* ***F.*** *Representative images of RBC ghost classification as distant/merozoites attached/complete overlap during live imaging supplemented with phalloidin 40 sec post egress start.* ***G.*** *Representative TEM image of Snf2L-HA-KO parasites not-induced/induced at ring stage 46 hpi + additional maturation in presence of compound 1.* ***H.*** *Representative images and quantification of egress phenotype and RBC ghost phenotype (as in F.) during phalloidin-supplemented live imaging of individual egressed noKO/iKO schizonts 46 h after induction.* ***I.*** *Immunofluorescence analysis of noKO/iKO schizonts 46 h after induction with DAPI, antiHA and antiGap45 as cytogenesis marker, antiAMA1 as apicoplast marker, respectively.*

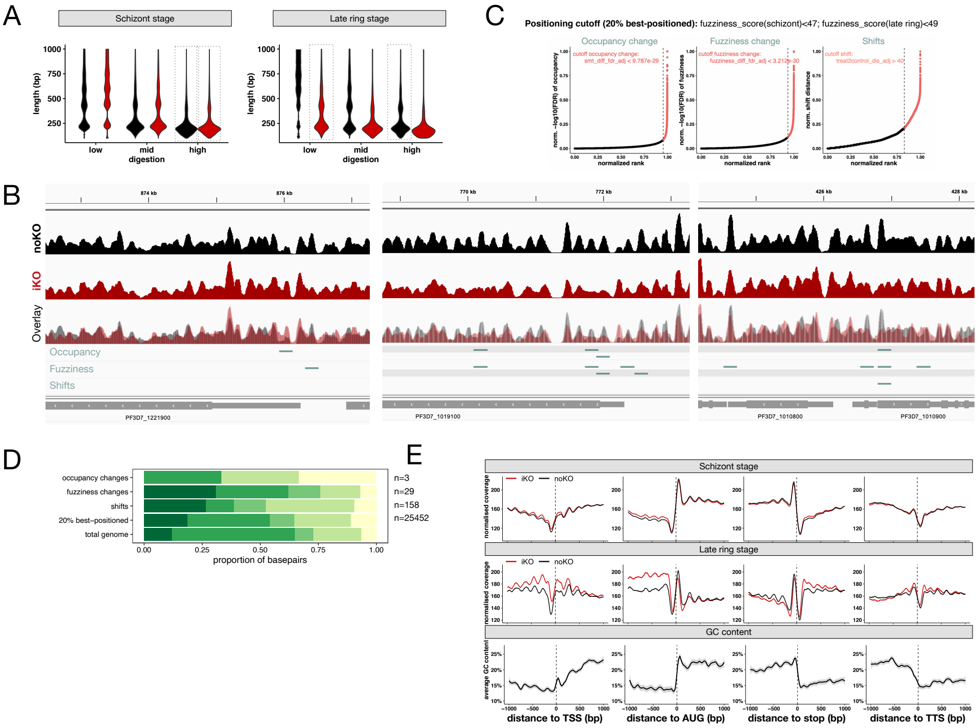

Supplement Figure 6: MNase

A. *Molarity-normalized DNA size distribution of tapestation D1000 electrophoresis for MNase digested chromatin at schizont / late ring stage of noKO (black) /iKO (red) samples. One representative replicate is shown, dotted boxes indicate samples used for analysis.* ***B****. Exemplary coverage plots of MNase-seq fragments at late ring stage upon noKO/iKO including nucleosome dynamics. Regions shown are chr12:872500–877200, chr10:768800–773200, chr10:424200–428200 genes are indicated in grey.* ***C.*** *Ranked normalized dynamics parameter (FDR of occupancy/fuzziness change or shift distance from DANPOS analysis) of late ring stage iKO/noKO chromatin, dynamic nucleosome cutoff is defined as slope=1 and noted. Stage-dependent positioning cutoff is noted as well (fuzziness score).* ***D.*** *Category, numbers, and localization of nucleosome dynamics in iKO/noKO at schizont stage (cutoff from B. applied), assigned to gene section annotations relative to base pairs.* ***E.*** *Average MNase-seq occupancy profiles of noKO/iKO at schizont stage/late ring stage around transcriptional landmark sites and corresponding GC-content profiles.*

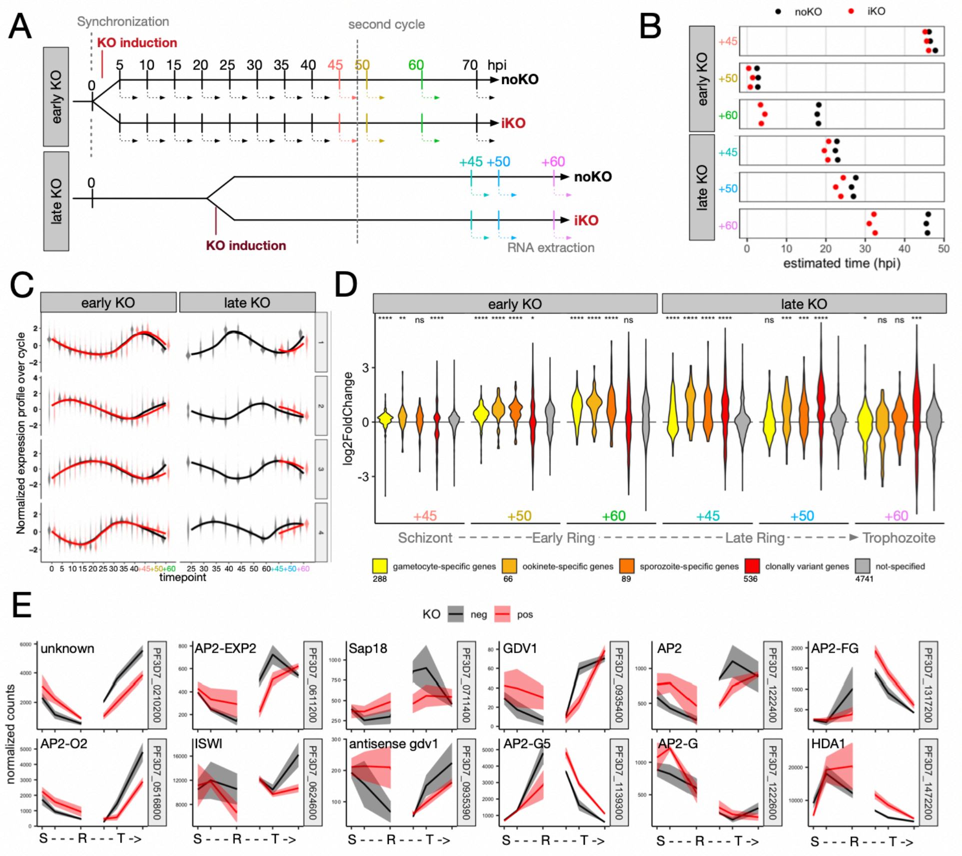

Supp 7: RNAseq

***A**. Experimental setup of Snf2L-KO timing and sampling for transcriptome analysis **B**. Cycle progression estimation of RNAseq samples as in A. **C**. Normalized relative expression profile of genes differentially expressed over all timepoints in noKO (black) and iKO (red), clustered according to expression profile over cycle. **D**. Expression change – log2(iKO/noKO) – at individual timepoints for stage-specific gene groups (see Table_S2). **E**. Gene expression profiles over individual timepoints of exemplary epigenetic regulators involved in gametocyte commitment* [38,39].

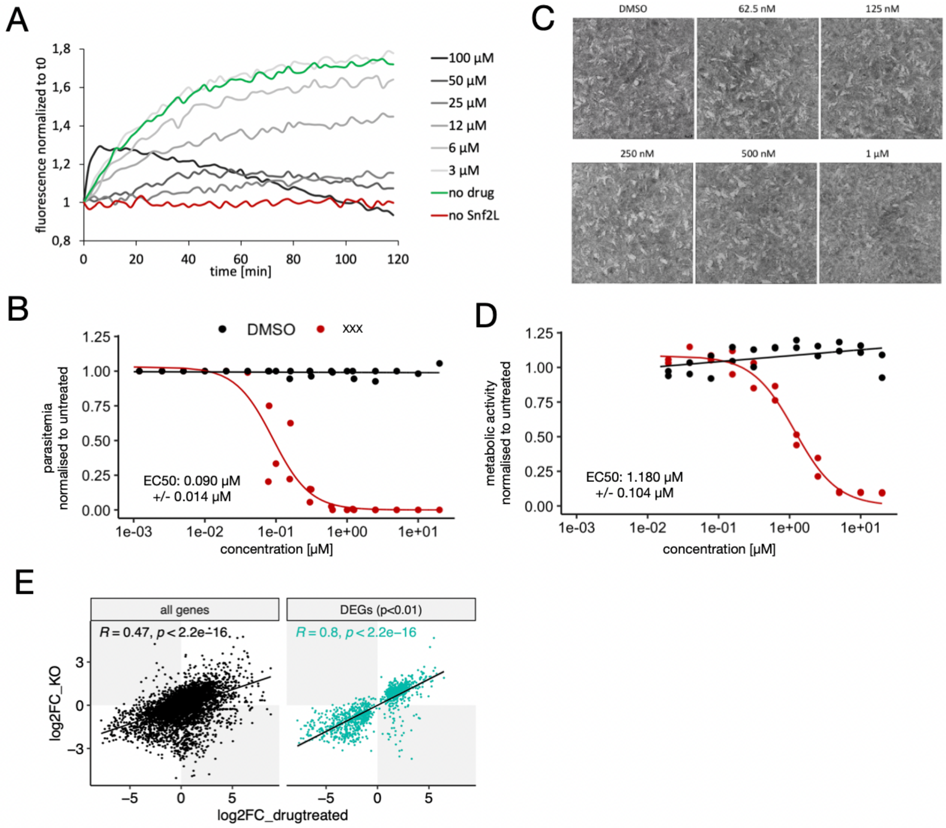

Supp 8: drug

__A. ATPase inhibition__. ATP hydrolysis kinetic of Snf2L in presence of XXX in varying concentrations (grey) with normalized fluorescence of ParM as readout. Snf2L (+DMSO) in absence of drug (green) serves positive control, samples without ATPase (red) as negative control. __B. Pf Toxicity__. Parasitemia after 72 hours in presence of varying concentration of XXX or DMSO correspondingly of three independent experiments, normalized to untreated parasitemia, EC50 determination by fitting dose response model. __C. Toxoplasma toxicity.__ Exemplary plaque assay of Toxoplasma gondii infected human foreskin fibroblasts incubated for 1 week before fixation and staining __D. HeLa toxicity.__ Metabolic activity of HeLa cells (monitored by XTT assay) in presence of varying concentration of XXX or DMSO correspondingly of two independent experiments, normalized to untreated, EC50 determination as in B __E.__ Pearson correlation between gene expression upon late Snf2L-KO (+60) and upon XXX treatment (+35) of all genes (left)/genes showing a significant change over both timecourse experiments (p<0.01) (right).

Methods:

- **Phylogenetic analysis and multiple sequence alignments**

Sequences of CREs used for phylogenetic analysis are listed in Table_S3. Phylogenetic trees were generated using *Geneious Tree Builder* (Geneious software 11.1.5*)*: Global alignment with free end gaps, Blosum62 as Cost Matrix, Jukes-Cantor Distance Model, Method Neighbor-Joining, Gap open penalty 10 and Gap extension penalty 0.2. For multiple sequence alignments (MSA), *Geneious Alignmen*t with same parameter, but Gap open penalty 20 and 5 refinement iterations was used. Pairwise identity within and between Metazoa/Apicomplexa was calculated from MSA and kernel smoothing was applied.

- **Nucleosome reconstitution**

DNA templates for nucleosome assembly were synthesized by PCR, using (Cy3-/Cy5-labelled) oligonucleotides binding flanking regions of 147 bp nucleosome positioning sequence (NPS) creating various linker lengths: 0-NPS-0, 6-NPS-47, 77-NPS-77 [45]. Recombinant histones - canonical *Hs*/*Pf* and variant *Pf* (H2A.Z/B.Z containing) - were expressed, purified and refolded as previously described [46]. *Bt* and *Gg* octamers were purified from calf thymus, or chicken blood respectively, as described in [47,48]. Nucleosome assembly was performed via gradient dialysis: Suitable ratios of histone octamer : DNA were mixed in 40-200 μl high salt buffer (10 mM Tris pH 7.6/2 M NaCl/1 mM EDTA/1 mM 2-mercaptoethanol/0.05% Igepal CA-630) supplemented with 200 ng/μl BSA and placed into small dialysis chambers. Starting in a beaker with 300 ml high salt buffer, salt concentration was slowly reduced by pumping 3 l of low salt buffer (10 mM Tris pH 7.6/50 mM NaCl/1 mM EDTA/1 mM 2-mercaptoethanol/0.05% Igepal CA-630) to it. Reconstituted nucleosomes were analyzed by gel electrophoresis, using 6% PAA 0.4xTBE gels and visualized by fluorescence scanning (Typhoon FLA-9500) or ethidium bromide staining.

- **CRE expression and purification**

*Pf*Snf2L (aa250-1426) was sequence-optimized with addition of a C-terminal 10xHis-Tag, ordered as synthetic gene (IDT), and cloned into pFL plasmid (Dr. Imre Berger, EMBL Grenoble). After transformation in DH10Bac EM YFP cells (Dr. Imre Berger), bacmid DNA was isolated and transfected into *Spodoptera frugiperda* Sf21 cells (Invitrogen). The produced initial virus was further propagated and used for large scale expression [49,50]. Cells expressing recombinant *Pf*Snf2L-10xHis or *Hs*Snf2L-6xHis were harvested and lysed in 20 mM Tris–HCl pH 7.6/500 mM KCl/1.5 mM $MgCl_2$/0.5 mM EGTA/5 mM ß-mercaptoethanol/10% glycerol/0.1% Igepal CA-630 using Branson Sonifier 250. Purification was performed via NiNTA agarose (Qiagen) according to manufacturer's recommendation. Protein concentration was estimated via Bradford assay and the purity was checked with Coomassie-stained SDS-PAGE.

- **Nucleosome binding and remodeling assays**

In vitro reconstituted nucleosomes in 10 μl 20 mM Tris pH 7.6/100 mM KCl/1.5 mM $MgCl_2$/0.5 mM EGTA/10% glycerol/200 ng/μl BSA were incubated for 60 min at 30 °C in absence/presence of recombinantly expressed CRE. In competitive binding assays 2x 15 nM nucleosomes + 0.02-0.6 μM CRE, in non-labelled binding assays 120 nM nucleosome + 700 nM CRE, in remodeling assays 30 nM nucleosome + 300 nM CRE + 1 mM ATP was used. Reactions were stopped after 60 min (unless noted differently) by addition of 1 μg competitor plasmid DNA and nucleosome positions were analyzed via 6 % native PAGE.

- **ATPase assays**

CRE (130-700 nM) in 20 mM Tris–HCl pH 7.6/120 mM KCl/1.5 mM $MgCl_2$/0.5 mM EGTA/10% glycerol was incubated together with 500 µM ATP and 0.2 µCi ^{32}P-γ-ATP in absence or presence of mononucleosomes (60-350 nM, various compositions) for 40 min at 30°C. Released ^{32}P-γ phosphate was separated from non-hydrolyzed ^{32}P-γ-ATP in three technical replicates by TLC on PEI-Cellulose F plates (Merck) [mobile phase: 50% acetic acid, 0.5 mM LiCl]. After phosphoimaging (Typhoon FLA-9500), signal intensities were quantified (Fuji Multi Gauge Software), the hydrolysis rate was calculated, corrected for chemical hydrolysis, and normalized to CRE concentration.

- **Plasmid construction**

A synthetic gene comprising of the native nucleotides 995-1894 of PF3D7_1104200, an artificial intron with loxP site [51,52], nucleotides 1895-4278 recodonized and a 3xHA-tag encoding sequence was ordered as synthetic gene (IDT) and cloned into the vector pT2A-X-KO [53]. The resulting plasmid pT2A-Snf2L-KO contains downstream of the *Pf*Snf2L-encoding part a skip peptide, a neomycin resistance gene to enable selection-linked integration, a second loxPsite and a GFP gene as well as an independent hDHFR gene.

- **Parasite culture & transfection**

P. falciparum clone 3D7 was cultured according to standard procedures in RPMI 1640 with Albumax® (Invitrogen), and synchronized adapted from [54]: Schizonts were purified on a bed of 70% Percoll®, incubated with new red blood cells for 1-2 h, before leftover schizonts were removed with Percoll and subsequent sorbitol treatment. About 10 µg of plasmid was used for transfection of DiCre-expressing parasites with the Amaxa™ P3 primary cell 4D-Nucleofector™ X Kit L (Lonza, Cologne, Germany) [34,55]. Successful transfection was selected with 2.5 nM of the antifolate WR99210 (Jacobus Pharmaceutical Company, Princeton, NJ, USA), starting one day post transfection with frequent exchange of media. Once resistant parasites were established, they were selected for genomic integration with 400 ug/ml G418 (Sigma Aldrich). After limiting dilution of drug-resistant parasites [56], genomic DNA of six clones was isolated using Qiagen Blood and Tissue kit. Integration was confirmed via genotyping PCR using Q5 polymerase (NEB) and primer as listed (Table_S4), and one clone was used for further phenotyping. Conditional DiCre-mediated recombination between loxP sites was performed as described [34]. For KO induction, synchronous parasites were treated with 100 nM rapamycin (Sigma Aldrich) for 4 h (DMSO treatment as control), washed and returned to culture. Gene excision was confirmed by genotyping PCR, mRNA levels were checked in RNAseq samples, protein level via Western blot.

- **Western blot analysis**

Parasites were isolated from RBCs by 0.1% saponin and protease inhibitor cocktail PIC (Roche) in PBS and boiled for 10 min in 62 mM Tris pH6.5, 25 % glycerol, 2 % SDS, 0.2 M DTT, 0.05 % OrangeG. Proteins were separated on 4-12 % SDS gels (Biorad), transferred onto a nitrocellulose membrane prior to immunoblotting. In this study, rat anti-HA (1:2000, Roche) and mouse anti-Enolase (1:1000, Prof GK Jarori, Tata Institute for Fundamental Research) were used, conjugated secondary antibodies and Odyssey® imaging system (LiCOR Biosciences) according to manufacturer's recommendation.

- **Immunofluorescence assays (IFA)**

Immunofluorescence assay were performed as in [55] with the addition of 0.0075 % glutaraldehyde during fixation. Primary antibodies (rat anti-HA, rabbit anti-Gap45 [57], rabbit anti-Ama1 [58]) were used 1:500. For image acquisition, Leica DMi8 Widefield microscope was used, image processing and quantification was performed with software Fiji v2.9.0 (ImageJ).

- **Assays for parasite growth (PG), reproduction (PR) and egress (PE)**

Growth was determined by microscopic counting of parasites from Giemsa-stained thin blood films and expressed as percentage parasitemia (% infected RBCs/RBCs). For reproduction and egress assays, equal numbers of mature schizonts were Percoll-purified. For PR, they were incubated in 4 ml RPMI with 1 % hematocrit for 2 h, before the number of rings was quantified from Giemsa stain. Live imaging of PE was performed as described [55], parasites were binned in groups 15 sec post egress (normal / clustered merozoites). For RBC staining, RPMI was supplemented with 0.1x phalloidin 594 Conjugate (Abcam, Cambridge) during live imaging. RBC ghost location 40 sec post egress was categorized (distant/attached/overlapping).

- **Transmission Electron Microscopy (TEM)**

iRBCs were washed in PHEM buffer (2.5 mM $MgCl_2$/35 mM KCl/5 mM EGTA/10 mM Hepes/30 mM PIPES, pH 7.2), fixed for 1 hour in a solution containing 2.5 % glutaraldehyde, 4% formaldehyde, 4% sucrose in 0.1 M PHEM buffer, postfixed in 1 % OsO_4 plus 0.8 % ferrocyanide and 5 mM $CaCl_2$ in 0.1 M cacodylate buffer for 1 hour, washed twice in cacodylate buffer (10 min, 1 h) and double-distilled water (5 min, 15 min), respectively and dehydrated in a graded acetone series which included *en bloc* staining with 1 % uranyl acetate in the 20 % step. The cells were finally embedded in Epon812 epoxy resin to enable ultrathin sectioning. To carry out electron microscopy, the ultrathin sections were post-stained with 1 % lead citrate for 2 min. Transmission electron microscopy was carried out using either a Zeiss EM 912 (Zeiss AG, Oberkochen, Germany), set to an acceleration voltage of 80 kV, operated in the zero-loss mode and equipped with a 2k x 2k slow-scan CCD camera (TRS Tröndle Restlichtverstärkersysteme, Moorenweis, Germany) or a JEOL F200 (JEOL, Freising, Germany), operated at 200 kV equipped with a XAROSA 20 mega pixel CMOS camera (EMSIS, Münster, Germany.)

- **Preparation of nuclear extracts and Co-immunoprecipitation (co-IP) experiments**

Nuclei of *Pf*Snf2L-HA and 3D7 parasites were prepared as in [59] and treated with 0.5 U/μl benzonase (Sigma Aldrich) in 20 mM HEPES pH7.9/10 mM KCl/0.1 mM EDTA/0.1 mM EGTA/1 mM DTT/0.65 % Igepal CA-630 and PIC for 30 min at room temperature. For extraction of nuclear proteins, KCl was added to 0.4 M, incubated for 30 min at room temperature and insoluble fraction was removed by centrifugation (5000 g, 30 min, 4 °C). The supernatant was diluted with 2.5 vol of 50 mM Tris pH 7.4/50 mM NaCl/1 mM EDTA/1 % Igepal CA-630 and PIC, and incubated overnight at

4°C under constant agitation with equilibrated anti-HA magnetic beads (Thermo Fisher). Beads were pelleted using a magnetic rack, washed 3x with latter buffer and 3x with 50 mM Tris-HCl pH 8. Beads were dried, stored at -20 °C and used for LC-MS/MS analysis of co-immunoprecipitated proteins in *Pf*Snf2L-HA parasites (3D7 as negative control). Collected fractions (input, flowthrough, beads) were analyzed on 4-12 % SDS-PAGE, silver-stained and in additional version probed anti-HA in western blot.

- **Mass spectrometry (LC-MS/MS) and data analysis**

Beads were incubated with 10 ng/µL trypsin in 1 M urea/50 mM NH_4HCO_3 for 30 min, washed with 50 mM NH_4HCO_3, and the supernatant digested overnight in presence of 1 mM DTT. Digested peptides were alkylated and desalted prior to LC–MS analysis. For LC–MS/MS purposes, desalted peptides were injected in an Ultimate 3000 RSLCnano system (Thermo Fisher), separated in a 15-cm analytical column (75 µm ID with ReproSil-Pur C18-AQ 2.4 µm from Dr. Maisch) with a 50-min gradient from 4 % to 40 % acetonitrile in 0.1 % formic acid. The effluent from the HPLC was directly electrosprayed into a QexactiveHF (Thermo Fisher) operated in data dependent mode to automatically switch between full scan MS and MS/MS acquisition. Survey full scan MS spectra (from m/z 350 to 1,600) were acquired with resolution R = 60,000 at m/z 400 (AGC target of 3×10^6). The 10 most intense peptide ions with charge states between 2 and 5 were sequentially isolated to a target value of 1×10^5 and fragmented at 30 % normalized collision energy. Typical mass spectrometric conditions were as follows: spray voltage, 1.5 kV; heated capillary temperature, 275 °C; ion selection threshold, 33.000 counts.

MaxQuant 1.6.14.0 was used to identify proteins and quantify by iBAQ with the following parameters: Database Uniprot_UP000001450_Plasmodiumfalciparum_20201007.fasta; MS tol, 10 ppm; MS/MS tol, 20 ppm Da; PSM FDR, 0.01; Protein FDR, 0.01 min; Peptide Length, 7; Variable modifications, Oxidation (M), Acetyl (Protein N-term); Fixed modifications, Carbamidomethyl (C); Peptides for protein quantitation, razor and unique; Min. peptides, 1; Min. ratio count, 2. MaxQuant iBAQ values were log2 transformed, missing values implemented with 8. Ribosomal proteins and hits detected with only 1 peptide were excluded. Identified proteins were considered as interaction partners of the bait, if $\log_2$(Snf2L-3HA) − $\log_2$(3D7) > 3 or $\log_2$(Snf2L-3HA) − $\log_2$(3D7) > 2 & FDR <0.05. The mass spectrometry proteomics data have been deposited to the ProteomeXchange Consortium via the PRIDE [60] partner repository with the dataset identifier PXD041155.

- **RNA-seq and data analysis**

Total RNA from iRBCs containing highly synchronized parasites was isolated using Whole Blood Quick RNA kit (Zymo Research) according to the manufacturer's protocol. RNA quality was checked using 4200 TapeStation System (Agilent) and 300 ng were used as input for Illumina Stranded mRNA Prep Ligation (Illumina). Libraries were sequenced on the Illumina NextSeq 2000 Sequencing System. Sequenced reads (2x57bp bp, paired-end, ~20 Mio reads/sample) were trimmed with trimmomatic v0.39 [61] and mapped to *P. falciparum* 3D7 genome v3.0 (plasmoDB.org, release 52, [62]) using STAR 2.7.9a [63]. PlasmoDB annotation was converted to GTF-format with gffread 0.12.1 [64].Preprocessing and mapping quality control was done with FastQC 0.11.8 [65], qualimap 2.2.2d [66], samtools 1.12 [67] and multiqc 1.9 [68]. The pipeline was implemented with snakemake 5.32.0 [69] and is available at https://github.com/SimHolz/Watzlowik_et_al_2023, so are the R scripts. RSubread/FeatureCounts 2.12.2 was utilized to calculate read counts, while differential expression analysis was performed by DESeq2 [70,71] adjusted P-value <0.05 as significance cutoff. Further analysis and visualization were done in R [72] using tidyverse [73] and ggpubr [74]. DEGreport [75] was used for clustering and topGO [76] for GO term enrichment analysis. For expression quantile calculation transcript per millions (TPM) normalization was used. RNA-Seq data were submitted to Gene Expression Omnibus (GEO) database (accession number GSE228949).

RNA-seq-based cell cycle progression was estimated in R by comparing the normalized expression values of each sample to the RNAseq data from [77] using the statistical model previously described [78].

stimation of Snf2L Knockout efficacy was done by mapping reads to the sequence of the recodonized transfected Snf2L gene and counting reads mapped to the $\text{Snf2L}_{\text{recodon}}$ part of the gene which is disintegrated upon knockout induction.

- **ChIP-seq + data analysis**

– to be completed –

- **MNase-seq + data analysis**

MNase-digestion was adapted from [8] with following modifications: Highly synchronous parasites were crosslinked and stopped as described. RBCs were lysed and nuclei were isolated as for pulldown experiments. Nuclei were resuspended in 75 μl 50 mM Tris pH7.4/4 mM $MgCl_2$/1 mM $CaCl_2$/0.075 % NP40/1 mM DTT, PIC with 0.75 U Micrococcal nuclease (Worthington Biochemicals Corporation) and 50 U Exonuclease III (NEB). Each sample was aliquoted in 3 x 25 μl and incubated for 2.5 / 5 / 10 min at 37 °C under agitation (low/mid/high digestion), before the reaction was stopped by adding 25 μl 2 % Triton X100/0.6 % SDS/300 mM NaCl/6 mM EDTA/PIC. and placed at 4 °C. Decrosslinking was performed at 45 °C overnight after adjusting to 1 % SDS/0.1 M $NaHCO_3$/0.5 M NaCl. Proteins were digested by addition of 40 μg of Proteinase K (Zymo Research) and incubation for 1 h at 55 °C. Subsequently, DNA was isolated using EXTRACTME DNA clean-up kit and Micro Spin columns (Blirt) as the manufacturer recommends. Digestion efficacy of extracted DNA fragments were analyzed with TapeStation 4200 System and DNA size distribution (molarity) was visualized using BioanalyzeR. For low digested samples, DNA fragments >700 bp were removed using SPRI beads, no size-selection step was applied for high digested samples.

1 ng of high/low digested samples was used as input for NEBNext Ultra II DNA library prep kit (NEB), according to manufacturer's protocol. Libraries were sequenced on the Illumina NextSeq 2000 Sequencing System. Sequenced reads (2x65 bp, paired-end, ~20 Mio reads/sample) were trimmed with skewer 0.2.2 [79] and subsequently mapped to *P. falciparum* 3D7 genome v3.0 (plasmoDB.org, release 52) using Bowtie2 2.3.5 [80] with "--very-sensitive --no-discordant --no-mixed --no-unal" options. Mapped fragments were filtered with deeptools 3.5.0 [81] for a mapping quality of at least 20, a fragment size between 75 -175 bp and proper read pairs. The remaining fragments were used for nucleosome calling with DANPOS (custom version, based on DANPOS3)[82]. Quality control was done with FastQC 0.11.8 [65], qualimap 2.2.2d [65], samtools 1.12 [67] and multiqc 1.9 [68] .The pipeline was implemented with snakemake 5.32.0 [69] and is available at https://github.com/SimHolz/Watzlowik_et_al_2023, MNase-Seq data at GEO (GSE228949). Further analysis was done with R etc.

- **Detailed analysis**

MNase-sequencing of schizont stage chromatin +/- Snf2L-KO was performed in triplicates, MNase-sequencing of late ring stage chromatin +/- Snf2L-KO in duplicates.

- DANPOS: Replicate bam files were put into a single directory respectively to be recognized as a single dataset by DANPOS. Nucleosome calling was performed with the following command: `python3 danpos.py dpos <Input> -o <outDir> -m 1 -c 51137214 --extend 73 -a 1 -jd 100 -e 1 -z 20 -s 1`
  For comparison and differential nucleosome positioning of two datasets the two inputs are separated by ":" like "iKO_0h_high/:noKO_0h_high/". The differential nucleosome positioning results were adjusted with a custom R script using simulated random nucleosome positions and Benjamini Hochberg Procedure to calculate FDR values and loess-smoothing for improved dyad position calling.
- DYNAMICs: Among the nucleosomes obtained from differential nucleosomes analysis in late ring stage, the following were defined as dynamically changed: Adjusted FDR values (-log10 transformed for occupancy and fuzziness changes, not transformed for shifts) were normalized to maximum change and ranked. Slope=1 was defined as cutoff (see FigS6B). Cutoff values were extracted and applied for differential schizont stage nucleosomes. Among dynamic nucleosomes, only the ones within the 20 % best-positioned nucleosomes in both stages were considered (20 % lowest fuzziness-score in noKO: <47 for schizont, <49 for late rings).
- Gene part assignment: Dynamic nucleosomes (<1 % for schizont/~20 % for late rings) were assigned to gene parts obtained from PlasmoDB annotation with a minimum overlap of 99 bp: 5'UTR, protein-coding (= CDS), 3'UTR, intergenic (= no feature assigned), others (= introns, pseudogenes, snoRNA, ncRNA, tRNA, snRNA, rRNA).
- Profiles: The transcriptional landmark sites (TSS, AUG, STOP, TTS) were extracted from PlasmoDB annotation for each gene on chromosome 1-14, only one site per gene considered. Occupancy profiles were obtained by aligning the coverage 1000 bp upstream and downstream of the mark for all available replicates and averaging. The corresponding GC-content around landmarks was aligned, averaged, and smoothed accordingly. Occupancy profiles around +1 nucleosome were created analogously.
- Nucleosome Dynamics Suite: BAM files were used as input for Nucleosome Dynamics program suite [40], utilizing the readBam, nucleR and txstart function. nucleR was run with "--type paired --fragmentLen 175 --thresholdPercentage 50" in addition to default parameters and txstart with "--p1.max.downstream 100" in addition to default parameters.
- NFR Width: Distance between +1 and -1 nucleosome as detected by the nucleosome dynamics txstart function was used as NFR width estimation.

- +1 Nucleosome Annotation: BAM files of replicates of noKO_24h_high and noKO_0h_high were merged respectively and used as input for Nucleosome Dynamics program suite [40], The 3'-end of the resulting gff from txstart was used as +1 nucleosome dyad annotation.
- Mean Fuzziness change calculation: Promoter regions were defined as 1000 bp upstream and 1000 bp downstream of the +1 nucleosomes identified via NucDyn. All called nucleosomes with a minimum overlap of 75 bp with the promoter region were averaged. Mean fuzziness scores were subtracted (iKO-noKO). Only promoters harboring at least 6 called nucleosomes were considered in this analysis.

- **ADP biosensor assay**

ATPase activity and inhibition were measured by ADP biosensor assay: In 20 μl, 0.2 μM TMR-maleimide-labelled ParM (prepared according to [83]) was mixed with 125 μM ATP, 100 ng plasmid pT11 DNA, 5 μM H4 peptide (aa8-25, AnaSpec) in 10 mM Tris pH8.6/1.5 mM $MgCl_2$/100 mM KCl/0.01 % Pluronic in presence (or absence as negative control) of 0.4 μM recombinantly expressed *Pf*Snf2L and XXX in varying concentrations. Resulted ADP binding to ParM is expressed by increasing fluorescence intensity and was kinetically measured at 28 °C in 2 min intervals over 2 h in a Tecan infinite F500 reader. Signal was normalized to timepoint 0.

- **Toxicity assay Plasmodium / Toxoplasma / HeLa**

Toxicity for Plasmodium was determined by culturing in presence of drug/DMSO for 72 hours and subsequent quantification of parasitemia in Giemsa-stained blood films. Toxicity for Toxoplasma was tested via plaque assay, whereby 1000 *T. gondii* tachyzoites inoculated onto human foreskin fibroblasts as in [84] were treated with drug/DMSO, fixed and stained 6 days later and evaluated with regard to plaque formation. Toxicity on human HeLa cells, cultured as in [48], was investigated by 48 hour drug/DMSO treatment and subsequent monitoring of metabolic activity using the Cell Proliferation Kit II-XTT (Sigma Aldrich) according to manufacturer's recommendation. EC50 values for A/C were obtained by fitting dose response model using three-parameter log-logistic models and estimated for B.

- **Gametocyte induction**

Gametocytes were generated using the nutrient deprivation induction method as described (ref). Briefly, synchronized trophozoites were cultured at ~4-5 % parasitemia before gametocytogenesis was induced by splitting out the culture to 2 % parasitemia in minimal fatty acid (mFA) media (Day 0). With that, drug / DMSO treatment was started. 22 hours post induction, media was replaced back to complete RPMI media. On Day 2, parasitemia was quantified in Giemsa-stained blood smears and 20 U/ml Heparin was added to the culture. The media was changed daily until quantification of gametocytemia on Day 8. Gametocyte conversion rate was calculated: GCR=Gametocytemia-Day8/Parasitemia-Day2.

References

1. Otto, T. D. *et al.* New insights into the blood-stage transcriptome of Plasmodium falciparum using RNA-Seq. *Mol. Microbiol.* **76**, 12–24 (2010).
2. Rovira-Graells, N. *et al.* Transcriptional variation in the malaria parasite Plasmodium falciparum. *Genome Res.* **22**, 925–938 (2012).
3. Bischoff, E. & Vaquero, C. In silico and biological survey of transcription-associated proteins implicated in the transcriptional machinery during the erythrocytic development of Plasmodium falciparum. *BMC Genomics* **11**, 34 (2010).
4. Painter, H. J., Campbell, T. L. & Llinás, M. The Apicomplexan AP2 family: integral factors regulating Plasmodium development. *Mol. Biochem. Parasitol.* **176**, 1–7 (2011).
5. Iyer, L. M., Anantharaman, V., Wolf, M. Y. & Aravind, L. Comparative genomics of transcription factors and chromatin proteins in parasitic protists and other eukaryotes. *Int. J. Parasitol.* **38**, 1–31 (2008).
6. Voss, T. S., Bozdech, Z. & Bártfai, R. Epigenetic memory takes center stage in the survival strategy of malaria parasites. *Current Opinion in Microbiology* **20**, 88–95 (2014).
7. Bunnik, E. M. *et al.* DNA-encoded nucleosome occupancy is associated with transcription levels in the human malaria parasite Plasmodium falciparum. *BMC Genomics* **15**, 347 (2014).
8. Kensche, P. R. *et al.* The nucleosome landscape of *Plasmodium falciparum* reveals chromatin architecture and dynamics of regulatory sequences. *Nucleic Acids Research* **44**, 2110–2124 (2016).
9. Toenhake, C. G. *et al.* Chromatin Accessibility-Based Characterization of the Gene Regulatory Network Underlying Plasmodium falciparum Blood-Stage Development. *Cell Host Microbe* **23**, 557-569.e9 (2018).

10. Ponts, N. *et al*. Nucleosome landscape and control of transcription in the human malaria parasite. *Genome Res*. **20**, 228–238 (2010).
11. Kafsack, B. F. C. *et al*. A transcriptional switch underlies commitment to sexual development in malaria parasites. *Nature* **507**, 248–252 (2014).
12. Filarsky, M. *et al*. GDV1 induces sexual commitment of malaria parasites by antagonizing HP1-dependent gene silencing. *Science* **359**, 1259–1263 (2018).
13. Watzlowik, M. T., Das, S., Meissner, M. & Längst, G. Peculiarities of Plasmodium falciparum Gene Regulation and Chromatin Structure. *Int J Mol Sci* **22**, 5168 (2021).
14. Gibney, E. R. & Nolan, C. M. Epigenetics and gene expression. *Heredity* **105**, 4–13 (2010).
15. Lai, W. K. M. & Pugh, B. F. Understanding nucleosome dynamics and their links to gene expression and DNA replication. *Nature Reviews Molecular Cell Biology* **18**, 548–562 (2017).
16. Lodde, V., Floris, M., Muroni, M. R., Cucca, F. & Idda, M. L. Non-coding RNAS in malaria infection. *WIREs RNA* **13**, (2022).
17. Rando, O. J. & Winston, F. Chromatin and Transcription in Yeast. *Genetics* **190**, 351–387 (2012).
18. Singh, A. K. & Mueller-Planitz, F. Nucleosome Positioning and Spacing: From Mechanism to Function. *Journal of Molecular Biology* **433**, 166847 (2021).
19. Becker, P. B. & Workman, J. L. Nucleosome Remodeling and Epigenetics. *Cold Spring Harbor Perspectives in Biology* **5**, a017905–a017905 (2013).
20. Narlikar, G. J., Sundaramoorthy, R. & Owen-Hughes, T. Mechanisms and Functions of ATP-Dependent Chromatin-Remodeling Enzymes. *Cell* **154**, 490–503 (2013).
21. Yen, K., Vinayachandran, V., Batta, K., Koerber, R. T. & Pugh, B. F. Genome-wide Nucleosome Specificity and Directionality of Chromatin Remodelers. *Cell* **149**, 1461–1473 (2012).
22. Rippe, K. *et al*. DNA sequence- and conformation-directed positioning of nucleosomes by chromatin-remodeling complexes. *Proc Natl Acad Sci U S A* **104**, 15635–15640 (2007).
23. Flaus, A. Identification of multiple distinct Snf2 subfamilies with conserved structural motifs. *Nucleic Acids Research* **34**, 2887–2905 (2006).
24. Ji, D. D. & Arnot, D. E. A Plasmodium falciparum homologue of the ATPase subunit of a multi-protein complex involved in chromatin remodelling for transcription. *Mol. Biochem. Parasitol*. **88**, 151–162 (1997).
25. Corona, D. F. V. *et al*. ISWI Regulates Higher-Order Chromatin Structure and Histone H1 Assembly In Vivo. *PLoS Biol* **5**, e232 (2007).
26. Längst, G. & Becker, P. B. Nucleosome mobilization and positioning by ISWI-containing chromatin-remodeling factors. *J Cell Sci* **114**, 2561–2568 (2001).
27. Hopfner, K.-P., Gerhold, C.-B., Lakomek, K. & Wollmann, P. Swi2/Snf2 remodelers: hybrid views on hybrid molecular machines. *Curr Opin Struct Biol* **22**, 225–233 (2012).
28. Gurova, K., Chang, H.-W., Valieva, M. E., Sandlesh, P. & Studitsky, V. M. Structure and function of the histone chaperone FACT – Resolving FACTual issues. *Biochimica et Biophysica Acta (BBA) - Gene Regulatory Mechanisms* **1861**, 892–904 (2018).
29. Alabert, C., Jasencakova, Z. & Groth, A. Chromatin Replication and Histone Dynamics. in *DNA Replication* (eds. Masai, H. & Foiani, M.) vol. 1042 311–333 (Springer Singapore, 2017).
30. Miao, J. *et al*. A unique GCN5 histone acetyltransferase complex controls erythrocyte invasion and virulence in the malaria parasite Plasmodium falciparum. *PLoS Pathog* **17**, e1009351 (2021).
31. Santos, J. M. *et al*. Red Blood Cell Invasion by the Malaria Parasite Is Coordinated by the PfAP2-I Transcription Factor. *Cell Host Microbe* **21**, 731-741.e10 (2017).
32. Gupta, M. K. *et al*. Role of Chromatin assembly factor 1 in DNA replication of Plasmodium falciparum. *Biochemical and Biophysical Research Communications* **495**, 1285–1291 (2018).
33. Bryant, J. M. *et al*. Exploring the virulence gene interactome with CRISPR / DC as9 in the human malaria parasite. *Molecular Systems Biology* **16**, (2020).
34. Collins, C. R. *et al*. Robust inducible Cre recombinase activity in the human malaria parasite *Plasmodium falciparum* enables efficient gene deletion within a single asexual erythrocytic growth cycle: Conditional Cre in the human malaria parasite. *Molecular Microbiology* **88**, 687–701 (2013).
35. de Koning-Ward, T. F., Dixon, M. W. A., Tilley, L. & Gilson, P. R. Plasmodium species: master renovators of their host cells. *Nat Rev Microbiol* **14**, 494–507 (2016).
36. Schwartz, U. *et al*. Characterizing the nuclease accessibility of DNA in human cells to map higher order structures of chromatin. *Nucleic Acids Research* **47**, 1239–1254 (2019).
37. Mbengue, A., Audiger, N., Vialla, E., Dubremetz, J.-F. & Braun-Breton, C. Novel *Plasmodium falciparum* Maurer's clefts protein families implicated in the release of infectious merozoites: Novel *P. falciparum* exported proteins. *Molecular Microbiology* **88**, 425–442 (2013).
38. Poran, A. *et al*. Single-cell RNA sequencing reveals a signature of sexual commitment in malaria parasites. *Nature* **551**, 95–99 (2017).

39. van Biljon, R. *et al*. Hierarchical transcriptional control regulates Plasmodium falciparum sexual differentiation. *BMC Genomics* **20**, 920 (2019).
40. Buitrago, D. *et al*. Nucleosome Dynamics: a new tool for the dynamic analysis of nucleosome positioning. *Nucleic Acids Research* **47**, 9511–9523 (2019).
41. Pickford, A. K. *et al*. Expression Patterns of Plasmodium falciparum Clonally Variant Genes at the Onset of a Blood Infection in Malaria-Naive Humans. *mBio* **12**, e0163621 (2021).
42. Barisic, D., Stadler, M. B., Iurlaro, M. & Schübeler, D. Mammalian ISWI and SWI/SNF selectively mediate binding of distinct transcription factors. *Nature* **569**, 136–140 (2019).
43. Cui, L. *et al*. PfGCN5-mediated histone H3 acetylation plays a key role in gene expression in Plasmodium falciparum. *Eukaryotic Cell* **6**, 1219–1227 (2007).
44. Coleman, B. I. *et al*. A Plasmodium falciparum histone deacetylase regulates antigenic variation and gametocyte conversion. *Cell Host Microbe* **16**, 177–186 (2014).
45. Hoffmeister, H. *et al*. CHD3 and CHD4 form distinct NuRD complexes with different yet overlapping functionality. *Nucleic Acids Res* **45**, 10534–10554 (2017).
46. Silberhorn, E. *et al*. Plasmodium falciparum Nucleosomes Exhibit Reduced Stability and Lost Sequence Dependent Nucleosome Positioning. *PLoS Pathog*. **12**, e1006080 (2016).
47. Laybourn, P. J. & Kadonaga, J. T. Role of nucleosomal cores and histone H1 in regulation of transcription by RNA polymerase II. *Science* **254**, 238–245 (1991).
48. Maldonado, R., Schwartz, U., Silberhorn, E. & Längst, G. Nucleosomes Stabilize ssRNA-dsDNA Triple Helices in Human Cells. *Molecular Cell* **73**, 1243-1254.e6 (2019).
49. Fitzgerald, D. J. *et al*. Protein complex expression by using multigene baculoviral vectors. *Nat Methods* **3**, 1021–1032 (2006).
50. Berger, I., Fitzgerald, D. J. & Richmond, T. J. Baculovirus expression system for heterologous multiprotein complexes. *Nat. Biotechnol*. **22**, 1583–1587 (2004).
51. Jones, M. L. *et al*. A versatile strategy for rapid conditional genome engineering using loxP sites in a small synthetic intron in Plasmodium falciparum. *Scientific Reports* **6**, 21800 (2016).
52. Das, S. *et al*. Processing of Plasmodium falciparum Merozoite Surface Protein MSP1 Activates a Spectrin-Binding Function Enabling Parasite Egress from RBCs. *Cell Host & Microbe* **18**, 433–444 (2015).
53. Birnbaum, J. *et al*. A genetic system to study Plasmodium falciparum protein function. *Nature Methods* **14**, 450–456 (2017).
54. Blackman, M. J. Chapter 11: Purification of Plasmodium falciparum Merozoites for Analysis of the Processing of Merozoite Surface Protein-1. in *Methods in Cell Biology* vol. 45 213–220 (Elsevier, 1995).
55. Das, S., Lemgruber, L., Tay, C. L., Baum, J. & Meissner, M. Multiple essential functions of Plasmodium falciparum actin-1 during malaria blood-stage development. *BMC Biology* **15**, (2017).
56. Thomas, J. A. *et al*. Development and Application of a Simple Plaque Assay for the Human Malaria Parasite Plasmodium falciparum. *PLoS ONE* **11**, e0157873 (2016).
57. Jones, M. L., Kitson, E. L. & Rayner, J. C. Plasmodium falciparum erythrocyte invasion: a conserved myosin associated complex. *Mol Biochem Parasitol* **147**, 74–84 (2006).
58. Collins, C. R., Withers-Martinez, C., Hackett, F. & Blackman, M. J. An Inhibitory Antibody Blocks Interactions between Components of the Malarial Invasion Machinery. *PLoS Pathog* **5**, e1000273 (2009).
59. Josling, G. A. *et al*. A Plasmodium Falciparum Bromodomain Protein Regulates Invasion Gene Expression. *Cell Host Microbe* **17**, 741–751 (2015).
60. Perez-Riverol, Y. *et al*. The PRIDE database resources in 2022: a hub for mass spectrometry-based proteomics evidences. *Nucleic Acids Research* **50**, D543–D552 (2022).
61. Bolger, A. M., Lohse, M. & Usadel, B. Trimmomatic: A Flexible Trimmer for Illumina Sequence Data. *Bioinformatics (Oxford, England)* **30**, 2114–2120 (2014).
62. Aurrecoechea, C. *et al*. PlasmoDB: A Functional Genomic Database for Malaria Parasites. *Nucleic Acids Research* **37**, D539-543 (2009).
63. Dobin, A. *et al*. STAR: Ultrafast Universal RNA-seq Aligner. *Bioinformatics (Oxford, England)* **29**, 15–21 (2013).
64. Pertea, G. & Pertea, M. GFF Utilities: GffRead and GffCompare. *F1000Res* **9**, ISCB Comm J-304 (2020).
65. Andrews Simon. FastQC - A Quality Control Tool for High Throughput Sequence Data.
66. Okonechnikov, K., Conesa, A. & García-Alcalde, F. Qualimap 2: Advanced Multi-Sample Quality Control for High-Throughput Sequencing Data. *Bioinformatics (Oxford, England)* **32**, 292–294 (2016).
67. Li, H. *et al*. The Sequence Alignment/Map Format and SAMtools. *Bioinformatics (Oxford, England)* **25**, 2078–2079 (2009).
68. Ewels, P., Magnusson, M., Lundin, S. & Käller, M. MultiQC: Summarize Analysis Results for Multiple Tools and Samples in a Single Report. *Bioinformatics (Oxford, England)* **32**, 3047–3048 (2016).
69. Mölder, F. *et al*. Sustainable data analysis with Snakemake. *F1000Res* **10**, 33 (2021).

70. Love, M. I., Huber, W. & Anders, S. Moderated estimation of fold change and dispersion for RNA-seq data with DESeq2. *Genome Biol* **15**, 550 (2014).
71. Liao, Y., Smyth, G. K. & Shi, W. featureCounts: an efficient general purpose program for assigning sequence reads to genomic features. *Bioinformatics* **30**, 923–930 (2014).
72. R Core Team. R: A Language and Environment for Statistical Computing. (2022).
73. Wickham, H. *et al*. Welcome to the Tidyverse. *Journal of Open Source Software* **4**, 1686 (2019).
74. Kassambara, A. Ggpubr: ‘ggplot2’ Based Publication Ready Plots. (2022).
75. Pantano, L. DEGreport: Report of DEG Analysis. (2022).
76. Alexa, A. & Rahnenfuhrer, J. topGO: Enrichment Analysis for Gene Ontology. (2022).
77. Painter, H. J. *et al*. Genome-wide real-time in vivo transcriptional dynamics during Plasmodium falciparum blood-stage development. *Nat Commun* **9**, 2656 (2018).
78. Lemieux, J. E. *et al*. Statistical estimation of cell-cycle progression and lineage commitment in *Plasmodium falciparum* reveals a homogeneous pattern of transcription in ex vivo culture. *Proc. Natl. Acad. Sci. U.S.A.* **106**, 7559–7564 (2009).
79. Jiang, H., Lei, R., Ding, S.-W. & Zhu, S. Skewer: A Fast and Accurate Adapter Trimmer for next-Generation Sequencing Paired-End Reads. *BMC bioinformatics* **15**, 182 (2014).
80. Langmead, B. & Salzberg, S. L. Fast Gapped-Read Alignment with Bowtie 2. *Nature Methods* **9**, 357–359 (2012).
81. Ramírez, F. *et al*. deepTools2: A next Generation Web Server for Deep-Sequencing Data Analysis. *Nucleic Acids Research* **44**, W160-165 (2016).
82. Chen, K. *et al*. DANPOS: Dynamic Analysis of Nucleosome Position and Occupancy by Sequencing. *Genome Research* **23**, 341–351 (2013).
83. Kunzelmann, S. & Webb, M. R. A Fluorescent, Reagentless Biosensor for ADP Based on Tetramethylrhodamine-Labeled ParM. *ACS Chemical Biology* **5**, 415–425 (2010).
84. Li, W. *et al*. A splitCas9 phenotypic screen in Toxoplasma gondii identifies proteins involved in host cell egress and invasion. *Nat Microbiol* **7**, 882–895 (2022).